

Role of E-cadherin in metastatic brain colonization



DISSERTATION ZUR ERLANGUNG DES
DOKTORGRADES DER NATURWISSENSCHAFTEN (DR. RER. NAT.)
DER FAKULTÄT FÜR BIOLOGIE UND VORKLINISCHE MEDIZIN
DER UNIVERSITÄT REGENSBURG

vorgelegt von
Daniela Christine Sparrer

aus
München

im Jahr
2020

Das Promotionsgesuch wurde eingereicht am:

10.07.2020

Die Arbeit wurde angeleitet von:

Prof. Dr. Dr. Michael P. Krahn

Unterschrift:

Table of contents

Table of contents	I
Abstract.....	VI
List of Figures	VII
List of Tables	IX
Abbreviations.....	X
1. Introduction.....	1
1.1. Metastatic colonization	1
1.1.1. Steps of metastatic colonization	1
1.1.2. Different patterns of colonization	3
1.1.3. The macro-metastasis/organ parenchyma interface (MMPI).....	5
1.1.4. Infiltrative MMPI patterns in human breast cancer brain metastases	5
1.2. Target mechanisms in metastatic colonization	6
1.2.1. Cell adhesion receptor E-cadherin.....	7
1.2.2. Contact inhibition mechanisms and E-cadherin.....	9
1.2.3. The metastatic microenvironment of brain metastases.....	11
1.3. Mouse models for the study of metastatic colonization in the brain	13
1.4. Aims of the study	16
2. Materials and Methods	17
2.1. Materials.....	17
2.1.1. Biological materials.....	17
2.1.1.1. Bacterial strains	17
2.1.1.2. Cell lines	17
2.1.1.2.1. Lentiviral production cell line	17
2.1.1.2.2. Parental murine tumor cell lines.....	17
2.1.1.2.3. Modified murine tumor cell lines.....	18
2.1.1.3. Mouse strains	18
2.1.2. Chemicals and reagents	18
2.1.3. Bacterial media and agarose plates.....	21
2.1.4. Cell culture media and additives	22
2.1.5. Buffers and solutions	22
2.1.6. Antibodies and fluorescent dyes	25
2.1.7. Oligonucleotides.....	26
2.1.8. Plasmids	28
2.1.9. Enzymes	29
2.1.10. Commercial kits	29

2.1.11. Consumables and instruments.....	30
2.1.12. Equipment.....	32
2.1.13. Software products and databases.....	34
2.2. Methods	35
2.2.1. Cloning	35
2.2.1.1. Knockdown vector	35
2.2.1.1.1. shRNA insert preparation	36
2.2.1.1.1.1. Phosphorylation of oligonucleotides.....	36
2.2.1.1.1.2. Annealing of phosphorylated oligonucleotides	36
2.2.1.1.2. Vector preparation.....	36
2.2.1.1.2.1. Cutting of vector.....	37
2.2.1.1.2.2. Agarose gel electrophoresis.....	37
2.2.1.1.2.3. Purification of vector	38
2.2.1.1.2.4. Dephosphorylation of vector	38
2.2.1.1.3. Ligation of construct.....	38
2.2.1.2. Overexpression vector	39
2.2.1.2.1. Gateway cloning technology.....	39
2.2.1.2.1.1. Preparation of Gateway entry vector	39
2.2.1.2.1.2. Transfer of gene cassette into Gateway destination vector	39
2.2.1.3. Transformation of chemically competent <i>E. coli</i> cells	41
2.2.1.4. DNA preparation.....	42
2.2.1.4.1. Mini-preparation.....	42
2.2.1.4.2. Restriction digestion.....	42
2.2.1.4.3. Midi-preparation and sequencing.....	43
2.2.2. Cell culture methods.....	44
2.2.2.1. Maintenance of murine tumor cell lines.....	44
2.2.2.2. Lentivirus-mediated gene delivery (transduction)	44
2.2.2.2.1. Lentiviral particle preparation	44
2.2.2.2.2. Transduction of target cells	45
2.2.2.2.3. Selection of single clones.....	45
2.2.2.2.4. Viral particle test.....	45
2.2.2.2.5. Stability of transduction	46
2.2.2.3. Assessment of cell viability and proliferation	46
2.2.2.3.1. Cell proliferation	46
2.2.2.3.2. MTT assay	47
2.2.2.3.3. BrdU assay	47

2.2.2.4. Functional <i>in vitro</i> assays	48
2.2.2.4.1. Cell migration assay with turned coverslips	48
2.2.2.4.2. Cell invasion assay in a modified Boyden chamber	49
2.2.2.4.3. Colony formation assay in soft agar	49
2.2.2.4.4. Spheroid formation assay using hanging drop method	50
2.2.3. <i>In vivo</i> experiments.....	52
2.2.3.1. Maintenance of animals	52
2.2.3.2. Cancer cell preparation for injection	52
2.2.3.3. Stereotactical intracortical injection.....	52
2.2.3.4. Animal monitoring and Hanging Wire test	54
2.2.3.5. Perfusion and brain tissue sample collection.....	54
2.2.4. Protein biochemical methods	55
2.2.4.1. Protein isolation	55
2.2.4.2. Protein quantification	55
2.2.4.3. Protein separation by SDS-PAGE	55
2.2.4.4. Protein analysis by Western blot.....	56
2.2.5. Gene expression analysis	57
2.2.5.1. Isolation of total RNA from tumor cells	57
2.2.5.2. Isolation of total RNA from brain tissues	57
2.2.5.3. Reverse transcription.....	58
2.2.5.4. Quantitative real-time PCR	58
2.2.5.4.1. Establishment of primers for qRT-PCR reactions.....	59
2.2.5.4.2. Data visualization with heatmaps	59
2.2.6. Staining.....	60
2.2.6.1. Staining of tumor cells	60
2.2.6.1.1. Phalloidin staining	60
2.2.6.1.2. Immunofluorescence staining	60
2.2.6.2. Staining of brain tissues	61
2.2.6.2.1. Hematoxylin and eosin staining	62
2.2.6.2.2. Immunohistochemical staining.....	62
2.2.6.2.2.1. CD3, CK8 and IBA1 staining.....	63
2.2.6.2.2.2. CD31 and VIM staining	64
2.2.6.2.2.3. ECAD staining	65
2.2.6.2.2.4. GFAP staining	66
2.2.6.2.3. Quantification of immunohistochemical staining.....	67
2.2.6.2.3.1. Quantification of ECAD staining	67

2.2.6.2.3.2. Quantification of CD31 staining	67
2.2.6.2.3.3. Quantification of IBA1, GFAP and CD3 staining	68
2.2.7. Microscopy	69
2.2.7.1. Bright field microscopy	69
2.2.7.2. Confocal microscopy.....	69
2.2.8. Statistical analysis	69
3. Results	70
3.1. Brain metastasis mouse models.....	71
3.1.1. MMPI patterns in brain metastasis mouse models	71
3.1.2. E-cadherin expression in brain metastasis mouse models	72
3.1.3. Metastatic microenvironment in brain metastasis mouse models.....	73
3.2. Characterization of murine brain metastasis model cell lines	75
3.2.1. Basic characterization of murine brain metastasis model cell lines.....	75
3.2.2. Functional characterization of murine brain metastasis model cell lines	77
3.2.3. Contact inhibition mechanisms in murine brain metastasis model cell lines	80
3.2.4. Gene expression signature of murine brain metastasis model cell lines.....	82
3.3. E-cadherin modifications in murine brain metastasis model cell lines.....	84
3.3.1. Establishment of E-cadherin modifications in murine brain metastasis model cell lines.....	84
3.3.1.1. E-cadherin overexpression in diffuse infiltrative cell lines	85
3.3.1.2. E-cadherin knockdown in epithelial infiltrative cell lines	87
3.3.2. Characterization of E-cadherin modifications in murine brain metastasis model cell lines.....	89
3.3.2.1. No effect of E-cadherin modifications on gene expression signature.....	89
3.3.2.2. Reduced migration and invasive capacity after E-cadherin overexpression	90
3.3.2.3. Increased migration and invasive capacity after E-cadherin knockdown.....	92
3.3.2.4. Colony formation ability after E-cadherin modifications.....	94
3.3.3. Effects of E-cadherin modifications on contact inhibition mechanisms.....	95
3.3.3.1. No rescue of contact inhibition after E-cadherin overexpression.....	95
3.3.3.2. Impaired contact inhibition after E-cadherin knockdown	97
3.3.4. Summary of <i>in vitro</i> characterization results	99
3.4. E-cadherin modifications in brain metastasis mouse models.....	100
3.4.1. Effects of E-cadherin modifications on overall survival	100
3.4.1.1. Prolonged survival after E-cadherin overexpression.....	100
3.4.1.2. Shortened survival after E-cadherin knockdown	102
3.4.1.3. Impact on colonization index	104
3.4.1.4. Correlation of overall survival and vimentin level.....	105

3.4.2.	Effects of E-cadherin modifications on MMPI pattern and infiltration	107
3.4.2.1.	Reduced infiltration at the MMPI after E-cadherin overexpression	107
3.4.2.2.	Increased infiltration at the MMPI after E-cadherin knockdown.....	109
3.4.3.	Effects of E-cadherin modifications on angiogenesis in brain metastases	111
3.4.4.	Effects of E-cadherin modifications on metastatic microenvironment	113
3.4.4.1.	Characterization of microglia/macrophages in the metastatic brain tissue after E-cadherin modifications	113
3.4.4.2.	Characterization of astrocytes in the metastatic brain tissue after E-cadherin modifications.....	115
3.4.4.3.	Characterization of T cells in the metastatic brain tissue after E-cadherin modifications.....	117
3.4.4.4.	Overview of changes in the metastatic microenvironment.....	119
3.4.5.	Impact of entity on angiogenesis and metastatic microenvironment.....	120
3.4.6.	Summary of <i>in vivo</i> characterization results	121
3.5.	Verification of the prognostic value of the gene expression signature	122
3.5.1.	Validation of gene expression signature in mouse models.....	122
3.5.2.	Application of gene expression signature on human metastases	124
4.	Discussion	125
4.1.	Selection of mouse models for the study of the MMPI in brain metastases	125
4.1.1.	Comparison of murine and human brain metastases	125
4.1.2.	Characterization of respective murine cancer cell lines	126
4.2.	Role of E-cadherin in metastatic brain colonization.....	127
4.2.1.	Impact of E-cadherin modifications in murine cancer cell lines.....	128
4.2.2.	Impact of E-cadherin modifications in brain metastasis mouse models	130
4.2.2.1.	Impact of E-cadherin level on infiltration grade at the MMPI	130
4.2.2.2.	Prolonged survival due to reduced infiltration at the MMPI after E-cadherin overexpression	131
4.2.2.3.	Shortened survival due to increased infiltration at the MMPI after E-cadherin knockdown	131
4.2.2.4.	Correlation of growth pattern and angiogenesis in metastatic tissue	133
4.2.2.5.	Impact of infiltration grade on the metastatic microenvironment	134
4.2.3.	Contact inhibition as potential therapeutic target mechanism	137
4.3.	Prognostic value of established gene expression signature	138
4.4.	Future research perspectives	139
5.	Summary and Conclusions	140
6.	Bibliography.....	143
	Acknowledgements.....	149
	Appendix.....	150

Abstract

Brain metastases are associated with a very poor prognosis and frequently occur in patients suffering from breast or colorectal cancer. During the process of metastatic colonization, successfully disseminated cancer cells settle in the brain and progress into macro-metastases. In this context, we recently summarized significant morphological differences at the macro-metastases/organ parenchyma interface (MMPI) with a strong influence on prognosis in several studies. While displacing metastases usually displayed a more favorable prognosis, infiltrative metastases had an unfavorable disease progression.

Since diffuse and epithelial infiltrative cells differed in their pathophysiology, the aim of this study was to investigate the potentially responsible mechanisms underlying this difference. In our lab, we previously established a variety of brain metastasis mouse models that allow the detailed characterization of the MMPI on a morphological and molecular basis. Interestingly, diffuse and epithelial infiltrative models showed differences in their innate expression levels of the cell adhesion receptor E-cadherin across species and entities. However, we hypothesized that E-cadherin is not only a marker for the type of infiltration, but also plays a critical functional role.

Thus, we performed specific opposing genetic modifications of E-cadherin in the corresponding cell lines of our brain metastasis mouse models representing the different infiltrative MMPI patterns to investigate the impact on the infiltration pattern and the metastatic microenvironment. Although both genetic approaches provoked profound phenotypic changes, they had no influence on the original characteristic of the cell. Nevertheless, the gain of E-cadherin decreased migratory and invasive capacity *in vitro*, while the artificial loss made cells more invasive across entities. This was reflected in the animal model with less aggressive metastases and prolonged survival after the overexpression of E-cadherin and increased aggressiveness and shortened survival in the knockdown cohorts. The switch of the infiltration pattern due to the E-cadherin modification in the metastatic outgrowth models, from diffuse to epithelial-like infiltrative after the gain of E-cadherin and the other way around after its loss, further resulted in an altered immune reaction of the metastatic microenvironment. In general, diffuse infiltrative patterns were associated with an increased immune response at the MMPI. Furthermore, we could establish a gene expression signature that clearly differentiated diffuse and epithelial infiltrative mouse models based on their metastatic cell character and even had a prognostic impact in murine and human metastases.

In conclusion, these data emphasize the essential role of the MMPI during metastatic colonization of the brain and might contribute to MMPI pattern-based therapeutic decisions for cancer patients in the future. The identified gene targets could represent a prognostic tool to classify the outcome of patients with metastases based on the analysis of their tumor gene expression signature.

List of Figures

Figure 1: Metastatic colonization	3
Figure 2: Correlation of MMPI and overall survival.....	4
Figure 3: Macro-metastasis/organ parenchyma interface (MMPI) patterns	5
Figure 4: Infiltrative MMPI patterns in human breast cancer brain metastases	6
Figure 5: E-cadherin expression in human breast cancer brain metastases.....	8
Figure 6: Role of E-cadherin and Hippo signaling pathway in contact inhibition.....	10
Figure 7: The metastatic microenvironment (MME) of brain metastases.....	12
Figure 8: Comparison of early and late brain colonization mouse models.....	15
Figure 9: Knockdown vector workflow	35
Figure 10: Step 2 of Gateway cloning technology	40
Figure 11: Schematic of cell migration assay with turned coverslips	48
Figure 12: Schematic of cell invasion assay in a modified Boyden chamber	49
Figure 13: Schematic of colony formation assay in soft agar.....	50
Figure 14: Schematic of spheroid formation assay using hanging drop method	51
Figure 15: Stereotactical intracortical injection of tumor cells	53
Figure 16: Schematic of brain tissue samples taken at the end of <i>in vivo</i> experiments	54
Figure 17: Workflow of CD31 IHC staining quantification	67
Figure 18: Workflow of IBA1/GFAP/CD3 IHC staining quantification	68
Figure 19: MMPI patterns in brain metastasis mouse models.....	72
Figure 20: E-cadherin expression in brain metastasis mouse models.....	73
Figure 21: Metastatic microenvironment in brain metastasis mouse models.....	74
Figure 22: Basic characterization of murine brain metastasis model cell lines <i>in vitro</i>	76
Figure 23: Functional 2D characterization of murine brain metastasis model cell lines <i>in vitro</i>	78
Figure 24: Functional 3D characterization of murine brain metastasis model cell lines <i>in vitro</i>	79
Figure 25: Contact inhibition mechanisms in murine brain metastasis model cell lines <i>in vitro</i>	81
Figure 26: Gene expression signature of murine brain metastasis model cell lines	82
Figure 27: E-cadherin overexpression in diffuse infiltrative murine brain metastasis model cell lines	86
Figure 28: E-cadherin knockdown in epithelial infiltrative murine brain metastasis model cell lines	88
Figure 29: No effect of E-cadherin modifications on gene expression signature.....	90
Figure 30: Effects of E-cadherin overexpression on migration, invasion and spheroid outgrowth <i>in vitro</i>	91
Figure 31: Effects of E-cadherin knockdown on migration, invasion and spheroid outgrowth <i>in vitro</i>	93
Figure 32: Effects of E-cadherin modifications on colony formation <i>in vitro</i>	94
Figure 33: Effects of E-cadherin overexpression on contact inhibition mechanisms <i>in vitro</i>	96
Figure 34: Effects of E-cadherin knockdown on contact inhibition mechanisms <i>in vitro</i>	98
Figure 35: Summary of E-cadherin modification effects in murine brain metastasis model cell lines	99
Figure 36: Effects of E-cadherin overexpression in diffuse infiltrative brain metastasis mouse models on survival.....	101

Figure 37: Effects of E-cadherin knockdown in epithelial infiltrative brain metastasis mouse models on survival.....	103
Figure 38: Effects of E-cadherin modifications in diffuse and epithelial infiltrative brain metastasis mouse models on colonization index.....	104
Figure 39: Correlation of overall survival and vimentin level in diffuse and epithelial infiltrative brain metastasis mouse models.....	106
Figure 40: Effects of E-cadherin overexpression in diffuse infiltrative brain metastasis mouse models on MMPI pattern and infiltration.....	108
Figure 41: Effects of E-cadherin knockdown in epithelial infiltrative brain metastasis mouse models on MMPI pattern and infiltration.....	110
Figure 42: Characterization of endothelial cells in the metastatic brain tissue after E-cadherin modifications.....	112
Figure 43: Characterization of microglia/macrophages in the metastatic brain tissue after E-cadherin modifications.....	114
Figure 44: Characterization of astrocytes in the metastatic brain tissue after E-cadherin modifications.....	116
Figure 45: Characterization of T cells in the metastatic brain tissue after E-cadherin modifications.....	118
Figure 46: Overview of changes in the metastatic microenvironment after E-cadherin modifications.....	119
Figure 47: Impact of entity on angiogenesis and metastatic microenvironment	120
Figure 48: Summary of E-cadherin modification effects in brain metastasis mouse models	121
Figure 49: Validation of gene expression signature in brain metastasis mouse models.....	123
Figure 50: Application of gene expression signature on human metastases.....	124
Figure 51: Schematic model of the role of E-cadherin in metastatic brain colonization.....	142

List of Tables

Table 1: Bacterial strains	17
Table 2: Lentiviral production cell line.....	17
Table 3: Parental murine tumor cell lines	17
Table 4: Modified murine tumor cell lines	18
Table 5: Mouse strains	18
Table 6: Chemicals and reagents	18
Table 7: Bacterial media and reagents.....	21
Table 8: Cell culture media and additives	22
Table 9: Buffers and solutions	22
Table 10: Antibodies and fluorescent dyes	25
Table 11: Oligonucleotides for shRNA constructs	26
Table 12: Sequencing primers for cloning vectors	26
Table 13: Primers for qRT-PCR	26
Table 14: Plasmids	28
Table 15: Specific enzymes.....	29
Table 16: Restriction enzymes.....	29
Table 17: Commercial kits	29
Table 18: Consumables and instruments	30
Table 19: Equipment.....	32
Table 20: Software products and databases	34
Table 21: Setup for construct ligation.....	39
Table 22: Overview of amplified plasmids	41
Table 23: Setup for restriction digestion of plasmids	43
Table 24: Cell lines with respective media and supplements	44
Table 25: Setup for viral particle test.....	46
Table 26: Composition of resolving and stacking gels	56
Table 27: Protocol of qRT-PCR program	59
Table 28: Phalloidin staining protocol	60
Table 29: IF staining protocol	61
Table 30: Alcohol concentration series for staining of brain tissue.....	62
Table 31: H&E staining protocol	62
Table 32: IHC staining protocol for CD3, CK8 and IBA1	63
Table 33: IHC staining protocol for CD31 and VIM	64
Table 34: IHC staining protocol for ECAD	65
Table 35: IHC staining protocol for GFAP	66
Table 36: E-cadherin modifications in murine brain metastasis model cell lines	84

Abbreviations

ANOVA	analysis of variance
APS	ammonium persulfate
ATP	adenosine 5'-triphosphate
BBB	blood-brain barrier
BSA	bovine serum albumin
CD3	cluster of differentiation 3
CD31	cluster of differentiation 31
cDNA	complementary DNA
CI	colonization index
CK8	cytokeratin-8
CNS	central nervous system
CTL	control
DAB	diaminobenzidine
ddH ₂ O	double-distilled water
DEG	differentially expressed gene
dH ₂ O	distilled water
DMEM	Dulbecco's modified Eagle medium
DNA	deoxyribonucleic acid
ECAD	E-cadherin
E-cadherin	epithelial cadherin
ECM	extracellular matrix
EDTA	ethylenediaminetetraacetic acid
EMT	epithelial-mesenchymal transition
EtBr	ethidium bromide
EtOH	ethanol
FAST-AP	FAST-alkaline phosphatase
FCS	fetal calf serum
FITC	fluorescein isothiocyanate
G418	geneticin
GFAP	glial fibrillary acidic protein
GOI	gene of interest
GTR	gross total resection
H&E	hematoxylin and eosin
HK	housekeeping gene

HRP	horseradish peroxidase
HSP90	heat shock protein 90
IBA1	allograft inflammatory factor 1
IF	immunofluorescence
IHC	immunohistochemistry
LB	Lysogeny broth
MME	metastatic microenvironment
MMP	modified milk powder
MMPI	macro-metastasis/organ parenchyma interface
MRI	magnetic resonance imaging
mRNA	messenger RNA
MTT	3-(4,5-dimethylthiazol-2-yl)-2,5-diphenyltetrazolium bromide
MΦ	macrophage
NaCl	sodium chloride
NaOH	sodium hydroxide
n.s.	not significant
OE	E-cadherin-overexpression
OS	overall survival
PBS	phosphate buffered saline
PFA	paraformaldehyde
PNK	T4 polynucleotide kinase
P/S	penicillin/streptomycin
p-YAP	phospho-YAP
qRT-PCR	quantitative real-time polymerase chain reaction
RNA	ribonucleic acid
ROI	region of interest
RPMI	Roswell Park Memorial Institute
RT	room temperature
SD	standard deviation
SDS	sodium dodecyl sulfate
SDS-PAGE	SDS polyacrylamide gel electrophoresis
sh	E-cadherin-knockdown
shRNA	short hairpin RNA
TAE	Tris-acetate-EDTA
TAZ	transcriptional coactivator with PDZ-binding motif

TBST	Tris-buffered saline with Tween 20
TE	Tris-EDTA
TEAD	transcriptional enhancer factor TEF-1
TEMED	tetramethylethylenediamine
UV	ultraviolet
VIM	vimentin
YAP	Yes-associated protein
YTA	yeast extract tryptone agar
β-CAT	β-catenin

Measurement units:

% (v/v)	volume per volume
% (w/v)	weight per volume
bp	base pairs
°C	degree Celsius
g	gram
<i>g</i>	relative centrifugal force
h	hour
l	liter
m	meter
M	Molar
min	minute
n	number
<i>n</i>	sample size
rpm	revolutions per minute
s	second
V	Volt
W	Watt

Metric prefixes:

c	centi (10 ⁻²)
m	milli (10 ⁻³)
μ	micro (10 ⁻⁶)
n	nano (10 ⁻⁹)

1. Introduction

1.1. Metastatic colonization

At a certain point during disease progression, many cancer cells spread from a primary tumor to the brain and attack the central nervous system (CNS). This usually has far-reaching consequences for the patient. CNS metastases are found in 8–10% of all cancer patients and 40% of patients with metastatic cancer and normally imply a decline in quality of life as they are generally associated with a very poor prognosis and have the worst survival rates compared to other sites (Chamberlain et al., 2017; S. G. Wu et al., 2017). While isolated soft tissue metastases have a median survival of 50 months (Tampellini et al., 1997) and bone metastases around 48 months (Sherry et al., 1986), cerebral metastases confer a much worse prognosis with a median survival of only 4 months after diagnosis (Nussbaum et al., 1996). The number of patients with brain metastases even seems to increase nowadays. The most likely reasons are prolonged patient survival due to more effective systemic therapies for the primary cancer and earlier detection due to advanced imaging systems (Chamberlain et al., 2017).

Apart from lung cancer and melanoma, breast and colorectal cancer account for the highest risk of brain metastases formation (Neagu et al., 2015). One of the major problems in their effective treatment is the fact that metastatic infiltration differs enormously from primary tumor invasion. While classical therapy methods such as surgery (removing the visible tumor tissue with a gross total resection (GTR)) or radiotherapy usually are used successfully for primary tumors, they often have only moderate effects in metastatic disease and can not completely remove the metastatic tissue in most cases (Chamberlain et al., 2017). However, systemic therapies targeting specific molecules appear as effective treatment options in a growing number of studies (Chamberlain et al., 2017).

1.1.1. Steps of metastatic colonization

The metastatic cascade consists of several steps. Initially, the primary tumor forms, starts growing and during progression single tumor cells seed into the surrounding tissue. Via intravasation, the tumor cells enter the circulatory systems and are spread through the whole body until they reach a distant organ site (for example, the CNS), where they leave the circulation again and form micro-metastases. Meanwhile the primary tumor continues to grow and at some point, the first diagnosis is made. However, at this time the initial seeding of disseminated cancer cells has already taken place in many cases and can not be prevented (Hosseini et al., 2016). The treatment of the primary tumor is thus only half the battle. With the currently available diagnostic tools, it is not possible to recognize this first step early enough to represent a feasible therapeutic approach. This leaves only one possible

targetable step to interfere, which is the colonization of the target organ, when the micro-metastases grow and form clinically detectable macro-metastases.

At least, metastatic colonization is a highly inefficient process in reality. This final step of the metastatic cascade represents the bottleneck of the whole process since only a tiny fraction of the large number of tumor cells that enter the circulatory system survives the travel. And from those the majority fail to extravasate from blood vessels resulting in an even smaller number of cells (less than 0.01%) that finally manage the successful colonization of distant organs (Fidler, 1970). Nevertheless, as single successfully spread cells are able to grow out to macro-metastases, each can play a decisive role. This emphasizes the importance to interfere with the colonization process via adequate therapies.

Since many years, the focus of our group lies on the investigation of the situation in the brain. Once disseminated cancer cells arrive in secondary organs, they have to circumvent local immune defenses to take over the distant tissue and adapt to its prevailing supportive niches (Blazquez et al., 2018; Chuang et al., 2013; Klemm et al., 2011; Pukrop et al., 2010; Pukrop et al., 2006; Rietkotter et al., 2015; Vanharanta et al., 2013). Again, the majority fail and die right at the beginning leaving only a small number of tumor cells that successfully survive the first immune response of the new host organ. They subsequently often stay in a latent phase and it can take weeks, months, or even years after the original seeding until they start to proliferate again. The following phases of metastatic colonization involve the formation of a micro-metastasis (<2 mm) and the establishment of a macro-metastasis (≥ 2 mm) with a specific metastatic microenvironment (MME). Once metastases exceed a certain size, they cause severe organ destruction and such target lesions (≥ 10 mm) can lead to organ failure and death (Blazquez et al., 2020b) (Figure 1).

Although clinicians try to prevent the formation of a micro-metastasis with different adjuvant therapies, this time window still represents a diagnostic gap. A potential seeding is not detectable at this stage and can only be treated upon suspicion. Furthermore, even after successful seeding not all micro-metastases progress into macro-metastases and patients with this dormant form of the disease characterized by inactive micro-metastases can show long-term survival under asymptomatic chronic conditions (Murray, 2017). During early phases (Stage I–III), micro-metastases are not clearly demarcated from the surrounding tissue. Only when they progress into macro-metastases and further to target lesions, they can be differentiated based on their outgrowth pattern.

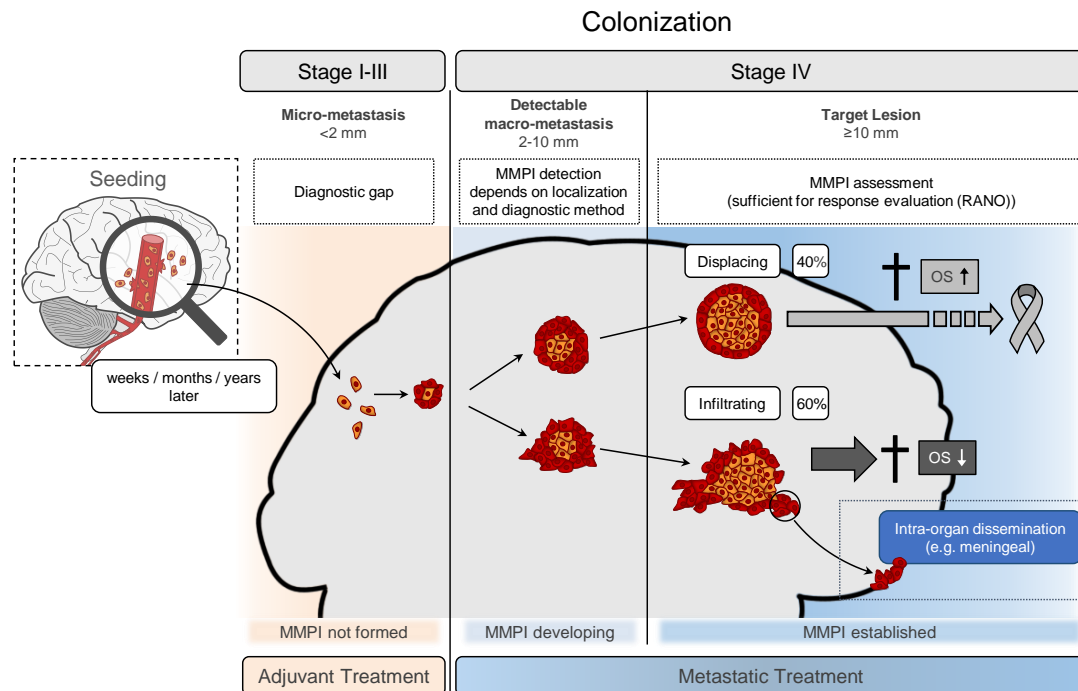


Figure 1: Metastatic colonization. Metastatic colonization can be subdivided into at least four different major phases: i) re-starting proliferation, ii) formation of a micro-metastasis (<2 mm), iii) establishing a macro-metastasis (≥2 mm) with its own metastatic microenvironment, and iv) organ destruction leading to organ failure and death. Taken from (Blazquez et al., 2020b) under a CC BY 4.0 license.

1.1.2. Different patterns of colonization

Various factors have been reported to strongly influence prognosis for the patient, including the biology of the entities, the existence of druggable mutations or the (non-) response to (immune) therapy. In recent years, several studies have acknowledged the presence of infiltrative tumor cells at the macro-metastasis/organ parenchyma interface (MMPI) as another factor with a significant impact on patient outcome. The MMPI is defined as the area where cells of the macro-metastasis (≥2 mm) and its metastatic microenvironment are in direct contact with the (healthy) adjacent organ parenchyma (Blazquez et al., 2020b). Clinicians and researchers had underestimated and overlooked this area before and simply assumed that the edge between metastatic and brain tissue was a clearly defined border. However, it has become evident in numerous histological analyses of MMPIs in brain metastases as well as liver and lung specimens that significant morphological differences exist even within the same tumor entity.

The most important issue is the grade of infiltration. We distinguish between two types of MMPIs that essentially differ from each other: non-infiltrative and infiltrative growth. Non-infiltrative or displacing MMPIs are characterized by metastatic cells that grow by pushing the adjacent (healthy) tissue aside.

This pattern is easy to recognize and has sharply defined borders. On the other hand, infiltrative MMPIs miss such a clear separation between metastasis and organ parenchyma, as tumor cells grow unrestricted in various patterns by infiltrating the surrounding tissue. While non-infiltrative metastases account for only 40% of brain metastases, the infiltrative type is found in 60% of cases (Blazquez et al., 2020b). Moreover, these differences have been shown to be prognostic with severe impact on clinical practice (Figure 2).

We already demonstrated the significant prognostic impact of the metastatic infiltration pattern in brain metastases in a previous study. In this prospective clinical basket trial, the 2-year overall survival (OS) of patients with non-infiltrative MMPIs was 43.5%, while that of patients with infiltrative MMPIs was only 6.6% (Siam et al., 2015). The situation was similar for liver metastases (Fonseca et al., 2018; van Dam et al., 2017) as well as metastases in the lung (Shiono et al., 2005). In general, the type of metastatic infiltration at the MMPI has a significant impact on survival. Non-infiltrative metastases account for a better prognosis with some patients being even long-term survivors while infiltrative metastases correlate with worse overall survival (Blazquez et al., 2020b). Therefore, the MMPI seems to be highly relevant for the correct management of metastatic disease and for reliable and reproducible research.

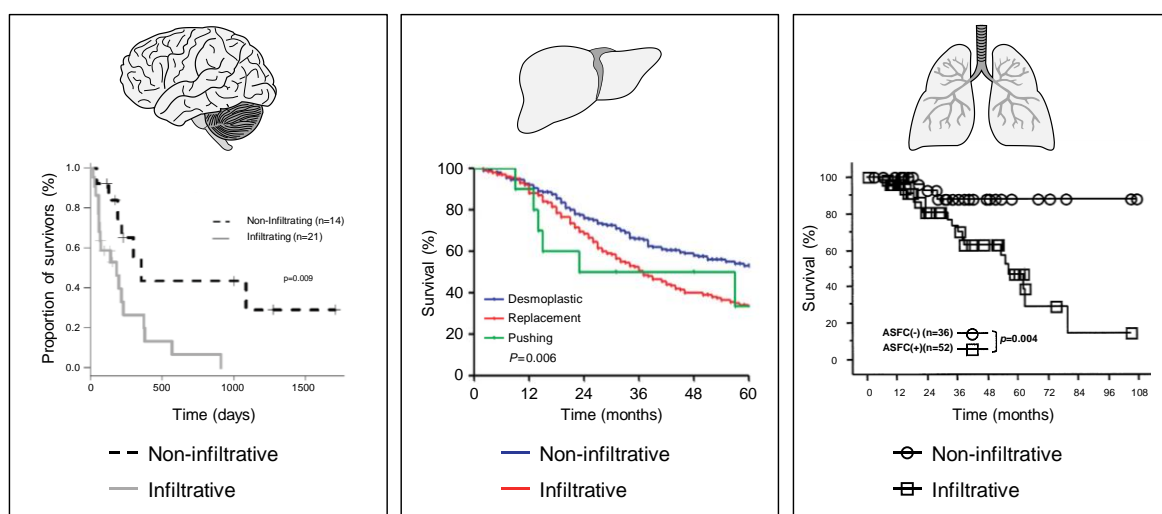


Figure 2: Correlation of MMPI and overall survival. Several studies show a correlation between the growth pattern of metastases at the MMPI and the overall survival of patients in brain, liver and lung metastases. Infiltrative MMPIs correlate with worse overall survival. Survival curves from separate studies were combined in a modified comparative overview. Survival curve of patients with brain metastases (left panel) was taken from (Siam et al., 2015) under a CC BY 3.0 license. Survival curve of patients with liver metastases (middle panel) was taken from (van Dam et al., 2017) under a CC BY-NC-SA 4.0 license. Survival curve of patients with lung metastases (right panel) was taken from (Shiono et al., 2005) with permission from Elsevier.

1.1.3. The macro-metastasis/organ parenchyma interface (MMPI)

Several different MMPI patterns have been described for brain, liver and lung metastases in the past. However, the exact terms and definitions of the histopathological criteria largely varied between studies. In order to facilitate day-to-day application of common terminology and thus enable fast and reliable MMPI pattern recognition, our group collected all designations found in the literature and developed uniform definitions (Blazquez et al., 2020b). We included these definitions into three main MMPI categories and nine subcategories (Figure 3):

- A. *Displacing MMPI*: with or without reactive pseudo-capsule, with a reactive multilayer pseudo-capsule
- B. *Epithelial infiltrative MMPI*: strand, cohort, glandular, angiotropic infiltration
- C. *Diffuse infiltrative MMPI*: diffuse infiltration with or without a visible macroscopic metastasis

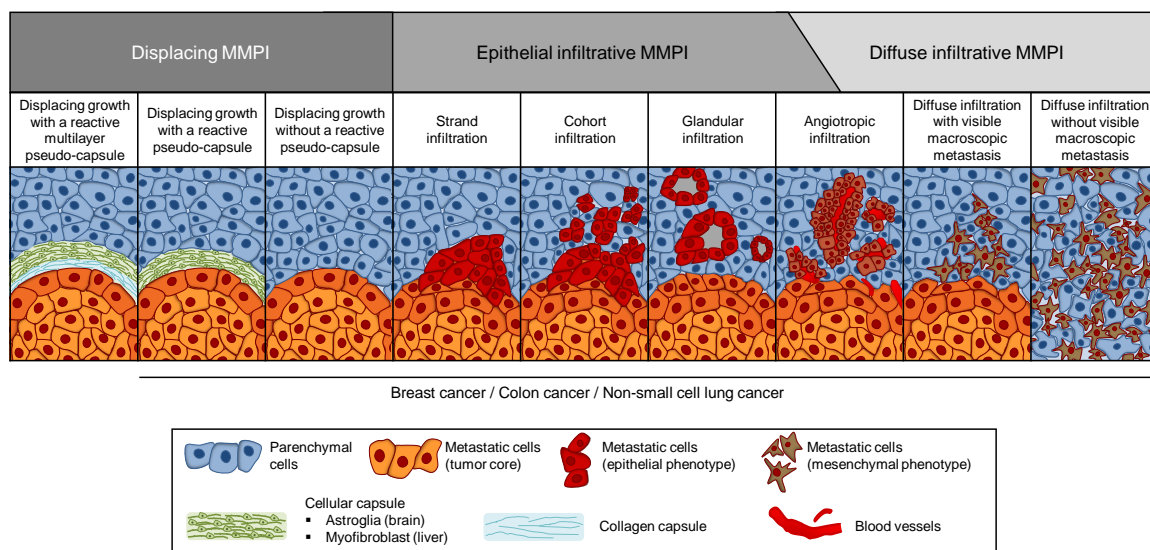


Figure 3: Macro-metastasis/organ parenchyma interface (MMPI) patterns. MMPI patterns are divided into three main categories: displacing, epithelial infiltrative and diffuse infiltrative MMPIs. Angiotropic infiltration (along the host tissues' blood vessels) can demonstrate epithelial as well as diffuse characteristics. Adapted from (Blazquez et al., 2020b) under a CC BY 4.0 license.

1.1.4. Infiltrative MMPI patterns in human breast cancer brain metastases

As infiltrative metastases are associated with worse survival rates and represent a major problem, the following study focuses on infiltrative MMPI patterns. In breast cancer, they usually present themselves as epithelial but sometimes also as diffuse infiltrative (Siam et al., 2015). An epithelial cohort infiltrative MMPI pattern is defined as clusters or groups of epithelial tumor cells that collectively infiltrate the adjacent organ parenchyma and are physically separated from the metastatic

boundaries. On the other hand, a diffuse infiltrative MMPI pattern is characterized by single tumor cells that deeply infiltrate the adjacent tissue (>1 mm) in a chain- or swarm-like (in other words, diffuse) way. Alike epithelial infiltrating cells, those presenting a diffuse infiltrative MMPI pattern usually acquire a more mesenchymal-like morphology (Blazquez et al., 2020b).

We could also confirm these distinguishable infiltration patterns in a recent study in an independent cohort of human brain metastases (Blazquez et al., 2020a) (Figure 4).

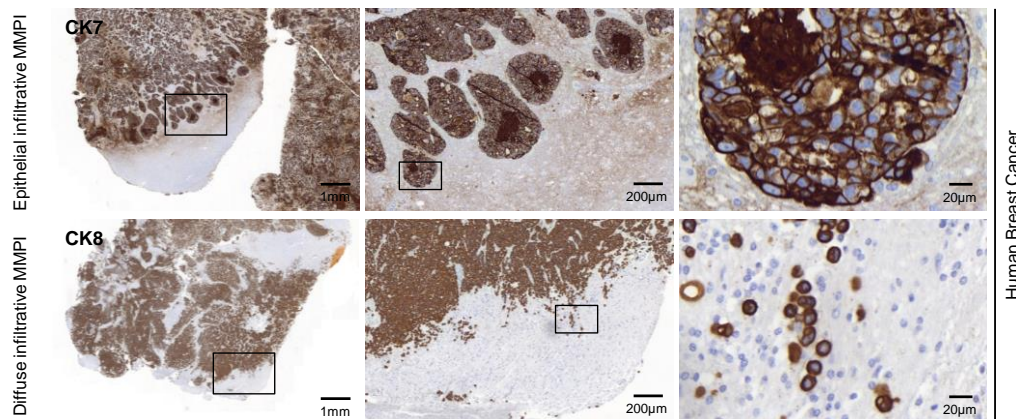


Figure 4: Infiltrative MMPI patterns in human breast cancer brain metastases. Cytokeratin-7 (CK7) and cytokeratin-8 (CK8) staining in tissue sections of human cerebral metastases. Representative images of epithelial cohort (upper row) and diffuse (lower row) MMPI patterns observed in brain metastases of breast cancer patients. Adapted from (Blazquez et al., 2020a) under a CC BY 4.0 license.

1.2. Target mechanisms in metastatic colonization

Metastatic colonization has many faces and remains a process that needs to be intensively studied. Finding an Achilles' heel of aggressive metastatic cancers is the overall goal and the reason why numerous researchers focus on various treatment strategies. Many different mechanisms are likely to cause colonization and express themselves through distinct phenotypes. As metastatic growth in the brain is one of the most aggressive and problematic forms due to the difficulties of complete removal by GTR, it provides a particular focus for target mechanism studies. It became already apparent that the efficacy of therapeutic concepts seems to be heavily dependent on the type of colonization and infiltration pattern. For example, antibody therapy against vascular endothelial growth factor A was only effective in preventing angiogenic growth during lung carcinoma metastasis formation but ineffective against vessel cooptive growth of melanoma cells (Kienast et al., 2010).

As we are able to distinguish different infiltrative MMPI patterns, the question arises as to the existence of different mechanisms and underlying pathophysiology. This is a prerequisite for identifying potential effective treatment strategies.

1.2.1. Cell adhesion receptor E-cadherin

The role of E-cadherin as a tumor suppressor gene in cancer development and progression has been extensively studied (Gall et al., 2013). Epithelial cadherin (E-cadherin), also known as Cadherin 1, is a single-pass transmembrane glycoprotein expressed by a variety of tissues and functions as a cell-cell adhesion receptor (Gall et al., 2013).

E-cadherin is often inactivated in tumors of breast cancer patients (Bajrami et al., 2018) and clinical studies report lower incidence of metastases in breast cancer patients with increased E-cadherin expression (Li et al., 2017). Besides its implication in breast cancer, it also has been shown to have a prognostic value in ovarian cancer (Rosso et al., 2017), non-small cell lung cancer (Esheba et al., 2017) and many other types. The functional loss of E-cadherin is generally associated with poor prognosis and survival and its clinical relevance is rapidly expanding (Wong et al., 2018). Lower levels of E-cadherin are always associated with increased dissemination and aggressiveness. Nevertheless, there are still no direct medicine approaches targeting this remarkable characteristic.

Loss of E-cadherin expression has often been associated with epithelial-mesenchymal transition (EMT) (Petrova et al., 2016). During the EMT process, tumor cells lose characteristic properties of epithelial cells including the apical-basal axis of polarity and cell-cell adhesion, and acquire properties of mesenchymal cells instead, including loose three-dimensional organization and increased motility (Romeo et al., 2019). However, this seems to be a chicken and egg issue, since there are controversial discussions whether the loss of E-cadherin is the cause or just an effect of EMT. Furthermore, EMT is probably not a black or white situation and cancer cells rather exhibit intermediate phenotypic and functional states (Romeo et al., 2019). Metastases often even completely retain E-cadherin expression excluding an absolute requirement of EMT for their occurrence (Petrova et al., 2016). We also previously noticed an upregulation of E-cadherin at the border of metastatic tissue and adjacent brain parenchyma in some epithelial infiltrative MMPIs and in the locally disseminated micro-metastases in our *in vivo* mouse models regardless of the cell line even when the metastatic core was E-cadherin negative or necrotic (Blazquez et al., 2020a). Petrova and colleagues argue that metastasis rather depends on reduced E-cadherin adhesive function and genetic deficits in E-cadherin cell surface regulation contribute to cancer progression (Petrova et al., 2016). In accordance, the tumorigenicity of cancer cells without detectable E-cadherin expression could be partially suppressed by re-expression of this cell adhesion molecule in a previous *in vitro* study (Navarro et al., 1991).

To capture its role in human brain metastases, we also evaluated the expression of E-cadherin at the MMPI in the previously mentioned patient material. Epithelial cohort infiltrative human breast cancer brain metastatic lesions expressed high levels of the epithelial marker E-cadherin, in particular at the MMPI, while the more aggressive diffuse infiltrative human breast cancer brain metastases showed no

expression at all (Figure 5 A). Additionally, we also found E-cadherin positive carcinoma cell clusters in adjacent blood vessels of human breast cancer brain metastases just like in our murine models (Blazquez et al., 2020a) (Figure 5 B).

These observations emphasize the essential role of E-cadherin in the metastatic process and highlight the importance of considering different MMPI patterns as independent entities for the accurate study of metastatic colonization.

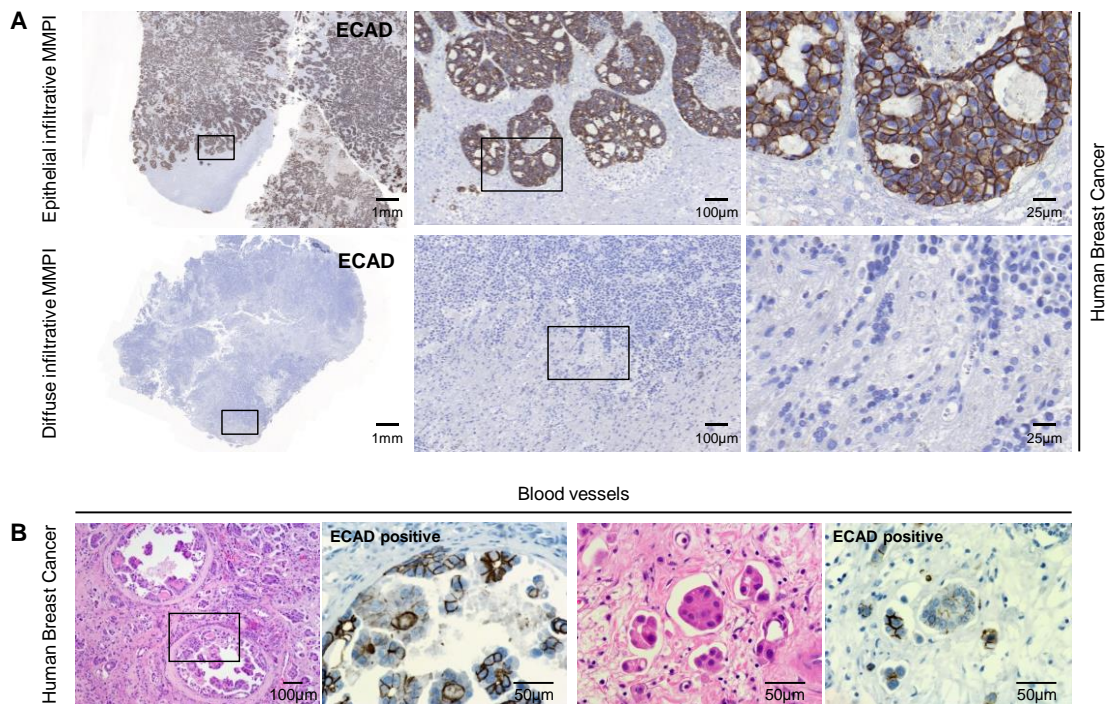


Figure 5: E-cadherin expression in human breast cancer brain metastases. (A) E-cadherin (ECAD) staining in tissue sections of epithelial cohort infiltrative human breast cancer brain metastases (upper row) and diffuse infiltrative human breast cancer brain metastases (lower row). **(B)** Intravascular E-cadherin positive cell clusters in breast cancer brain metastases. Modified from (Blazquez et al., 2020a) under a CC BY 4.0 license.

Padmanaban and colleagues recently showed the importance of E-cadherin for the whole metastatic process. Loss of E-cadherin resulted in reduced cancer cell proliferation and survival, circulating tumor cell number, seeding of cancer cells in distant organs and metastasis outgrowth (Padmanaban et al., 2019). However, the authors provide no information which steps of the metastatic cascade are involved or how the colonization process in a distant organ is affected. As their model systems only cover the steps prior to colonization (such as intravasation, survival in the circulation and extravasation), the impact of E-cadherin on a direct colonization model remains unknown.

1.2.2. Contact inhibition mechanisms and E-cadherin

Normal cells control their outgrowth once they sense neighboring cells. They stop to proliferate with increasing cell density due to cell-cell contacts and this phenomenon is called contact inhibition of proliferation (Mendonsa et al., 2018). It is essential for the correct development of tissues and organs and only switched off in critical situations including the fast regeneration of tissues for closure of wounds. However, one of the hallmarks of cancer is uncontrolled growth due to the loss of contact inhibition (Hanahan et al., 2000, 2011).

Without cell contact, the transcriptional activators Yes-associated protein (YAP) and transcriptional coactivator with PDZ-binding motif (TAZ) in the cytoplasm are active and can translocate to the nucleus, where they induce the expression of several growth factors and other genes promoting cell survival and proliferation upon binding to transcriptional enhancer factor TEF-1 (TEAD) (Dong et al., 2007). Upon cell contact, the homophilic ligation of E-cadherin receptors in adjacent cell membranes leads to the release of growth inhibitory signals via different signaling cascades including the Hippo pathway (Gumbiner et al., 2014; Kim et al., 2011). Interestingly, E-cadherin can inhibit cell growth with these adherens junctions independently of other cell interactions (Perrais et al., 2007) although tight junctions and apical polarity complexes are also formed. Besides proliferation, the Hippo pathway also regulates cellular functions such as development and regeneration of tissue and plays a role in cancer progression and metastasis (Mendonsa et al., 2018). Downstream of the E-cadherin-catenin complex, several players, including kinases and scaffold proteins, orchestrate in a cascade as the core of the Hippo pathway finally resulting in the phosphorylation of YAP and TAZ. This stops their translocation to the nucleus, eventually leads to their degradation and thus prevents the expression of cell proliferation genes (Figure 6 A).

Therefore, E-cadherin seems to play an important role in contact inhibition of proliferation and cancer progression (Mendonsa et al., 2018). In normal cells, E-cadherin establishes cell-cell contacts with increasing density and the cell-cell adhesion finally induces contact inhibition resulting in cells growing in a monolayer. Mutations or the loss of E-cadherin can lead to disrupted cell-cell adhesion and thus prevent the activation of the Hippo signaling kinase cascade. This results in the loss of contact inhibition and cells continue to proliferate and grow on top of each other (Figure 6 B).

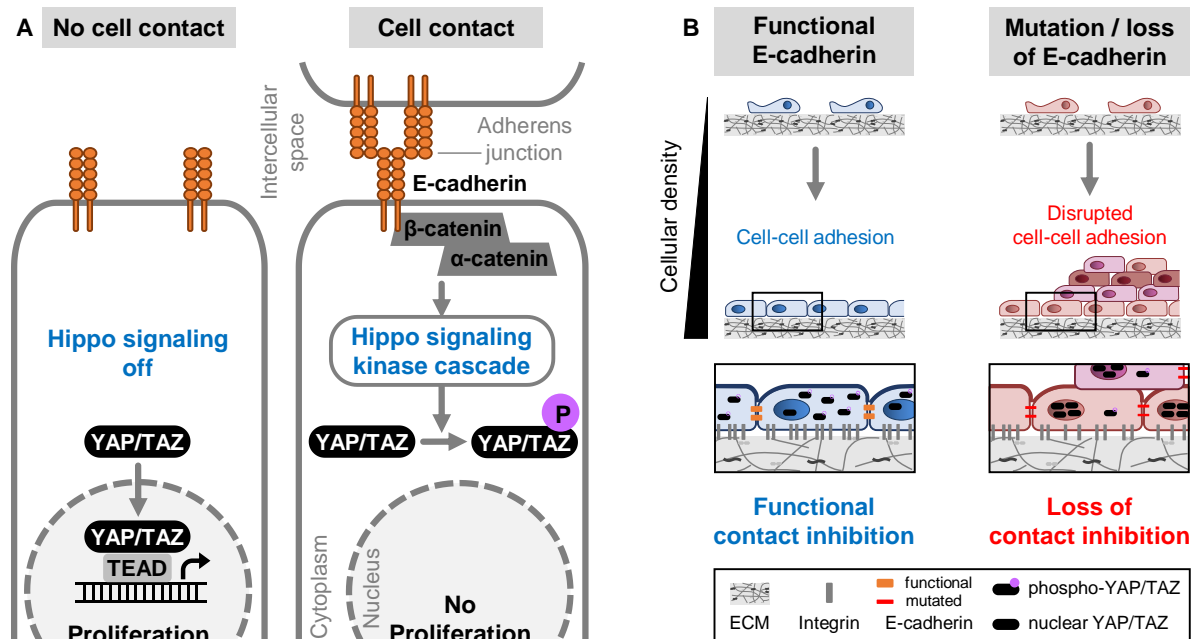


Figure 6: Role of E-cadherin and Hippo signaling pathway in contact inhibition. (A) Model for an E-cadherin-mediated Hippo signaling pathway. Without cell contact, the Hippo pathway is inactivated. The transcriptional activators YAP and TAZ can translocate from the cytoplasm to the nucleus and bind TEAD resulting in the expression of different target genes and activation of cell proliferation and survival. Upon E-cadherin-mediated cell adhesion, the Hippo signaling pathway is activated and a multi-step kinase cascade leads to the phosphorylation of YAP/TAZ. Phosphorylated YAP remains in the cytoplasm, is eventually degraded and cell growth is inhibited. **(B)** Role of E-cadherin in contact inhibition. In cells with functional E-cadherin, cell-cell adhesion can induce contact inhibition with increasing density resulting in cells growing in a monolayer. Mutations or the loss of E-cadherin can lead to disrupted cell-cell adhesion and result in the loss of contact inhibition and cells proliferating continuously and growing on top of each other.

Massague and colleagues revealed the importance of YAP/TAZ during metastasis outgrowth in vessel cooptive cancer models as well-established promoters of tumor growth and metastasis (Er et al., 2018). This mechanism could be a feasible target for treatment of cancer metastases. The blockade of contact inhibition can be achieved by inhibition of the Hippo pathway and several inhibitory components already have proved to work as tumor suppressors (Zhao et al., 2010) among them also YAP inhibitors. However, a systematic analysis of YAP or cell contact inhibition in distinct metastatic colonization patterns has not been performed yet. Therefore, it remains unclear if YAP inhibition could be a general target mechanism to prevent colonization or if it is only effective in distinct colonization patterns.

1.2.3. The metastatic microenvironment of brain metastases

The area around tumors or cancer cells, the metastatic microenvironment, is comprised of various components. Besides the extracellular matrix (ECM) and surrounding blood vessels, it also contains different immune cells, fibroblasts, bone marrow-derived inflammatory cells, lymphocytes and many signaling molecules (Spill et al., 2016). All those players have their specific roles and act together in a complex network. When foreign tumor cells reach a distant organ, they are detected by cells of the immune system, reliably attacked and killed by apoptosis. This protects the organ from further tumor growth and damage. Therefore, the MME plays an important role in the metastatic process and changes in the MME have been demonstrated to influence tumor development and growth as well as the efficacy of treatments (Spill et al., 2016).

The CNS differs from other host organs and has a unique milieu. When a metastatic lesion occurs, the immune cells initially fight against the intruders and neuroinflammation as well as astrogliosis occur. Organ-foreign cells are isolated from the rest of the organ and colonization is prevented. The MME of brain metastases is mainly composed of microglia/macrophages, astrocytes and T cells.

Microglia are the resident macrophage cells and main innate immune effectors in the brain tissue and are widely distributed in the healthy brain parenchyma (Berghoff et al., 2015). In case of an injury, they immediately accumulate at the area of the lesion and act as rapid responders to decrease inflammation and destroy the pathogens before neural damage occurs. Microglia also produce a number of growth and repair factors to promote repair of already damaged CNS tissue. Normally this very efficient process defends the organ from serious damage. However, besides their tumor suppressive function microglia can also help tumors to grow by suppressing the adaptive immune response (Berghoff et al., 2015). We could visualize this tumor promoting function in a well established *ex vivo* brain slice coculture model with vital brain slices and malignant cancer cells. Invasive cancer cells were somehow able to recruit the aid of microglia/macrophages, attract them to the tumor site and hijack them to invade into the surrounding tissue (Chuang et al., 2013; Pukrop et al., 2010).

Astrocytes are the most abundant glial cells of the CNS and easy to recognize by their characteristic star-shaped appearance (Xing et al., 2013). Although their main function is the maintenance of the blood-brain barrier (BBB) and nutrient supply for the brain tissue, they can be activated under pathological conditions and often accumulate around brain metastatic lesions also suggesting a potential tumor-supporting role (Xing et al., 2013). In a previous study of our group, the general glial response of astrocytes and microglia is depicted in human brain metastases (Figure 7 A).

T cells are the main adaptive immune system effector cells, normally almost absent in healthy CNS and only accumulate in the brain under pathological conditions (Berghoff et al., 2015).

Different subpopulations have opposite functions by either suppressing the tumor (cytotoxic T cells) or the immune response (regulatory T cells) and thus can generate an immune-suppressive microenvironment as well (Berghoff et al., 2015).

In summary, metastatic cells have to overcome the local immune defense to colonize the brain tissue and key players of this immune response are microglia/macrophages, astrocytes and T cells. Figure 7 B shows a schematic model of the MME at infiltrative MMPIs based on previous findings (Blazquez et al., 2020a; Chuang et al., 2013; Doron et al., 2019; Siam et al., 2015) and emphasizes the MMPI as a very reactive zone.

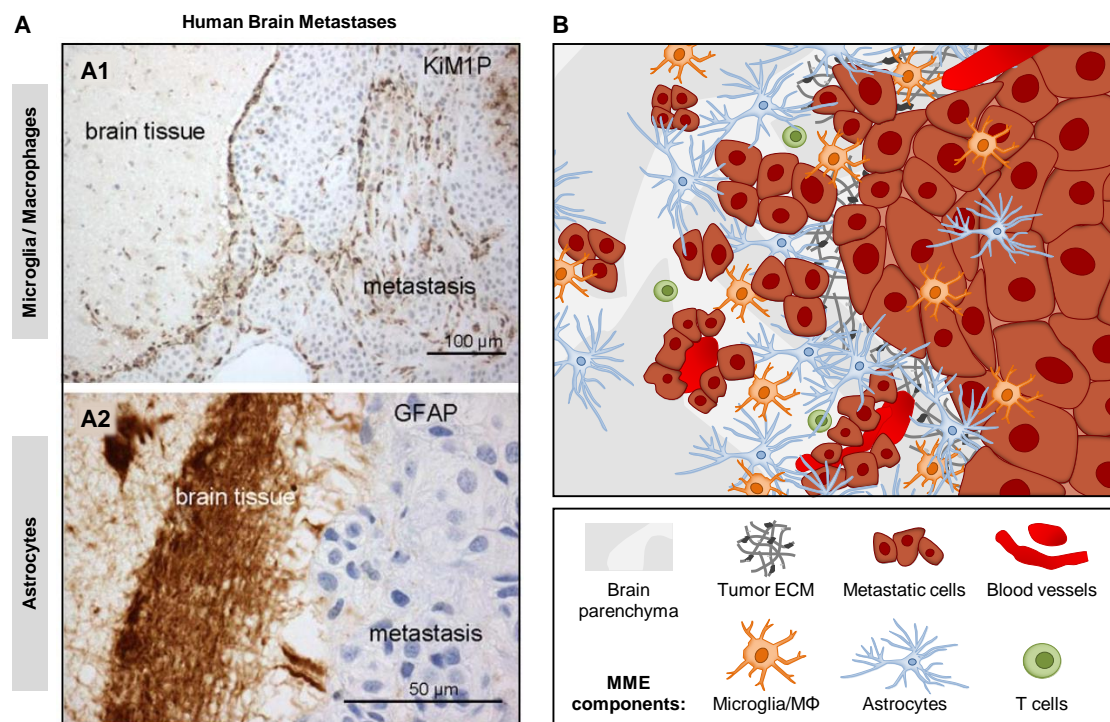


Figure 7: The metastatic microenvironment (MME) of brain metastases. (A) Distribution of microglia/macrophages (M Φ) and astrocytes in human brain metastases: (A1) Activated microglia/macrophages (KiM1P) accumulate in the adjacent brain tissue and at the interface. The majority infiltrate into the metastatic tissue. (A2) Activated astrocytes (GFAP) accumulate in the adjacent brain tissue and form a barrier at the interface to the metastatic tissue. Images of human brain metastases were taken from (Chuang et al., 2013) with permission from John Wiley & Sons. (B) Schematic model of the MME at infiltrative MMPIs based on previous findings. Metastatic cells have to overcome the local immune defense to colonize the brain tissue. Key players of the immune response are microglia/macrophages, astrocytes and T cells.

Taken together, the interactions between metastatic and immune cells influence every step of the metastatic cascade and the immune system can be both friend and foe. The fate of a tumor therefore depends on the balance between anti-tumor immunity and tumor-supporting inflammation. The mutual interference between cancer cells and immune cells opens up a range of new treatment

possibilities for cancer patients. Targeted immune therapies are promising candidates currently under investigation in neo-adjuvant as well as in metastatic settings of various carcinomas and some already have significantly improved the survival rates of cancer patients in stadium IV in several tumor entities. However, not every patient responds to such therapies or even develops a resistance during the course of treatment. It is presumed that this phenomenon relates to the immune exclusion phenotype, which is characterized by the absence of an immune infiltrate inside the metastatic lesion. In fact, recent studies indicate that tumor cells displaying a predominantly mesenchymal phenotype are associated with this immune exclusion (Romeo et al., 2019).

We think that the MMPI pattern itself could have a direct influence on the recruitment and disposition of immune cells within the macro-metastasis, the local damage response and formation of the MME. In diffuse infiltrative patterns, metastatic cells generally grow in a less compact manner and are spread over a larger area. Immune cells could thus enter the metastatic region by passing the MMPI barrier and fight against the foreign intruders inside the metastatic lesion. In contrast, compact metastases of the epithelial infiltrative type could allow the formation of a barrier and provide a defined area for immune cells to attack. This could affect the response to specific therapies and the MMPI could thus serve as a prognostic tool in clinical practice.

1.3. Mouse models for the study of metastatic colonization in the brain

Various mouse models are available for the study of metastatic colonization in the brain. They all rely on the formation of metastases arising from successful tumor cells after injection into mice. We differentiate them based on the stage of the metastatic colonization process they represent best into early and late brain colonization mouse models (Figure 8).

Early brain colonization models mainly focus on initial steps of the metastatic colonization process including the extravasation of tumor cells from the circulation and infiltration into target organ tissue. They differ in the site of tumor cell injection and can be subdivided into orthotopic (organ of origin) and ectopic models (organ different from origin). Although orthotopic models (for example, implanting breast cancer cells into mammary fat pad or colon cancer cells into cecal wall) can lead to spontaneous metastases in the brain, it usually takes a longer time. Many cells already fail during the first steps of the metastatic cascade when they have to seed from the primary tumor into the surrounding tissue, intravasate and survive in the circulation. Ectopic injections on the other hand show increased success rates in the formation of brain metastases as they are mainly performed directly into the circulatory system and thus enable a rapid transport of a larger number of tumor cells to distant organ sites including the brain. Popular injection sites range with increasing difficulty from fast and easy tail vein injections to intra-cardiac injections into the left ventricle and the more complex direct injection into

the internal carotid artery (Kienast et al., 2010; Latacz et al., 2020). However, they all have disadvantages, be it that the majority of cells is trapped in the lungs instead of the brain after a tail vein injection or the frequent colonization of other organs in an unpredictable manner after carotid artery injections.

In all those early models, cancer cells have to break through the blood-brain barrier to establish metastases in the brain. It is still not known how exactly they accomplish this crossing. A recent study revealed that tumor cells release extracellular vesicles that can pass the BBB through transcytosis and alter cells of the barrier itself as well as host cells of the target tissue to weaken the blockade and make the brain parenchyma more susceptible for the colonization of metastatic cancer cells (Morad et al., 2019). Nevertheless, only a small fraction of tumor cells manages the passage and metastatic lesions are not formed on a regular basis. Furthermore, the number of successful cells can not be controlled. This impedes a detailed study of MMPI patterns resulting from several different cell lines.

In contrast, our late brain colonization model circumvents this hindrance via direct injection of tumor cells into the brain. By surrounding the BBB, we can measure the effects on colonization mechanisms of a large number of cells. In the highly aggressive cell lines, macro-metastases arise within a few days. The stereotactic injection technique is commonly used in various fields of brain research and has been previously established in our lab with different murine cancer cell lines (Blazquez et al., 2020a; Blazquez et al., 2018). This system represents the late colonization step of the brain very well and the resulting metastases are well comparable to the lesions observed in human patients. Our model has several advantages compared to the early colonization approach. The stereotactic procedure with fixed coordinates ensures that tumor cells are always injected into the same area in a reproducible manner. The number of injected cells can be precisely controlled and potential treatment effects are directly measurable. This facilitates the detailed characterization of MMPI patterns in a sufficient number of animals and further enables a comparison between entities and modified cell lines.

When tumor cells form micro-metastases and further progress to macro-metastases during the last steps of metastatic colonization, they have to overcome the local immune defense to colonize in the tissue. As we use syngeneic models (injecting murine tumor cells into mice with a functional immune system) instead of the commonly used xenograft approach (tumor cells of human origin are injected into immunocompromised mice), we can study the MME in a realistic setting and aim to understand this important mechanism in the colonization of the brain.

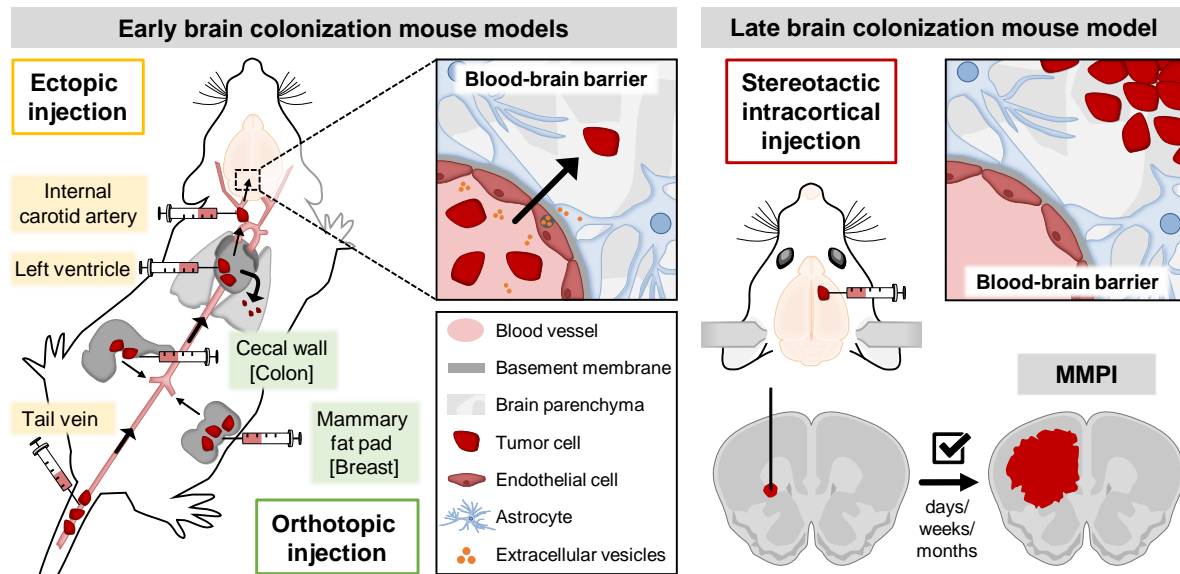


Figure 8: Comparison of early and late brain colonization mouse models. Early brain colonization models are distinguished depending on the site of tumor cell injection. In the late brain colonization model, tumor cells are stereotactically injected directly into the cortex of syngeneic mice. The blood-brain barrier represents the fundamental distinction between both approaches. In early models, it prevents the majority of tumor cells from entering the brain tissue and forming metastases. The late model circumvents this hindrance and ensures the reliable outgrowth of brain metastases for a detailed study of MMPI patterns between model systems and entities.

1.4. Aims of the study

The metastatic infiltration pattern in brain metastases has a prognostic impact and makes the understanding of underlying mechanisms and pathophysiology in different MMPI patterns essential for clinical treatment studies. We previously developed uniform definitions to enable fast and reliable MMPI pattern recognition and confirmed them in human brain metastases in a recent study focusing on the infiltrative categories that are generally associated with worse survival rates.

Diffuse infiltrative cells clearly differ from epithelial infiltrative ones in their pathophysiology. Therefore, we aim to elaborate the potentially responsible underlying mechanisms. We think that the infiltration pattern correlates with overall survival, has an influence on the metastatic microenvironment and might result from differences in cellular signaling mechanisms. Furthermore, we hypothesize that the cell adhesion protein E-cadherin is not only a characteristic marker for the type of infiltration, but also plays a critical functional role.

Thus, the first aim of this thesis is the genetic modification of the innate level of E-cadherin in the corresponding cell lines of our brain metastasis mouse models representing the different infiltrative MMPI patterns. Initially, the resulting overexpression and knockdown cell lines will be characterized *in vitro* and subsequently injected into the brains of syngeneic mice to investigate the functional impact of E-cadherin level on survival, infiltration grade and the metastatic microenvironment *in vivo*. An additional aim will be the establishment of a characteristic gene expression signature with a potentially prognostic impact.

In the frame of this study, I want to contribute to our understanding of the role of E-cadherin during metastatic colonization in the context of the MMPI phenotype and shed some light on the mechanisms underlying metastatic infiltration of tumor cells in the brain parenchyma.

In detail, the following aims are pursued in this study:

- 1) Opposing genetic modification of E-cadherin in diffuse and epithelial infiltrative cell lines via lentiviral overexpression or knockdown
- 2) Characterization of resulting functional effects concerning proliferation, 2D migratory and invasive capacity, 3D culture outgrowth ability and contact inhibition mechanisms *in vitro*
- 3) Investigation of E-cadherin modification effects on overall survival, MMPI pattern, infiltration grade, angiogenesis and MME in brain metastasis mouse models *in vivo*
- 4) Identification of a characteristic gene expression signature as a potential prognostic tool

2. Materials and Methods

2.1. Materials

2.1.1. Biological materials

2.1.1.1. Bacterial strains

The bacterial strains used in this thesis are listed in Table 1.

Table 1: Bacterial strains.

Name	ccdB resistance	Application	Source
DB3.1	yes	amplification of plasmid DNA	Invitrogen
DH5alpha	no	amplification of plasmid DNA	Invitrogen

2.1.1.2. Cell lines

2.1.1.2.1. Lentiviral production cell line

The lentiviral production cell line used in this thesis is listed in Table 2.

Table 2: Lentiviral production cell line.

Name	Species/cell type	Origin	Reference
HEK293T	human embryonic kidney	ATCC (Wesel)	(Graham et al., 1977)

2.1.1.2.2. Parental murine tumor cell lines

The parental murine tumor cell lines used in this thesis are listed in Table 3.

Table 3: Parental murine tumor cell lines.

Name	Species/cell type	Background	Origin/obtained from	Reference
410.4	mouse breast cancer	BALB/c	Prof. F. Balkwill (London, UK)	(Miller et al., 1983)
CMT93Var	mouse colon cancer	C57BL/6	Dr. med. C. Hackl (Regensburg)	(Franks et al., 1978)
CT26	mouse colon cancer	BALB/c	ATCC (Wesel)	(Brattain et al., 1980)
E0771-LG	mouse breast cancer	C57BL/6	Prof. J. Pollard (Edinburgh, UK)	(Kitamura et al., 2019)

2.1.1.2.3. Modified murine tumor cell lines

The modified murine tumor cell lines used in this thesis are listed in Table 4.

Table 4: Modified murine tumor cell lines.

Name	Origin	E-cadherin modification
410.4-pLKO.1-scrambled-shRNA	410.4	Control
410.4-pLKO.1-mE-cadherin-shRNA	410.4	Knockdown
CMT93Var-pLKO.1-scrambled-shRNA	CMT93Var	Control
CMT93Var-pLKO.1-mE-cadherin-shRNA	CMT93Var	Knockdown
CT26-pLenti-empty	CT26	Control
CT26-pLenti-mE-cadherin	CT26	Overexpression
E0771-LG-pLX302-empty	E0771-LG	Control
E0771-LG-pLX302-mE-cadherin	E0771-LG	Overexpression

2.1.1.3. Mouse strains

Adult mice were obtained from Charles River (Hannover, Germany) and constantly kept under standard laboratory conditions in the animal facility. All animals were fed a soy-free diet.

The mouse strains used in this thesis are listed in Table 5.

Table 5: Mouse strains.

Name	Syngeneic intracortical injections	Source
BALB/c	410.4, CT26	Charles River
C57BL/6	CMT93Var, E0771-LG	Charles River

2.1.2. Chemicals and reagents

The chemicals and reagents used in this thesis are listed in Table 6.

Table 6: Chemicals and reagents.

Product	Company
2-Mercaptoethanol	Sigma-Aldrich
2-Propanol 70% (v/v)	B. Braun
Acetic acid	Merck Millipore
Agar	Sigma-Aldrich
Agarose	Biozym Scientific
Agarose NEEO ultra-quality	Carl Roth

Ammonium persulfate (APS)	VWR
Ampicillin	Carl Roth
Antibody diluent	Dako
Adenosine 5'-triphosphate (ATP) disodium salt hydrate	Sigma-Aldrich
Bepanthen eye and nose ointment	Bayer Vital GmbH
Bovine serum albumin (BSA)	Carl Roth
BSA standard ampules	Gibco/Thermo Fisher Scientific
Bromophenol blue	Carl Roth, Pharmacia Biotech
Chloramphenicol	Carl Roth
Crystal violet solution	Sigma-Aldrich
Diethyl ether	Merck Millipore
Dimethyl sulfoxide	Sigma-Aldrich
Deoxyribonucleic acid (DNA) gel loading dye (6x)	Thermo Fisher Scientific
Domitor 1 mg ml ⁻¹	Orion Pharma
Eosin Y solution	Carl Roth
Ethanol (EtOH)	Merck Millipore, Carl Roth
Ethidium bromide (EtBr)	Sigma-Aldrich
Ethylenediaminetetraacetic acid (EDTA)	Merck Millipore, Carl Roth
Extracellular matrix	R&D Systems
ExtrAvidin-Peroxidase	Sigma-Aldrich
Fluorescent mounting medium	Dako
Formic acid	Carl Roth
GeneRule 1 kilo bases (kb) DNA ladder	Thermo Fisher Scientific
GeneRuler 50 bp DNA ladder	Thermo Fisher Scientific
Glycerol	Sigma-Aldrich
Glycine	Sigma-Aldrich
Hematoxylin solution	Merck
Hydrochloric acid 37%	Carl Roth
Hydrochloric acid solution (adjust pH)	Fluka Analytical
Hydroxytricarballic acid	Merck
Isopropanol	Merck Millipore
Kanamycin	Carl Roth
Ketamin 10%	Medistar
Metamizol 500 mg ml ⁻¹	WDT
Methanol	Merck Millipore
Methylene blue	Sigma-Aldrich
Modified milk powder (MMP), blotting grade (nonfat dry milk)	Carl Roth
NaCl 0.9% isotonic saline solution	B. Braun
Orange DNA loading dye (6x)	Thermo Fisher Scientific
Paraformaldehyde (PFA)	Merck Millipore

Paraplast bulk	Leica
PBS powder without Ca^{2+} , Mg^{2+}	Merck
Perhydrol hydrogen peroxide 30%	Merck
Phosphatase inhibitor PhosSTOP (10x)	Roche
Polybrene	Sigma-Aldrich
Polyethylenimine	Polysciences
Ponceau S solution	AppliChem
Potassium acetate	Merck
Precision Plus Protein Dual Color standard	Bio-Rad
Protease inhibitor cocktail tablets, EDTA free	Roche
Restore Western blot stripping buffer	Thermo Fisher Scientific
Rimadyl Carprofen	Zoetis
RNaseOUT recombinant ribonuclease inhibitor (40 U/ μl)	Invitrogen/Thermo Fisher Scientific
Roti phenol/chloroform/isoamyl alcohol	Carl Roth
Roti-Histokitt II	Carl Roth
Rotiphorese Gel 30 (30% (v/v) acrylamide/bisacrylamide solution)	Carl Roth
Rotipuran trichloromethane/chloroform	Carl Roth
Sodium acetate water-free	Carl Roth
Sodium chloride (NaCl)	Carl Roth, Thermo Fisher Scientific
Sodium deoxycholate (>97%)	Sigma-Aldrich
Sodium dodecyl sulphate (SDS)	Carl Roth, Merck
Sodium hydroxide (NaOH) solution (adjust pH)	Merck
Softasept N	B. Braun
Target Retrieval solution, citrate pH 6.1 (10x)	Dako
Tetramethylethylenediamin (TEMED)	Sigma-Aldrich
Thiazolyl blue tetrazolium bromide	Sigma-Aldrich
Tri-Sodium citrate dihydrate	Merck
Tris wash buffer (pH 6)	Merck Millipore
Triton X-100	Sigma-Aldrich
Trizma acetate (Tris-Acetate)	Sigma-Aldrich
Trizma base (Tris-Base)	Sigma-Aldrich
Trizma HCl (Tris-HCl)	Sigma-Aldrich
TRIzol reagent	Invitrogen/Thermo Fisher Scientific
Trypton	Becton-Dickinson
Tween 20	Sigma-Aldrich
UltraPure DNase/RNase-free distilled water	Invitrogen/Thermo Fisher Scientific
Water, DPEC-treated	Sigma-Aldrich
Xylol	Carl Roth
Yeast extract	Becton-Dickinson

2.1.3. Bacterial media and agarose plates

Selective culture medium with a dilution of 1:1000 of the required antibiotic stock concentration was used for cultivation of *Escherichia coli* (*E. coli*) strains under sterile conditions. Stock concentrations were 100 mg ml⁻¹ for ampicillin, 50 mg ml⁻¹ for kanamycin and 30 mg ml⁻¹ for chloramphenicol. Agarose plates and media were stored at 4 °C and preheated before usage.

The bacterial media and reagents used in this thesis are listed in Table 7. They were prepared with sterile H₂O and, if necessary, subsequently autoclaved.

Table 7: Bacterial media and reagents.

Name		Composition
Lysogeny broth (LB) medium	1%	tryptone
	0.5%	yeast extract
	1%	NaCl
	ad	H ₂ O
LB ₀ agar plates	10%	tryptone
	5%	yeast extract
	5%	NaCl
	15%	agar
LB _{amp} agar plates		pH 7.0
		LB ₀
LB _{kana} agar plates	100 mg ml ⁻¹	ampicillin
		LB ₀
LB _{chlor} agar plates	50 mg ml ⁻¹	kanamycin
		LB ₀
Yeast extract tryptone agar (YTA) medium	30 mg ml ⁻¹	chloramphenicol
	100 mg ml ⁻¹	ampicillin
	16%	tryptone
	10%	yeast extract
	5%	NaCl
	ad	H ₂ O

2.1.4. Cell culture media and additives

The media and additives used for the culture of cell lines in this thesis are listed in Table 8.

Table 8: Cell culture media and additives.

Product	Company
Dulbecco's modified Eagle medium (DMEM) (1 g l ⁻¹ glucose)	Merck Millipore
Dulbecco's modified Eagle medium (4.5 g l ⁻¹ glucose)	Sigma-Aldrich
Dulbecco's phosphate buffered saline (PBS) without Ca ²⁺ , Mg ²⁺	Gibco/Thermo Fisher Scientific
Fetal calf serum (FCS)	PAN Biotech, Life technologies
Geneticin (G418)	Roche, Sigma-Aldrich
Penicillin/Streptomycin (P/S)	Merck Millipore, Sigma-Aldrich
Puromycin	Sigma-Aldrich
Roswell Park Memorial Institute (RPMI) 1640 medium	Gibco/Thermo Fisher Scientific
Trypsin-EDTA (10x)	Sigma-Aldrich

2.1.5. Buffers and solutions

The buffers and solutions used in this thesis are listed in Table 9. They were prepared with sterile H₂O and, if necessary, subsequently autoclaved.

Table 9: Buffers and solutions.

Name	Composition
6x DNA loading dye blue	10 mM Tris-Base/Tris-HCl 0.03% bromophenol blue
Ampicillin	1 g ampicillin 10 ml H ₂ O
Blotting buffer	25 mM Tris-Base/Tris-HCl 192 mM glycine 20% (v/v) methanol ad 1 l H ₂ O
BSA 5%	5% (w/v) BSA in TBST
Chloramphenicol	300 mg chloramphenicol 10 ml H ₂ O
Citrate buffer	solution A: 2.1 g tri-sodium citrate dihydrate in 100 ml H ₂ O solution B: 29.41 g hydroxytricarballic acid in 1 l H ₂ O

	2 ml	solution A
	98 ml	solution B
	ad 1 l	H ₂ O
		pH 6.0
Crystal violet staining solution	0.005%	crystal violet solution
	10%	EtOH
Electrophoresis buffer	25 mM	Tris-Base/Tris-HCl
	192 mM	glycine
	0.1%	(w/v) SDS
	ad 1 l	H ₂ O
HCl alcohol 0.22%	1 l	isopropanol
	6 ml	hydrochloric acid 37%
Kanamycin	500 mg	kanamycin
	10 ml	H ₂ O
Laemmli buffer (4x)	2 g 5 ml ⁻¹	SDS in H ₂ O
	10 mg	bromophenol blue
	40%	(v/v) glycerol
	20%	(v/v) stacking gel buffer
	20%	(v/v) 2-mercaptoethanol
MMP 5%	5%	(w/v) MMP in TBST
MTT lysis buffer	5%	(v/v) formic acid in isopropanol
MTT stock solution	5 mg ml ⁻¹	MTT in PBS
P1 mini buffer	50 mM	Tris-Base/Tris-HCl (pH 8.0)
	10 mM	EDTA
	100 µg	ribonuclease A
	ad	H ₂ O
P2 mini buffer	200 mM	NaOH
	1%	SDS
	ad	H ₂ O
P3 mini buffer	3 M	potassium acetate
	ad	H ₂ O
Peroxidase solution 3%	10%	hydrogen peroxide 30%
	90%	PBS
PFA solution 4%	24 g	PFA
	540 ml	distilled water (dH ₂ O)
		solve at 60 °C
	6–9 drops	NaOH
	60 ml	10x PBS
		pH 7.3

Resolving gel buffer	1.5 M 2%	Tris-Base/Tris-HCl (w/v) SDS pH 8.8
RIPA lysis buffer	50 mM 150 mM 0.1% 0.5% 1% 10x 100x	Tris-Base/Tris-HCl (pH 7.2) NaCl (w/v) SDS (w/v) Na-deoxycholate Triton X-100 added fresh: phosphatase inhibitor protease inhibitor
Stacking gel buffer	0.5 M 2%	Tris-Base/Tris-HCl (w/v) SDS pH 6.8
Tris-acetate-EDTA (TAE) buffer	40 mM 1 mM 0.1% ad	Tris-Acetate EDTA glacial acetic acid H ₂ O
Tris-buffered saline with Tween20 (TBST)	20 mM 150 mM ad 1 l 0.1%	Tris-Base/Tris-HCl NaCl H ₂ O pH 7.6 (v/v) Tween20
Tris-EDTA (TE) buffer	5 ml 1 ml 494 ml	Tris-Base/Tris-HCl EDTA H ₂ O pH 8.0
Triton X 0.5%	0.5%	(v/v) Triton X-100 in PBS

2.1.6. Antibodies and fluorescent dyes

The antibodies and fluorescent dyes used in this thesis are listed in Table 10.

Table 10: Antibodies and fluorescent dyes.

Name	Source	Label	Application/Dilution	Company/Cat. Nr.
CD3 (SP7)	Rabbit	—	IHC (1:150)	DCS Diagnostics (#CI597R06)
CD31 (PECAM-1) (D8V9E) XP	Rabbit	—	IHC (1:100)	Cell Signaling (#77699)
Cytokeratin 8 (phospho S431)	Rabbit	—	IHC (1:100), WB (1:1000 in BSA)	Abcam (#ab59434)
DAPI	—	—	IF (1:1000)	Sigma-Aldrich (#D8417)
E-cadherin (24E10)	Rabbit	—	IF (1:50), IHC (1:200), WB (1:1000 in BSA)	Cell Signaling (#3195)
E-cadherin (Clone 36)	Mouse	—	WB (1:1000 in BSA)	BD (#610181)
Glial Fibrillary Acidic Protein	Rabbit	—	IHC (1:200)	Dako (#Z0334)
HSP90 α / β (F-8)	Mouse	—	WB (1:5000 in BSA)	Santa Cruz (#sc-13119)
Iba-1	Rabbit	—	IHC (1:1000)	Wako (#019-19741)
Mouse IgG (H+L)-HRP	Donkey	HRP	WB (1:10,000)	Jackson (#715-035-150)
Mouse IgG+IgM (H+L)-FITC	Goat	FITC	IF (1:100)	Dianova (#115-095-068)
Mouse IgG-HRP	Goat	HRP	WB (1:2000)	Santa Cruz (#sc-2005)
Phalloidin-FITC	<i>Amanita phalloides</i>	FITC	IF (1:100)	Sigma-Aldrich (#P5282)
Phospho-YAP (Ser127)	Rabbit	—	WB (1:1000 in MMP)	Cell Signaling (#4911)
Rabbit IgG (H+L)-Biotin	Goat	Biotin	IHC (1:250)	Dianova (#111-065-144)
Rabbit IgG (H+L)-FITC	Goat	FITC	IF (1:300)	Thermo Fisher Scientific (#31635)
Rabbit IgG (H+L)-HRP	Donkey	HRP	WB (1:10,000)	Jackson (#711-035-152)
Rabbit IgG-HRP	Goat	HRP	WB (1:2000)	Santa Cruz (#sc-2004)
Vimentin (D21H3) XP	Rabbit	—	IF (1:50), IHC (1:100), WB (1:1000 in BSA)	Cell Signaling (#5741)
YAP (D8H1X) XP	Rabbit	—	WB (1:1000 in MMP)	Cell Signaling (#14074)
β -Actin (AC-15)	Mouse	—	WB (1:10,000 in BSA)	Sigma-Aldrich (#A5441)
β -Actin (C4)	Mouse	—	WB (1:1000 in BSA)	Santa Cruz (#sc-47778)
β -Catenin (E-5)	Mouse	—	IF (1:50), WB (1:1000 in MMP)	Santa Cruz (#sc-7963)

BSA: bovine serum albumin, FITC: fluorescein isothiocyanate, HRP: horseradish peroxidase, IF: immunofluorescence, IHC: immunohistochemistry, MMP: modified milk powder, WB: Western blot

2.1.7. Oligonucleotides

The oligonucleotides listed in Table 11 were designed with MIT server and used for shRNA constructs.

Table 11: Oligonucleotides for shRNA constructs.

Name	Sequence (5'–3')	Source
control-siRNA-F	CCGG AATTCTCCGAACGTGTCACGT CTCGAG ACGTGACACGTTCCGAGAATT TTTTG	Microsynth
control-siRNA-R	AATTCAAAAA AATTCTCCGAACGTGTCACGT CTCGAG ACGTGACACGTTCCGAGAATT	Microsynth
mE-Cad-siRNA-F	CCGG TACCCGGGACAATGTGTATTA CTCGAG TAATACACATTGTCCCGGGTA TTTTG	Microsynth
mE-Cad-siRNA-R	AATTCAAAAA TACCCGGGACAATGTGTATTA CTCGAG TAATACACATTGTCCCGGGTA	Microsynth

The oligonucleotides listed in Table 12 were used for sequencing of vector constructs.

Table 12: Sequencing primers for cloning vectors.

Primer	Used for vector	Sequence (5'–3')	Source
M13-seq-F	pENTR	CGTTGTAAACGACGGCCAG	Microsynth
M13-seq-R	pENTR	CAGGAAACAGCTATGAC	Microsynth
hU6-seq-F	pLKO.1	GGGCCTATTTCCCATGATTC	Microsynth
pLKO-seq-R	pLKO.1	AAGTGGATCTCTGCTGTCCC	Microsynth

The primers for qRT-PCRs listed in Table 13 were designed with the PerlPrimer software.

Table 13: Primers for qRT-PCR.

Name	Description	Direction	Sequence (5'–3')	Source
mmBlvrb	Biliverdin Reductase B	Forward	TAAGATTCTGCAAGAGTCAGG	Sigma-Aldrich
		Reverse	CCAGTTAGTGGTTGGTCTC	Sigma-Aldrich
mmCDH1	Cadherin 1	Forward	GAAATCACATCTTATACCGCTC	Sigma-Aldrich
		Reverse	CGTCTTCTCTGTCCATCTC	Sigma-Aldrich
mmCLDN4	Claudin-4	Forward	CCAGCAACTATGTGTAAGGT	Sigma-Aldrich
		Reverse	GATAACAAAGGCAATGTGGA	Sigma-Aldrich
mmCLDN7	Claudin-7	Forward	CCGAATAGCTATGACTGGAG	Sigma-Aldrich
		Reverse	ACAATCTGATGACCAATCCA	Sigma-Aldrich
mmDPYSL3	Dihydropyrimidinase-like 3	Forward	GCTCTATGAGATCTTCACCTG	Sigma-Aldrich
		Reverse	GCAATGATATCTCCATTCTCG	Sigma-Aldrich

mmGAPDH	Glyceraldehyde-3-Phosphate Dehydrogenase	Forward	CATCTTGGGCTACACTGAG	Sigma-Aldrich
		Reverse	CTGTAGCCGTATTCATTGTC	Sigma-Aldrich
mmGPX2	Glutathione Peroxidase 2	Forward	CTCAATGAGCTGCAATGTC	Sigma-Aldrich
		Reverse	CAGGTCGGACATACTTGAG	Sigma-Aldrich
mmGPX4	Glutathione Peroxidase 4	Forward	GTCTGCCTGGATAAGTACAG	Sigma-Aldrich
		Reverse	CTAGCTGAGTGTAGTTTACGT	Sigma-Aldrich
mmITGA2	Integrin Alpha-2	Forward	GGTCCTAAATTCATCTTCTCC	Sigma-Aldrich
		Reverse	TCTGTTTGTATCCCAGTCAG	Sigma-Aldrich
mmITGA3	Integrin Alpha-3	Forward	ATCAATGTGACCAATTCACC	Sigma-Aldrich
		Reverse	TGGTCTCGTTATTAGCTTGG	Sigma-Aldrich
mmITGB1	Integrin Beta-1, Fibronectin Receptor Beta	Forward	CAACTGTGATAGGTCTAATGG	Sigma-Aldrich
		Reverse	ATAGCATTCAAAACACGAC	Sigma-Aldrich
mmKRT19	Cytokeratin-19	Forward	CACTACTTTAAGACCATCGAG	Sigma-Aldrich
		Reverse	ATCTGTAGGACAATCTTGGAG	Sigma-Aldrich
mmKRT8	Cytokeratin-8	Forward	ATGAACAAGGTGGAAGTAGAG	Sigma-Aldrich
		Reverse	ATCTCCTCTTCATGGATCTG	Sigma-Aldrich
mmL1CAM	L1 cell adhesion molecule	Forward	CCCACCTTAGGATCTACTGGA	Sigma-Aldrich
		Reverse	GAATGATTGTCTGAGGTAAGC	Sigma-Aldrich
mmMgst1	Microsomal Glutathione S-Transferase 1	Forward	CTTTACCTCCTATGCAACGA	Sigma-Aldrich
		Reverse	ACCTTGTTGGTTATCCTCTG	Sigma-Aldrich
mmPAK2	p21 (RAC1) Activated Kinase 2 (DPYSL3-Interacting Kinase)	Forward	AAGTTCTACGACTCCAACAC	Sigma-Aldrich
		Reverse	TCATCATCTTCTCTGTCAC	Sigma-Aldrich
mmPGK1	Phosphoglycerate Kinase 1	Forward	TGTCCAAACTAGGAGATGTC	Sigma-Aldrich
		Reverse	CCTTGGCAAAGTAGTTCAG	Sigma-Aldrich
mmSNAI1	Snail Family Zinc Finger 1	Forward	TGAAGATGCACATCCGAAGC	Sigma-Aldrich
		Reverse	CAGTGGGAGCAGGAGAATG	Sigma-Aldrich
mmSNAI2	Snail Family Zinc Finger 2	Forward	CAAGGACACATTAGAACTCAC	Sigma-Aldrich
		Reverse	TTCTTTACATCAGAGTGGGTC	Sigma-Aldrich
mmTwist1	Twist Basic Helix-Loop-Helix Transcription Factor 1	Forward	GTACATCGACTTCTGTACCA	Sigma-Aldrich
		Reverse	TTGCCATCTTGGAGTCCAG	Sigma-Aldrich
mmTwist2	Twist Basic Helix-Loop-Helix Transcription Factor 2	Forward	TACATAGACTTCTCTACCAGG	Sigma-Aldrich
		Reverse	GGTCATCTTATTGTCCATCTCG	Sigma-Aldrich
mmVimentin	Vimentin	Forward	CGGCTGCGAGAGAAATTGC	Sigma-Aldrich
		Reverse	CCACTTCCGTTCAAGGTCAAG	Sigma-Aldrich
mmWWTR1	WW Domain Containing Transcription Regulator 1	Forward	CATGGACGAGATGGATACAG	Sigma-Aldrich
		Reverse	GAGAGGGATCAGATCTTCAG	Sigma-Aldrich

mmXdh	Xanthine Dehydrogenase	Forward	AACACAAGTAACCTCATCCT	Sigma-Aldrich
		Reverse	TTTGTTCCTTCCTCACCTC	Sigma-Aldrich
mmYAP1	Yes-Associated Protein 1	Forward	GTTACAGATGGAGAAGGAGAG	Sigma-Aldrich
		Reverse	GATTGATATTCCGTATTGCCTG	Sigma-Aldrich
mmZEB1	Zinc Finger E-box Binding Homeobox 1	Forward	CAGTATTACCAGGAGGCA	Sigma-Aldrich
		Reverse	CACACTCGTTGTCTTTCAC	Sigma-Aldrich
mmZEB2	Zinc Finger E-box Binding Homeobox 2	Forward	CCACGATCCAGACCACAATTA	Sigma-Aldrich
		Reverse	TACTCTTCGATGCTCACTGC	Sigma-Aldrich

2.1.8. Plasmids

The plasmids used in this thesis are listed in Table 14.

Table 14: Plasmids.

Plasmid	Characteristic	Bacterial resistance in <i>E. coli</i>	Selectable marker	Source
pENTR-Cdh1	Gateway entry vector	Kanamycin	—	Addgene (#49776)
pLX302	Gateway destination vector	Chloramphenicol + Ampicillin	Puromycin	Addgene (#25896)
pLenti CMV/TO Neo DEST (685-3)	Gateway destination vector	Chloramphenicol + Ampicillin	G418	Addgene (#17292)
pLKO.1 puro	Destination vector for shRNA insert	Ampicillin	Puromycin	Addgene (#8453)
pMD2.G	Lentiviral enveloping plasmid	Ampicillin	—	Addgene (#12259)
pCMV-dR8.2 dvpr	Lentiviral packaging plasmid	Ampicillin	—	Addgene (#8455)

2.1.9. Enzymes

The specific enzymes and restriction enzymes used in this thesis are listed in Table 15 and Table 16.

Table 15: Specific enzymes.

Name	Buffer	Source
FAST-alkaline phosphatase (AP)	10x FAST-AP buffer	Thermo Fisher Scientific
T4 DNA ligase	T4 ligase buffer	Thermo Fisher Scientific
T4 polynucleotide kinase (PNK)	10x PNK reaction buffer A	Thermo Fisher Scientific
DNase I (10 U μl^{-1})	10x DNase I incubation buffer	Roche
Ribonuclease A	—	Roth

Table 16: Restriction enzymes.

Name	Restriction site	Buffer	Source
BshT I (AgeI)	A/CCGGT	10x orange	Fermentas/Thermo Fisher Scientific
EcoRI	G/AATTC	10x EcoRI buffer	Fermentas/Thermo Fisher Scientific
NdeI	CA/TATG	10x orange	Fermentas/Thermo Fisher Scientific
PstI (Tth111I)	GACN/NGTC	10x blue	Fermentas/Thermo Fisher Scientific

2.1.10. Commercial kits

The commercial kits used in this thesis are listed in Table 17 and were used according to manufacturer's instructions.

Table 17: Commercial kits.

Product	Utilization	Company
BrdU cell proliferation ELISA kit	Measuring cell proliferation	Abcam
Clarity Western ECL substrate	Developing Western blot	Bio-Rad
Dako REAL detection system, alkaline phosphatase/RED, rabbit/mouse	IHC stainings	Dako
DC (detergent compatible) protein assay	Measuring protein concentration	Bio-Rad
Gateway LR Clonase II enzyme mix	LR Clonase reaction	Thermo Fisher Scientific
High Pure RNA isolation kit	RNA preparation	Roche
iScript cDNA synthesis kit	cDNA synthesis	Bio-Rad
iTaq Universal SYBR Green supermix	qRT-PCR	Bio-Rad
Liquid DAB+ substrate chromogen system	IHC stainings	Dako
MycoAlert mycoplasma detection kit	Mycoplasma test	Lonza
Nucleo Bond PC 20/100	Midi-preparation	Magery-Nagel

Nucleo Spin gel and PCR clean-up	Vector purification	Magery-Nagel
SignalFire ECL reagent	Developing Western blot	Cell Signaling
Trans-Blot Turbo RTA mini nitrocellulose transfer kit	Western blot	Bio-Rad
ZytoChem Plus (HRP) Anti-Rabbit kit	IHC stainings	Zytomed Systems

2.1.11. Consumables and instruments

The consumables and instruments used in this thesis are listed in Table 18.

Table 18: Consumables and instruments.

Product	Company
10 cm petri dish (coated)	Sarstedt
10 cm petri dish (un-coated)	Sarstedt
10 mm low-phytoestrogen and soy-free diet	SSNIF
384-well plates (FrameStar skirted PCR plate)	4titude
96 Biosphere filter tips (0.1–10 µl)	Sarstedt
96 Biosphere filter tips (2–20 µl)	Sarstedt
96-well plates	Nunc
Alu foil	Roth
Amersham Protran membrane (0.45 µm, nitrocellulose)	Sigma-Aldrich
Autoclavable bags	SteriClin
Bone wax	B. Braun
Bulb-headed probe	Wameda
Cell culture flasks (25/75 cm ²)	Sarstedt
Cell scraper (25 cm)	Sarstedt
Centrifuge tubes (15/50 ml)	Sarstedt
Combitips advanced (0.1 ml)	Eppendorf
Cryotubes (1.8 ml)	Thermo Fisher Scientific
Disposable glass pasteur pipettes (230 mm)	VWR
Disposable pestle tissue homogenizer (1.5 ml)	VWR
Dubois decapitation scissors, curved end	Hermle
Embedding cassettes UniLink	R. Langenbrinck GmbH
ES-Compresses	Hartmann
Folded filters (Qual.) (Ø 240 mm)	Sartorius
Gauze balls	Gazin
Glass coverslips (18 × 18 mm)	Carl Roth
Glass coverslips (Ø 12 mm)	Carl Roth
Graduated filter tips, TipOne (10/100/1000 µl)	Sarstedt
Hamilton microliter syringe (701N) (10 µl)	VWR

Immersol 518F oil	Carl Zeiss
Iris scissors, straight	Hermle
Micro tube (1.5 ml)	Sarstedt
Microscope slides (25 × 75 × 1 mm)	Thermo Fisher Scientific
Microtome blades R-35	Feather
Multiply-Pro cup (0.2 ml)	Sarstedt
Nitril extra-sensitive gloves	Nitrisense
Nitrocellulose blotting membrane (0.45 µm)	GE Healthcare Life Sciences
Noyes eye scissors, straight pattern	Hermle
Nuclease-free reaction tubes (0.5/1.5 ml)	Eppendorf
Parafilm M laboratory film	Pechiney Plastic packaging
pH indicator sticks	T.H. Geyer
Pipette tips (10/20/200/1000 µl)	Sarstedt
Pipette tips, epT.I.P.S. standard (10/100/1000 µl)	Eppendorf
Polycarbonate membrane (10 µm pore size)	Pieper Filter
qPCR adhesive clear seal	4titude
Reaction tubes (0.2/0.5/1.5/2 ml)	Sarstedt
Rotilabo blotting papers (1.5 mm)	Carl Roth
SafeSeal micro tube (2 ml)	Sarstedt
Safety-Multifly-Set infusion cannulas	Sarstedt
Sample vials	T.H.Geyer
Semkin standard forceps	Hermle
Seralon polyamide suture (DR-009, USP 7/0, EP 0.5)	Serag-Wiessner GmbH
Serological pipettes (2/5/10 ml)	Sarstedt
Serological pipettes (10/50 ml)	Greiner Bio-one
Serological pipettes (25 ml)	Nerbe Plus
Serological pipettes, Stripetten (2/5 ml)	Corning
Sterican needle (22G, 27G)	B. Braun
Sterile scalpel	Feather
Syringe with Luer-Lok connection fitting (1/5/10 ml)	B. Braun
TC plates (6/12/24/96-well)	Sarstedt
TC dish 150, standard	Sarstedt
Tissue forceps, straight pattern	Hermle
Trans-Blot Turbo mini nitrocellulose transfer pack	Bio-Rad
Trans-Blot Turbo mini-size nitrocellulose membranes	Bio-Rad
Trans-Blot Turbo mini-size transfer stacks	Bio-Rad
Wecker spatula	Hermle

2.1.12. Equipment

The lab equipment used in this thesis is listed in Table 19.

Table 19: Equipment.

Product	Label	Company
Analytical balance	R180D	Sartorius
Autoclave	5050 ELV	Tuttnauer
Autoclave	Varioklav 135S	HP Medizintechnik GmbH
Automatic flake ice machine	Scotsman AF100	Scotsman
Block thermostat	HLC BT 130	Ditabis/HLC
Cell counting chamber	Neubauer Improved	LO Laboroptik Marienfeld
Cell culture incubator	CB 160	Binder
Cell culture incubator	Heraeus	Thermo Fisher Scientific
Centrifuge	Biofuge 15	Sepatech
Centrifuge	Biofuge fresco	Thermo Fisher Scientific
Centrifuge	Biofuge pico	Thermo Fisher Scientific
Centrifuge	CT15RE	Himac
Centrifuge	Microstar 12	VWR
Chemical balance	BL 1500 S	Sartorius
Chemical balance	L610D	Sartorius
Chemical balance	SI-2002A	Denver Instrument
Chemiluminescence system	ImageQuant LAS-4000	Fujifilm
CO ₂ incubator	BB 6220	Heraeus Instruments
Confocal laser scanning microscope	Leica TCS SP8	Leica Microsystems
Cooling plate	CP 60	Microm
Drying cabinet	UT6200	Heraeus Instruments
Drying chamber	UT 6120	Thermo Fisher Scientific
Ductless recirculating fume hood	CaptairBio I-130	Erlab
Electric pipetting aid	Accu-jet pro	Brand
Electric pipetting aid	Pipetboy	Integra
Electrophoresis power supply	EPS 301	Amersham Pharmacia Biotech
Electrophoresis power supply	LKB GPS200/400	Pharmacia
Electrophoresis system	Mini-PROTEAN Tetra cell	Bio-Rad
ELISA reader	TECAN Sunrise Infinite F50	Tecan Group
Floor centrifuge	Varifuge 3.0 RS	Heraeus Instruments
Gel imaging system	Gel Doc XR+	Bio-Rad
Heating and drying table	MEDAX	Medax
Heating/shaking block	Thermomixer 5436	Eppendorf
Heating/shaking block	Thermomixer R	Eppendorf
Incubator shaker	Unitron	Infors HT

Inverted microscope	PrimoVert	Carl Zeiss
Laminar air flow bench	LaminAir HB2472	Heraeus Instruments
Laminar flow hood	Herasafe HS18	Heraeus Instruments
Light microscope	Eclipse TS100	Nikon
Light microscope	Olympus CX40	Olympus
LightCycler	QuantStudio 5, 384-well	Thermo Fisher Scientific
Light/fluorescence microscope	EVOS FL	Thermo Fisher Scientific
Magnetic stirring bar retriever	MR3001	Heidolph Instruments
Magnetic stirrer and heating plate	IKA RCT	Ikamag
Microliter pipette, automatical	Multipette plus	Eppendorf
Microliter pipettes	100–1000µl, 20–200µl, 2–20µl, 0.2–2µl	Gilson/Eppendorf
Microwave	8018 E	Privileg
Microwave	KOR 6D07SL	Daewoo
Mini centrifuge	ProFuge 10K	Stratagene
Mini shaker	IKA MS2	IKA Lab equipment
Mini shaker	Sunflower 3D	BioSan
pH meter	538 MultiCal	WTW
pH meter	CG842	Schott
Platform shaker	Duomex 1030	Heidolph Instruments
Power supply	Standard Power Pack P25	Biometra
Roller shaker	RS-TR05	Phoenix Instrument
Single-lens reflex camera	Canon EOS 600D	Canon
Slides scanner system	Pannoramic 250	Sysmex
Sliding microtome	HM 400 R	Microm
Spectrophotometer	NanoDrop 1000	Thermo Fisher Scientific
Spectrophotometer	NanoDrop 2000	Thermo Fisher Scientific
Stereotaxic drill	Jacobs Chuck (18,000 rpm)	Kopf Instruments
Surface shaker	Reax 3	Heidolph Instruments
Table centrifuge	5810R	Eppendorf
Table centrifuge	Allegra X-15R	Beckman Coulter
Table centrifuge	Megafuge 1.0 Sepatech	Kendro Laboratory Products
Table centrifuge	Megafuge 3.0R	Heraeus Instruments
Table centrifuge	Multifuge 3	Heraeus Instruments
Thermal cycler	PTC-200	MJ Research
Tissue float bath	GFL 1052	GFL
Transilluminator	Ultraviolet (UV) slider	Intas
Tumble mixer	RM5	Nichols Institute Diagnostics
Ultra-precise small animal stereotaxic instrument	Model 963	Kopf Instruments
Vortex shaker	REAX 2000	Heidolph Instruments

Vortex shaker	Vortex Genie 2	Intas
Water bath	SW-20C	Julabo GmbH
Water purification system	MilliQ	Millipore
Western blot transfer system	Trans-Blot SD Semi-Dry	Bio-Rad
Western blot transfer system	Trans-Blot Turbo	Bio-Rad

2.1.13. Software products and databases

The software products and databases used in this thesis are listed in Table 20.

Table 20: Software products and databases.

Product	Utilization	Company
BioGPS (database)	Database for gene and protein function	BioGPS
CaseViewer (version 2.3)	Imaging editor for slide images	3DHISTECH Ltd.
DNA Dynamo (version 1.498)	Theoretical cloning, sequence analysis	Blue Tractor Software Ltd
EndNote (version X8.2)	Citation program	Clarivate Analytics
Genevestigator (version 7)	Designing primers	Nebion AG
GraphPad Prism (version 7)	Graphs and statistics	GraphPad Software
Heatmapper (online tool)	Creating heatmaps	omicX
Image Lab (on device)	Image analysis of agarose gels	Bio-Rad
ImageJ (win64) (version 1.51s)	Analyzing data, editing pictures	Wayne Rasband
ImageQuant LAS 4000 (on device)	Chemiluminescence imaging	Fujifilm
LAS X (Leica Application Suite X) (version 3.7)	Imaging editor for confocal images	Leica Microsystems
Microsoft Office 2013	Managing data, writing text, editing pictures	Microsoft
NanoDrop (on device)	DNA/RNA measurement	Thermo Fisher Scientific
NCBI (database)	Database for genomic information, BLAST tool	NCBI
PerlPrimer (version 1.1.21)	Designing primers	(Marshall, 2004)
QuantStudio Design & Analysis (version 1.5.0)	Analyzing qRT-PCR data	Applied Biosystems /Thermo Fisher Scientific

2.2. Methods

2.2.1. Cloning

2.2.1.1. Knockdown vector

For generation of stable cell lines showing a downregulation of E-cadherin, short hairpin RNA (shRNA) vectors had to be constructed. An overview of the cloning workflow is shown in Figure 9.

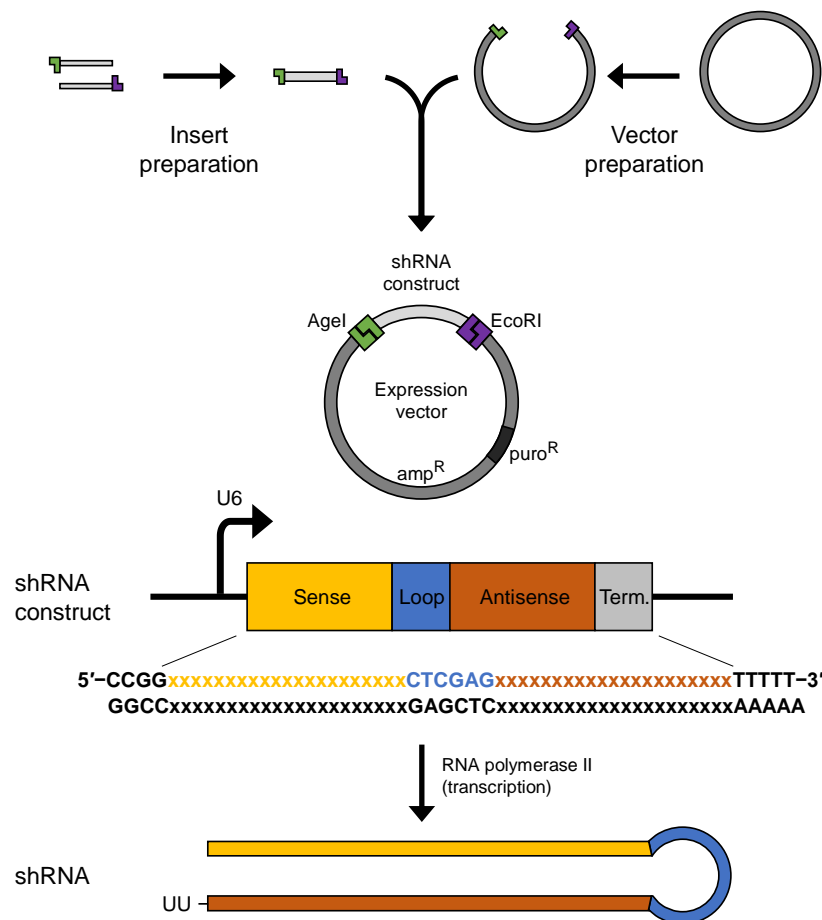


Figure 9: Knockdown vector workflow. For the construction of a knockdown vector, shRNA insert and vector are prepared with restriction enzymes, ligated and amplified in bacteria. After successful delivery to a cell nucleus, double-stranded RNA is continuously expressed from the construct in the nucleus, transported into the cytoplasm and leads to permanent silencing of the gene of interest. Modified from (<http://www.addgene.org/protocols/plko/>).

Designing tools were used to identify active E-cadherin shRNA sequences as well as a control shRNA sequence (scrambled shRNA) and oligonucleotides were ordered from a synthesizing company (Microsynth). These short pieces of synthetic single-stranded DNA, which were complementary to the target messenger RNA (mRNA), were then fused to double-stranded inserts. Both ends were designed to offer sites for restriction enzymes for the subsequent ligation with a vector backbone.

After introduction of the vector construct into a host cell and successful delivery to the cell nucleus, double-stranded RNA was continuously expressed from the construct in the nucleus and transported into the cytoplasm. There it could bind target mRNA and inactivate it, which in turn caused sequence-specific gene silencing.

2.2.1.1.1. shRNA insert preparation

Preparation of the shRNA insert included oligonucleotide phosphorylation, denaturation of all secondary structures and annealing of complementary strands.

2.2.1.1.1.1. Phosphorylation of oligonucleotides

Reagents

- Oligonucleotide forward (100 μ M)
- Oligonucleotide reverse (100 μ M)
- T4 polynucleotide kinase
- 10x PNK reaction buffer A
- ATP (2 mM)

Procedure

For each shRNA, 5 μ l oligonucleotide forward, 5 μ l oligonucleotide reverse, 1 μ l buffer, 0.5 μ l ATP and 0.5 μ l PNK were mixed together in small tubes and the mixture was incubated overnight at 37 °C. On the next day, PNK was heat-inactivated for 10 min at 75 °C and the phosphorylated oligonucleotides were centrifuged down shortly.

2.2.1.1.1.2. Annealing of phosphorylated oligonucleotides

For the annealing of the phosphorylated oligonucleotides, 15 μ l TE buffer was added, vortexed shortly and boiled for 2 min at 95 °C. The tube was cooled down to room temperature (RT) for 1 h and stored on ice.

2.2.1.1.2. Vector preparation

The pLKO.1 vector had to be prepared for shRNA construct insertion. One of the most common methods in molecular biology is cloning by restriction digest. Insert and expression vector have to be formerly designed or digested to create compatible ends. This enables the cloning of the desired insert into a certain expression vector. Agarose gel electrophoresis can be used to purify the digested vector from any undigested rests. To minimize the risk of re-ligation the vector is cut with two enzymes and dephosphorylated using alkaline phosphatase.

2.2.1.1.2.1. Cutting of vector

Reagents

- Restriction enzymes (AgeI + EcoRI)
- 10x Compatible restriction buffer
- pLKO.1 puro plasmid

Procedure

1 µg plasmid, 4 µl buffer and 2 µl enzyme were filled up with double-distilled water (ddH₂O) to a total volume of 40 µl, mixed well and centrifuged down for 20 s at 16,000 *g*. The mixture was incubated overnight at 37 °C and the digested vector was purified from a 1% methylene blue stained agarose gel on the next day.

2.2.1.1.2.2. Agarose gel electrophoresis

Agarose gel electrophoresis is a common method used to purify cutted vectors after plasmid digestion and for control digestion of plasmid DNA. For vector purification, the agarose gels were stained with methylene blue and for plasmid DNA control digestion they were stained with ethidium bromide. As both chemicals incorporate into double-stranded DNA, they could be visualized directly in the gel (methylene blue) or under UV light (EtBr). Molecular weight markers were used to determine the molecular size of the DNA product.

Reagents

- Agarose
- TAE buffer
- Ethidium bromide (10 mg ml⁻¹) (for control digestion of plasmid DNA)
- Methylene blue (for purification of digested vector)
- Loading dye (6x DNA gel loading dye, 6x Orange DNA loading dye)
- Standard (Gene Ruler 1 kb DNA ladder, 50 bp DNA ladder)

Procedure

0.7 g agarose was boiled with 70 ml TAE buffer. For control digestion of plasmid DNA, 20 µl ethidium bromide was added to the melted agarose. The gel mixture was poured in the gel holder, the gel comb was inserted and polymerization took place for 1 h at RT. The gel was then placed in the gel box (electrophoresis unit), fully covered with TAE buffer and the gel comb was removed. 4 µl loading dye was added to 20 µl of each sample and 10 µl DNA ladder standard solution and the samples were loaded in the wells. The electrophoresis was performed for approximately 30 min at 130 V. The bands were visualized with methylene blue or under UV light in case of EtBr addition.

2.2.1.1.2.3. Purification of vector

The required band was cut out from the methylene-blue stained gel as accurate as possible and transferred into a 1.5 ml Eppendorf tube. Then the desired cutted vector was purified with the Nucleo Spin Gel and PCR Clean-Up Kit according to the manufacturer's instructions.

2.2.1.1.2.4. Dephosphorylation of vector

To avoid the re-ligation of the digested and purified vector, the 5' end had to be dephosphorylated.

Reagents

- Purified vector
- FAST-AP
- 10x FAST-AP buffer

Procedure

26 µl of the purified vector was mixed with 3 µl buffer and 1 µl FAST-AP. The mixture was centrifuged shortly and incubated at least 30 minutes at 37 °C before the enzyme was heat-inactivated for 20 min at 75 °C.

2.2.1.1.3. Ligation of construct

The ligation of shRNA insert and vector was the last step of the cloning procedure.

Reagents

- T4 DNA ligase
- T4 ligase buffer
- pLKO.1 vector, digested and purified
- shRNA insert

Procedure

Three ligations were set up according to Table 21. The ligations were incubated 3 h at RT or overnight at 16 °C and then transformed into DH5alpha competent cells and plated on ampicillin plates as explained later (see 2.2.1.3).

Table 21: Setup for construct ligation.

	Control	Ligation
ddH ₂ O	17.25 µl	16.25 µl
T4 ligase buffer	2 µl	2 µl
Insert	—	1 µl
Vector	0.5 µl	0.5 µl
T4 DNA ligase	0.25 µl	0.25 µl

2.2.1.2. Overexpression vector

For generation of stable cell lines showing an upregulation of E-cadherin, expression vectors had to be constructed. After introduction of the vector construct into a host cell and successful delivery to the cell nucleus, E-cadherin mRNA was continuously expressed from the construct in the nucleus and transported into the cytoplasm where it was translated into protein at the ribosomes. As the parental cell lines showed different resistances to selection antibiotics, different expression vectors were required. For speed and efficiency, the Gateway cloning technology was chosen. It has been developed by Invitrogen to easily insert a gene of interest (GOI) into various destination vectors for usage in cell culture without labor-intensive and time-consuming procedures like in classical molecular cloning processes.

2.2.1.2.1. Gateway cloning technology

2.2.1.2.1.1. Preparation of Gateway entry vector

In the first step, the GOI had to be cloned into an entry vector. The entry vector containing the mouse E-cadherin gene cassette (pENTR-Cdh1) was a gift from Jamie Davies (Addgene plasmid #49776; <http://n2t.net/addgene:49776>; RRID:Addgene_49776).

2.2.1.2.1.2. Transfer of gene cassette into Gateway destination vector

In the second step, the GOI from the entry vector had to be subcloned into a destination vector using an enzyme-mediated site-specific recombination reaction (LR reaction) which produced the expression vector (Figure 10).

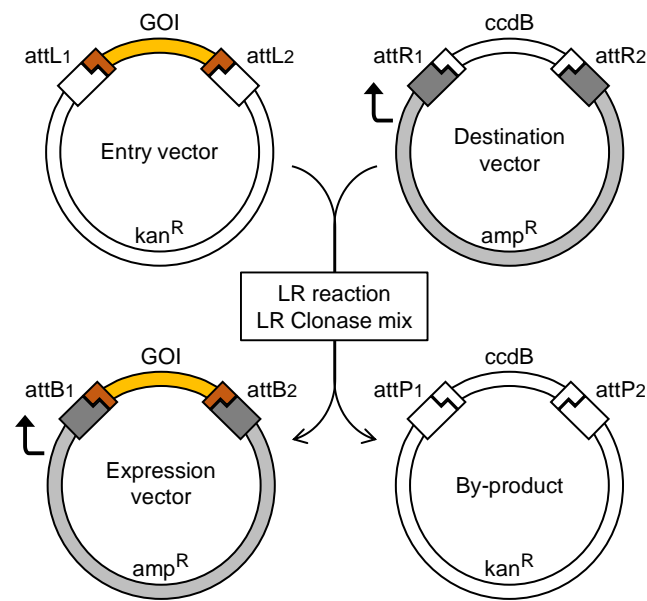


Figure 10: Step 2 of Gateway cloning technology. The entry vector is transcriptionally silent and contains the gene of interest (GOI) flanked by the attL1 and attL2 recombination sites as well as the gene for kanamycin resistance (kan^R). In order to produce the desired expression vector, the GOI has to be subcloned into a destination vector that contains all the sequence information necessary for expression: two recombination sites (attR1 and attR2) that flank a gene for negative selection, ccdB (the encoded protein is toxic for the standard *E. coli* strains) and the gene for ampicillin resistance (amp^R). Both plasmids are mixed and the LR Clonase enzyme mix is added. In a directional specific reaction, attL1 reacts with attR1 and attL2 with attR2. Two constructs, the intended expression vector and a by-product, are the result of this recombination. Two forms of selection, the antibiotic resistance and the negative selection by the toxic ccdB protein, affect the expression vector and ensure high levels of positive clones after transformation to a standard cloning strain (for example, DH5alpha). Modified from (https://www.embl.de/pepcore/pepcore_services/cloning/cloning_methods/recombination/gateway/).

Reagents

- Destination vectors (pLX302 and pLenti CMV/TO Neo DEST (685-3))
- Entry vector (pENTR-Cdh1)
- Gateway LR Clonase II enzyme mix

Procedure

50 ng destination vector, 75 ng entry vector and 0.25 µl LR Clonase were mixed to a total volume of 5 µl with ddH₂O, centrifuged shortly and incubated for at least 2 h at 25 °C. Afterwards, 2 µl LR reaction was transformed into DH5alpha competent bacteria and plated on ampicillin plates.

2.2.1.3. Transformation of chemically competent *E. coli* cells

This method is used to transfer a desired ligated plasmid into bacterial cells for cultivation and amplification of the amount of plasmid. In this thesis, the *E. coli* strains DH5alpha and DB3.1 were used for transformation. The cells became competent by the CaCl₂ method, which made the cell membrane permeable to plasmid DNA. An overview of the amplified plasmids with the respective competent *E. coli* strains and selection antibiotics is shown in Table 22.

Table 22: Overview of amplified plasmids.

Plasmid	Competent <i>E. coli</i> strain	Selection antibiotic
pENTR-Cdh1	DH5alpha	Kanamycin
pLenti CMV/TO Neo DEST (685-3)	DB3.1	Chloramphenicol + Ampicillin
pLenti-mE-cadherin	DH5alpha	Ampicillin
pLKO.1	DH5alpha	Ampicillin
pLKO.1-mE-cadherin-shRNA	DH5alpha	Ampicillin
pLKO.1-scrambled-shRNA	DH5alpha	Ampicillin
pLX302	DB3.1	Chloramphenicol + Ampicillin
pLX302-mE-cadherin	DH5alpha	Ampicillin

Reagents

- Competent *E. coli* cells (DH5alpha, DB3.1)
- Vector (ligation mix or LR reaction mix)
- LB medium
- LB plates with appropriate antibiotic (selection plates)

Procedure

A tube of competent *E. coli* cells was slowly thawed on ice. Plasmid DNA (20 µl of the ligation mix or 2 µl of the LR reaction mix) was added to the cells, flicked and the mixture was incubated on ice for 30 min. Heat shock was performed for 1 min at 42 °C and the mixture was placed back on ice for 5 min. Next, 200 µl pre-warmed (37 °C) LB medium without antibiotics was added and the mixture was shaken for 30 min at 37 °C. Meanwhile, selection plates were pre-warmed at 37 °C. Finally, the mixture was spread onto a selection plate and incubated inverted overnight at 37 °C.

2.2.1.4. DNA preparation

After the transformation process, in which vector DNA was amplified only in selected cells containing the vector of interest, the DNA had to be isolated. In the first step of DNA preparation, cells from grown colonies were picked from the plate with sterile tips and inoculated in 2 ml LB medium (overnight) or YTA medium (several hours) supplemented with 2 µl appropriate selection antibiotic (see 2.2.1.3). After amplification overnight at 37 °C with continuous agitation, the mini-preparation and following midi-preparation were used to isolate the plasmid DNA.

2.2.1.4.1. Mini-preparation

The mini-preparation of plasmid DNA is a small-scale isolation of plasmid DNA from bacteria used to test constructs after restriction digestion on agarose gels and select positive clones for further amplification.

Reagents

- P1 mini buffer
- P2 mini buffer
- P3 mini buffer
- 100% EtOH
- 70% EtOH

Procedure

1.5 ml of the overnight culture was poured into an Eppendorf tube and centrifuged for 1 min at 3500 *g*. The pellet was resuspended in 100 µl P1 mini buffer. 200 µl P2 mini buffer was added and vortexed. After addition of 150 µl P3 mini buffer, tubes were inverted 3–4 times. The samples were centrifuged for 6 min at 19,000 *g* at 4 °C while new tubes with 900 µl 100% EtOH were prepared. The supernatant was transferred into the prepared tubes and mixed well by inverting 6–8 times. The samples were centrifuged for 12 min at 21,500 *g* at 4 °C and the supernatant was discarded. The pellets were washed with 1 ml 70% EtOH and centrifuged for 3 min at 19,000 *g*. Supernatant was removed completely and the pellets were dried at 65 °C in an incubator and finally dissolved in 25 µl ddH₂O.

2.2.1.4.2. Restriction digestion

In the next step, isolated plasmid DNA was tested for positive insertion of desired construct. Restriction enzymes were used to cut the plasmid DNA in a site-specific manner and agarose gel electrophoresis was used to separate different band patterns and identify plasmids with correct insertion.

The enzymes used for restriction digestion of each plasmid and expected positive band patterns are shown in Table 23.

Table 23: Setup for restriction digestion of plasmids.

Plasmid	Restriction enzymes	Expected positive band sizes
pLenti-mE-cadherin	Psyl (= Tth111I)	7192 bp + 3674 bp
pLKO.1 puro for all shRNAs	NdeI + EcoRI	6958 bp + 126 bp
pLX302-mE-cadherin	Psyl (= Tth111I)	8750 bp + 1907 bp

Reagents

- Plasmid DNA from mini-preparation
- Appropriate buffer
- Restriction enzymes

Procedure

10 µl plasmid DNA, 2 µl buffer and 0.5 µl of each restriction enzyme were mixed with ddH₂O to a final volume of 20 µl and incubated for 1 h at 37 °C. Agarose gel electrophoresis was performed as described previously (see 2.2.1.1.2.2) and band patterns were verified in a transilluminator under UV light.

2.2.1.4.3. Midi-preparation and sequencing

The midi-preparation of plasmid DNA is a large-scale isolation of plasmid DNA from bacteria used to produce large amounts of the construct for later usage (for example, lentiviral particle production). After successful control digestion, the positive clones could be inoculated for further amplification and midi-preparation. An Erlenmeyer flask was prepared with 55 ml LB medium and 55 µl appropriate selection antibiotic (see 2.2.1.3). 5 µl of the remaining overnight mini-cultures was added to the flasks and midi-cultures were incubated overnight at 37 °C with continuous agitation. On the next day, the midi-cultures were centrifuged, plasmid DNA was purified with the Nucleo Bond PC 20/100 kit according to the manufacturer's instructions, and a sample was sent to Microsynth AG for further sequencing.

2.2.2. Cell culture methods

2.2.2.1. Maintenance of murine tumor cell lines

Tumor cells were cultivated at 37 °C and 5% CO₂ in a humidified incubator. They were passaged twice a week by washing once with PBS, detaching by incubation with 1 ml 1x Trypsin-EDTA for up to 15 min and splitting in a ratio of 1:5–1:20. All experiments were performed with mycoplasma-free cells confirmed by regular tests. For maintenance of various cell lines over a longer period, they were frozen in dimethyl sulfoxide with 90% FCS and stored in liquid nitrogen. An overview of all cell lines with respective media and supplements is shown in Table 24.

Table 24: Cell lines with respective media and supplements.

Cell line	Culture medium	Supplement	Selection antibiotic
410.4	DMEM (1 g l ⁻¹)	10% FCS	—
410.4-pLKO.1-mE-cadherin-shRNA	DMEM (1 g l ⁻¹)	10% FCS	1 µg ml ⁻¹ puromycin
410.4-pLKO.1-scrambled-shRNA	DMEM (1 g l ⁻¹)	10% FCS	1 µg ml ⁻¹ puromycin
CMT93Var	DMEM (1 g l ⁻¹)	10% FCS	—
CMT93Var-pLKO.1-mE-cadherin-shRNA	DMEM (1 g l ⁻¹)	10% FCS	1 µg ml ⁻¹ puromycin
CMT93Var-pLKO.1-scrambled-shRNA	DMEM (1 g l ⁻¹)	10% FCS	1 µg ml ⁻¹ puromycin
CT26	RPMI 1640	10% FCS	—
CT26-pLenti-empty	RPMI 1640	10% FCS	400 µg ml ⁻¹ G418
CT26-pLenti-mE-cadherin	RPMI 1640	10% FCS	400 µg ml ⁻¹ G418
E0771-LG	RPMI 1640	10% FCS	—
E0771-LG-pLX302-empty	RPMI 1640	10% FCS	1 µg ml ⁻¹ puromycin
E0771-LG-pLX302-mE-cadherin	RPMI 1640	10% FCS	1 µg ml ⁻¹ puromycin
HEK293T	DMEM (4.5 g l ⁻¹)	10% FCS	—

2.2.2.2. Lentivirus-mediated gene delivery (transduction)

Cell lines with stable knockdown or overexpression of the cell adhesion protein E-cadherin were generated through shRNA-mediated gene silencing or introduction of expression vectors by lentivirus-mediated gene delivery. After transduction, lentiviral vectors could integrate into the nucleus of the target cells and led to stable expression of the gene of interest. The following procedures were carried out in a S2 cell culture lab and 1% P/S was added to the culture medium to avoid contaminations.

2.2.2.2.1. Lentiviral particle preparation

For virus preparation, 8×10^6 HEK293T cells were seeded in a 150 mm cell culture dish and allowed to adhere overnight to reach a confluence of 80%. On the next morning, the medium was replaced with

20 ml serum-free DMEM (4.5 g l⁻¹ glucose). 15 µg lentiviral plasmid, 3.75 µg enveloping plasmid pMD2.G and 11.25 µg packaging plasmid pCMV-dR8.2-dvpr were mixed with DMEM (4.5 g l⁻¹ glucose) to a total volume of 1230 µl, vortexed and 120 µl polyethylenimine was added. The mixture was vortexed again for 10 s, incubated for 15 min at RT and added dropwise to the cells. Plates were incubated for 6 h at 37 °C before the medium was replaced with 30 ml DMEM (4.5 g l⁻¹ glucose) with 10% FCS.

For virus collection, the medium was collected after 72 h and centrifuged for 15 min at 3000 g to remove large cell particles. The supernatant was transferred into new tubes and centrifuged for 2 h at 75,000 g and 4 °C to pellet viral particles. The pellet was dissolved in 150 µl DMEM (4.5 g l⁻¹ glucose) with 10% FCS by gentle pipetting and left on ice overnight at 4 °C. On the next morning, the viral particle suspension was mixed again and frozen in small aliquots at -80 °C.

2.2.2.2.2. Transduction of target cells

The day before transduction, tumor cells were seeded in 100 mm cell culture dishes and allowed to adhere overnight to reach a confluence of 60–80%. On the next morning, the medium was replaced with only 8 ml of the appropriate culture medium with 10% FCS. 8 µl Polybrene (8 mg ml⁻¹) and 50 µl of the viral particle suspension was simultaneously added dropwise to the plate and evenly distributed by gentle circular movements. Plates were incubated for 6 h at 37 °C before the medium was replaced with 10 ml of the appropriate culture medium with 10% FCS. On the next day, appropriate selection antibiotics (puromycin or G418) were added and plates were incubated to get rid of any untransduced tumor cells. The selection medium was replaced every other day until single colonies remained.

2.2.2.2.3. Selection of single clones

Single clones were selected using a microscope, picked with sterile tips and transferred into 24-well plates containing appropriate culture medium with 10% FCS and selection antibiotics. Cells were expanded by appropriate cell-culture techniques until sufficient cell numbers were available for protein isolation to quantify the expression level of E-cadherin by Western blot analysis (see 2.2.4). Positive clones were further expanded in 100 mm cell culture dishes.

2.2.2.2.4. Viral particle test

The absence of any viral particles in the modified cell lines was confirmed by a marker rescue assay (Forestell et al., 1996). Virus test cell lines were chosen according to their sensitivity to selection antibiotics of modified cell lines confirmed by antibiotic kill curves. An overview of the test setup is shown in Table 25. Modified cells were incubated for 48 h in culture medium without selection

antibiotic. Meanwhile, 2×10^6 virus test cells were seeded in 100 mm cell culture dishes and allowed to adhere overnight to reach a confluence of 50%. On the next morning, the medium of the modified cell lines was collected and centrifuged for 15 min at 3000 *g* to remove large cell particles. The medium of the virus test cell lines was replaced with the supernatant and 10 μ l Polybrene (8 mg ml⁻¹) was added dropwise to the plates and evenly distributed by gentle circular movements. Plates were incubated for 72 h at 37 °C before appropriate selection antibiotics were added and plates were further incubated for up to two weeks. The selection medium was replaced every other day and confluence of remaining cells was assessed until no surviving cells were visible (virus test negative) or single colonies remained (virus test positive). In the latter case, the procedure had to be repeated. Viral particle-free modified cell lines could be then transferred into a S1 cell culture lab.

Table 25: Setup for viral particle test.

Modified cell line	Virus test cell line	Selection antibiotic
410.4-pLKO.1 variants	HEK293T	0.75 μ g ml ⁻¹ puromycin
CMT93Var-pLKO.1 variants	HEK293T	0.75 μ g ml ⁻¹ puromycin
CT26-pLenti variants	410.4	1000 μ g ml ⁻¹ G418
E0771-LG-pLX302 variants	HEK293T	0.75 μ g ml ⁻¹ puromycin

2.2.2.2.5. Stability of transduction

The modified cell lines were cultivated in the absence of selection antibiotics for up to four weeks and protein lysates were isolated once a week. Stability of transduction was confirmed by Western blot analysis (see 2.2.4). This was essential for subsequent animal experiments without use of antibiotics.

2.2.2.3. Assessment of cell viability and proliferation

In the beginning, cell lines were tested for basic features such as cell viability and proliferation. All cellular assays were conducted at least in triplicate and in case of modified tumor cell lines in culture media without selection antibiotics.

2.2.2.3.1. Cell proliferation

To assess cell proliferation rates, 5×10^4 , 1×10^5 and 1.5×10^5 cells per well were seeded in duplicates in 24-well plates and incubated for 48 h. Cells were then trypsinized and the cell number was determined. The proliferation rate was calculated as follows:

$$\text{proliferation rate} = \frac{\text{mean cell number (48 h)}}{\text{seeded cell number}}$$

2.2.2.3.2. MTT assay

The viability of cells can be determined by assessment of their metabolic activity. The colorimetric MTT assay measures the reduction of the soluble yellow tetrazolium dye 3-(4,5-dimethylthiazol-2-yl)-2,5-diphenyltetrazolium bromide (MTT) to the insoluble purple formazan. This process is driven by NAD(P)H-dependent cellular oxidoreductase enzymes in the endoplasmic reticulum and is only carried out by living cells. In apoptotic or necrotic cells with an altered metabolism this process is impaired.

5×10^4 cells per well were seeded in duplicates in 24-well plates and incubated for 24 h, 48 h and 72 h. At each end point, confluence and amount of dead cells were assessed. The medium was replaced with 500 μ l 10% MTT solution in culture medium and cells were incubated for 4 h at 37 °C. The medium was carefully aspirated and the formazan complexes were lysed in 500 μ l MTT lysis buffer for 10 min at RT in the dark on a shaker. The intensity was proportional to the amount of enzyme activity in the cells and a photometer was used to quantify the colored reaction product by measuring the extinction at 550 nm in triplicates.

2.2.2.3.3. BrdU assay

The viability of cells can also be determined by assessment of the amount of newly synthesized DNA of actively proliferating cells. The colorimetric BrdU assay detects BrdU that can be incorporated into the genomic DNA of proliferating cells during DNA synthesis in place of thymidine.

2×10^4 cells per well were seeded in triplicates in 96-well plates and incubated overnight. Subsequently, the BrdU Cell Proliferation ELISA Kit was used according to manufacturer's instructions. Briefly, cells were labeled by the addition of BrdU reagent for 4 h at 37 °C. The following fixation of the cells for 30 min at RT led to the denaturation of DNA. After addition of a detector anti-BrdU monoclonal antibody, which bound to any incorporated BrdU within 1 h, secondary horseradish peroxidase (HRP)-conjugated goat anti-mouse antibody was added for 30 min to bind to the detector antibody. Finally, the peroxidase catalyzed the added substrate tetra-methylbenzidine during an incubation time of 30 min which converted the solution from colorless to blue and finally to yellow after the addition of a stop solution. The intensity was proportional to the amount of incorporated BrdU in the cells and a photometer was used to quantify the colored reaction product by measuring the extinction at 450 nm.

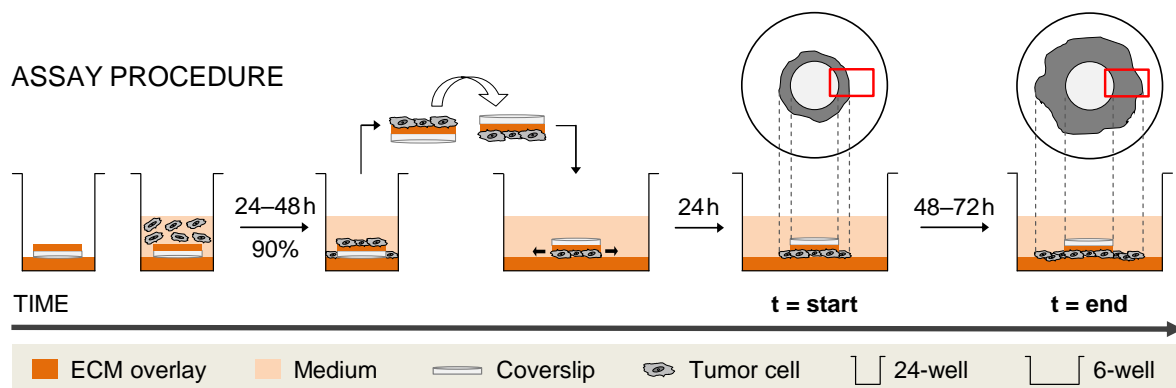
2.2.2.4. Functional *in vitro* assays

Next, cell lines were tested in various functional assays concerning migration behavior and invasive capacity as well as spheroid and colony formation ability *in vitro*. All cellular assays were conducted at least in triplicate and in case of modified tumor cell lines in culture media without selection antibiotics.

2.2.2.4.1. Cell migration assay with turned coverslips

The ability of tumor cells to migrate into the surrounding area was analyzed by ECM-based migration assays using turned coverslips (Figure 11).

Coverslips were placed into 24-well plates and coated with ECM diluted 1:4 in serum-free medium. 5×10^5 cells were seeded onto coated coverslips and incubated for 24 h until they reached confluence. On the next day, coverslips were turned over upside-down into 6-well plates coated with ECM and incubated for up to 96 h. The distance of migrated cells was measured after 24 h (start) and 72 h or 96 h (end) depending on the cell line using the EVOS FL microscope. Migration speed (μm per day) and number of spreaders (cells per mm^2) were analyzed using the ImageJ software.



ASSAY ANALYSIS

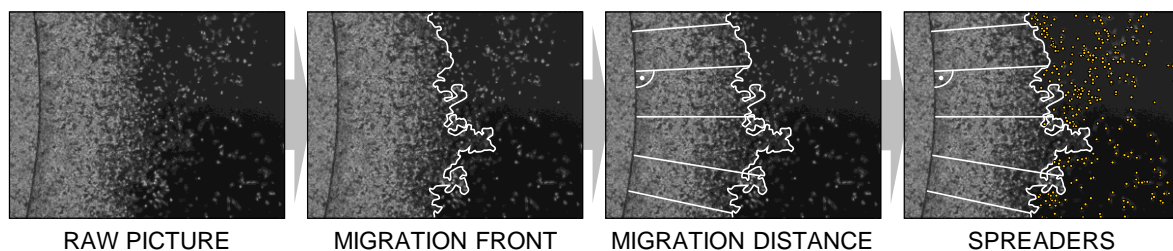


Figure 11: Schematic of cell migration assay with turned coverslips.

2.2.2.4.2. Cell invasion assay in a modified Boyden chamber

The ability of tumor cells to invade through a membrane was analyzed by micro-invasion assays in a modified Boyden chamber (Figure 12).

The modified Boyden chamber consists of two plates, a lower one with normal wells and an upper one with wells without bottom. Both plates can be sealed tightly with screws. First, the base wells were completely filled with culture medium and sealed with a polycarbonate membrane (10 μm pore diameter) previously coated with ECM diluted 1:4 in serum-free medium. The upper plate was placed onto the membrane, top wells were filled with culture medium and allowed to equilibrate for 30 min at 37 °C. Next, the equilibration medium was removed, 1×10^5 cells were seeded into top wells and incubated for 96 h. Afterwards, the chamber was carefully disassembled and the medium in base wells was resuspended thoroughly to detach the tumor cells that had invaded through the membrane from top wells. Finally, the number of invaded cells was counted using a Neubauer counting chamber.

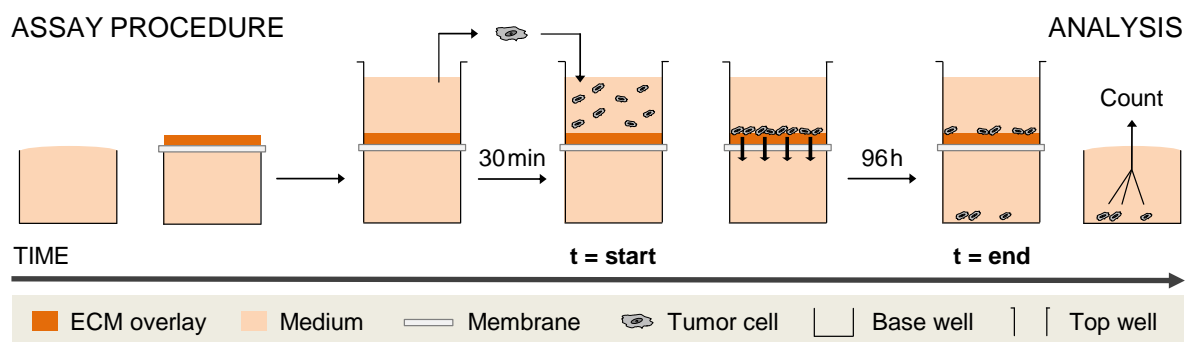


Figure 12: Schematic of cell invasion assay in a modified Boyden chamber.

2.2.2.4.3. Colony formation assay in soft agar

The ability of tumor cells to grow in anchorage-independent conditions was analyzed by soft agar colony formation assays (Figure 13).

For the base agar layer, 1.0% agarose was mixed with supplemented culture medium (20% FCS, 1% P/S) in equal parts, layered into 6-well plates and allowed to solidify for 30 min at RT. For the top agar layer, 5×10^4 cells were resuspended in supplemented culture medium (10% FCS, 1% P/S) mixed with 0.5% agarose and layered onto 1.0% agar beds in 6-well plates. Supplemented culture medium (10% FCS, 1% P/S) was added on top of cells and replaced with fresh medium twice a week for up to five weeks (depending on cell line). Images were taken of five fields for each well on three subsequent focus layers using the EVOS FL microscope. Colonies were counted using the ImageJ software and classified into three groups: small (0.001–0.005 mm^2), medium (0.0051–0.05 mm^2) and large (>0.05 mm^2). Finally,

the wells were stained with 0.5 ml crystal violet staining solution for 1 h at 37 °C, washed twice with ddH₂O and whole well images were taken with a single-lens reflex camera.

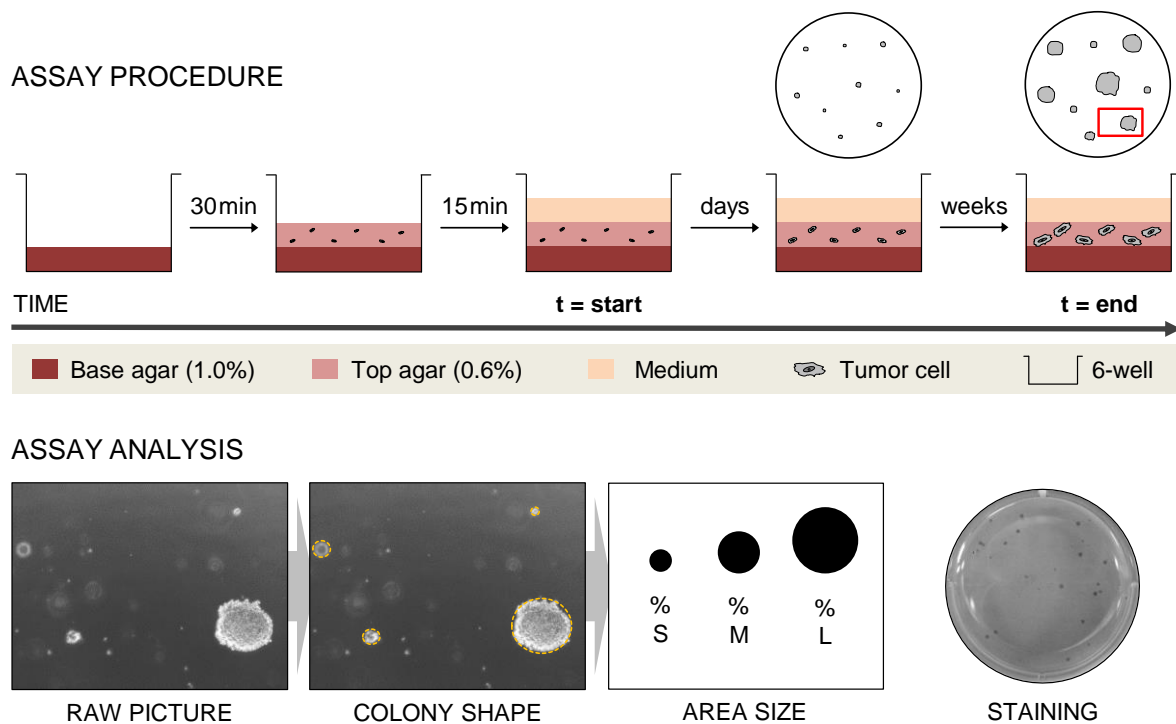


Figure 13: Schematic of colony formation assay in soft agar.

2.2.2.4.4. Spheroid formation assay using hanging drop method

The ability of tumor cells to form a spheroid in anchorage-independent conditions and its subsequent outgrowth were analyzed by spheroid formation assays using the hanging drop method (Figure 14).

First, a single cell suspension (0.25×10^5 in 0.5 ml) was prepared. The bottom of a 100 mm cell culture dish was filled with 10 ml PBS to act as a hydration chamber. The lid was inverted and 25 μ l drops of the cell suspension (1250 cells per drop) were placed onto it with sufficient distance between them. The lid was carefully inverted, placed onto the PBS-filled bottom chamber and incubated for 72 h leading to the formation of spheroids in those hanging drops. Next, 24-well plates were prepared with 1 ml culture medium per well. After careful removal of the PBS, the plate was inverted and pictures (pre) were taken from spheroids using the EVOS FL microscope. Formed spheroids were then very carefully transferred in separated 24-wells and incubated for up to 96 h. One image was taken after 3 h when spheroids had settled down (start) and then every 24 h until the end of the experiment at 96 h (end). Spheroid outgrowth (mm²) was analyzed using the ImageJ software.

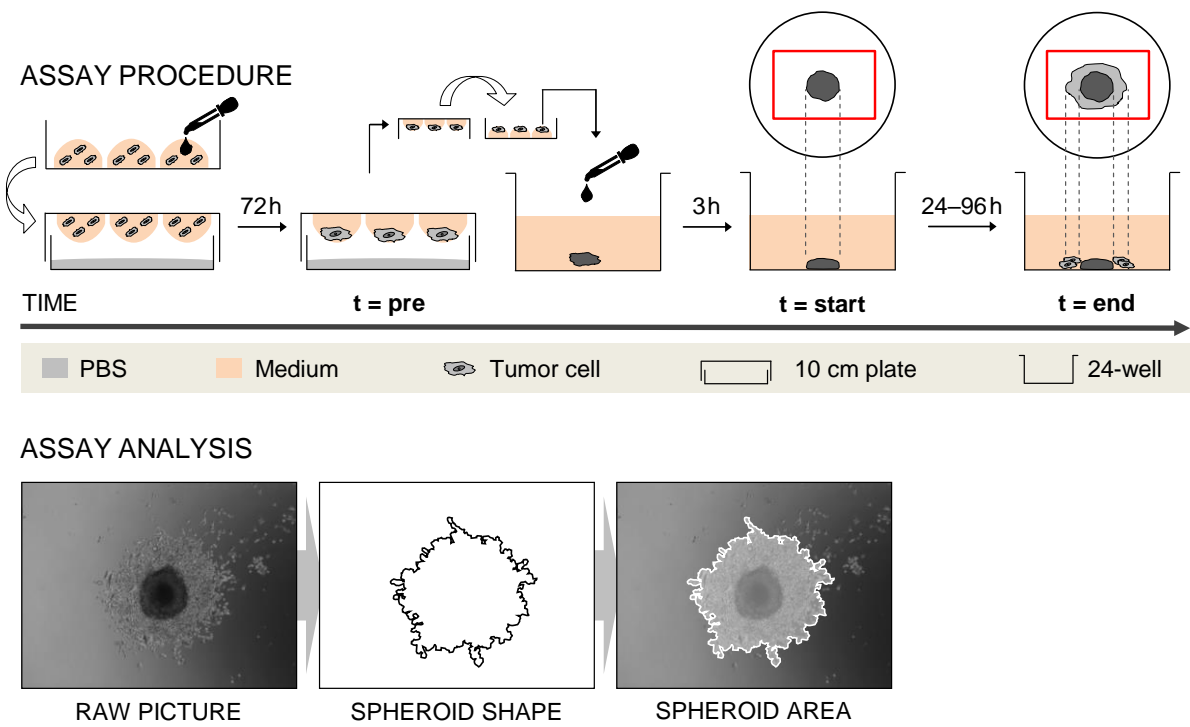


Figure 14: Schematic of spheroid formation assay using hanging drop method.

2.2.3. *In vivo* experiments

All animal work was approved by the local veterinary authorities from the Government of Bavaria based on European guidelines and national regulations of the German animal protection act (permission no. 55.2-2532-2-908).

2.2.3.1. Maintenance of animals

Adult female mice were obtained from Charles River (Hannover, Germany) and constantly kept under standard laboratory conditions (12 h light/dark cycle, lights on at 07:00 h, 22 ± 2 °C, $50 \pm 5\%$ humidity, low-phytoestrogen and soy-free diet and tap water ad libitum). They were group-housed in standard mouse cages with sawdust bedding and allowed to habituate for at least three weeks after arrival. At the beginning of the experiments, all mice were 12 to 13 weeks old.

2.2.3.2. Cancer cell preparation for injection

One or two days prior to the experiment, cells were seeded in culture flasks and allowed to adhere to reach a confluence of 70–80%. First, the level of confluence was assessed and bright-field images were taken. Gel matrix was prepared, consisting of one part of culture medium and two parts of ECM, and kept at 4 °C. Cells were trypsinized, counted and the desired number of cells (1×10^3 cells per animal) was centrifuged for 5 min at 800 *g*. Supernatant was removed, cells were resuspended in gel matrix (3 μ l per animal) and stored on ice until injection.

2.2.3.3. Stereotactical intracortical injection

To assess the effects of E-cadherin modification in our late brain colonization *in vivo* model, control and modified tumor cells were stereotactically injected into the cortical region of syngeneic mice as depicted in Figure 15. Briefly, anesthetic solution consisting of 100 μ l Ketamin 10%, 25 μ l Domitor (1 mg ml^{-1}) and 875 μ l NaCl 0.9% was prepared (B). The mouse was weighted (A) and anesthetized by intraperitoneal injection of the anesthetic solution ($7.5 \text{ } \mu\text{l g}^{-1}$ body weight for BALB/c, $5 \text{ } \mu\text{l g}^{-1}$ body weight for C57BL/6) (C). Eyes were protected against dehydration during the whole process by Bepanthen application. After disinfection, a small incision was made in the middle of the head and the periosteum of the right skull cup was carefully removed with a sterile scalpel (D). Next, the mouse was placed into a stereotaxic frame and fixed with ear bars in order to hold the skull in a horizontal position to the ground (E). A drill hole of approximately 1 mm of diameter was stereotactically bored 1.5 mm rostral and 1.5 mm right lateral of the bregma using a stereotaxic tooth-technical drill (F+G). An opening or damaging of the dura mater must be avoided during this process. The previously prepared cell suspension was mixed and 3 μ l were drawn up in a 10 μ l Hamilton syringe with tapered

cannula tip which was then fixed in the holder of the stereotaxic frame in a position directly above the skull hole and with the open end of the cannula to the left side. The cannula was inserted 3.5 mm deep in the brain and pulled back 0.5 mm forming a small cavity for the cell suspension. Subsequently, the cells were injected directly into the cortical region of the brain over a period of 60 seconds and the cannula was left in the same position for additional two minutes to ensure the establishment of the cells in the brain parenchyma (H). After removal of the cannula and simultaneous rinse of the injection site with NaCl 0.9%, the skull hole was closed with bone wax. The skin on the head was sutured (I), a painkiller (10% Rimadyl in NaCl 0.9%) was injected subcutaneously ($5 \mu\text{g g}^{-1}$ body weight) (J) and the mouse was placed on a thermal plate to recover from anesthesia (K).

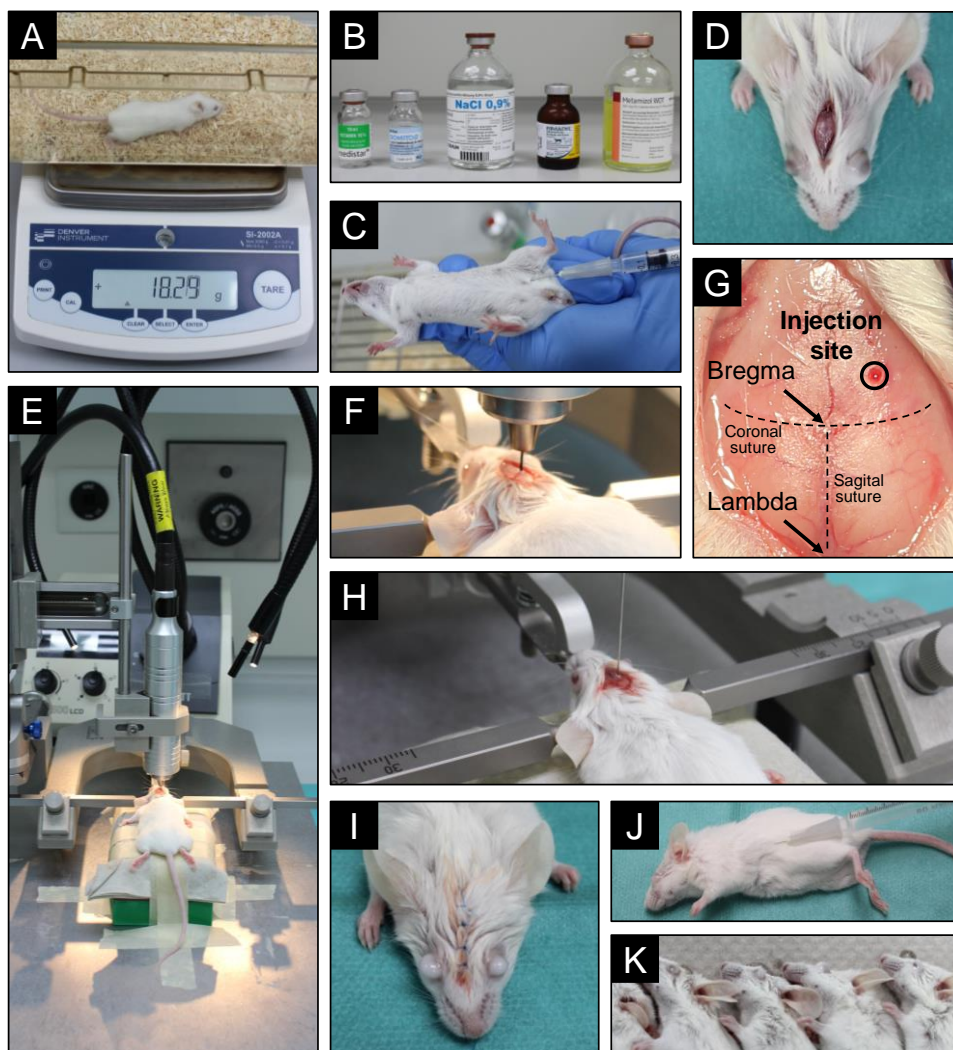


Figure 15: Stereotactical intracortical injection of tumor cells. A 12-to-13-week-old mouse is (A) weighed and (B+C) put under anesthesia by intraperitoneal injection. (D) A small incision is made in the middle of the head and the periosteum of the right skull cup is removed carefully with the help of a sterile scalpel. (E) The mouse is placed into a stereotaxic frame and (F+G) a drill hole of approximately 1 mm of diameter is stereotactically bored 1.5 mm rostral and 1.5 mm right lateral of the bregma. (H) The cell suspension ($3 \mu\text{l}$) is stereotactically injected into the cortex using a Hamilton syringe. (I) The skin is stitched up and (J) a painkiller is administered subcutaneously. (K) Finally, the mouse is allowed to recover from anesthesia on a thermal plate.

2.2.3.4. Animal monitoring and Hanging Wire test

After injection, mice were regularly monitored for their physical fitness and any emerging sensory or motor deficits. Animals were weighed at least once a week, as body weight loss is often an indicator for or accompanied by neurological symptoms. As soon as the mice showed abnormalities in their behavior, they were submitted to the Hanging Wire test. This test evaluates motor functions by assessing muscle strength, coordination, and orientation of the animals and is useful to indirectly identify neurological dysfunctions caused by metastatic outgrowth (Blazquez et al., 2018). Briefly, a wire was stretched between two platforms 35 cm above the ground of a cage covered with soft bedding. Animals were hang with their fore limbs to the wire and had to reach one of the platforms. Mice that did not manage this task within 60 seconds or dropped to the ground were sacrificed due to advanced metastatic growth.

2.2.3.5. Perfusion and brain tissue sample collection

A perfusion set with 10 ml PBS in a syringe was prepared. The mouse was anesthetized with diethyl ether and an incision was made in the skin of the abdomen. The thorax was opened and the peritoneum was cut through to expose the heart. The needle was inserted into the left main heart chamber and a small hole was cut into the right cardiac atrium for the drainage of blood during injection of PBS. The perfusion washed out the blood from the circulatory system and stiffened the brain tissue. The mouse was decapitated, the brain was taken out and cut in pieces according to the schematic in Figure 16. The anterior parts were immediately shock frozen in liquid nitrogen and stored at -80°C until homogenization for RNA isolation and further gene expression analysis by quantitative real-time polymerase chain reactions (qRT-PCR) (see 2.2.5.4). The posterior part of the metastatic brain was fixated in 4% PFA for 48 h, washed and stored in PBS at RT until embedding in paraffin and further investigation of MMPi patterns by immunohistochemical (IHC) stainings (see 2.2.6.2).

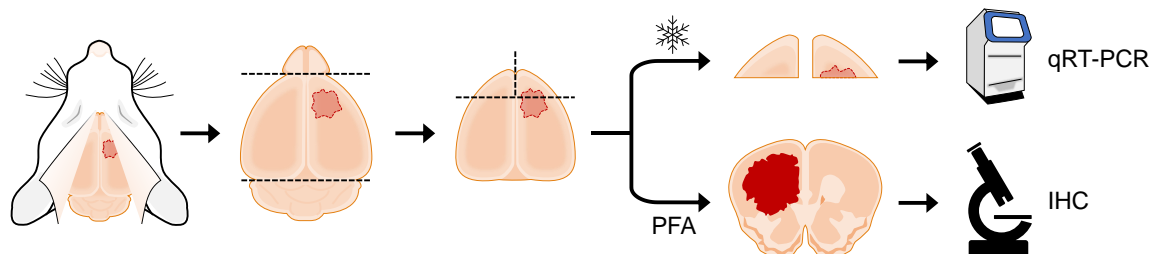


Figure 16: Schematic of brain tissue samples taken at the end of *in vivo* experiments.

2.2.4. Protein biochemical methods

2.2.4.1. Protein isolation

For the generation of whole cell lysates, 2.5×10^5 cells per well were seeded in 6-well plates and incubated for 24 h, 48 h and 72 h. Confluence was assessed and images were taken with the EVOS FL microscope. Cells were washed once with cold PBS and harvested from the well with 50–100 μ l RIPA lysis buffer using a cell scraper. The detergent components Na-deoxycholate and Triton X-100 helped to solubilize proteins while protease and phosphatase inhibitors prevented proteolysis and inactivated phosphatases. After incubation for 30 min on ice, lysates were centrifuged for 10 min at 16,000 *g* and 4 °C to pellet cell debris and DNA. Supernatants containing dissolved proteins were collected and stored at –20 °C.

2.2.4.2. Protein quantification

A colorimetric method for determining the total level of protein in a solution is the detergent compatible protein assay. It is similar to the widely used Lowry assay (Lowry et al., 1951), but has been modified to save time. The assay is based on the formation of complexes between Cu^{2+} and peptide bonds of the protein sample in alkaline medium. Cu^{2+} is reduced to Cu^{1+} , which further reacts with the Folin-Ciocalteu reagent finally resulting in a blue color. The intensity is proportional to the amount of total protein concentration in the sample and can be quantified.

Samples were diluted in 10 μ l ddH₂O (1:20) and a BSA standard curve (0/25/125/250/500/1000/15,000 μ g ml^{–1}) was included in each measurement. The assay was carried out according to the manufacturer's instructions and a photometer was used to quantify the colored reaction product by measuring the extinction at 700 nm in duplicates.

2.2.4.3. Protein separation by SDS-PAGE

Proteins from whole cell lysates were separated according to their molecular weight by discontinuous SDS polyacrylamide gel electrophoresis (SDS-PAGE) as described previously (Laemmli, 1970) by using two-layer gels. After preparation and polymerization of the resolving gel (10%), a stacking gel (5%) was layered on top (Table 26). Protein samples (10–20 μ g) were mixed with 4x Laemmli loading buffer and denatured for 5 min at 95 °C. Protein disulfide bonds were reduced by the 2-Mercaptoethanol content of the buffer and the SDS ingredient quantitatively bound to proteins and applied a negative charge in proportion to their mass, which enabled the separation according to their molecular weight during the electrophoresis. The gel was placed in an electrophoresis chamber filled with electrophoresis buffer. The samples were loaded onto the gel and a prestained protein standard

marker was included to determine protein size. Proteins were first pooled in the stacking gel for 30 min at 90 V and subsequently separated in the resolving gel for around 90 min at 130 V.

Table 26: Composition of resolving and stacking gels.

Component	Resolving gel 10%	Stacking gel 5%
ddH ₂ O	1975 µl	1725 µl
Acrylamide solution (30%)	1675 µl	415 µl
Resolving gel buffer	1250 µl	—
Stacking gel buffer	—	315 µl
APS (10%) (w/v)	50 µl	25 µl
TEMED	5 µl	2.5 µl

2.2.4.4. Protein analysis by Western blot

After separation through SDS-PAGE, proteins were transferred onto a nitrocellulose membrane for subsequent detection by specific antibodies. Resolving gel, nitrocellulose membrane and Whatman blotting paper were equilibrated in appropriate blotting buffer and stacked together in a blot sandwich with the gel on top of the membrane covered by two sheets of paper on each side. The protein transfer was performed using either a traditional semi-dry transfer system (Trans-Blot SD Semi-Dry) at 15 V for 90 min at RT or a high-performance transfer system (Trans-Blot Turbo) at 25 V for 7 min at RT. Afterwards, the membrane was stained with 0.5% Ponceau S solution to verify loading and transfer efficiency. After thorough washing of the membrane with TBST, unspecific binding sites were saturated by incubation with blocking solution (5% MMP or 5% BSA in TBST) for 1 h at RT. Next, membranes were incubated with the specific primary antibodies (see 2.1.6) in the corresponding blocking solution (MMP or BSA) overnight at 4 °C. Membranes were washed three times with TBST for 5 min each, incubated with secondary HRP-conjugated antibodies (see 2.1.6) in the corresponding blocking solution for 1 h at RT and washed again three times in TBST for 5 min each. Substrate was added according to manufacturer's instructions (Clarity Western ECL substrate or SignalFire ECL Reagent) to detect the HRP. This enzyme catalyzed the oxidation of luminol and produced a chemiluminescence signal, which was detected in the LAS-4000 imager. Protein expression was quantified by analyzing the intensities of bands with the ImageJ software and calculating the ratio of protein of interest to corresponding loading control (β -actin or heat shock protein 90 (HSP90)).

2.2.5. Gene expression analysis

2.2.5.1. Isolation of total RNA from tumor cells

For the isolation of total RNA from tumor cells, 2.5×10^5 cells per well were seeded in 6-well plates and incubated for 24 h, 48 h and 72 h. Isolation was performed using the spin column-based High Pure RNA isolation kit according to manufacturer's instructions. Briefly, cells were washed once with PBS and lysed in 400 μ l lysis/binding buffer supplemented with 200 μ l PBS. The buffer components made cell membranes permeable, induced protein denaturation and inactivated RNases. After vortexing for 15 s to support cell lysis, the samples were loaded onto spin columns and centrifuged for 15 s at 8000 g . Nucleic acids bound to the column while proteins, salts and cellular debris passed through and were discarded afterwards. 10 μ l DNase I in 90 μ l DNase I incubation buffer was added directly on the column and incubated for 15 min at RT to digest the bound DNA. After three washing steps with different buffers, the remaining RNA was eluted into a new tube with 50 μ l nuclease-free water by centrifugation for 1 min at 8000 g . Concentration and purity of the RNA were measured using a NanoDrop spectrophotometer and samples were stored at -80°C .

2.2.5.2. Isolation of total RNA from brain tissues

Total RNA was extracted from murine brain metastases samples that had been dissected after the end of *in vivo* experiments (see 2.2.3.5). RNA extraction had to be carried out under RNase free conditions to prevent the degradation of the RNA. Isolation was performed using the TRIzol reagent. It consists of phenol for phase separation and guanidine isothiocyanate for denaturation of proteins as well as RNases. Small tissue samples were homogenized in 1 ml TRIzol, 200 μ l chloroform was added, mixed for 15 s and incubated for 5 min at RT. Samples were centrifuged for 15 min at 20,000 g and 4°C which resulted in an upper aqueous phase containing the RNA and a lower red organic phase made up of the chloroform and phenol dissolving the hydrophobic lipids. DNA also precipitated into the organic phase due to the acidity of the mixture. In the interphase, the hydrophilic proteins were present. To proceed with the RNA extraction, the aqueous supernatant was transferred into a clean tube without disrupting the interphase layer. To precipitate RNA out of the phase, 500 μ l isopropanol was added and the mixture was incubated for 10 min at RT. Following centrifugation for 30 min at 13,000 g and 4°C , the RNA pellet was washed in 1 ml 70% EtOH for 10 min at 20,000 g and 4°C . During this time, a DNA digestion mix was prepared with 1 μ l DNase I ($10\text{ U } \mu\text{l}^{-1}$), 0.5 μ l RNase OUT ($40\text{ U } \mu\text{l}^{-1}$), 5 μ l 10x DNase I incubation buffer and nuclease-free water to a final volume of 50 μ l. The pellet was resuspended in this DNA digestion mix and incubated for 20 min at 37°C in order to remove any contaminating DNA. The remaining RNA was purified by adding 150 μ l nuclease-free water and 200 μ l phenol/chloroform/isoamyl alcohol. Vortexing for 30 s and centrifugation for 2 min at 20,000 g and

4 °C resulted again in a phase separation with an upper aqueous phase containing the RNA. The aqueous supernatant was transferred into a clean tube again and 20 µl sodium acetate (3 M, pH 4.8) and 200 µl isopropanol was added. After incubation for 30 min at 4 °C, the samples were centrifuged for 30 min at 20,000 *g* and 4 °C to precipitate the RNA. The pellet was washed twice in 1 ml ice-cold 70% EtOH for 5 min at 20,000 *g* and 4 °C and air-dried for 10–15 min at 37 °C. Finally, the RNA pellet was eluted with 20 µl nuclease-free water for 10 min at 42 °C. Concentration and purity of the RNA were measured using a NanoDrop spectrophotometer and samples were stored at –80 °C.

2.2.5.3. Reverse transcription

The isolated RNA was reverse transcribed into complementary DNA (cDNA) using the iScript cDNA synthesis kit. 1 µg of total RNA was mixed with 4 µl 5x iScript reaction mix and 1 µl iScript reverse transcriptase and nuclease-free water was added to a final volume of 20 µl. The reaction mix was incubated in a thermal cycler for 5 min at 25 °C to anneal the primers. Next, cDNA was synthesized for 30 min at 42 °C and the enzymatic reaction was stopped afterwards by degradation of the reverse transcriptase for 5 min at 85 °C. After cooling, each sample was diluted with nuclease-free water in a ratio of 1:5 and stored at –20 °C for up to one month.

2.2.5.4. Quantitative real-time PCR

Changes in gene expression can be analyzed with quantitative real-time PCR. This method uses cDNA as a template and SYBR Green as a detection dye due to its ability to intercalate into all double stranded DNA and emit green light at 522 nm. In the first step, hot-start iTaq DNA polymerase was activated. Next, amplification of the gene of interest happened during 40 cycles of DNA denaturation, primer annealing and elongation. The fluorescent signal intensity increased proportionally to the amount of amplified GOI and could be plotted versus the cycle number. The Ct value was defined by the number of the cycle in which the fluorescence reached the threshold level and was normalized to the expression of two housekeeping genes (HK) (= Δ Ct value). Following amplification, a melting curve was produced by slowly heating up the samples, while constantly measuring the green fluorescence. This procedure gave the melting point of the amplified DNA.

The primers used for this thesis (see 2.1.7) were designed as described in 2.2.5.4.1. All procedures were carried out on ice. The reaction mixture consisted of 5.6 µl iTaq Universal SYBR Green Supermix, each 0.3 µl of forward and reverse primers (10 µM) and 1.8 µl nuclease-free water. For each gene, 8 µl of the corresponding reaction mix was prepared in a 384-well plate in triplicates. 2 µl cDNA solution (10 ng diluted in nuclease-free water in a ratio 1:1) was added to each well, the plate was sealed and centrifuged for 5 min at 400 *g* and 4 °C. Negative controls (no primer, no template) were included,

qRT-PCR was carried out using the QuantStudio 5 Real-Time PCR System according to the following protocol (Table 27) and analyzed with the QuantStudio Design & Analysis software. Gene expression of murine cell line and brain tissue samples was quantified relative to the expression of the housekeeping genes *Gapdh* and *Pgk1*. To allow statistical evaluation of groups including samples where fluorescence did not reach the threshold level within the scale, the Ct value was set to 40.0 (equivalent to no expression). Purity of the qRT-PCR products was determined through analysis of their respective melting curves.

Table 27: Protocol of qRT-PCR program.

Step	Temperature	Duration	Repetition
Activation of Taq DNA polymerase:	95 °C	12 min	40 cycles
Denaturation:	95 °C	15 s	
Annealing and elongation:	60 °C	1 min	
Melting curve analysis:	95 °C	15 s	
	60–95 °C	2 °C/min	

2.2.5.4.1. Establishment of primers for qRT-PCR reactions

For each GOI, a specific primer pair is needed for qRT-PCR analyses. The PerlPrimer software (Marshall, 2004) was used to design several primer pairs per target and their efficiency was subsequently tested to choose the most suitable ones. Comparable primer efficiencies are essential for the analysis of relative gene expression using ΔC_t values as this method assumes an amplification efficiency of 100%. A primer efficiency of 100% means that during each PCR cycle the PCR product is exactly doubled. The BioGPS database (C. Wu et al., 2009) was used to choose appropriate positive controls, which were cell lines or tissues showing high expression of the GOI. First, cDNA of those positive controls was produced and serial dilution series were prepared. Next, qRT-PCR was performed as described in 2.2.5.4 and the measured Ct values were plotted against the amount of input cDNA. The QuantStudio Design & Analysis software was used to calculate the slope of the resulting graph. A slope of -3.33 equals a primer efficiency of 100%. Primers with an efficiency of 90–110% were chosen for further analysis.

2.2.5.4.2. Data visualization with heatmaps

To visualize gene expression data from a large number of qRT-PCR samples, heatmaps were created using the free available online tool Heatmapper from omicX (<https://omictools.com/heatmapper-tool/>). It further enabled the unsupervised hierarchical clustering of genes depicted by dendrograms to reveal sample groups with similar expression profiles.

2.2.6. Staining

2.2.6.1. Staining of tumor cells

5×10^4 cells were seeded on coverslips in 24-well plates and incubated for 48 h at 37 °C. After fixation with 300 µl 4% PFA for 10 min at RT, coverslips were washed twice with 500 µl PBS for 5 min. The following staining procedures were performed at RT and are described below (see 2.2.6.1.1 and 2.2.6.1.2). Finally, coverslips were turned and placed onto slides with fluorescent mounting medium and allowed to solidify for 24 h at 4 °C. Slides were stored at 4 °C until images could be taken with a SP8 Leica confocal laser scanning microscope.

2.2.6.1.1. Phalloidin staining

Phalloidin is a phallotoxin derived from the death cap mushroom (*Amanita phalloides*), which is often used for visualization of cell morphology in microscopy. The bicyclic peptide selectively binds to actin filaments, which are present in almost all eukaryotic cells, and thus can make cellular structures visible by previous conjugation to fluorescent dyes (for example, FITC).

First, coverslips were incubated in 0.5% Triton X solution for 10 min to make cell membranes permeable. Following incubation in blocking buffer for 30 min, cells were stained with FITC-conjugated Phalloidin (see 2.1.6) for 1 h. For visualization of cell nuclei, coverslips were incubated with DAPI for 5 min. Washing steps were included in between each time (Table 28).

Table 28: Phalloidin staining protocol.

Reagent	Incubation
500 µl PBS	5 min wash
500 µl 0.5% Triton X-100 in PBS	10 min
500 µl PBS	3 x 5 min wash
500 µl blocking buffer (1% BSA in PBS)	30 min
500 µl PBS	3 x 5 min wash
200 µl Phalloidin-FITC in blocking buffer	1 h
500 µl PBS	3 x 5 min wash
200 µl DAPI (1:2000 in PBS)	5 min

2.2.6.1.2. Immunofluorescence staining

Cellular localization of E-cadherin was visualized with immunofluorescence (IF) stainings. First, coverslips were incubated in 0.5% Triton X solution for 10 min to make cell membranes

permeable. After subsequent incubation in blocking buffer for 30 min to block unspecific binding sites, cells were stained with primary antibody against E-cadherin (see 2.1.6) for 2 h. Secondary FITC-conjugated antibody (see 2.1.6) was added for 1 h to bind to the primary antibody. For visualization of cell nuclei, coverslips were incubated with DAPI for 5 min. Washing steps were included in between each time (Table 29). Negative controls (only secondary antibody) were performed to exclude unspecific staining.

Table 29: IF staining protocol.

Reagent	Incubation
500 µl PBS	5 min wash
500 µl 0.5% Triton X-100 in PBS	10 min
500 µl PBS	3 x 5 min wash
500 µl blocking buffer (1% BSA in PBS)	30 min
500 µl PBS	3 x 5 min wash
200 µl primary antibody in blocking buffer	2 h
500 µl PBS	3 x 5 min wash
200 µl secondary antibody in blocking buffer	1 h
500 µl PBS	3 x 5 min wash
200 µl DAPI (1:2000 in PBS)	5 min

2.2.6.2. Staining of brain tissues

Collected brain tissues (see 2.2.3.5) were routinely processed into cassettes, dehydrated and embedded in paraffin at the Institute of Pathology of the University Hospital Regensburg. Next, they were sectioned into 3 µm slices with a sliding microtome, floated on a warm water bath to remove wrinkles and placed on glass slides by a technical assistant. Slices were allowed to dry overnight at RT and backed in an oven for 30 min at 60 °C on the next day. For the staining protocols, tissue samples were taken through a decreasing alcohol concentration series (Table 30) consisting of short changes of xylol, alcohol and water to hydrate the tissue. The subsequent staining steps varied between investigated targets and are described below (see 2.2.6.2.1 and 2.2.6.2.2). Afterwards, samples were rinsed, taken back through an increasing alcohol concentration series (Table 30) consisting of short changes of water, alcohol, and xylol to dehydrate the tissue and finally sealed with coverslips using Roti-Histokitt II. Samples were scanned at the Institute of Pathology of the University Hospital Regensburg using the Panoramic 250 slides scanner system, prepared with the CaseViewer software and further analyzed using the ImageJ software.

Table 30: Alcohol concentration series for staining of brain tissue.

Decreasing alcohol concentration series		Increasing alcohol concentration series	
Reagent	Incubation	Reagent	Incubation
Xylol	5–10 min	Deionized water	short
Xylol	5–10 min	70% EtOH	3–5 min
100% EtOH	3–5 min	96% EtOH	3–5 min
100% EtOH	3–5 min	96% EtOH	3–5 min
96% EtOH	3–5 min	100% EtOH	3–5 min
96% EtOH	3–5 min	100% EtOH	3–5 min
70% EtOH	3–5 min	Xylol	5–10 min
Deionized water	short	Xylol	5–10 min

2.2.6.2.1. Hematoxylin and eosin staining

Hematoxylin and eosin (H&E) staining is still the gold standard to visualize cell morphology in tissue sections and recognize different tissue types. Nucleic acids are stained by the blue-purple colored hematoxylin and proteins are stained by the pink eosin. This results in blue cell nuclei and pink cytoplasm and extracellular matrix in H&E stained tissues (Cardiff et al., 2014). After hydrating the tissue, slices were stained with the nuclear dye hematoxylin, washed, and counterstained with eosin (Table 31).

Table 31: H&E staining protocol.

Reagent	Incubation
Hematoxylin	5 min
Warm tap water	5–10 min
72% dH ₂ O/28% HCl alcohol 0.22%	short
Warm tap water	5–10 min
Eosin + 1 drop of 100% acetic acid	3 min
Warm tap water	3 min

2.2.6.2.2. Immunohistochemical staining

Different immunohistochemical stainings were used to visualize morphological features of brain metastases. For evaluation of the MMPI pattern, brain slices were stained against vimentin (VIM) for diffuse infiltrative mouse models and cytokeratin-8 (CK8) for epithelial infiltrative ones. For evaluation of E-cadherin expression, brain slices were stained against E-cadherin (ECAD). For visualization of angiotropic infiltration, endothelial cells were stained with cluster of differentiation 31 (CD31)

antibody. For evaluation of the corresponding MME, brain slices were stained with the following immune panel: microglia/macrophages were detected with allograft inflammatory factor 1 (IBA1), astrocytes with glial fibrillary acidic protein (GFAP) and T cells with cluster of differentiation 3 (CD3).

2.2.6.2.2.1. CD3, CK8 and IBA1 staining

After hydrating the tissue, slices were incubated in 1x Target Retrieval solution for 30 min at 330 W in a microwave to break protein cross-links, expose the epitopes and antigens and enhance staining intensity. They were allowed to cool down and incubated in 3% peroxidase solution to block endogenous peroxidase activity in the tissue. Unspecific binding sites were blocked with antibody diluent before slices were stained with the corresponding first antibodies (see 2.1.6) overnight at RT. Secondary biotin-conjugated goat anti-rabbit antibody was added for 1 h at RT to bind to the primary antibody. The slices were incubated with ExtrAvidin-Peroxidase for 1 h at RT in order to form conjugates between the ExtrAvidin protein and biotin. Next, samples were incubated in a substrate-chromogen diaminobenzidine (DAB) solution for 10 min at RT in the dark. The peroxidase catalyzed the substrate DAB resulting in stable, brown colored stain at the site of the target antigen. For visualization of cell nuclei, the slices were finally stained with hematoxylin for 20 s. Washing steps were included in between each time (Table 32).

Table 32: IHC staining protocol for CD3, CK8 and IBA1.

Reagent	Incubation
1x Target Retrieval solution, citrate pH 6.1	30 min 330 W, allow to cool down
Deionized water	short wash 3x
Tris wash buffer (pH 6)	10 min wash
100 µl 3% peroxidase solution	10 min
Tris wash buffer (pH 6)	10 min wash
100 µl antibody diluent	20 min
100 µl primary antibody in antibody diluent	overnight at RT
Tris wash buffer (pH 6)	10 min wash
100 µl Rabbit IgG (H+L)-Biotin (1:250) in antibody diluent	1 h RT
Tris wash buffer (pH 6)	10 min wash
100 µl ExtrAvidin-Peroxidase (1:1000) in antibody diluent	1 h RT
Tris wash buffer (pH 6)	10 min wash
100 µl DAB solution (1:50)	10 min RT
Tris wash buffer (pH 6)	10 min wash
Hematoxylin	20 s
Warm tap water	1 min wash
Deionized water	short wash

2.2.6.2.2.2. CD31 and VIM staining

After hydrating the tissue, slices were incubated in citrate buffer for 30 min at 330 W in a microwave to break protein cross-links, expose the epitopes and antigens and enhance staining intensity. They were allowed to cool down and incubated in 3% peroxidase solution to block endogenous peroxidase activity in the tissue. Unspecific binding sites were blocked with antibody diluent before slices were stained with the corresponding first antibodies (see 2.1.6) for 1 h at RT. Secondary biotin-conjugated goat anti-rabbit antibody was added for 1 h at RT to bind to the primary antibody. The slices were incubated with Streptavidin-HRP-Conjugate (Reagent 3, ZytoChem Plus (HRP) Anti-Rabbit kit) for 15 min at RT in order to form conjugates between the streptavidin protein and biotin. Next, samples were incubated in a substrate-chromogen DAB solution for 10 min at RT in the dark. The peroxidase catalyzed the substrate DAB resulting in stable, brown colored stain at the site of the target antigen. For visualization of cell nuclei, the slices were finally stained with hematoxylin for 20 s. Washing steps were included in between each time (Table 33).

Table 33: IHC staining protocol for CD31 and VIM.

Reagent	Incubation
Citrate buffer pH 6	30 min 330 W, allow to cool down
Deionized water	short wash 3x
Tris wash buffer (pH 6)	10 min wash
100 µl 3% peroxidase solution	10 min
Tris wash buffer (pH 6)	10 min wash
100 µl antibody diluent	20 min
100 µl primary antibody in antibody diluent	1 h RT
Tris wash buffer (pH 6)	10 min wash
100 µl Rabbit IgG (H+L)-Biotin (1:250) in antibody diluent	1 h RT
Tris wash buffer (pH 6)	10 min wash
100 µl Streptavidin-HRP-Conjugate (Reagent 3)	15 min RT
Tris wash buffer (pH 6)	10 min wash
100 µl DAB solution (1:50)	10 min RT
Tris wash buffer (pH 6)	10 min wash
Hematoxylin	20 s
Warm tap water	1 min wash
Deionized water	short wash

2.2.6.2.2.3. ECAD staining

After hydrating the tissue, slices were incubated in 1x Target Retrieval solution for 30 min at 330 W in a microwave to break protein cross-links, expose the epitopes and antigens and enhance staining intensity. They were allowed to cool down and stored overnight at 4 °C. On the next day, they were incubated in 3% peroxidase solution to block endogenous peroxidase activity in the tissue. Unspecific binding sites were blocked with blocking solution (Reagent 1, ZytoChem Plus (HRP) Anti-Rabbit kit) before slices were stained with the first antibody (see 2.1.6) for 3 h at RT. Biotinylated secondary anti-rabbit antibody (Reagent 2, ZytoChem Plus (HRP) Anti-Rabbit kit) was added for 30 min at RT to bind to the primary antibody. The slices were incubated with Streptavidin-HRP-Conjugate (Reagent 3, ZytoChem Plus (HRP) Anti-Rabbit kit) for 15 min at RT in order to form conjugates between the streptavidin protein and biotin. Next, samples were incubated in a substrate-chromogen DAB solution for 10 min at RT in the dark. The peroxidase catalyzed the substrate DAB resulting in stable, brown colored stain at the site of the target antigen. For visualization of cell nuclei, the slices were finally stained with hematoxylin for 2 min. Washing steps were included in between each time (Table 34).

Table 34: IHC staining protocol for ECAD.

Reagent	Incubation
1x Target Retrieval solution, citrate pH 6.1	30 min 330 W, allow to cool down
Deionized water	short wash 3x, incubate overnight at 4 °C
Tris wash buffer (pH 6)	10 min wash
100 µl 3% peroxidase solution	10 min
Tris wash buffer (pH 6)	10 min wash
100 µl blocking solution (Reagent 1)	8 min
Tris wash buffer (pH 6)	5 min wash
100 µl primary antibody in blocking solution (Reagent 1)	3 h RT
Tris wash buffer (pH 6)	10 min wash
100 µl biotinylated secondary antibody, rabbit (Reagent 2)	30 min RT
Tris wash buffer (pH 6)	10 min wash
100 µl Streptavidin-HRP-Conjugate (Reagent 3)	15 min RT
Tris wash buffer (pH 6)	10 min wash
100 µl DAB solution (1:50)	10 min RT
dH ₂ O	stop reaction
Hematoxylin	2 min
Warm tap water	1 min wash
Deionized water	short wash

2.2.6.2.2.4. GFAP staining

After hydrating the tissue, slices were incubated in 1x Target Retrieval solution for 30 min at 330 W in a microwave to break protein cross-links, expose the epitopes and antigens and enhance staining intensity. They were allowed to cool down and stored overnight at 4 °C. On the next day, they were incubated in 3% peroxidase solution to block endogenous peroxidase activity in the tissue. Unspecific binding sites were blocked with antibody diluent before slices were stained with the first antibody (see 2.1.6) for 1 h at RT. Biotinylated secondary antibody (Reagent AB2, Dako REAL detection system) was added for 15 min at RT to bind to the primary antibody. The slices were incubated with streptavidin alkaline phosphatase (Reagent AP, Dako REAL detection system) for 15 min at RT in order to form conjugates between the streptavidin protein and biotin. Next, samples were incubated with chromogen solution (Chromogens Red 1 + 2 + 3 (1:25) in AP substrate buffer, Dako REAL detection system) for 1.5 min at RT in the dark. The alkaline phosphatase catalyzed the hydrolysis of phosphate groups from the substrate molecules resulting in stable, red colored stain at the site of the target antigen. For visualization of cell nuclei, the slices were finally stained with hematoxylin for 2 min. Washing steps were included in between each time (Table 35).

Table 35: IHC staining protocol for GFAP.

Reagent	Incubation
1x Target Retrieval solution, citrate pH 6.1	30 min 330 W, allow to cool down
Deionized water	short wash 3x, incubate overnight at 4 °C
Tris wash buffer (pH 6)	10 min wash
100 µl 3% peroxidase solution	10 min
Tris wash buffer (pH 6)	10 min wash
100 µl antibody diluent	20 min
100 µl primary antibody in antibody diluent	1 h RT
Tris wash buffer (pH 6)	10 min wash
100 µl biotinylated secondary antibody (Reagent AB2)	15 min RT
Tris wash buffer (pH 6)	10 min wash
100 µl streptavidin alkaline phosphatase (Reagent AP)	15 min RT
Tris wash buffer (pH 6)	10 min wash
100 µl chromogen solution (Chromogens Red 1 + 2 + 3 (1:25) in AP substrate buffer)	1.5 min RT
Tris wash buffer (pH 6)	10 min wash
Hematoxylin	20 s
Warm tap water	1 min wash
Deionized water	short wash

2.2.6.2.3. Quantification of immunohistochemical staining

After stained brain slices had been scanned, images of whole brain slices or different regions of interest (ROI) were taken with the CaseViewer software and further analyzed using the ImageJ software. For this purpose, different methods were established to quantify the expression of E-cadherin, assess the number of endothelial cells and evaluate the immune reaction of the metastatic microenvironment with spatial resolution. This enabled a quantifiable comparison of changes in E-cadherin levels (ECAD), angiotropic infiltration (CD31) or the microenvironment concerning microglia/macrophage response (IBA1), astrocytic reaction (GFAP) and T cell response (CD3) between entities and after genetic modification of the different models. Three representative samples were analyzed for each group.

2.2.6.2.3.1. Quantification of ECAD staining

E-cadherin staining was quantified in images of whole brain slices. Briefly, the channels of the RGB image were split using color deconvolution. The brown channel was selected, a previously established threshold (defined by pre-analysis) was applied and the percentage of stained area was measured in relation to whole brain area.

2.2.6.2.3.2. Quantification of CD31 staining

CD31 staining was quantified in images of whole brain slices. First, ROIs were defined manually for brain and metastatic tissue based on the clearly identifiable MMPI and the size of the respective areas was measured. Next, the channels of the RGB image were split using color deconvolution. The brown channel was selected and converted to a mask. Particles representing endothelial cells were separately counted in ROIs of both brain and metastatic tissue based on previously established settings (defined by pre-analysis). Microvessel density was calculated as counts per mm² in respective tissue (Figure 17).

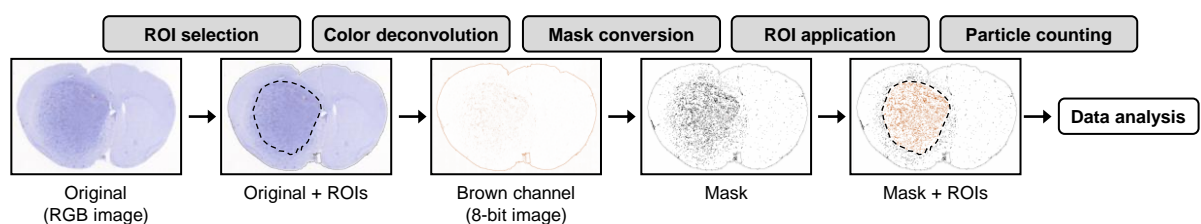


Figure 17: Workflow of CD31 IHC staining quantification.

2.2.6.2.3.3. Quantification of IBA1, GFAP and CD3 staining

IBA1, GFAP and CD3 stainings were quantified in triplicate images of selected ROIs. The following ROIs were evaluated: metastatic core, metastatic margin, MMPI, adjacent brain tissue and contralateral brain tissue (Figure 18).

IBA1/GFAP

Briefly, the channels of the RGB images were split using color deconvolution. The appropriate channels (brown for IBA1, red for GFAP) were selected and previously established thresholds (defined by pre-analysis) were applied. Finally, the percentage of stained area was measured.

CD3

The channels of the RGB image were split using color deconvolution and the brown channel was selected. Briefly, the contrast was enhanced and a suitable threshold was applied before the image was converted to a mask. After noise removal and watershed separation, particles representing T cells were counted based on previously established settings (defined by pre-analysis). T cell density was calculated as counts per mm² in respective brain region.

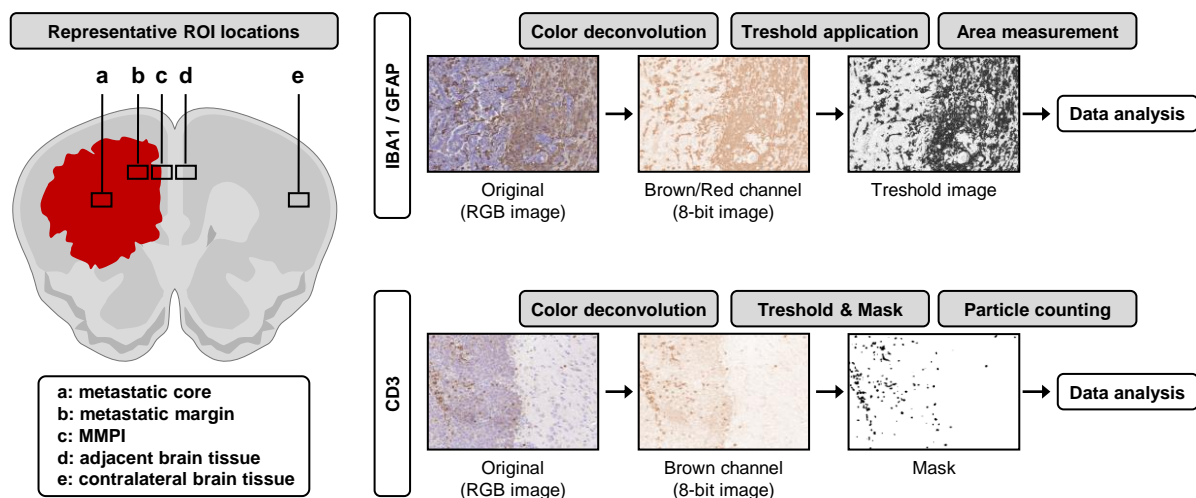


Figure 18: Workflow of IBA1/GFAP/CD3 IHC staining quantification.

2.2.7. Microscopy

2.2.7.1. Bright field microscopy

Cell morphology of parental and modified tumor cells was evaluated by bright field microscopy. 2.5×10^5 cells were seeded in 6-well plates and incubated for up to 72 h at 37 °C. After 24 h, 48 h and 72 h, images were taken after washing the cells with PBS to visualize cell morphology at different stages of confluence using the EVOS FL microscope at 4x and 10x magnification. This device was also used to take images for analysis of various functional *in vitro* assays investigating migration, colony formation and spheroid formation.

2.2.7.2. Confocal microscopy

Phalloidin and immunofluorescence stainings of parental and modified tumor cells were evaluated with a SP8 Leica confocal laser scanning microscope and the corresponding LAS X software. Two different lasers (405 nm for DAPI, 488 nm for FITC) were used to acquire images with a 63x oil immersion objective. To avoid cross-talk between channels a sequential acquisition mode was applied.

2.2.8. Statistical analysis

All experiments were performed at least in biological triplicates unless stated otherwise. Statistical analysis was performed with GraphPad Prism 7 software. Data sets were analyzed with unpaired *t*-test (one variable, two groups), one-way analysis of variance (ANOVA) (one variable, three or more groups), or two-way ANOVA with or without repeated measurements (two variables, two or more groups) depending on the experimental design. ANOVAs were followed by appropriate post-hoc tests including Dunnett's (comparing every mean to a control mean), Tukey's (comparing every mean with every other mean) or Sidak's (comparing selected pairs of means) multiple comparisons. For Kaplan-Meier survival analysis, a log-rank test was performed. For contingency tables, a chi-square test was used. Data are displayed as mean + standard deviation (SD) unless stated otherwise. *P* values less than 0.05 were considered as being statistically significant (**P* < 0.05; ***P* < 0.01; ****P* < 0.001; *****P* < 0.0001). Data were plotted with GraphPad Prism 7 software.

3. Results

The existence of different MMPI patterns and their prognostic impact strongly suggested the study of their underlying mechanisms and pathophysiology. It is necessary to understand these differences on a molecular level for the identification of potential effective treatments. Hence, appropriate mouse models were required for the detailed study of the different infiltrative MMPI patterns identified in human brain metastases as described in the introduction (see 1.1.4).

The first step of this thesis was to choose suitable brain metastasis mouse models and compare their morphological features. One of the key differences between diffuse and epithelial infiltrative MMPI models was their innate level of E-cadherin, a cell adhesion receptor that seems to play an essential role in the metastatic process. In addition, initial comparisons of the metastatic microenvironment already showed differences in immune infiltrate components between models.

A detailed characterization of the respective diffuse and epithelial infiltrative murine brain metastasis model cell lines confirmed the significant differences in their migration behavior and invasive capacity *in vitro*. Since low levels of E-cadherin were associated with higher migration and invasiveness across entities, the modification of this cell adhesion receptor in the metastatic outgrowth models appeared to be a suitable target to switch the pattern of the MMPIs.

The establishment of stable overexpression and knockdown cell lines was accomplished by opposing genetic modifications of the innate E-cadherin expression using a lentiviral approach. This enabled the comparative study of E-cadherin level effects on brain colonization. The first part focused on the direct impact on the cell lines by performing the same panel of *in vitro* assays as used for the wild-type characterization. Across entities, the gain of E-cadherin decreased migration and invasive capacity, while the artificial loss made them more invasive.

Because of these promising *in vitro* findings, the modified cell lines were injected into syngeneic mice and investigated in the *in vivo* situation. In the animal model, the overexpression of E-cadherin led to less aggressive metastases while the knockdown even increased aggressiveness and infiltrative metastatic outgrowth. Both approaches altered the MMPI and had a significant impact on overall survival and the metastatic microenvironment.

An additional aim of this thesis was to find prognostic gene targets that could represent a tool to classify the outcome of patients with metastases based on the analysis of their tumor gene expression signature. Indeed, we could establish a gene signature that clearly differed between diffuse and epithelial infiltrative cell lines of mesenchymal or epithelial character. It reliably distinguished between metastases according to the associated survival rates in our mouse models and even demonstrated its prognostic impact in human patient samples.

3.1. Brain metastasis mouse models

For the following study of the role of E-cadherin in metastatic brain colonization, the first step was to choose suitable brain metastasis mouse models that represent the different infiltrative MMPI patterns observed in human brain metastases. As already described in the introduction, our group has established a late brain colonization model, where tumor cells are stereotactically implanted into the cortex of syngeneic mice, for a variety of murine cancer cell lines. As the mice have a functional immune system, the simultaneous investigation of MMPI patterns and MME mechanisms in an intact system is possible.

3.1.1. MMPI patterns in brain metastasis mouse models

I decided to study the mechanisms in different entities commonly involved in brain metastases in order to find mechanisms that are robust between entities and could be generally valid. Therefore, I chose breast and colon entities as both cancer types are among the ones accounting for the highest risk of brain metastases formation. I was able to match both infiltrative MMPI patterns to two of our brain metastasis mouse models, one of breast and the other one of colon origin. Different histological markers were used for the detection of metastatic growth and MMPI pattern in the brain parenchyma: the mesenchymal marker vimentin for diffuse infiltrative models and the epithelial marker cytokeratin-8 for epithelial infiltrative ones.

The diffuse infiltrative MMPI pattern was best recognizable in the E0771-LG model, a highly tumorigenic breast cancer cell line, and the CT26 model, a highly metastatic colon cancer cell line (Figure 19 A). Vimentin shows cell-specific expression in intermediate filaments of cells with mesenchymal origin and is used to visualize growth patterns of carcinomas without noticeable expression of epithelial markers. The vimentin staining revealed diffuse infiltration with a visible macroscopic metastasis characterized by tumor cells with mesenchymal-like features deeply infiltrating the adjacent tissue (Blazquez et al., 2020b).

The epithelial infiltrative MMPI pattern was best recognizable in the 410.4 model, a moderate metastatic breast cancer cell line, and the CMT93Var model, a low to moderate metastatic colon cancer cell line (Figure 19 B). Cytokeratin-8 shows cell-specific expression in intermediate filaments of epithelial cells and is widely used in pathology for the diagnosis of adenocarcinoma. The cytokeratin-8 staining revealed epithelial infiltration characterized by clusters of tumor cells physically separated from the metastatic border that collectively infiltrated into the adjacent brain parenchyma as cohorts or, in case of CMT93Var, as clusters with an inner lumen in a glandular appearance (Blazquez et al., 2020b).

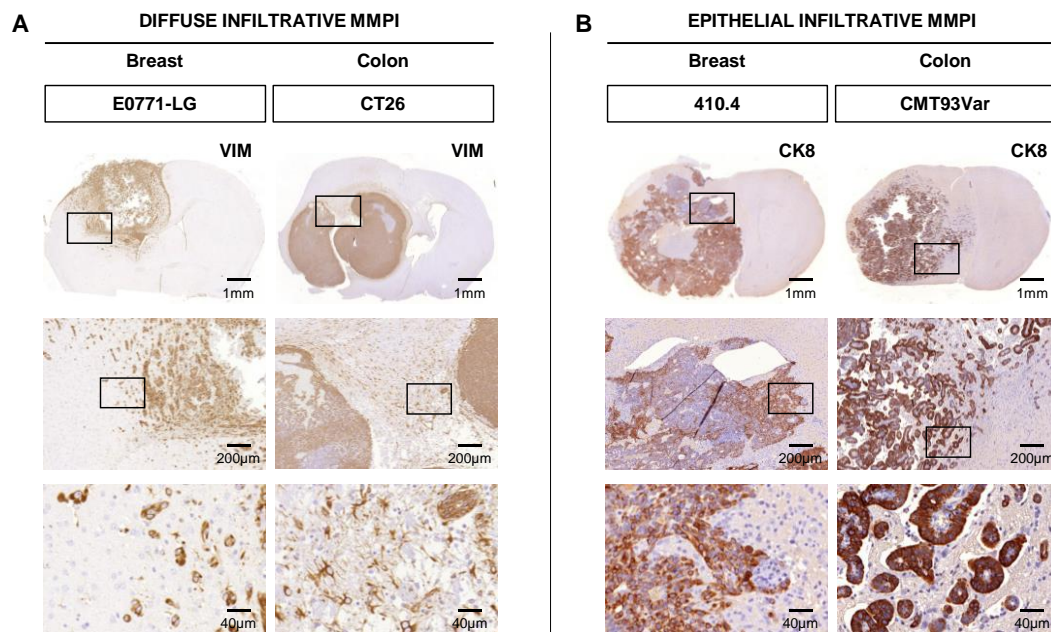


Figure 19: MMPI patterns in brain metastasis mouse models. IHC staining of vimentin (VIM) and cytokeratin-8 (CK8) in tissue sections of brain metastases of **(A)** diffuse infiltrative E0771-LG (breast) and CT26 (colon) and **(B)** epithelial infiltrative 410.4 (breast) and CMT93Var (colon) cancer cells. Representative images of coronal brain sections and images of the MMPI at higher magnifications are shown.

3.1.2. E-cadherin expression in brain metastasis mouse models

Analogous to the human models, I compared the E-cadherin expression in the brain tissue samples between diffuse and epithelial infiltrative brain metastasis mouse models with immunohistochemistry analyses. The diffuse infiltrative MMPI models E0771-LG (breast) and CT26 (colon) showed no visible E-cadherin staining (Figure 20 A) while the epithelial infiltrative MMPI models 410.4 (breast) and CMT93Var (colon) showed pronounced E-cadherin staining within the metastatic tissue (Figure 20 B). In case of the epithelial infiltrative models, the E-cadherin staining revealed again the characteristic epithelial patterns with cluster and glandular infiltration. The quantification of ECAD staining emphasized the significant difference between MMPI patterns (Figure 20 C).

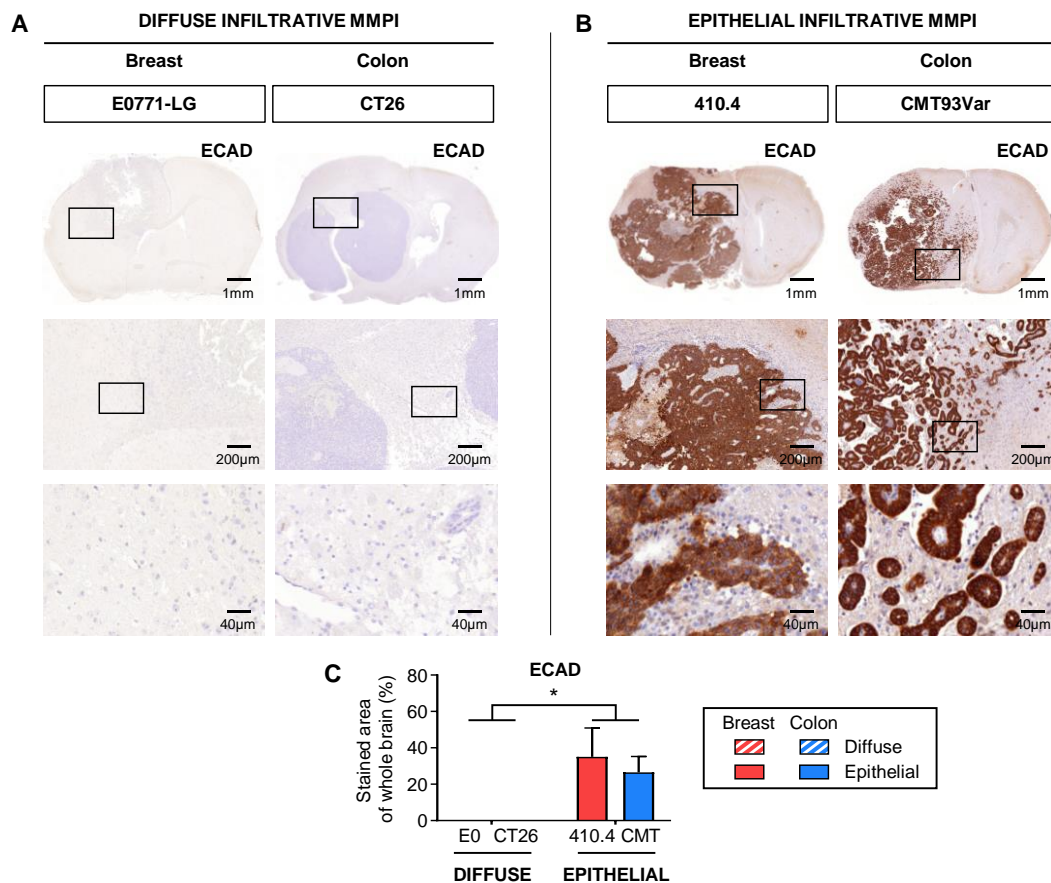


Figure 20: E-cadherin expression in brain metastasis mouse models. IHC staining of E-cadherin (ECAD) in tissue sections of brain metastases of **(A)** diffuse infiltrative E0771-LG (breast) and CT26 (colon) and **(B)** epithelial infiltrative 410.4 (breast) and CMT93Var (colon) cancer cells. Representative images of coronal brain sections and images of the MMPI at higher magnifications are shown. **(C)** Quantification of E-cadherin staining is indicated as the percentage of stained area in whole brain slices (mean + SD, $n = 3$; two-way ANOVA followed by Tukey's multiple comparisons; $*P < 0.05$).

3.1.3. Metastatic microenvironment in brain metastasis mouse models

Since different infiltrative MMPI patterns could influence the immune cell composition within the macro-metastasis and the formation of the MME, I compared the expression of major CNS immune response components at the MMPI between diffuse and epithelial infiltrative models. Initial histological stainings of the metastatic brain tissue with an activated microglia/macrophage marker (IBA1), GFAP as a marker for astrocytic activation and a pan-T cell marker (CD3) already revealed noticeable MMPI pattern-specific differences. While both breast cancer models showed a clear activation of astrocytes, I saw enormous morphological differences in other immune cell composition. The epithelial type, represented by 410.4, displayed high levels of activated microglia/macrophages and T cells, while both cell types were almost absent at the diffuse MMPI of E0771-LG (Figure 21).

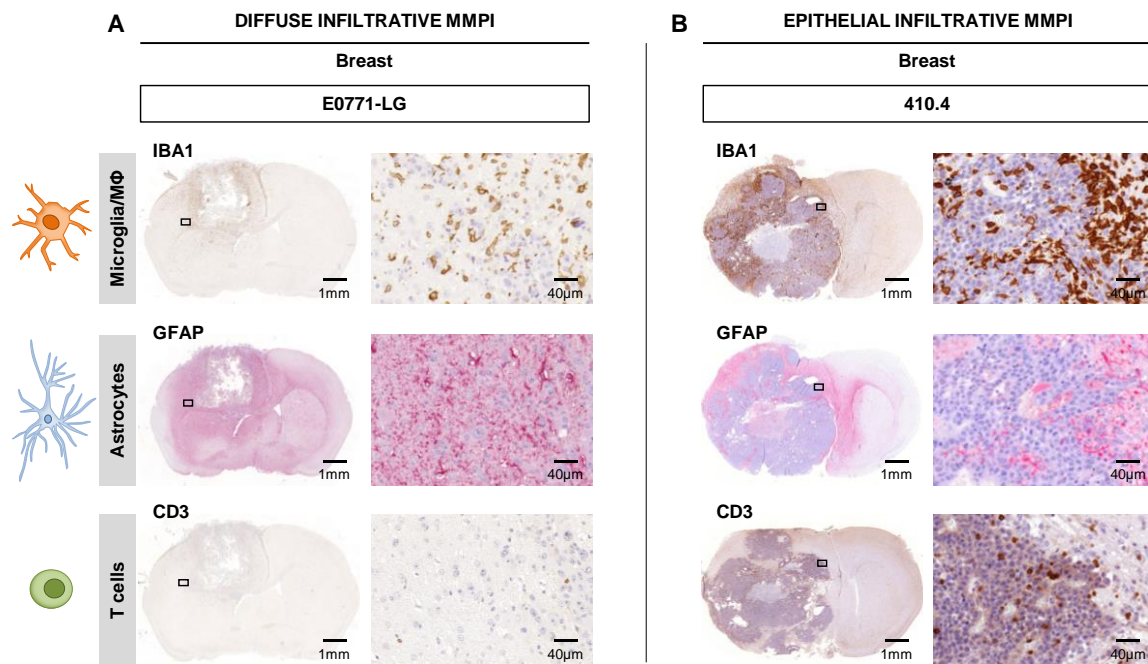


Figure 21: Metastatic microenvironment in brain metastasis mouse models. IHC staining of immune response components in tissue sections of brain metastases of **(A)** diffuse infiltrative E0771-LG and **(B)** epithelial infiltrative 410.4 breast cancer cells. Brain metastases were stained with antibodies against activated microglia/macrophages (MΦ) (IBA1), activated astrocytes (GFAP) and T cells (CD3). Representative images of coronal brain sections and images of the MMPI at higher magnifications are shown.

These profound morphological differences in the MME emphasized the importance of a systematic investigation and quantification of microenvironment components in all available animal models via immunohistological and morphometric analyses.

3.2. Characterization of murine brain metastasis model cell lines

I went on with the detailed *in vitro* characterization of the murine brain metastasis model cell lines that generated the diffuse and epithelial infiltrative MMPI patterns. The diffuse infiltrative cell lines E0771-LG (breast) and CT26 (colon) were compared to the epithelial infiltrative cell lines 410.4 (breast) and CMT93Var (colon) first concerning basic features such as morphology, protein expression and proliferation rates. I continued with various 2D and 3D functional assays assessing migration behavior and invasive capacity as well as spheroid and colony formation ability. This was followed by the study of contact inhibition mechanisms. Finally, I performed gene screenings and developed characteristic expression signatures for the respective MMPI model cell lines.

3.2.1. Basic characterization of murine brain metastasis model cell lines

The E0771-LG cell line is a highly metastatic subclone isolated from experimental lung metastases originating from the parental E0771 cell line, which was originally isolated from a spontaneous mammary gland tumor of a C57BL/6 mouse (Kitamura et al., 2019). It was obtained from Prof. J. Pollard (Edinburgh, UK) and has a very high metastatic potential. The CT26 cell line is an undifferentiated colon carcinoma line originally isolated from an N-nitroso-N-methylurethane induced colon tumor of a BALB/c mouse (Brattain et al., 1980). It is commercially available at ATCC and has a high metastatic property and tumor initiating potential. Both cell lines are adherent and display a mesenchymal phenotype with fibroblast-like morphology (Figure 22 A1).

The 410.4 cell line was generated through serial transplantations of 410 LM derived from a single lung nodule isolated after subcutaneous injection of a single spontaneously arising mammary tumor of a BALB/cfC3H mouse (Miller et al., 1983). It was obtained from Prof. F. Balkwill (London, UK) and has a moderate metastatic potential. The CMT93Var cell line is a more metastatic subclone of the commercially available parental polyploid colorectal CMT93 originally isolated from a rectal tumor of a C57BL/6 mouse (Franks et al., 1978). The variant has been shown to be more aggressive when injected intracortically compared to the parental line and was obtained from Dr. med. C. Hackl (Regensburg). CMT93Var cells have a low to moderate metastatic potential. Both cell lines are adherent and display an epithelial phenotype with cobblestone-like morphology and pronounced cell-cell contacts when they reach confluence (Figure 22 A2).

I reinforced the differences in E-cadherin expression between the diffuse and epithelial infiltrative cell lines morphologically by immunofluorescence and on protein and RNA level by Western blot and quantitative RT-PCR analysis, respectively. The morphological features and the localization of E-cadherin on a cellular level are depicted in detail in confocal images of Phalloidin and E-cadherin stainings (Figure 22 B). In epithelial cell lines, E-cadherin was mainly localized in the cell membranes,

especially at regions of cell-cell contacts. Both epithelial cell lines expressed higher protein and RNA levels of the epithelial markers E-cadherin, cytokeratin-8 and β -catenin while the diffuse cell line E0771-LG displayed extremely high levels of the mesenchymal marker vimentin (Figure 22 C+D). Despite those distinct molecular characteristics, I could not observe any MMPI pattern-specific differences concerning cell proliferation or survival rates (Figure 22 E–G).

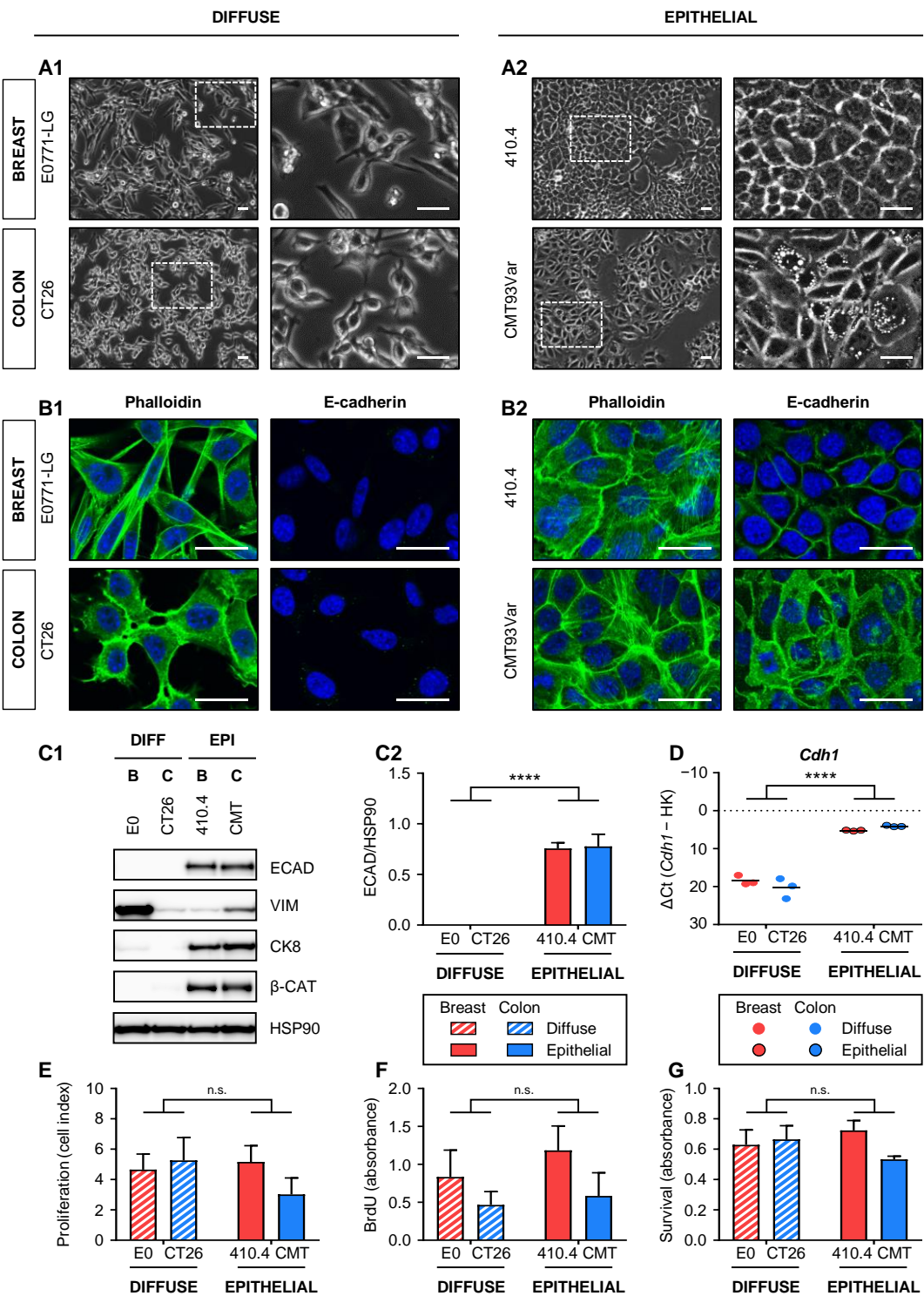


Figure 22: Basic characterization of murine brain metastasis model cell lines *in vitro*. Diffuse infiltrative E0771-LG (E0) (breast) and CT26 (colon) cells and epithelial infiltrative 410.4 (breast)

and CMT93Var (CMT) (colon) cells are characterized concerning morphology, protein expression, proliferation and viability *in vitro*. **(A)** Phase contrast images of **(A1)** diffuse and **(A2)** epithelial murine breast and colon cancer cells. Enlarged sections of the characteristic cell morphology are also shown. **(B)** Confocal microscopy images of **(B1)** diffuse and **(B2)** epithelial murine breast and colon cancer cells after Phalloidin or E-cadherin staining of cells (green) and nuclear staining with DAPI (blue). All scale bars represent 30 μm . **(C)** Western blot analysis of epithelial (E-cadherin (ECAD), cytokeratin-8 (CK8) and β -catenin (β -CAT)) and mesenchymal markers (vimentin (VIM)). **(C1)** Representative bands for all indicated proteins and one representative loading control are shown (B: breast, C: colon, DIFF: diffuse, EPI: epithelial). **(C2)** Quantification of E-cadherin protein expression is displayed as band intensities normalized to corresponding loading controls (HSP90). **(D)** Quantitative RT-PCR analysis of E-cadherin (*Cdh1*). *Gapdh* and *Pgk1* were used as housekeeping genes (HK; shown are mean and individual values). **(E)** Cell proliferation rate, **(F)** BrdU cell proliferation analysis and **(G)** MTT assay showing cell survival after 48 h (mean + SD, $n = 3$; two-way ANOVA followed by Tukey's multiple comparisons; **** $P < 0.0001$, n.s. = not significant).

3.2.2. Functional characterization of murine brain metastasis model cell lines

Our group uses a broad spectrum of functional 2D and 3D assays to assess migration behavior and invasive capacity as well as spheroid and colony formation ability *in vitro* that have been established and refined over the years (see 2.2.2.4). In these assays, I could observe pronounced MMPI pattern-specific differences concerning migration, invasion and spheroid outgrowth.

The ECM-based migration assay using turned coverslips analyzes the ability of tumor cells to migrate into the surrounding area. The diffuse infiltrative cell lines migrated faster and displayed significantly more spreaders, which are single tumor cells detached from the migration front that deeply invade into the surrounding area (Figure 23 A). Furthermore, the diffuse cell lines had a slightly higher invasive capacity compared to the epithelial cell lines when I analyzed the ability of tumor cells to invade through a membrane by micro-invasion assays in a modified Boyden chamber (Figure 23 B).

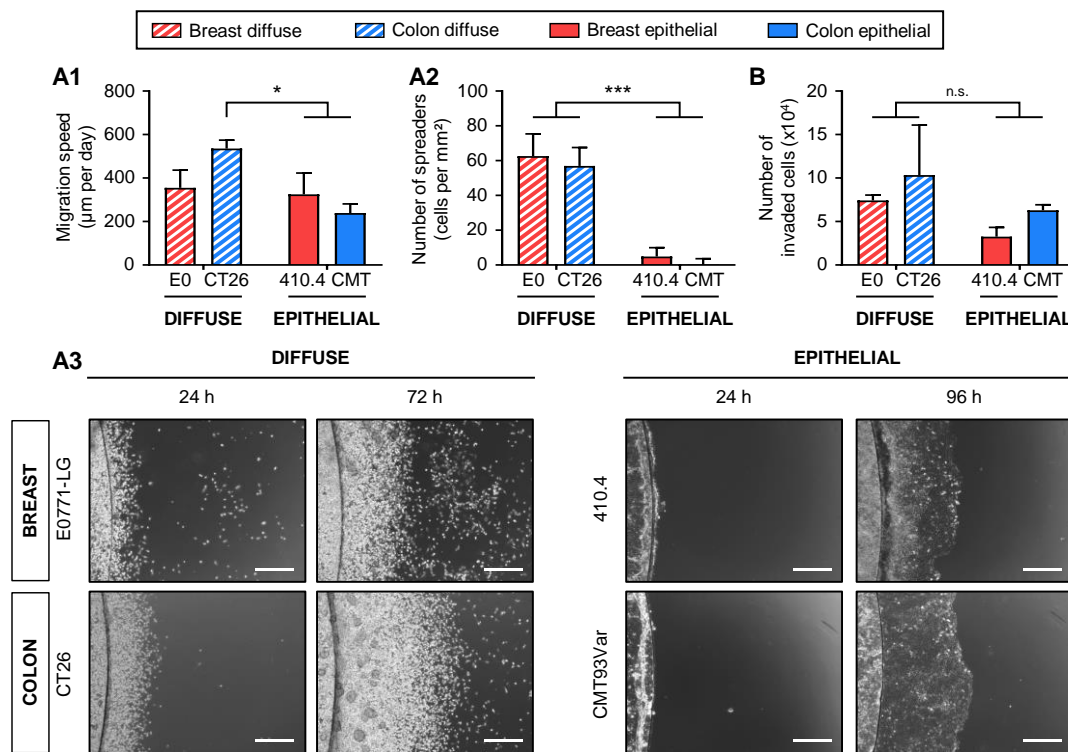


Figure 23: Functional 2D characterization of murine brain metastasis model cell lines *in vitro*. Diffuse infiltrative E0771-LG (E0) (breast) and CT26 (colon) cells and epithelial infiltrative 410.4 (breast) and CMT93Var (CMT) (colon) cells are characterized concerning migration behavior and invasive capacity *in vitro*. **(A)** ECM-based migration assay. **(A1)** Migration speed is indicated as µm per day, **(A2)** number of spreaders is displayed as cells per mm² and **(A3)** representative images are shown. Scale bars represent 500 µm. **(B)** Modified Boyden chamber invasion assay. The invasive capacity is indicated as number of invaded cells through a membrane (mean + SD, $n = 3$; two-way ANOVA followed by Tukey's multiple comparisons; * $P < 0.05$, *** $P < 0.001$, n.s. = not significant).

Besides those 2D methods, I also used 3D cell culture models that mimic the formation of micro-metastases and metastatic outgrowth in the brain. I investigated the ability of the different infiltrative cell lines to form spheroids in anchorage-independent conditions in hanging drops and analyzed their subsequent outgrowth in wells. Both diffuse cell lines formed spheroids with larger outgrowth compared to the epithelial 410.4 and the CMT93Var was not able to form quantifiable spheroids at all (Figure 24 A). The situation was similar when I analyzed their ability to grow in anchorage-independent conditions in soft agar (Figure 24 B). Compared to the diffuse CT26 less colonies grew in case of both epithelial cell lines.

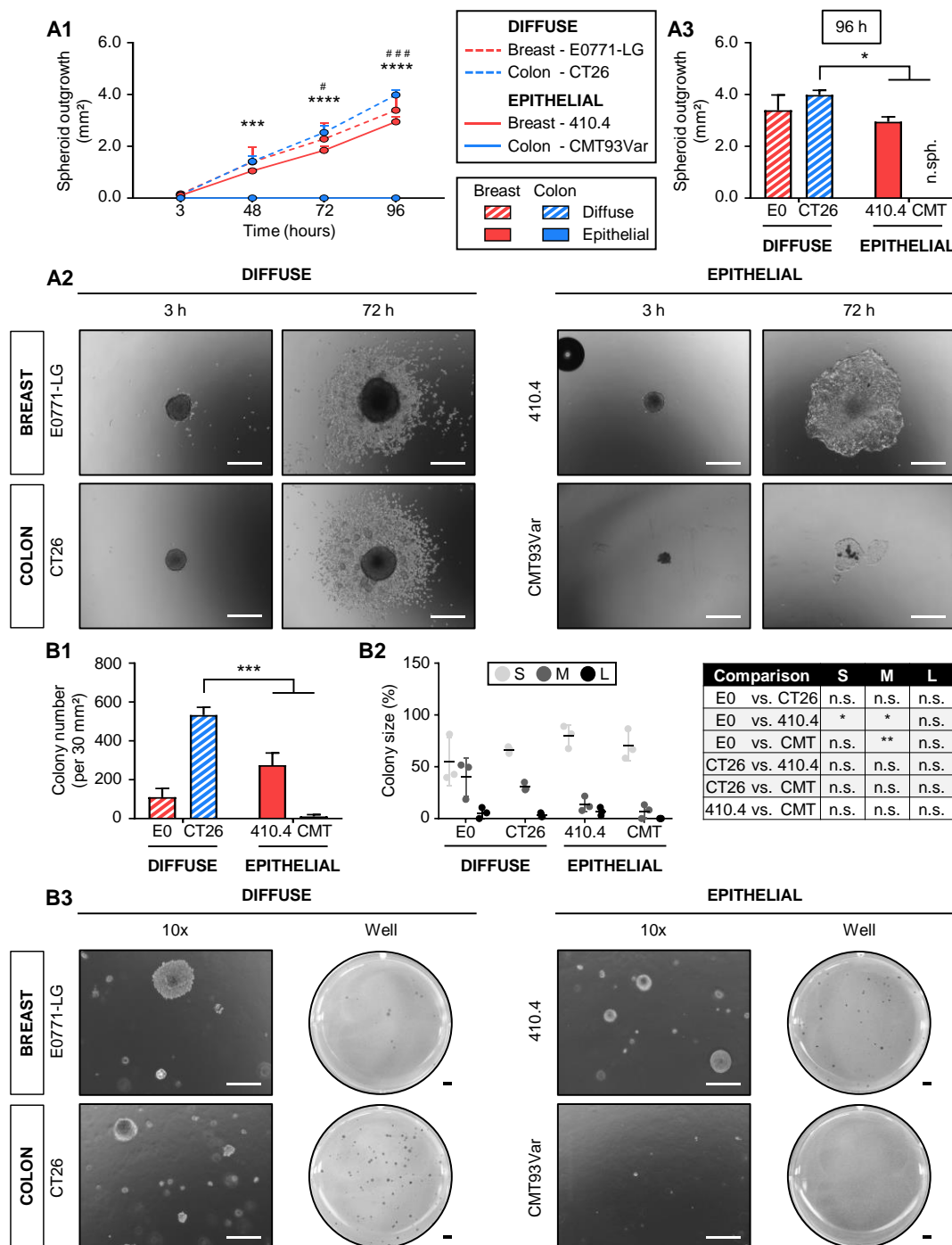


Figure 24: Functional 3D characterization of murine brain metastasis model cell lines *in vitro*. Diffuse infiltrative E0771-LG (E0) (breast) and CT26 (colon) cells and epithelial infiltrative 410.4 (breast) and CMT93Var (CMT) (colon) cells are characterized concerning spheroid outgrowth and colony formation ability *in vitro*. **(A)** Spheroid formation assay using hanging drop method. **(A1)** Spheroid outgrowth is indicated in mm² and **(A2)** representative images are shown. Scale bars represent 500 μ m (mean + SD, $n = 3$; two-way ANOVA with repeated measures followed by Tukey's multiple comparisons; *** $P < 0.001$, **** $P < 0.0001$ (E0771-LG/CT26/410.4 vs. CMT93Var); # $P < 0.05$, ### $P < 0.001$ (CT26 vs. 410.4)). **(A3)** Spheroid outgrowth after 96 h is displayed separately in mm² (mean + SD, $n = 3$; two-way ANOVA followed by Tukey's multiple comparisons; * $P < 0.05$; n.s. = no outgrowth of quantifiable spheroids). **(B)** Colony formation assay in soft agar. **(B1)** Number of colonies per 30 mm², **(B2)** percentage of colony size separated into three groups (S: small, M: medium, L: large) and **(B3)** representative images are shown. Scale bars represent 200 μ m (mean + SD, $n = 3$;

two-way ANOVA followed by Tukey's multiple comparisons; * $P < 0.05$, ** $P < 0.01$, *** $P < 0.001$, n.s. = not significant).

3.2.3. Contact inhibition mechanisms in murine brain metastasis model cell lines

As already explained in the introduction, the mechanisms of contact inhibition and the cell-adhesion receptor E-cadherin are inseparably linked (see 1.2.2). Due to the pronounced differences in innate E-cadherin levels between the diffuse and epithelial infiltrative murine brain metastasis model cell lines, the next logical step was to examine these mechanisms and draw a comparison between them.

I therefore investigated the mechanisms of contact inhibition in the diffuse and epithelial infiltrative cell lines by quantification of the protein ratio of the Hippo signaling pathway component YAP and its phosphorylated form phospho-YAP (p-YAP) in a confluence assay. In case of intact contact inhibition, the p-YAP/YAP ratio rises with increasing confluence. Although all cell lines grew to confluence in a similar way after cultivation for up to 96 h (Figure 25 A), I saw huge differences in the p-YAP/YAP ratio. The epithelial infiltrative cell lines (410.4 and CMT93Var) showed functional contact inhibition with a rising ratio whereas both diffuse infiltrative cell lines (E0771-LG and CT26) showed a tonic YAP signaling and seemed to be independent of contact inhibition (Figure 25 B). I could therefore confirm contact inhibition as one mechanism that clearly differed between the diffuse and epithelial infiltrative MMPI models. This could be an important target for specific tumor therapies in patients.

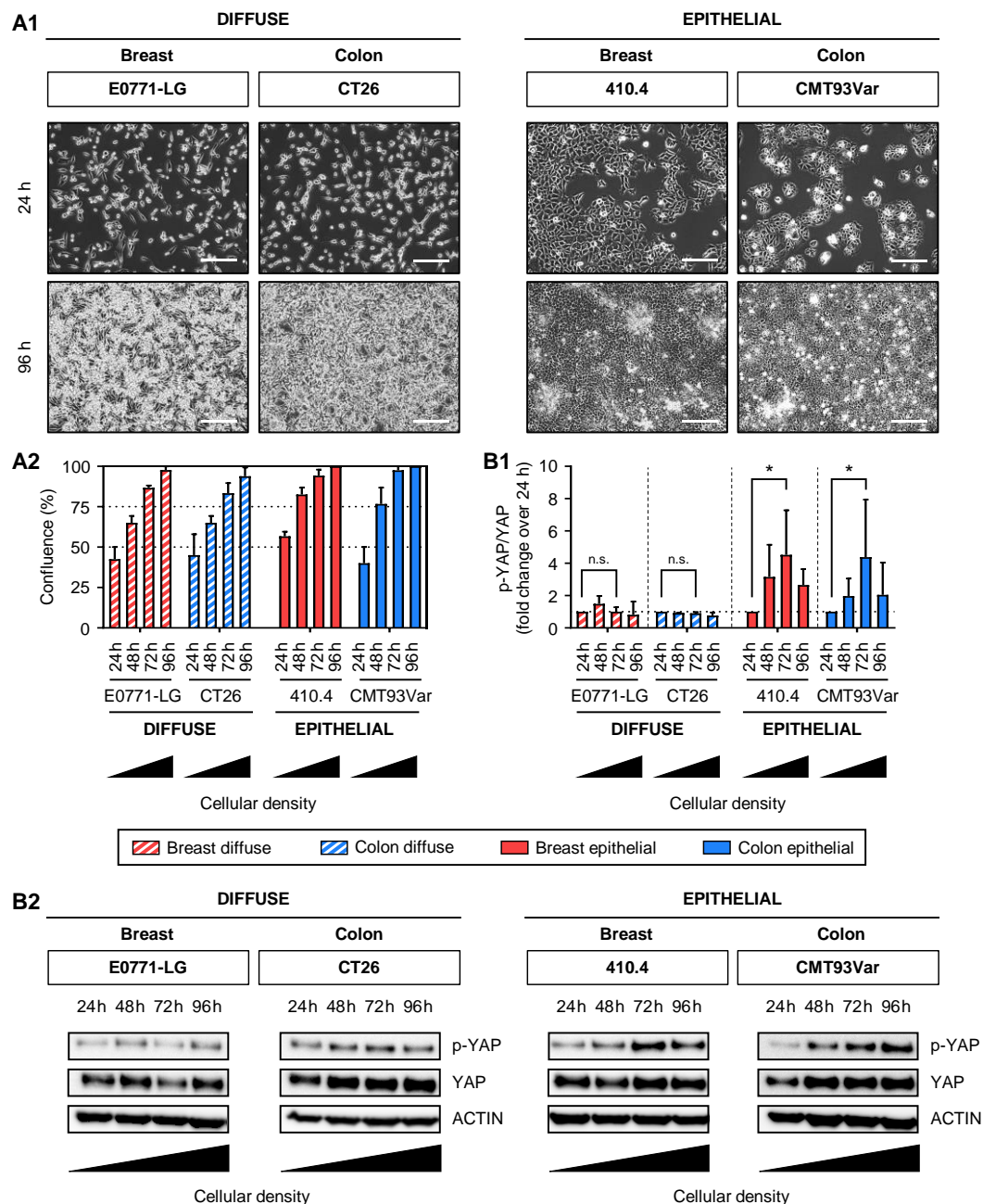


Figure 25: Contact inhibition mechanisms in murine brain metastasis model cell lines *in vitro*. Diffuse infiltrative E0771-LG (breast) and CT26 (colon) cells and epithelial infiltrative 410.4 (breast) and CMT93Var (colon) cells are characterized concerning contact inhibition mechanisms *in vitro*. **(A)** Confluence assay. **(A1)** Representative images at low and high confluence are shown and **(A2)** level of cellular confluence during cultivation is displayed in percent. Scale bars represent 200 μ m. **(B)** Western blot analysis of phospho-YAP (p-YAP) and YAP over time as measurement for functional contact inhibition. **(B1)** Protein band intensities of p-YAP and YAP were normalized to corresponding loading controls (ACTIN) and the ratio was calculated. Quantification of p-YAP/YAP expression is displayed as fold change over 24 h. **(B2)** Representative bands for all indicated proteins and one representative loading control are shown (mean + SD, $n = 3$; two-way ANOVA followed by Dunnett's multiple comparisons; $*P < 0.05$, n.s. = not significant).

3.2.4. Gene expression signature of murine brain metastasis model cell lines

To further characterize the differences between diffuse and epithelial infiltrative murine brain metastasis model cell lines, I performed quantitative RT-PCR screenings of selected gene targets based on previous proteomics analyses and microarray data in our lab and found several differentially expressed genes (DEGs) (Figure 26). By clustering the gene expression data, I could identify two clusters with distinct patterns: genes in cluster 1 were highly expressed in diffuse infiltrative cell lines while cluster 2 consisted of genes showing high expression in epithelial infiltrative cell lines.

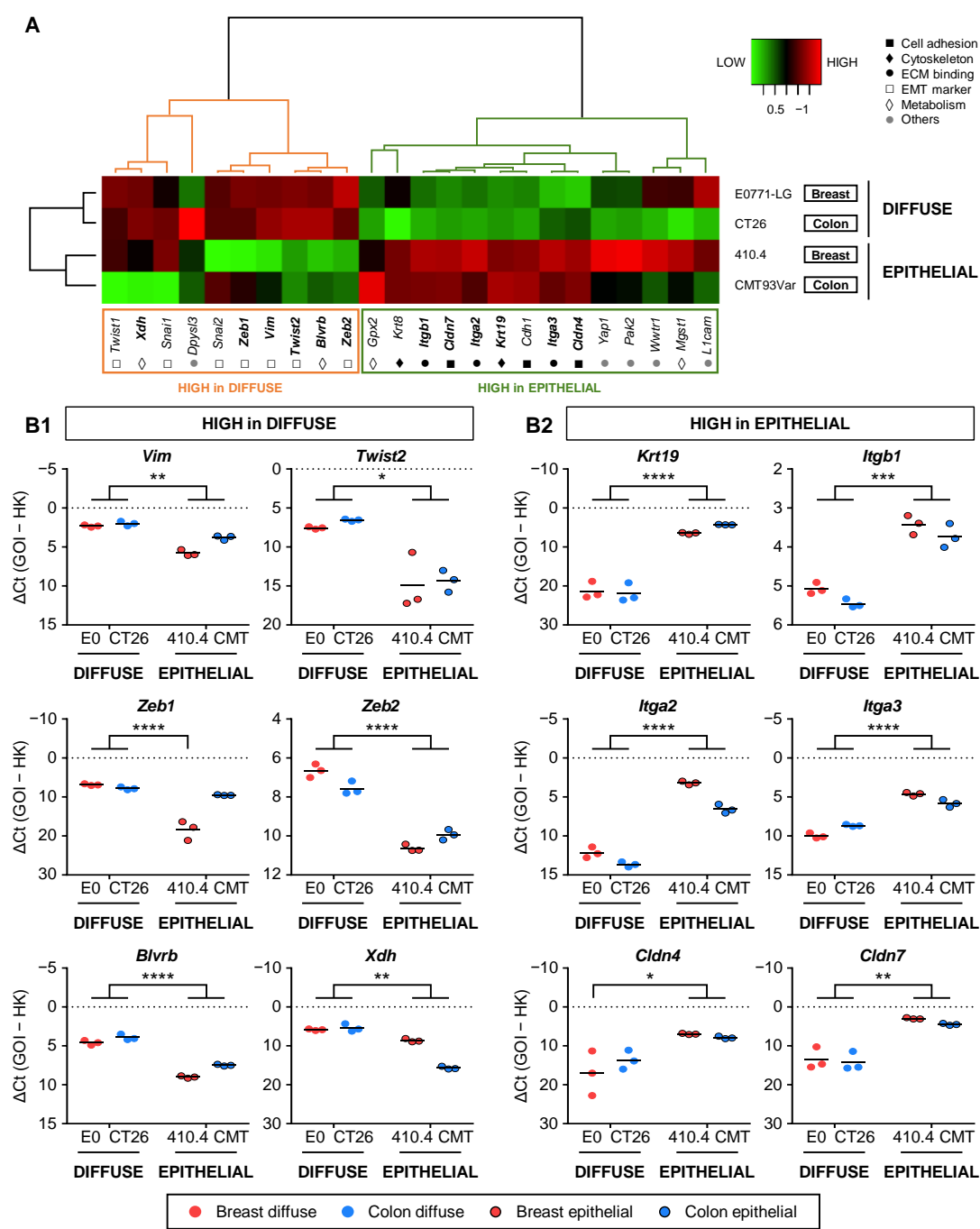


Figure 26: Gene expression signature of murine brain metastasis model cell lines. Quantitative RT-PCR analysis of the indicated genes (GOI) in diffuse infiltrative E0771-LG (breast) and CT26 (colon)

cells and epithelial infiltrative 410.4 (breast) and CMT93Var (colon) cells. *Gapdh* and *Pgk1* were used as housekeeping genes (HK). **(A)** Heatmap displaying \log_2 transformed z-scores of 24 genes. Unsupervised hierarchical clustering reveals two gene clusters with distinct expression profiles, as highlighted by dendrogram coloring (orange, green). **(B)** Representative candidate genes of **(B1)** cluster 1 ('HIGH in DIFFUSE') and **(B2)** cluster 2 ('HIGH in EPITHELIAL') (mean and individual values, $n = 3$; two-way ANOVA followed by Tukey's multiple comparisons; * $P < 0.05$, ** $P < 0.01$, *** $P < 0.001$, **** $P < 0.0001$).

In summary, the data demonstrated the existence of significant differences between the diffuse and epithelial infiltrative MMPI cell types. On the one hand, the diffuse infiltrative E0771-LG and CT26 lost the expression of E-cadherin, had no functional contact inhibition and showed increased migration and invasion capacity compared to the epithelial type. They seem to be independent of E-cadherin expression for successful organ colonization.

In contrast, the epithelial infiltrative 410.4 and CMT93Var cells retained the expression of this adhesion molecule at the MMPI infiltration front, showed intact contact inhibition and had a lower migration and invasion capacity compared to the diffuse type. They seem to depend on E-cadherin expression and epithelial barrier formation for initial outgrowth and 3D colony formation *in vitro*.

The different dependencies of the diffuse and epithelial infiltrative cell lines on E-cadherin point to different molecular mechanisms supporting both types of breast and colon cancer infiltration at the MMPI. Due to these findings, former observations in our group (Blazquez et al., 2020a) and other publications emphasizing its importance for metastasis and cancer progression (Mendonsa et al., 2018; Padmanaban et al., 2019), I decided to focus on the role of the cell adhesion receptor E-cadherin in the further course of this thesis.

3.3. E-cadherin modifications in murine brain metastasis model cell lines

The specific genetic modification of E-cadherin in the metastatic outgrowth models appeared to be a suitable target to switch the pattern of the MMPIs. Therefore, I established stable cell lines with altered levels of E-cadherin and continued with a detailed characterization concerning their morphology, molecular characteristics, migratory and invasive behavior as well as 3D outgrowth ability *in vitro*. Additionally, I assessed the impact of modified E-cadherin levels on contact inhibition mechanisms.

3.3.1. Establishment of E-cadherin modifications in murine brain metastasis model cell lines

Taken together, the data pointed to a different role of E-cadherin at the MMPI of diffuse and epithelial infiltrative MMPI models. Thus, to further investigate the impact of E-cadherin on infiltration and colonization of brain metastases, I specifically modified the expression of E-cadherin according to the MMPI phenotypes in an opposing way (Table 36).

Entity	Breast			
Parental cell line	E0771-LG		410.4	
MMPI pattern	Diffuse		Epithelial	
E-cadherin expression	Low		High	
Genetic modification	Empty vector	E-cadherin vector	Scrambled shRNA	E-cadherin shRNA
Modified cell line	E0771-LG CTL	E0771-LG OE	410.4 CTL	410.4 sh

Entity	Colon			
Parental cell line	CT26		CMT93Var	
MMPI pattern	Diffuse		Epithelial	
E-cadherin expression	Low		High	
Genetic modification	Empty vector	E-cadherin vector	Scrambled shRNA	E-cadherin shRNA
Modified cell line	CT26 CTL	CT26 OE	CMT93Var CTL	CMT93Var sh

E-cadherin overexpression	E-cadherin knockdown
---------------------------	----------------------

Table 36: E-cadherin modifications in murine brain metastasis model cell lines. The diffuse infiltrative E0771-LG (breast) and CT26 (colon) cell lines were stably transfected with empty (CTL) or E-cadherin expression (OE) vectors. The epithelial infiltrative 410.4 (breast) and CMT93Var (colon) cells were stably transfected with scrambled shRNA (CTL) or E-cadherin shRNA (sh) vectors.

For the generation of cell lines with stable overexpression or knockdown of the cell adhesion protein E-cadherin, I introduced expression vectors or shRNA-mediated gene silencing by lentivirus-mediated gene delivery (transduction). After transduction, lentiviral vectors can integrate into the nucleus of the target cells and lead to stable expression of the gene of interest. This method enables the extensive study of modified cell lines in cell culture without the need for repeated reintroduction of constructs into the cells for maintenance of manipulation effect and furthermore enables the study of long-term effects in *in vivo* models without additional administration of potentially interfering substances.

I started with the construction of different E-cadherin expression vectors, scrambled shRNA vectors and E-cadherin shRNA vectors, which involved numerous molecular cloning processes (data not shown). A detailed description of cloning procedures is listed in the methods section (see 2.2.1). Next, I produced lentiviral particles containing the respective constructs and generated the different modified cell lines by lentiviral transductions. I used empty (CTL) or E-cadherin expression (OE) vectors in the diffuse infiltrative E0771-LG (breast) and CT26 (colon) cell lines for upregulation of E-cadherin on the one hand, and scrambled shRNA (CTL) or E-cadherin shRNA (sh) vectors in the epithelial infiltrative 410.4 (breast) and CMT93Var (colon) cell lines for downregulation of E-cadherin on the other hand. For each parental cell line, I chose one control and two different modified cell lines with the most pronounced changes in E-cadherin levels for the further studies (data not shown). A detailed description of lentiviral transduction procedures is listed in the methods section (see 2.2.2.2).

3.3.1.1. E-cadherin overexpression in diffuse infiltrative cell lines

First, I confirmed the successful stable lentiviral transduction of E0771-LG and CT26 breast and colon cancer cells resulting in control (CTL) and E-cadherin-overexpression (OE) lines on protein and RNA level by Western blot and quantitative RT-PCR analysis (Figure 27 A–C, I–K). Contrary to the current concept of EMT, these modifications did not substantially affect other cell characteristic markers on protein level. There was neither an increase of the epithelial marker cytokeratin-8 nor a decrease of the mesenchymal marker vimentin. Instead, both proteins showed stable levels across all groups. However, the level of β -catenin, a binding partner of E-cadherin, was increased particularly in CT26 (Figure 27 A1+I1).

As expected, the modification of E-cadherin had a significant impact on cell morphology. E-cadherin overexpression in E0771-LG and CT26 cells changed their mesenchymal phenotype with fibroblast-like morphology (control lines) towards a more epithelial-like phenotype with some cobblestone-like features (E0771-LG OE) or star-like morphology (CT26 OE) with increased cell-cell contacts (Figure 27 D+L).

The overexpression of E-cadherin was also visible on the cellular level. Morphological features and the localization of E-cadherin within the cells are depicted in detail in confocal images of Phalloidin and E-cadherin stainings. Compared to the control situation without any stained areas, a weak E-cadherin staining was visible in all OE lines, especially in CT26 (Figure 27 E+M). However, E-cadherin was mainly localized in the cytoplasm of cells, which was different from the situation observed in epithelial wild-type cell lines where E-cadherin was mainly localized at the cell membranes and especially in regions of cell-cell contacts (see 3.2.1).

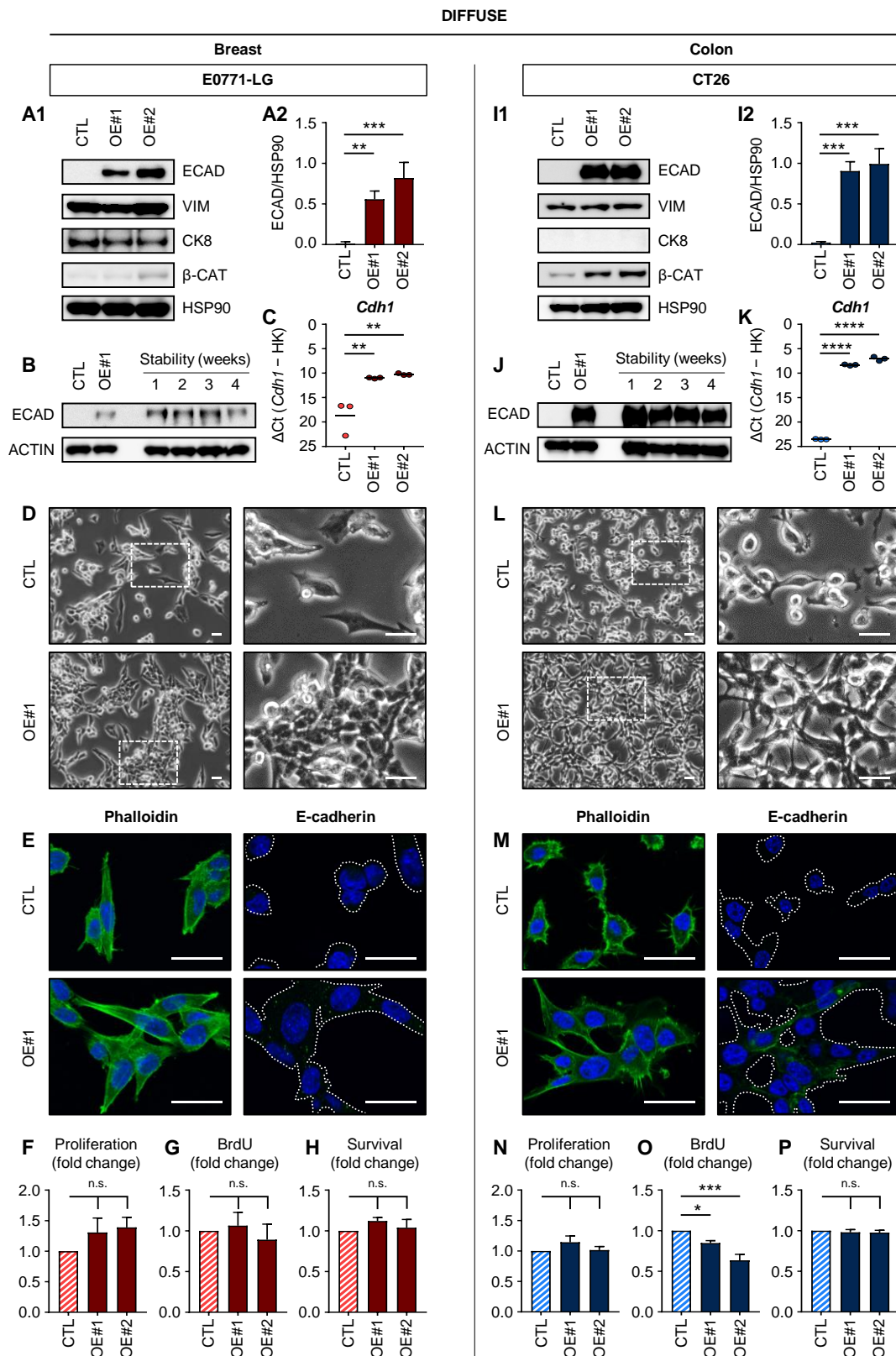


Figure 27: E-cadherin overexpression in diffuse infiltrative murine brain metastasis model cell lines. Characterization of **(A–H)** E0771-LG and **(I–P)** CT26 control (CTL) and E-cadherin-overexpression (OE) breast and colon cancer cells after stable lentiviral transduction of E0771-LG and CT26 with the empty vector or E-cadherin vector, respectively. **(A+I)** Western blot analysis of epithelial (E-cadherin (ECAD), cytokeratin-8 (CK8) and β -catenin (β -CAT)) and mesenchymal markers (vimentin (VIM)). **(A1+I1)** Representative bands for all indicated proteins and one representative loading control are

shown. **(A2+I2)** Quantification of E-cadherin protein expression is displayed as band intensities normalized to corresponding loading controls (HSP90). **(B+J)** Stability of E-cadherin overexpression verified by Western blot analysis after cultivation without selection antibiotics for up to four weeks. Representative blots are shown. **(C+K)** Quantitative RT-PCR analysis of E-cadherin (*Cdh1*). *Gapdh* and *Pgk1* were used as housekeeping genes (HK; shown are mean and individual values). **(D+L)** Phase contrast images. Enlarged sections of the changed cell morphology are also shown. **(E+M)** Confocal microscopy images after Phalloidin or E-cadherin staining of cells (green) and nuclear staining with DAPI (blue). Scale bars represent 30 μm . **(F+N)** Cell proliferation rate, **(G+O)** BrdU cell proliferation analysis and **(H+P)** MTT assay showing cell survival after 48 h are displayed as fold change over control cell line (mean + SD, $n = 3$; one-way ANOVA followed by Dunnett's multiple comparisons; $*P < 0.05$, $**P < 0.01$, $***P < 0.001$, $****P < 0.0001$, n.s. = not significant).

Overall, the overexpression of E-cadherin had no major effects on cell proliferation and survival rates in E0771-LG or CT26 (Figure 27 F–H, N–P). This was particularly important for the following functional characterization of the cells, as it precluded proliferation-induced effects of E-cadherin modification on migration and invasion.

3.3.1.2. E-cadherin knockdown in epithelial infiltrative cell lines

In the same manner, I confirmed the successful stable lentiviral transduction of 410.4 and CMT93Var breast and colon cancer cells resulting in control (CTL) and E-cadherin-knockdown (sh) lines on protein and RNA level by Western blot and quantitative RT-PCR analysis (Figure 28 A–C, I–K). Again, these modifications did not substantially affect other cell characteristic markers on protein level. There was neither a decrease of the epithelial marker cytokeratin-8 nor an increase of the mesenchymal marker vimentin. However, the level of the E-cadherin binding partner β -catenin was decreased particularly in 410.4 (Figure 28 A1+I1).

As expected, also the downregulation of E-cadherin had a significant impact on cell morphology. E-cadherin knockdown in 410.4 and CMT93Var cells turned their epithelial phenotype with cobblestone-like morphology (control lines) towards a more mesenchymal-like phenotype with fibroblast-like features and less cell-cell contacts (Figure 28 D+L).

The knockdown of E-cadherin was also visible on the cellular level. Morphological features and the localization of E-cadherin within the cells are depicted in detail in confocal images of Phalloidin and E-cadherin stainings. Compared to the control situation with strong E-cadherin expression mainly localized at the cell membranes, especially in regions of cell-cell contacts, only a weak E-cadherin staining was visible in both sh lines (Figure 28 E+M). Interestingly, the diminished E-cadherin signal was mainly localized in the cytoplasm of cells instead of the cell membrane. This reflected the situation in the E-cadherin overexpression cell lines (see 3.3.1.1).

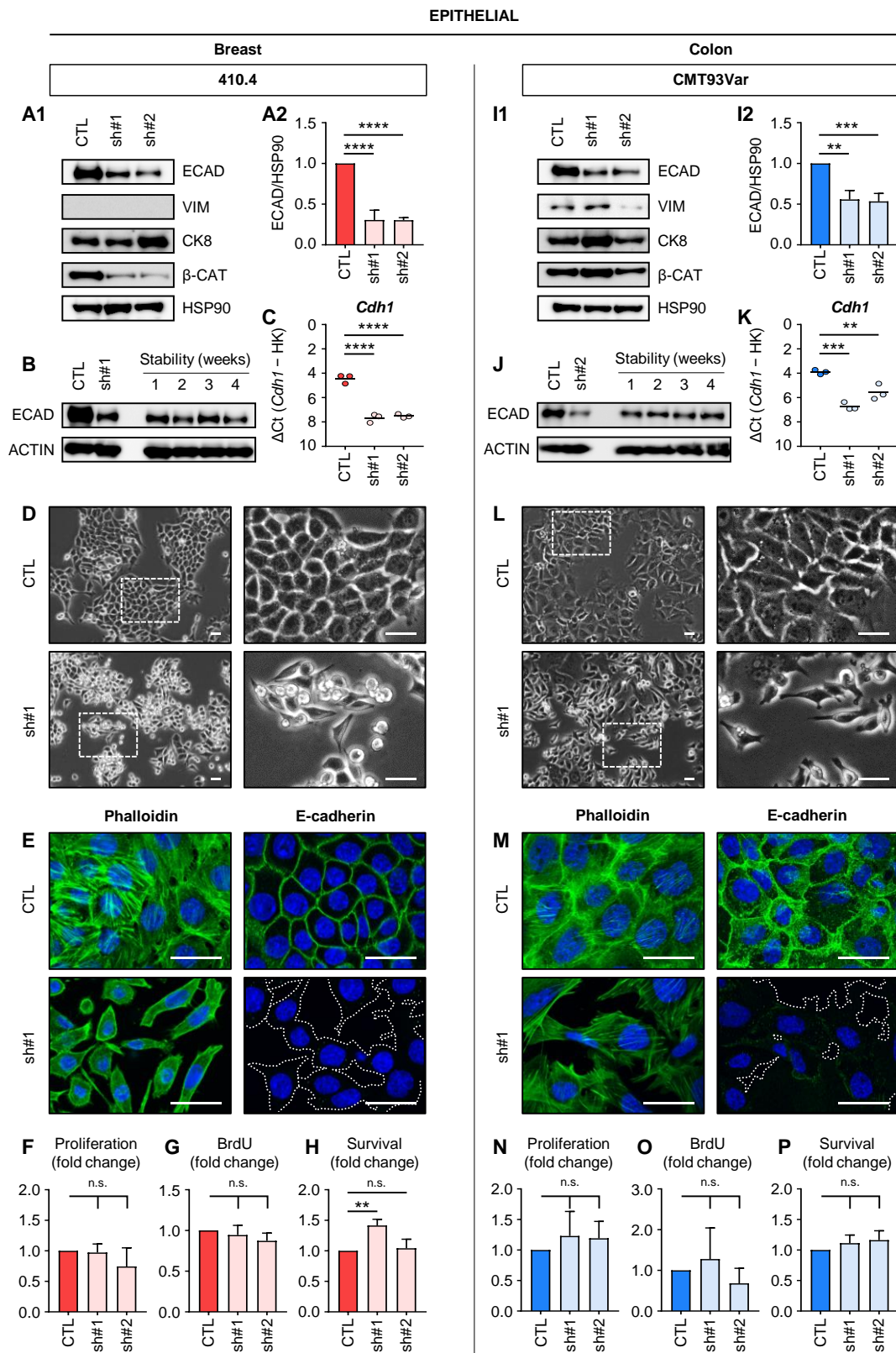


Figure 28: E-cadherin knockdown in epithelial infiltrative murine brain metastasis model cell lines. Characterization of **(A–H)** 410.4 and **(I–P)** CMT93Var control (CTL) and E-cadherin-knockdown (sh) breast and colon cancer cells after stable lentiviral transduction of 410.4 and CMT93Var with the scrambled shRNA or E-cadherin shRNA, respectively. **(A+I)** Western blot analysis of epithelial (E-cadherin (ECAD), cytokeratin-8 (CK8) and β-catenin (β-CAT)) and mesenchymal markers (vimentin (VIM)). **(A1+I1)** Representative bands for all indicated proteins and one representative loading control

are shown. **(A2+I2)** For quantification of E-cadherin protein expression, band intensities were normalized to corresponding loading controls (HSP90) and are displayed as fold change over control cell line. **(B+J)** Stability of E-cadherin overexpression verified by Western blot analysis after cultivation without selection antibiotics for up to four weeks. Representative blots are shown. **(C+K)** Quantitative RT-PCR analysis of E-cadherin (*Cdh1*). *Gapdh* and *Pgk1* were used as housekeeping genes (HK; shown are mean and individual values). **(D+L)** Phase contrast images. Enlarged sections of the changed cell morphology are also shown. **(E+M)** Confocal microscopy images after Phalloidin or E-cadherin staining of cells (green) and nuclear staining with DAPI (blue). Scale bars represent 30 μm . **(F+N)** Cell proliferation rate, **(G+O)** BrdU cell proliferation analysis and **(H+P)** MTT assay showing cell survival after 48 h are displayed as fold change over control cell line (mean + SD, $n = 3$; one-way ANOVA followed by Dunnett's multiple comparisons; $**P < 0.01$, $***P < 0.001$, $****P < 0.0001$, n.s. = not significant).

Consistent with the findings from the E-cadherin overexpression, also the knockdown of E-cadherin overall had no major effects on cell proliferation and survival rates in 410.4 or CMT93Var (Figure 28 F–H, N–P).

3.3.2. Characterization of E-cadherin modifications in murine brain metastasis model cell lines

Having confirmed that the E-cadherin modifications had no major effects on cell proliferation and survival rates in neither of the groups, I could preclude any proliferation-induced effects in the following experiments. I continued with the detailed molecular and functional characterization of all modified murine brain metastasis model cell lines investigating the gene expression of DEGs via qRT-PCRs (see 3.2.4) and using the same functional assays assessing migration behavior and invasive capacity as well as spheroid and colony formation ability as previously for the parental wild-type cell lines (see 3.2.2).

3.3.2.1. No effect of E-cadherin modifications on gene expression signature

By quantitative RT-PCR analysis of previously identified DEGs in all modified cell lines, I confirmed that the E-cadherin modifications did not alter the gene expression signature of the diffuse and epithelial infiltrative cell lines to any substantial extent (Figure 29). Although the altered level of E-cadherin was clearly visible in the heatmap, it was not reflected in the rest of the signature. Unsupervised hierarchical clustering still revealed the same two gene clusters with sole high expression in diffuse cells with mesenchymal character or epithelial cells with epithelial character as described earlier (see 3.2.4) independent of E-cadherin modifications. That means that E-cadherin alone was not able to switch the signature that included cell adhesion markers, ECM binding integrins, EMT markers, cytoskeletal components and metabolic genes.

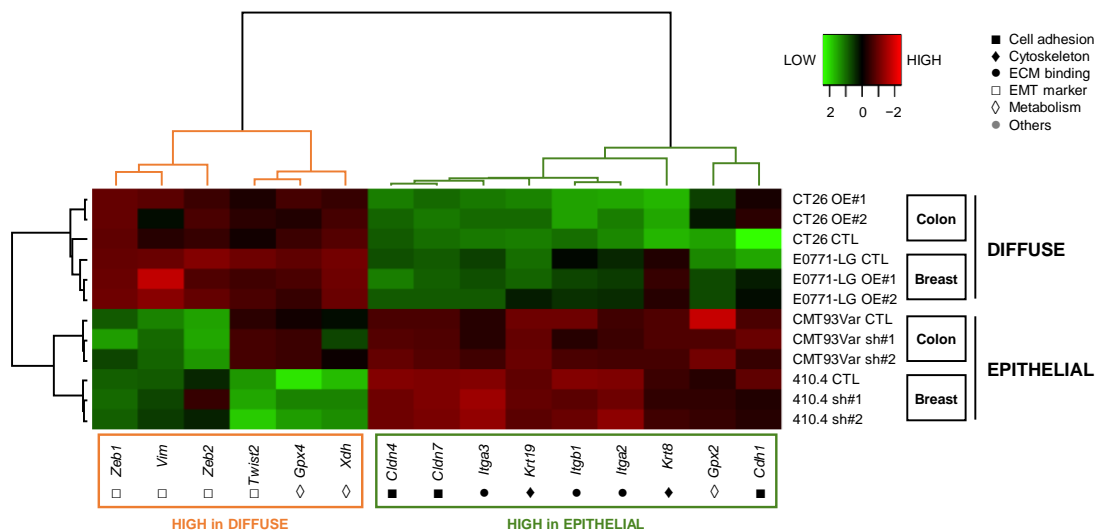


Figure 29: No effect of E-cadherin modifications on gene expression signature. Quantitative RT-PCR analysis of previously established differentially expressed genes in murine brain metastasis model cell lines after E-cadherin modifications (CTL: control, OE: E-cadherin-overexpression, sh: E-cadherin-knockdown). *Gapdh* and *Pgk1* were used as housekeeping genes. Heatmap displaying \log_2 transformed z-scores. Unsupervised hierarchical clustering reveals the same two gene clusters with distinct expression profiles independent of E-cadherin modification (cluster 1 ('HIGH in DIFFUSE') and cluster 2 ('HIGH in EPITHELIAL')), as highlighted by dendrogram coloring (orange, green).

3.3.2.2. Reduced migration and invasive capacity after E-cadherin overexpression

E-cadherin overexpression led to a significant decrease in the migration speed in E0771-LG breast cancer cells and a significantly reduced number of spreaders in CT26 colon cancer cells in the ECM-based migration assay using turned coverslips (Figure 30 A+D). Additionally, invasive capacity of cells with upregulated E-cadherin levels was significantly decreased in micro-invasion assays in a modified Boyden chamber compared to control cells (Figure 30 B+E).

Furthermore, E-cadherin overexpression also had an impact on spheroid outgrowth. Initially all groups were able to form spheroids under anchorage-independent conditions in hanging drops, but I observed a significant reduction of the outgrowth area after overexpression of E-cadherin in both models in concordance with the previous results (Figure 30 C+F).

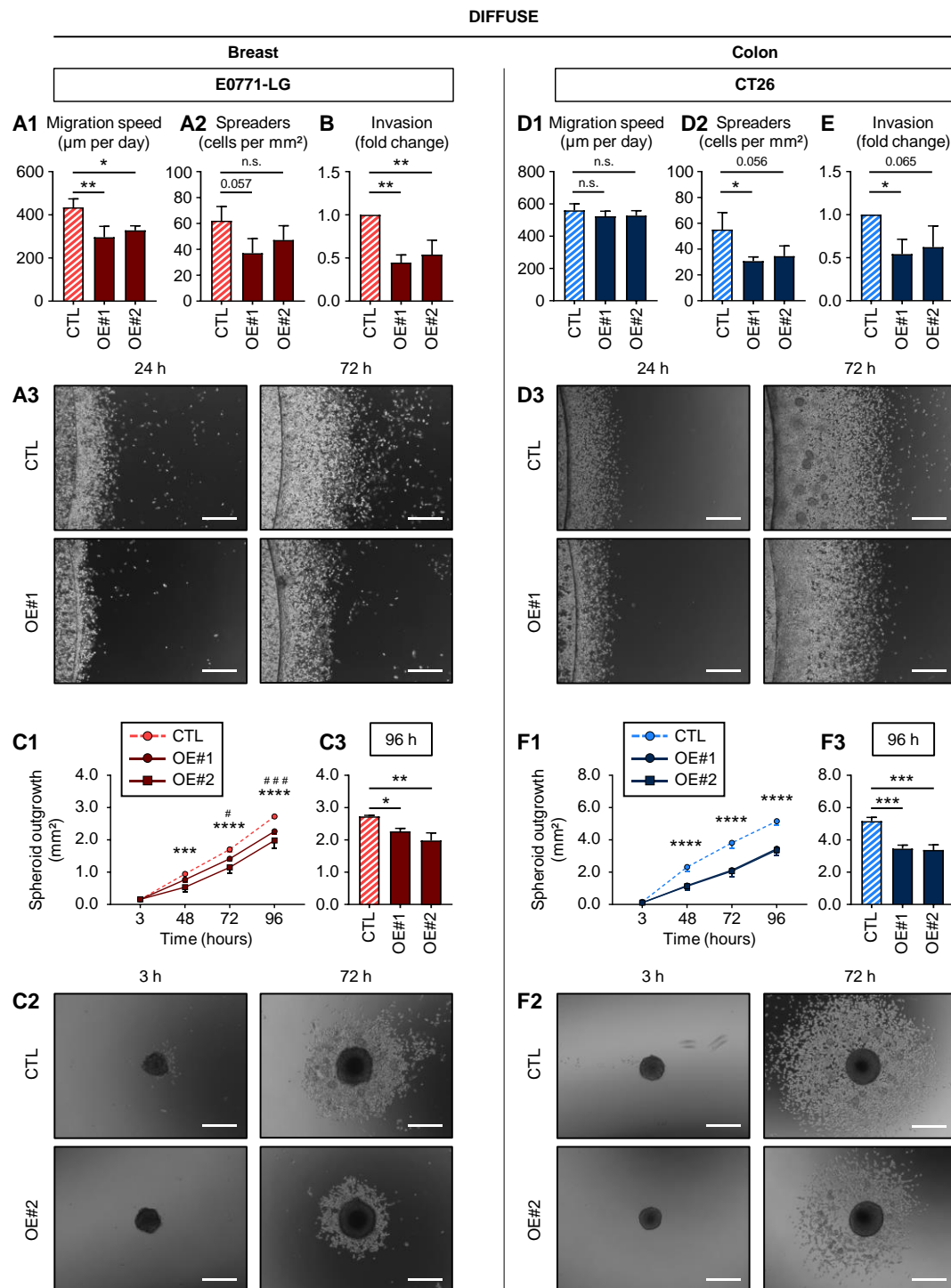


Figure 30: Effects of E-cadherin overexpression on migration, invasion and spheroid outgrowth *in vitro*. Functional characterization of **(A–C)** E0771-LG and **(D–F)** CT26 control (CTL) and E-cadherin-overexpression (OE) breast and colon cancer cells *in vitro*. **(A+D)** ECM-based migration assay. **(A1+D1)** Migration speed is indicated as μm per day, **(A2+D2)** number of spreaders is displayed as cells per mm^2 and **(A3+D3)** representative images are shown. Scale bars represent 500 μm . **(B+E)** Modified Boyden chamber invasion assay. The invasiveness of OE cells is indicated as fold change over control cells (mean + SD, $n = 3$; one-way ANOVA followed by Dunnett's multiple comparisons; * $P < 0.05$, ** $P < 0.01$, n.s. = not significant). **(C+F)** Spheroid formation assay using hanging drop method. **(C1+F1)** Spheroid outgrowth is indicated in mm^2 over time and **(C2+F2)** representative images are shown. Scale bars represent 500 μm (mean + SD, $n = 3$; two-way ANOVA with repeated measures followed by Dunnett's

multiple comparisons; E0771-LG: *** $P < 0.001$, **** $P < 0.0001$ (CTL vs. OE#1); # $P < 0.05$, ### $P < 0.001$ (CTL vs. OE#2); CT26: **** $P < 0.0001$ (CTL vs. OE#1/OE#2)). **(C3+F3)** Spheroid outgrowth after 96 h is displayed separately in mm² (mean + SD, $n = 3$; one-way ANOVA followed by Dunnett's multiple comparisons; * $P < 0.05$, ** $P < 0.01$, *** $P < 0.001$).

3.3.2.3. Increased migration and invasive capacity after E-cadherin knockdown

In contrast, E-cadherin knockdown in 410.4 breast and CMT93Var colon cancer cells significantly increased the migration speed and the number of spreaders in the ECM-based migration assay using turned coverslips (Figure 31 A+D) as well as the invasive capacity in micro-invasion assays in a modified Boyden chamber compared to control cells (Figure 31 B+E).

However, and contrary to expectation, the downregulation of E-cadherin did not lead to an increase of the spheroid outgrowth area and even had an impact on spheroid formation ability. In contrast to the control line, the 410.4 breast cancer knockdown cells were not even able to form spheroids under anchorage-independent conditions in hanging drops any more and remained as single cells growing to confluency over time (Figure 31 C). This observation represents an interesting finding and indicates that the epithelial infiltrative 410.4 cells highly depend on E-cadherin for their initial outgrowth and spheroid formation. The situation was similar in all CMT93Var colon cancer lines where neither the control nor the knockdown cells were able to form quantifiable spheroids (Figure 31 F). Although it was not a surprise in this case, as already the wild-type cell line had shown no spheroid formation ability compared to the other diffuse and epithelial infiltrative cell lines. The impact of E-cadherin on colonization thus seems to be context-dependent.

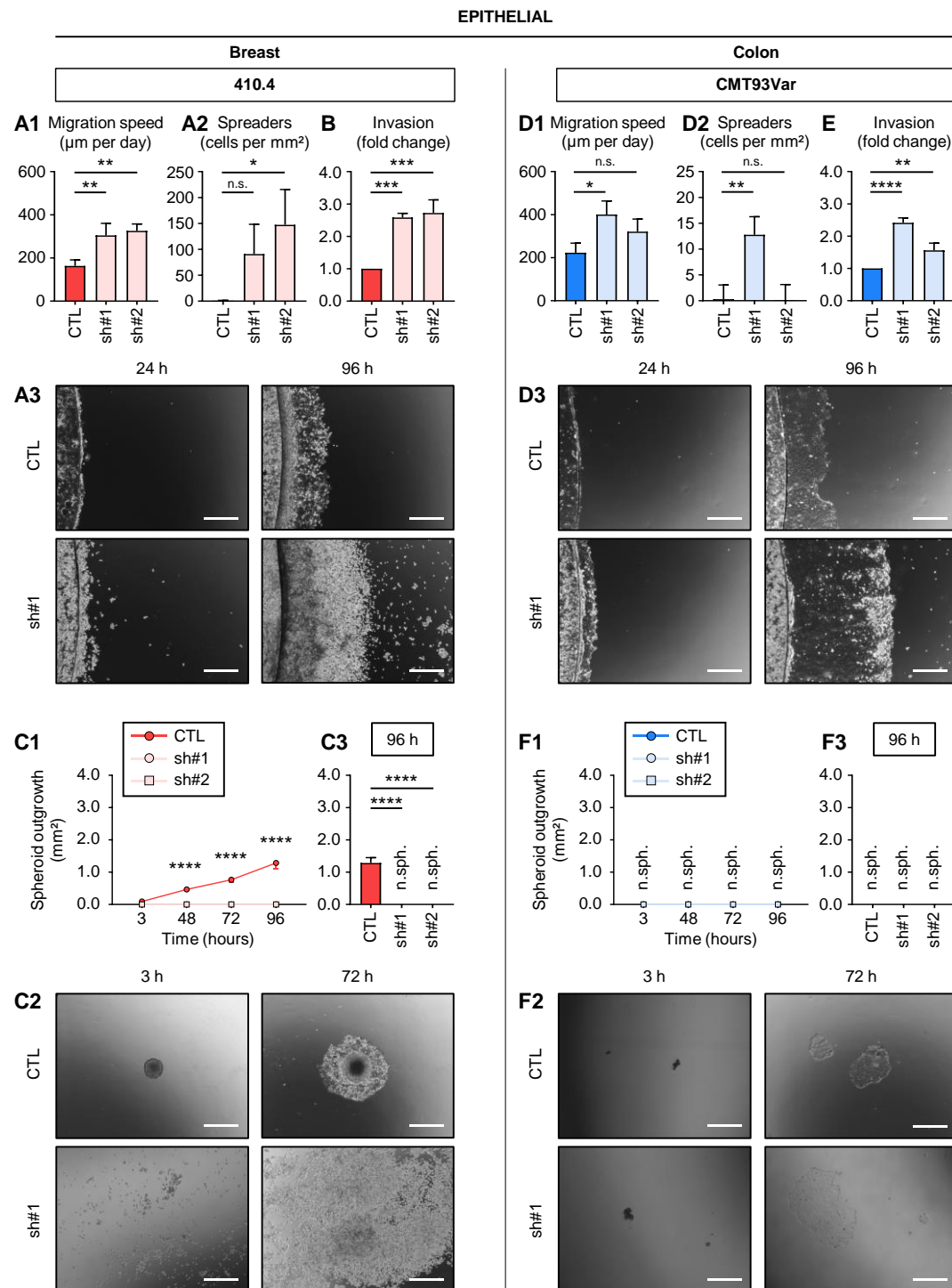


Figure 31: Effects of E-cadherin knockdown on migration, invasion and spheroid outgrowth *in vitro*. Functional characterization of (A–C) 410.4 and (D–F) CMT93Var control (CTL) and E-cadherin-knockdown (sh) breast and colon cancer cells *in vitro*. (A+D) ECM-based migration assay. (A1+D1) Migration speed is indicated as μm per day, (A2+D2) number of spreaders is displayed as cells per mm² and (A3+D3) representative images are shown. Scale bars represent 500 μm. (B+E) Modified Boyden chamber invasion assay. The invasiveness of sh cells is indicated as fold change over control cells (mean + SD, $n = 3$; one-way ANOVA followed by Dunnett's multiple comparisons; * $P < 0.05$, ** $P < 0.01$, *** $P < 0.001$, **** $P < 0.0001$, n.s. = not significant). (C+F) Spheroid formation assay using hanging drop method. (C1+F1) Spheroid outgrowth is indicated in mm² over time and (C2+F2) representative images are shown. Scale bars represent 500 μm (mean + SD, $n = 3$; two-way ANOVA with repeated

measures followed by Dunnett's multiple comparisons; 410.4: **** $P < 0.0001$ (CTL vs. sh#1/sh#2); n.sph. = no outgrowth of quantifiable spheroids). **(C3+F3)** Spheroid outgrowth after 96 h is displayed separately in mm² (mean + SD, $n = 3$; one-way ANOVA followed by Dunnett's multiple comparisons; **** $P < 0.0001$; n.sph. = no outgrowth of quantifiable spheroids).

3.3.2.4. Colony formation ability after E-cadherin modifications

Nevertheless, all cell lines were still able to grow in anchorage-independent conditions in soft agar independent of the E-cadherin modifications. Although I observed a slight decrease in colony number in one overexpression line in both diffuse E0771-LG (data not shown) and CT26 (Figure 32 A) and a noticeable increase in both knockdown lines of the epithelial 410.4 (Figure 32 B) in concordance with previous findings, none of these changes were significant. Again, differences between control and knockdown groups for CMT93Var were almost not quantifiable due to the low number of colonies (data not shown), as expected after the initial characterization of wild-type cell lines where CMT93Var also displayed the lowest colony rates compared to the other diffuse and epithelial infiltrative cell lines.

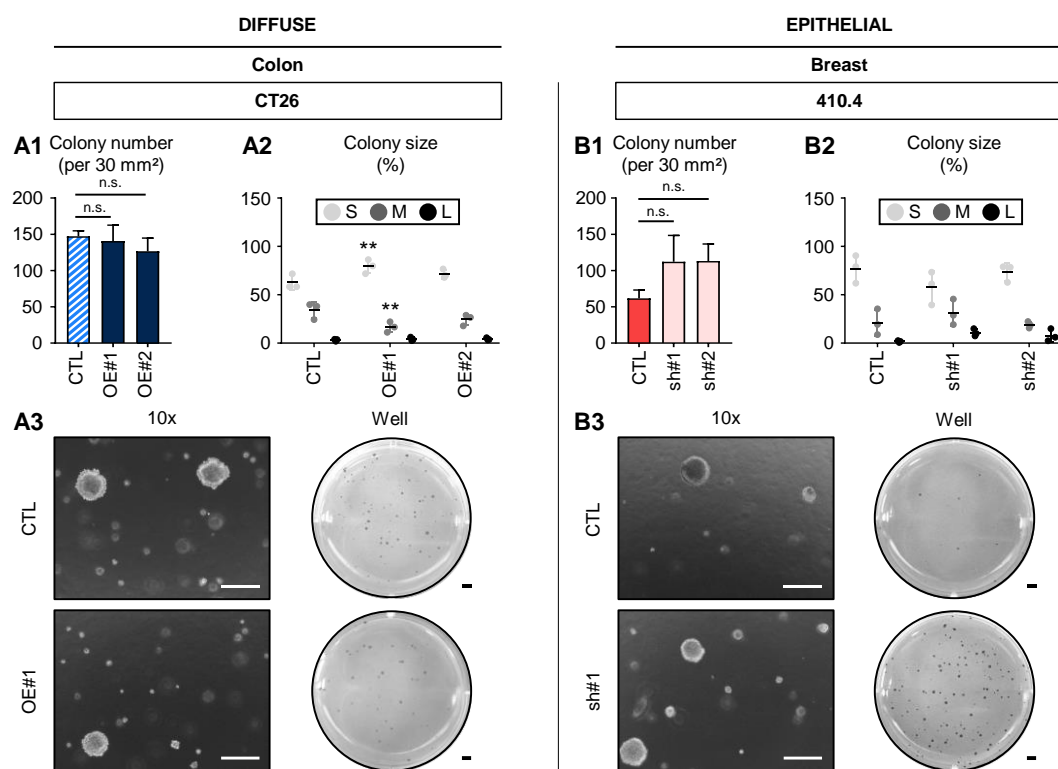


Figure 32: Effects of E-cadherin modifications on colony formation *in vitro*. Colony formation assay in soft agar of **(A)** CT26 control (CTL) and E-cadherin-overexpression (OE) colon cancer cells and **(B)** 410.4 control (CTL) and E-cadherin-knockdown (sh) breast cancer cells. **(A1+B1)** Number of colonies per 30 mm² is displayed (mean + SD, $n = 3$; one-way ANOVA followed by Dunnett's multiple comparisons; n.s. = not significant). **(A2+B2)** Percentage of colony size separated into three groups (S: small, M: medium, L: large) is indicated (mean + SD, $n = 3$; two-way ANOVA followed by Dunnett's multiple comparisons; ** $P < 0.01$ vs. CTL). **(A3+B3)** Representative images are shown. Scale bars represent 200 µm.

3.3.3. Effects of E-cadherin modifications on contact inhibition mechanisms

Having identified contact inhibition as one mechanism that clearly differed between diffuse and epithelial infiltrative MMPI model cell lines (see 3.2.3), the next step was to clarify whether E-cadherin modifications had an impact on this system. Again, I performed confluence assays with all modified cell lines and quantified the protein ratio of phospho-YAP and YAP, which rises with increasing confluence in case of intact contact inhibition.

3.3.3.1. No rescue of contact inhibition after E-cadherin overexpression

Contrary to expectations, E-cadherin overexpression had no effect on contact inhibition at all. All cell lines grew to confluence after cultivation for up to 96 h (Figure 33 A+C), but the p-YAP/YAP ratio did not rise with increasing cell density in any of the diffuse infiltrative E0771-LG (breast) or CT26 (colon) E-cadherin-overexpression cell lines (Figure 33 B+D). This demonstrates that the E-cadherin overexpression could not restore contact inhibition. Instead, the cells continued to show a tonic YAP signaling without functional contact inhibition.

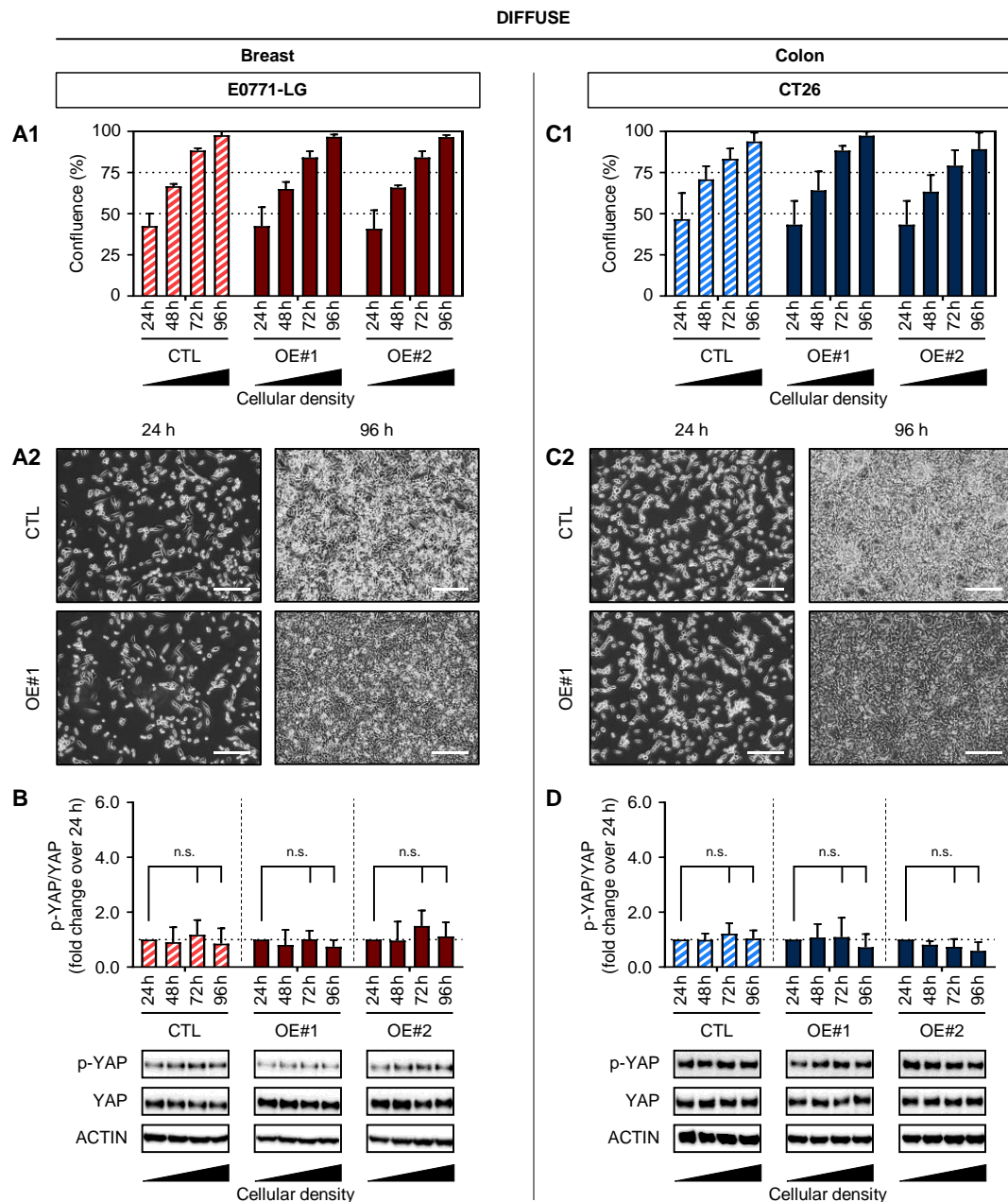


Figure 33: Effects of E-cadherin overexpression on contact inhibition mechanisms *in vitro*. Characterization of (A–B) E0771-LG and (C–D) CT26 control (CTL) and E-cadherin-overexpression (OE) breast and colon cancer cells concerning contact inhibition mechanisms *in vitro*. (A+C) Confluence assay. (A1+C1) Level of cellular confluence during cultivation is displayed in percent and (A2+C2) representative images at low and high confluence are shown. Scale bars represent 200 μ m. (B+D) Western blot analysis of phospho-YAP (p-YAP) and YAP over time as measurement for functional contact inhibition. Protein band intensities of p-YAP and YAP were normalized to corresponding loading controls (ACTIN) and the ratio was calculated. Quantification of p-YAP/YAP expression is displayed as fold change over 24 h. Representative bands for all indicated proteins and one representative loading control are shown (mean + SD, $n = 3$; two-way ANOVA followed by Dunnett's multiple comparisons; n.s. = not significant).

3.3.3.2. Impaired contact inhibition after E-cadherin knockdown

In contrast, the situation was different after downregulation of E-cadherin. Although control as well as knockdown cell lines grew to confluence after cultivation for up to 96 h (Figure 34 A+C), I saw noticeable differences in the ratio of p-YAP and YAP. In both epithelial infiltrative 410.4 (breast) and CMT93Var (colon) control cell lines the p-YAP/YAP ratio rose with increasing cell density pointing to intact contact inhibition mechanisms. However, the knockdown abolished the increase of the p-YAP/YAP ratio by confluence as expected. This demonstrates that the E-cadherin knockdown led to loss of contact inhibition (Figure 34 B+D). It further emphasizes that epithelial infiltrative cell lines seem to depend on E-cadherin levels for maintenance of functional contact inhibition.

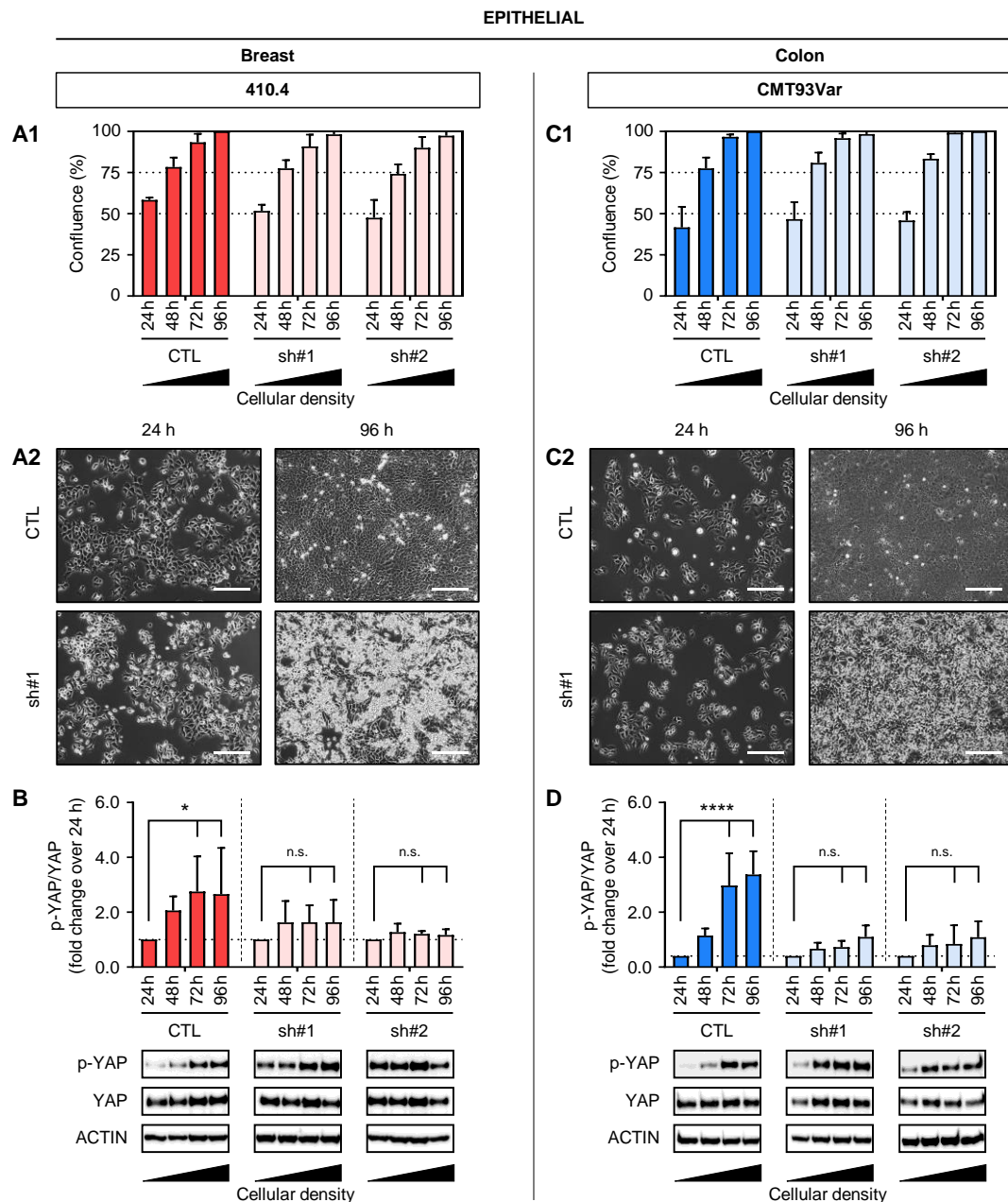


Figure 34: Effects of E-cadherin knockdown on contact inhibition mechanisms *in vitro*. Characterization of **(A–B)** 410.4 and **(C–D)** CMT93Var control (CTL) and E-cadherin-knockdown (sh) breast and colon cancer cells concerning contact inhibition mechanisms *in vitro*. **(A+C)** Confluence assay. **(A1+C1)** Level of cellular confluence during cultivation is displayed in percent and **(A2+C2)** representative images at low and high confluence are shown. Scale bars represent 200 μm . **(B+D)** Western blot analysis of phospho-YAP (p-YAP) and YAP over time as measurement for functional contact inhibition. Protein band intensities of p-YAP and YAP were normalized to corresponding loading controls (ACTIN) and the ratio was calculated. Quantification of p-YAP/YAP expression is displayed as fold change over 24 h. Representative bands for all indicated proteins and one representative loading control are shown (mean + SD, $n = 3$; two-way ANOVA followed by Dunnett's multiple comparisons; * $P < 0.05$, **** $P < 0.0001$, n.s. = not significant).

3.3.4. Summary of *in vitro* characterization results

In summary, the modifications of the cell adhesion receptor E-cadherin in diffuse and epithelial infiltrative murine brain metastasis model cell lines had major implications on their morphology and migratory and invasive behavior *in vitro* (Figure 35). Although both approaches provoked profound phenotypic changes, with a switch from diffuse to more epithelial-like morphology in case of E-cadherin upregulation and the other way around in case of downregulation, all modified lines maintained their original cell character with mesenchymal or epithelial equipment. Furthermore, the modifications of E-cadherin did not result in a switch of their gene expression signature including cell adhesion markers, ECM binding integrins, EMT markers, cytoskeletal components and metabolic genes. While the overexpression of E-cadherin reduced migration behavior and invasive capacity in breast and colon cancer cells, the knockdown led to an increase in both aspects. Consistently, spheroid outgrowth was reduced after overexpression. However, all modified cells maintained their ability to form colonies under anchorage-independent conditions in 3D models. Although contact inhibition could not be restored by E-cadherin overexpression, it was actually lost in the knockdown cells.

These data demonstrated the different dependencies of diffuse and epithelial infiltrative models on the cell adhesion receptor E-cadherin *in vitro* and reinforced the theory of different molecular mechanisms supporting both types of breast and colon cancer infiltration.

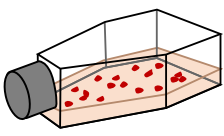












DIFFUSE			EPITHELIAL	
Breast [E0771-LG]	Colon [CT26]		Breast [410.4]	Colon [CMT93Var]
E-cadherin overexpression			E-cadherin knockdown	
Diffuse 	Epithelial-like 	Cell morphology Main intermediate filament Gene expression signature 2D Migration & Invasion 3D Spheroids 3D Colonies Contact inhibition	Epithelial 	Diffuse-like 
Vimentin <input type="checkbox"/>	Vimentin <input type="checkbox"/>		Cytokeratin <input type="checkbox"/>	Cytokeratin <input type="checkbox"/>
<input type="checkbox"/>	<input type="checkbox"/>		<input type="checkbox"/>	<input type="checkbox"/>
				
			No spheroids	<input type="checkbox"/>
<input type="checkbox"/>	<input type="checkbox"/>		<input type="checkbox"/>	<input type="checkbox"/>
Not intact <input type="checkbox"/>	Not intact <input type="checkbox"/>		Intact 	Intact 

Figure 35: Summary of E-cadherin modification effects in murine brain metastasis model cell lines (white bar: no change, grey arrow: increase/gain, black arrow: decrease/loss).

3.4. E-cadherin modifications in brain metastasis mouse models

After the promising results in different cellular assays, the next step was to clarify if the findings could be applied to the situation in the living animal. In the following part of this thesis, I put emphasis on the detailed characterization of effects of E-cadherin modifications in both diffuse and epithelial infiltrative brain metastasis mouse models. To this end, I used our well-established late brain colonization model and injected control and modified cell lines stereotactically into the cortex of syngeneic mice. The resulting brain metastases were perfectly suited for the study of the role of E-cadherin in metastatic brain colonization to reveal underlying mechanisms and outcomes on various levels. First on a descriptive basis by comparing the survival curves of mice. Next, on a morphological basis by investigating the growth patterns, especially at the MMPI, and quantifying the infiltration grade into the surrounding brain parenchyma. The characterization of the surrounding metastatic microenvironment was also included in this context. Finally, on a molecular basis by analyzing the expression of previously identified DEGs in the metastatic tissue compared to the situation in the healthy brain.

The modified groups were pooled to one cohort in the following analyses if not stated otherwise.

3.4.1. Effects of E-cadherin modifications on overall survival

The first aim was to compare the colonization potential of control and modified cell lines *in vivo* by analyzing the overall survival of the groups and comparing the survival curves. For this purpose, I stereotactically injected 1000 cells of the respective line into the right hemisphere of syngeneic mice as described in the methods section (see 2.2.3). The required numbers of injected cells needed to obtain brain metastases within a reasonable time had been previously established for each wild-type cell line in our lab. Therefore, I chose the lowest possible number that had led to successful organ colonization in all models and used it for all control and modified cell lines. Equal numbers of injected cells enabled better comparability between diffuse and epithelial infiltrative brain metastasis models.

3.4.1.1. Prolonged survival after E-cadherin overexpression

In diffuse infiltrative E0771-LG, metastases appeared very early within approximately 2 weeks in all mice and E-cadherin overexpression had no effect on overall survival (median OS = 15.5 days in CTL and 14 days in OE) (Figure 36 A). The increased level of E-cadherin in the overexpression group was only detectable by quantitative RT-PCR analysis of the metastatic brain tissue (Figure 36 B) but not visible in IHC stainings (Figure 36 C). In comparison to that, the diffuse infiltrative CT26 needed almost the double amount of time until metastases occurred. Nevertheless, they were still quite aggressive with metastases appearing within 3 to 4 weeks and E-cadherin overexpression significantly prolonged

survival (median OS = 23 days in CTL and 26.5 days in OE, $P = 0.0055$) (Figure 36 D). Furthermore, the increased level of E-cadherin was detectable by quantitative RT-PCR analysis of the metastatic brain tissue (Figure 36 E) and visible in IHC stainings (Figure 36 F).

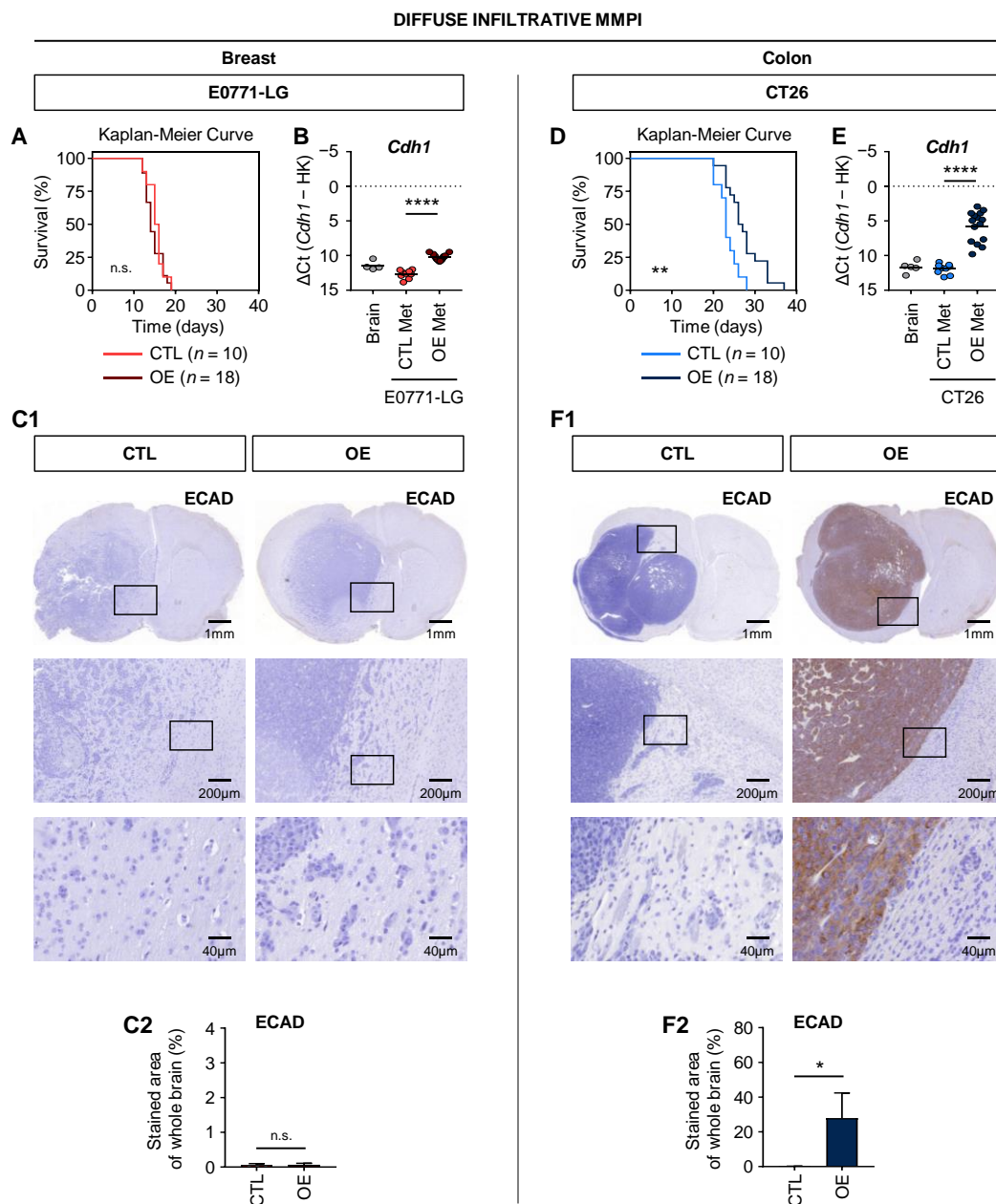


Figure 36: Effects of E-cadherin overexpression in diffuse infiltrative brain metastasis mouse models on survival. Effects of E-cadherin overexpression in (A–C) E0771-LG and (D–F) CT26 breast and colon cancer brain metastases. (A+D) Kaplan-Meier survival curves of mice injected with control (CTL; $n = 10$) and E-cadherin-overexpression cells (OE; $n = 18$; log-rank test; ** $P < 0.01$, n.s. = not significant). (B+E) Quantitative RT-PCR analysis of E-cadherin (*Cdh1*) expression in brain metastases of control (CTL Met) and E-cadherin-overexpression (OE Met) cells as well as only ECM injected brains of control mice (Brain; C57BL/6 for E0771-LG, BALB/c for CT26). *Gapdh* and *Pgk1* were used as housekeeping genes (HK; mean and individual values; $n \geq 4$; one-way ANOVA followed by Tukey's multiple comparisons; **** $P < 0.0001$). (C+F) IHC staining of E-cadherin (ECAD) in tissue sections of CTL and OE brain metastases. (C1+F1) Representative images of coronal brain sections and images of the MMPI at higher

magnifications are shown. **(C2+F2)** Quantification of E-cadherin staining is indicated as the percentage of stained area in whole brain slices (mean + SD, $n = 3$; unpaired t -test; * $P < 0.05$, n.s. = not significant).

3.4.1.2. Shortened survival after E-cadherin knockdown

As expected based on the *in vitro* findings, E-cadherin knockdown in epithelial infiltrative models had the opposite effect. In epithelial infiltrative 410.4, it took approximately 4 months until metastases appeared in all mice in the control group. Compared to that, E-cadherin knockdown had a severe impact on overall survival as metastases occurred already after 2 months in all mice (median OS = 114 days in CTL and 64 days in sh, $P < 0.0001$) (Figure 37 A). I saw a similar trend in epithelial infiltrative CMT93Var, where 6 of 10 mice of the control group also developed metastases after approximately 4 months. E-cadherin knockdown again shortened the overall survival with metastases occurring after 3.5 months in 13 of 17 mice (median OS = 118.5 days in CTL and 101 days in sh), although the effect was not as prominent as in 410.4 (Figure 37 D). Mice remaining symptom-free until the end of the experiments were sacrificed at day 200. Subsequent IHC stainings confirmed the absence of any brain metastases in these mice (data not shown). The reduced level of E-cadherin was detectable by quantitative RT-PCR analysis of the metastatic brain tissue (Figure 37 B+E) and visible in IHC stainings (Figure 37 C+F) for both 410.4 and CMT93Var models.

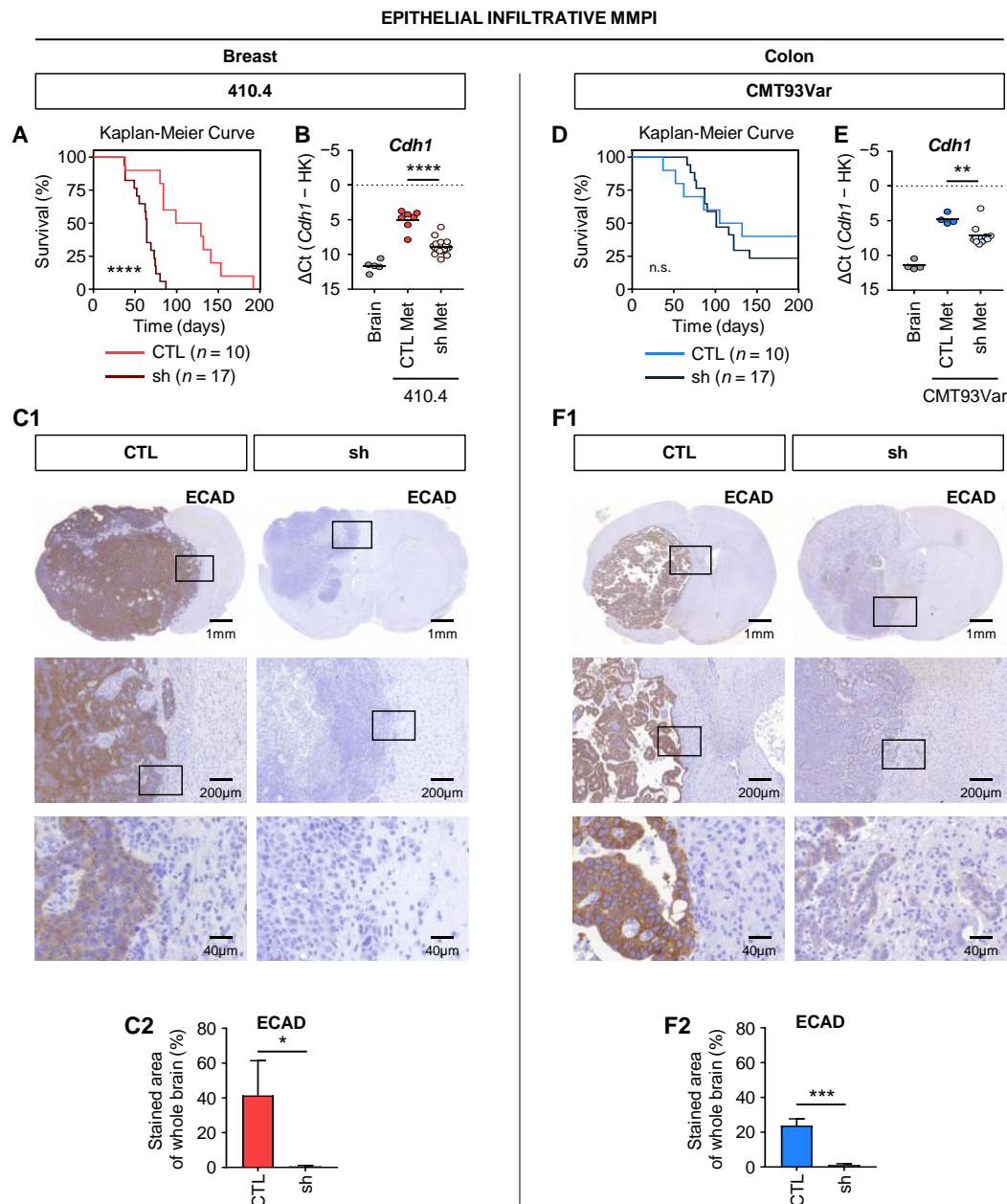


Figure 37: Effects of E-cadherin knockdown in epithelial infiltrative brain metastasis mouse models on survival. Effects of E-cadherin knockdown in (A–C) 410.4 and (D–F) CMT93Var breast and colon cancer brain metastases. (A+D) Kaplan-Meier survival curves of mice injected with control (CTL; $n = 10$) and E-cadherin-knockdown cells (sh; $n = 17$; log-rank test; **** $P < 0.0001$, n.s. = not significant). (B+E) Quantitative RT-PCR analysis of E-cadherin (*Cdh1*) expression in brain metastases of control (CTL Met) and E-cadherin-knockdown (sh Met) cells as well as only ECM injected brains of control mice (Brain; BALB/c for 410.4, C57BL/6 for CMT93Var). *Gapdh* and *Pgk1* were used as housekeeping genes (HK; mean and individual values; $n \geq 4$; one-way ANOVA followed by Tukey's multiple comparisons; ** $P < 0.01$, **** $P < 0.0001$). (C+F) IHC staining of E-cadherin (ECAD) in tissue sections of CTL and sh brain metastases. (C1+F1) Representative images of coronal brain sections and images of the MMPI at higher magnifications are shown. (C2+F2) Quantification of E-cadherin staining is indicated as the percentage of stained area in whole brain slices (mean + SD, $n = 3$; unpaired t -test; * $P < 0.05$, *** $P < 0.001$).

3.4.1.3. Impact on colonization index

The colonization index (CI) is an easy and accurate method to compare different metastatic brain colonization models and findings from survival studies across entities. It was previously established in our lab as a precise and useful tool to quantify the aggressiveness of different cancer cell lines *in vivo*. This mathematical formula includes three parameters to calculate the colonization capacity: (i) the rate of mice with successful brain colonization (in percent), (ii) the number of injected cells and (iii) the median overall survival of the mice (in days) (Figure 38 A). First, I compared the colonization capacities of all control cell lines. While the diffuse infiltrative E0771-LG and CT26 displayed a highly aggressive colonization potential, it was low in the case of the epithelial infiltrative 410.4 and CMT93Var (Figure 38 B). The effects of E-cadherin modifications on colonization capacities are summarized in a table and overall effects (increase (+) or decrease (-) compared to control group) are depicted (Figure 38 C). The overexpression resulted in a less aggressive colonization potential in CT26, while the knockdown had the opposite effect in 410.4 and CMT93Var.

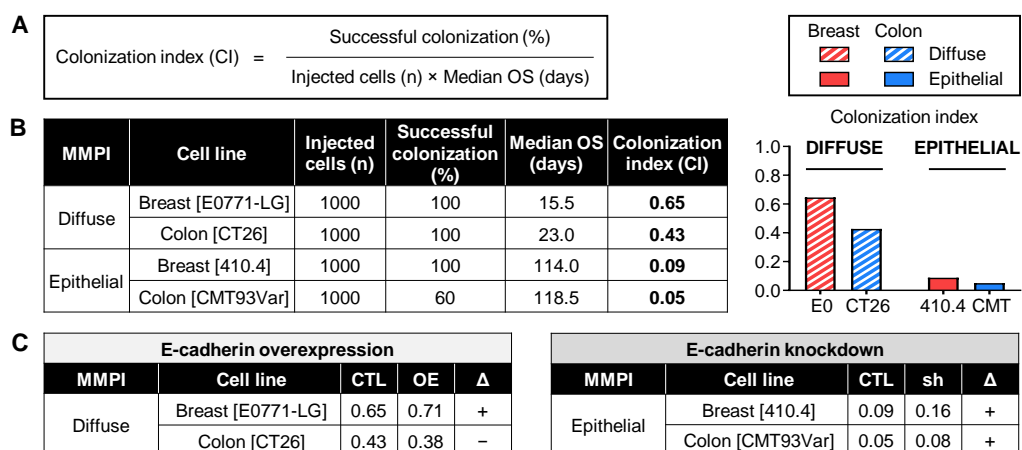


Figure 38: Effects of E-cadherin modifications in diffuse and epithelial infiltrative brain metastasis mouse models on colonization index. (A) The colonization index (CI) is a mathematical formula used to compare the colonization potential of different cancer cell lines *in vivo*. Cell lines with high CI are considered more aggressive than cell lines with low CI. **(B)** CI comparison of diffuse (E0771-LG (E0) and CT26) and epithelial (410.4 and CMT93Var (CMT)) infiltrative breast and colon control cancer cell lines. **(C)** Effect of E-cadherin modification on CI. Respective control (CTL) is compared to E-cadherin-overexpression (OE) or E-cadherin-knockdown (sh) group and the difference (increase (+) or decrease (-)) is displayed.

3.4.1.4. Correlation of overall survival and vimentin level

In an additional step, I split the pooled survival curves of the E-cadherin modification groups and compared them separately. In both diffuse models, as well as the epithelial 410.4, the separate groups (OE#1 and OE#2, sh#1 and sh#2) showed the same effects in general (Figure 39 A1+B1+C1). However, in epithelial infiltrative CMT93Var I observed contradictory effects for sh#1 and sh#2. Compared to the control group, where metastases appeared after 4 months in 60 percent of mice (median OS = 118.5 days), E-cadherin knockdown shortened overall survival in mice injected with sh#1 to 3 months (median OS = 87 days) but even prolonged it in the sh#2 cohort to almost 6 months (median OS = 161.5 days) (Figure 39 D1). Interestingly, colonization was successful in all mice injected with sh#1, but only in fifty percent of the sh#2 animals. The colonization index reflected the increased colonization capacity of sh#1 (0.11) compared to the control line (0.05) and even showed the decrease in case of sh#2 (0.03) (data not shown). This difference in aggressiveness could not be explained by the level of E-cadherin, which was reduced in both knockdown groups (data not shown). Hence, other factors had to be responsible for the observation.

In the search for possible candidates, I could identify the mesenchymal marker vimentin to be differentially expressed in the CMT93Var cell lines. Along with the intended knockdown of E-cadherin, the CMT93Var sh#2 cells had lost most of their vimentin expression. This difference was present on RNA level in the gene cluster analysis data and on protein level in Western blots. For better visualization, I calculated the protein expression ratios of vimentin and E-cadherin and noticed that prolonged survival correlated with decreasing ratios in overexpression lines (Figure 39 A2+B2) while shortened survival correlated with increasing ratios in knockdown lines (Figure 39 C2+D2). CMT93Var sh#2 represented the only exception of the knockdown lines showing a decreased ratio instead. This pointed out the altered vimentin level as the underlying factor for the prolonged survival of this group. Additionally, the protein expression ratios of cytokeratin-8 and E-cadherin are displayed to confirm that this effect was specific for vimentin. Although this epithelial marker showed similar correlations of ratio and survival in general, it was not differentially expressed in CMT93Var sh#1 and sh#2 and consequently not involved in their opposing survival rates. An overview of all correlations is also shown below (Figure 39 E). In summary, the mesenchymal factor vimentin seemed to play a crucial role in long-term survival.

Due to these findings, the CMT93Var sh#2 group was not included in further analyses.

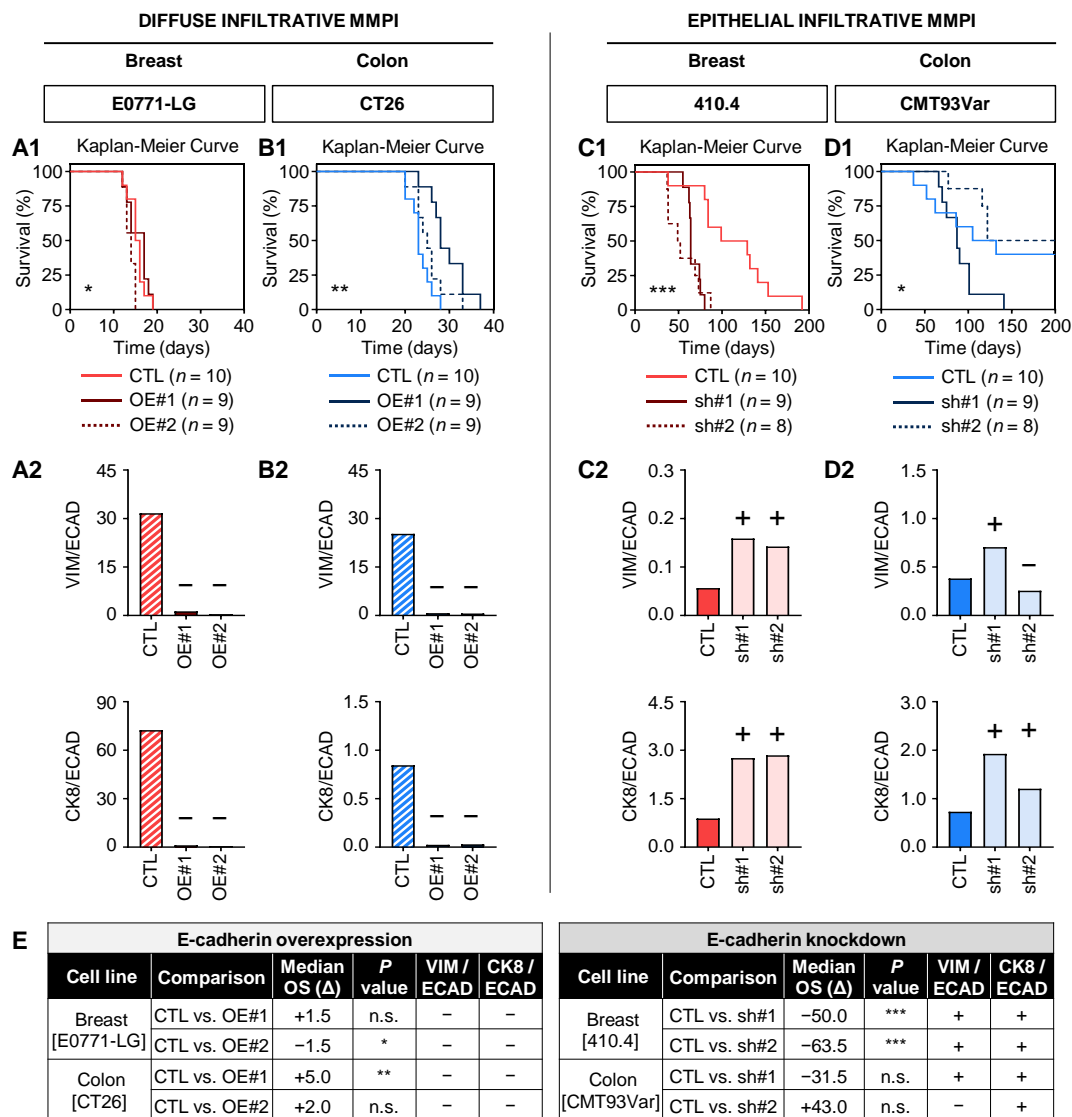


Figure 39: Correlation of overall survival and vimentin level in diffuse and epithelial infiltrative brain metastasis mouse models. Comparison of (A) E0771-LG, (B) CT26, (C) 410.4 and (D) CMT93Var breast and colon cancer brain metastases. (A1+B1+C1+D1) Kaplan-Meier survival curves of mice injected with control (CTL; $n = 10$) and E-cadherin-overexpression (OE; $n = 9$) or E-cadherin-knockdown (sh; $n = 8-9$) cells displayed as separate groups (#1 and #2; log-rank test for overall effect; * $P < 0.05$, ** $P < 0.01$, *** $P < 0.001$). (A2+B2+C2+D2) Quantification of E-cadherin (ECAD), vimentin (VIM) and cytokeratin-8 (CK8) protein expression in murine brain metastasis model cell lines after E-cadherin modifications (CTL: control, OE: E-cadherin-overexpression, sh: E-cadherin-knockdown). Protein expression was normalized to corresponding loading controls and the ratios of VIM/ECAD and CK8/ECAD are displayed. (E) Summary table relating overall survival of separate groups to protein ratios of VIM/ECAD and CK8/ECAD. Respective control (CTL) is compared to E-cadherin-overexpression (OE) or E-cadherin-knockdown (sh) group and the difference (increase (+) or decrease (-)) is displayed (log-rank test; * $P < 0.05$, ** $P < 0.01$, *** $P < 0.001$, n.s. = not significant).

3.4.2. Effects of E-cadherin modifications on MMPI pattern and infiltration

In the next parts of this work, I focused on morphological features of the brain metastases and investigated whether E-cadherin modifications affected the brain colonization and outgrowth pattern of breast and colon cancer cells. For this purpose, I compared the MMPI patterns resulting from control and modified cell lines and quantified the infiltration grade into the surrounding brain parenchyma by analyzing IHC stainings of coronal brain sections.

3.4.2.1. Reduced infiltration at the MMPI after E-cadherin overexpression

Metastatic growth in the diffuse infiltrative brain metastasis mouse models resulting from the highly metastatic E0771-LG and CT26 was visualized again by vimentin stainings. As already described, it is used for carcinomas without noticeable expression of epithelial markers. VIM stainings displayed the diffuse infiltrative patterns with metastatic cells deeply infiltrating the adjacent brain tissue. However, compared to the control group, where numerous single metastatic cells invaded hundreds of μm far into the brain parenchyma, infiltration was less pronounced after E-cadherin overexpression in E0771-LG and manifested in a more compact diffuse infiltrative MMPI. Furthermore, metastatic cells were stuck together as clusters of several single cells and invaded mainly in those small cohorts (Figure 40 A). The phenotype thus became more similar to the epithelial infiltrative pattern characterized by clusters of tumor cells collectively infiltrating the adjacent tissue. I could observe the same phenomenon in the colon CT26 models, although infiltration is generally less pronounced compared to the breast E0771-LG (Figure 40 C).

The overexpression of E-cadherin definitely had a strong influence on the metastatic growth pattern of both breast and colon cancer cells. In order to emphasize this phenotypic switch and express it in numbers, I analyzed all metastases in a systematic approach. I quantified the extent of infiltrative growth into the brain parenchyma along the MMPI and classified the metastatic growth pattern as highly infiltrative ($>2/3$), moderately infiltrative ($2/3-1/3$), or low infiltrative ($<1/3$). In contrast to the highly infiltrative growth of the control group (CTL, 89%), the E-cadherin-overexpression cohort revealed a predominantly moderate infiltration pattern (OE, 75%) in E0771-LG (Figure 40 B). In the CT26 models, the infiltrative growth accordingly switched from moderate in control mice (CTL, 86%) to low in mice injected with E-cadherin-overexpression cells (OE, 63%) (Figure 40 D). In both cases, the difference was significant ($P = 0.002$ for E0771-LG, $P = 0.033$ for CT26).

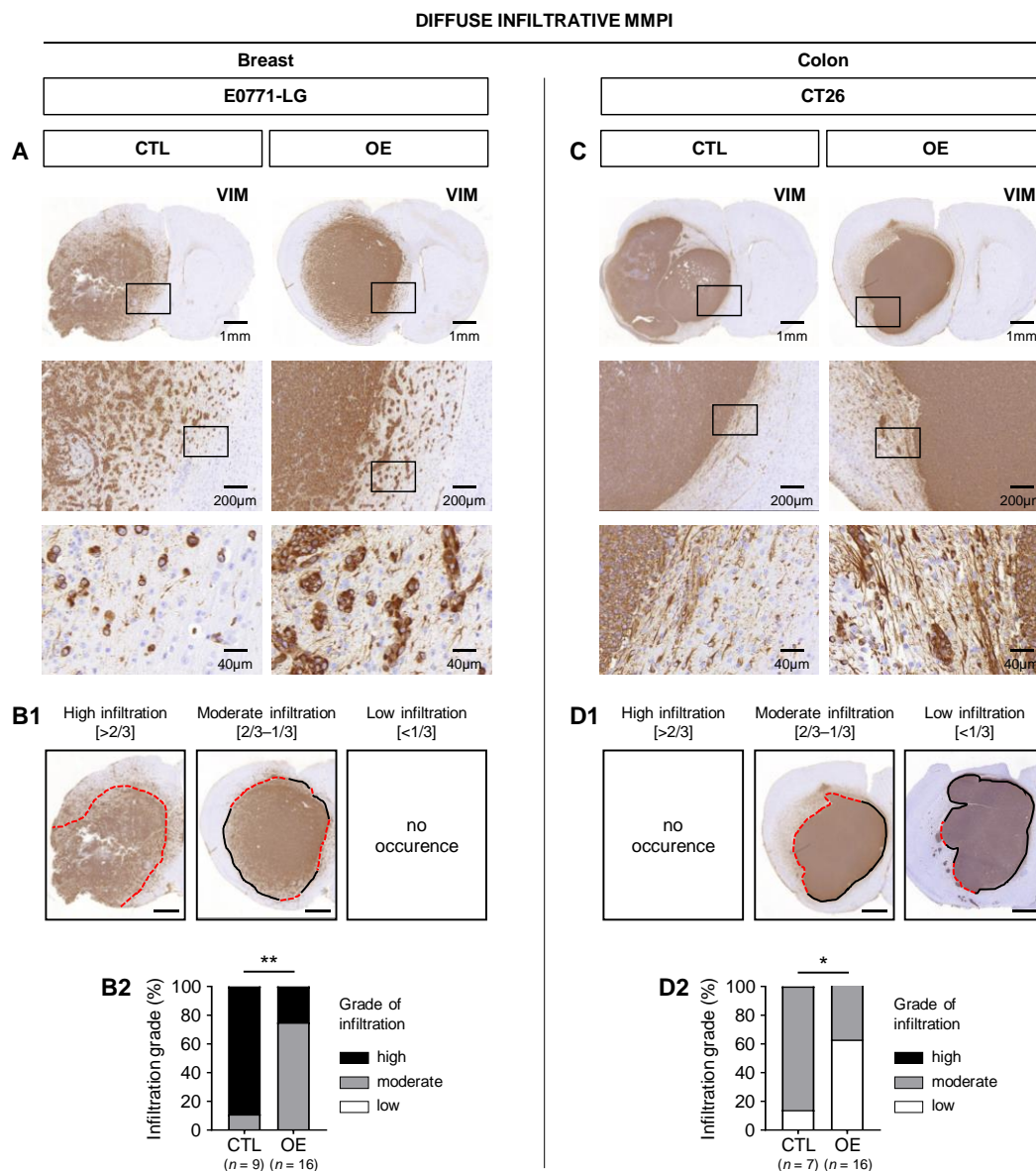


Figure 40: Effects of E-cadherin overexpression in diffuse infiltrative brain metastasis mouse models on MMPI pattern and infiltration. Effects of E-cadherin overexpression in (A–B) E0771-LG and (C–D) CT26 breast and colon cancer brain metastases. Comparison of MMPI patterns and infiltration grade in control (CTL) and E-cadherin-overexpression (OE) mice. (A+C) IHC staining of vimentin (VIM) in tissue sections of brain metastases. Representative images of coronal brain sections and images of the MMPI at higher magnifications are shown. (B+D) Infiltration grade of brain metastases. (B1+D1) Representative images of high (>2/3), moderate (2/3–1/3), and low (<1/3) infiltration are shown. Brain metastases were stained against VIM. The black solid line indicates no infiltration, while the red dotted line marks zones of infiltration within the brain metastases. Scale bars represent 1 mm. (B2+D2) Quantification of the metastatic infiltration pattern is displayed as percentage of infiltration grade ($n = 7–16$; chi-square test; $*P < 0.05$, $**P < 0.01$).

3.4.2.2. Increased infiltration at the MMPI after E-cadherin knockdown

Metastatic growth in the epithelial infiltrative brain metastasis mouse models resulting from the moderately to low metastatic 410.4 and CMT93Var was visualized again by cytokeratin-8 stainings. As described previously, it is widely used by pathologists to recognize growth patterns of adenocarcinomas. In both control cohorts, CK8 stainings displayed the typical epithelial infiltrative patterns characterized by clusters of metastatic cells collectively infiltrating the adjacent brain parenchyma. However, while only some bulks of metastatic cells invaded into the brain parenchyma as cohorts in the 410.4 control group, infiltration was more pronounced after E-cadherin knockdown. Metastatic cells invaded farer into the surrounding tissue and were predominantly isolated from each other or in small groups (Figure 41 A). The phenotype was thus becoming more similar to the diffuse infiltrative pattern characterized by numerous single metastatic cells infiltrating the adjacent tissue on their own. I could observe a comparable effect in the colon CMT93Var models. Here, the phenotype switched from metastases showing almost no infiltrative growth with glandular appearance in the control cohort to higher infiltration displayed by small clusters with inner lumen or even individual cells invading further away from the metastatic border (Figure 41 C).

Thus, the knockdown of E-cadherin had an even stronger influence on the metastatic growth pattern of both breast and colon cancer cells than the overexpression depicted above. Again, I analyzed all metastases systematically and classified them as high, moderate or low infiltrative as described before. In contrast to the predominantly low infiltrative growth of the control group (CTL, 78%), the E-cadherin-knockdown cohort displayed significantly increased infiltration rates with moderate growth (sh, 64%) in 410.4 ($P = 0.0301$, Figure 41 B). In the CMT93Var models, I observed the most drastic effect of E-cadherin modification among all investigated brain metastasis models. The infiltrative growth switched from exclusively low in control mice (CTL, 100%) to entirely high in mice injected with E-cadherin-knockdown cells (sh, 100%) ($P = 0.0005$, Figure 41 D) and the infiltration depth often exceeded 1 mm.

Interestingly, the infiltration pattern in the previously featured CMT93Var sh#2 cohort was similar to the respective control group showing only low infiltrative growth (data not shown). This reflected the results of prolonged survival *in vivo* and confirmed its exclusion from further analyses.

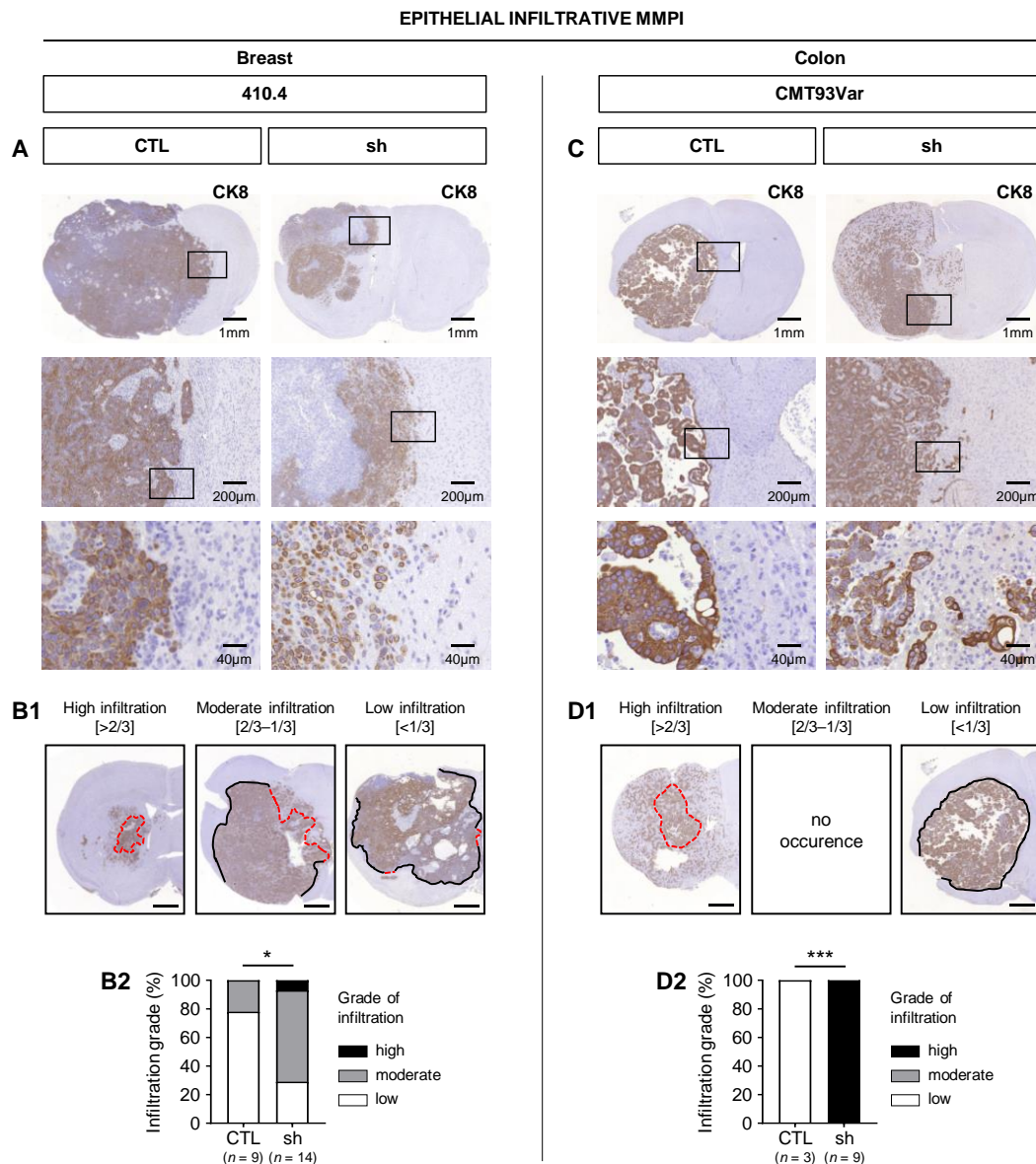


Figure 41: Effects of E-cadherin knockdown in epithelial infiltrative brain metastasis mouse models on MMPI pattern and infiltration. Effects of E-cadherin knockdown in (A–B) 410.4 and (C–D) CMT93Var breast and colon cancer brain metastases. Comparison of MMPI patterns and infiltration grade in control (CTL) and E-cadherin-knockdown (sh) mice. (A+C) IHC staining of cytokeratin-8 (CK8) in tissue sections of brain metastases. Representative images of coronal brain sections and images of the MMPI at higher magnifications are shown. (B+D) Infiltration grade of brain metastases. (B1+D1) Representative images of high (>2/3), moderate (2/3–1/3), and low (<1/3) infiltration are shown. Brain metastases were stained against CK8. The black solid line indicates no infiltration, while the red dotted line marks zones of infiltration within the brain metastases. Scale bars represent 1 mm. (B2+D2) Quantification of the metastatic infiltration pattern is displayed as percentage of infiltration grade ($n = 3–14$; chi-square test; $*P < 0.05$, $***P < 0.001$).

3.4.3. Effects of E-cadherin modifications on angiogenesis in brain metastases

Besides the uncontrolled growth and the capability to invade into surrounding tissues, another hallmark of cancer is the induction of angiogenesis for the growth of new blood vessels (Hanahan et al., 2000). They ensure the optimal supply with oxygen and nutrients for invading cancer cells. Angiotropic infiltration is thereby defined as tumor cells growing as sheaths around blood vessels and protruding far into the adjacent tissue by this way. The sheaths either consist of groups of cancer cells or single cells (Blazquez et al., 2020b). Diffuse and epithelial infiltrative models often show mixed patterns including angiotropic growth (see 1.1.3). The inner surface of blood vessels is covered by endothelial cells that can be visualized in histological stainings by detecting the platelet endothelial cell adhesion molecule, also known as CD31. After staining for this endothelial marker, I analyzed brain metastases of all models for vessel number and density as described in the methods section (see 2.2.6.2.3.2).

First, I compared the total amount of endothelial cells in the control cohorts of the diffuse and epithelial infiltrative models and found an overall effect of the MMPI pattern ($P = 0.026$). In both diffuse models, the metastatic tissue exhibited a lower vessel density in comparison to the number of vessels in the equivalent epithelial models (data not shown).

Next, I characterized the effects of E-cadherin modifications and their resulting altered growth patterns on endothelial cells and vessel density in metastatic and brain tissue. In general, I observed significantly higher number of vessels with larger diameters after overexpression ($P = 0.038$) (Figure 42 A+B) and lower numbers and decreased size after knockdown of E-cadherin ($P = 0.021$) (Figure 42 D+E) in metastatic tissues of breast cancer models. I saw no difference in brain tissues, except for a slight decrease after overexpression probably due to less angiotropic growth because of less infiltration. Effects of E-cadherin modifications were not as demarcated in colon lines as they displayed lower numbers of vessels in general, although the same tendencies were present (data not shown).

High magnifications of stainings for metastatic (VIM/CK8) and endothelial cells (CD31) in consecutive brain slices of control cohorts displayed typical angiotropic growth patterns of metastatic cells as sheets of many cells around long vessels in diffuse E0771-LG (Figure 42 C) or surrounding small vessels in epithelial 410.4 breast cancer models (Figure 42 F).

Taken together, vessel number, size and density in the metastatic tissue seemed to depend on the growth pattern as they were increased in more compact metastases after E-cadherin overexpression and decreased in looser metastases after knockdown (Figure 42 G).

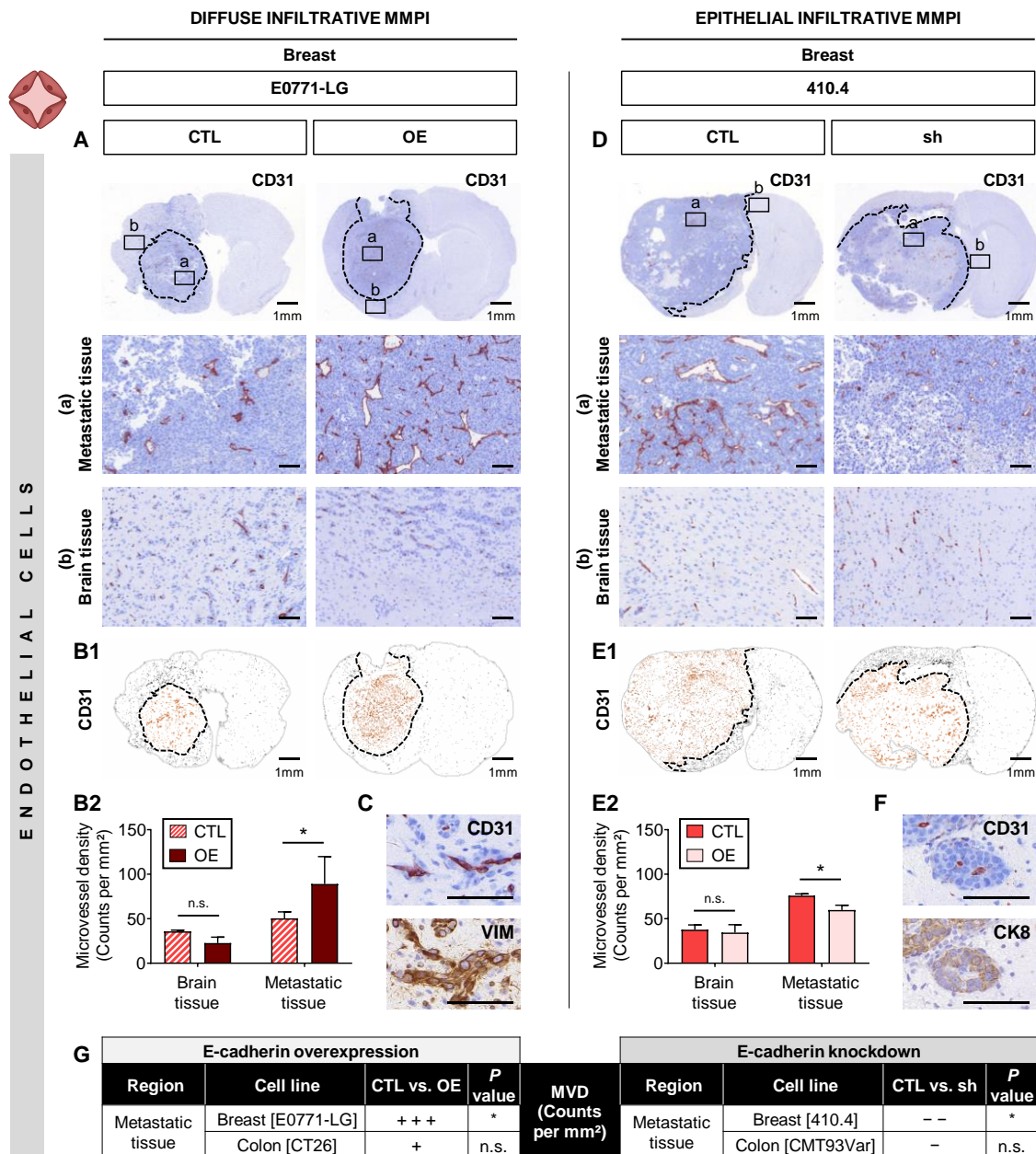


Figure 42: Characterization of endothelial cells in the metastatic brain tissue after E-cadherin modifications. IHC staining of endothelial cells (CD31) in tissue sections of mice with breast cancer brain metastasis of (A–C) E0771-LG control (CTL) and E-cadherin-overexpression (OE) cells and (D–F) 410.4 control (CTL) and E-cadherin-knockdown (sh) cells. (A+D) Representative images of coronal brain sections and images of metastatic tissue and brain tissue at higher magnification are shown. Unlabeled scale bars represent 100 μ m. (B+E) Quantification of CD31 staining. (B1+E1) The black dotted line indicates the MMPI. CD31 counts are displayed as masks in different colors (orange: metastatic tissue counts, black: brain tissue counts) and (B2+E2) microvessel density (MVD) is indicated as counts per mm² in respective brain region (mean + SD). (C+F) Representative images of endothelial cells (CD31) and angiotropic growth of metastatic cells in (C) diffuse E0771-LG CTL (VIM) or (F) epithelial 410.4 CTL (CK8) in consecutive brain slices at high magnification are shown. Scale bars represent 100 μ m. (G) Comparison of endothelial cells (MVD) in the metastatic brain tissue after E-cadherin modifications. Respective control (CTL) is compared to E-cadherin-overexpression (OE) or E-cadherin-knockdown (sh) group and the difference (increase (+) or decrease (–)) is displayed ($n = 3$; two-way ANOVA followed by Sidak’s multiple comparisons; * $P < 0.05$, n.s. = not significant).

3.4.4. Effects of E-cadherin modifications on metastatic microenvironment

As described earlier, initial histological stainings of the metastatic brain tissue of diffuse and epithelial infiltrative breast cancer models had revealed profound morphological differences in the MME between MMPI types (see 3.1.3). This required a systematic investigation and quantification of microenvironment components in all available animal models via immunohistological and morphometric analyses. In the following, I addressed the question whether the modification of E-cadherin could influence the interaction of breast and colon cancer cell lines with the immune cells and their infiltration pattern and distribution within the metastatic tissue. The MMPI had already been assessed in stainings of the metastatic tissue for VIM (E0771-LG and CT26) or CK8 (410.4 and CMT93Var), which facilitated the selection of specific ROIs. After staining for respective markers of the previously established immune panel in consecutive coronal brain slices, I analyzed the microglia/macrophage response, astrocytic reaction and T cell response in separated brain regions (metastatic core, metastatic margin, MMPI and adjacent brain tissue) compared to contralateral brain tissue representing the healthy control situation as described in the methods section (see 2.2.6.2.3.3).

3.4.4.1. Characterization of microglia/macrophages in the metastatic brain tissue after E-cadherin modifications

Microglia are the resident macrophage cells in the brain. In their activated state, they can be quantified in IHC stainings for IBA1. At first, I had a look at their general distribution within the brain. Overall, I found activated microglia/macrophages in the adjacent brain tissue and even higher levels inside the metastatic lesions in all brain colonization models. However, I only saw very low levels in the contralateral hemispheres representing the situation in the healthy brain parenchyma where microglia are not activated and rather widely distributed. This situation was not changed by any of the E-cadherin modifications in contrast to the other regions.

In the diffuse infiltrative models, the distribution of activated microglia/macrophages did not significantly change after overexpression of E-cadherin in any of the selected regions. Although I noticed a slight decreasing trend at the MMPI and adjacent brain parenchyma in E0771-LG (breast) (Figure 43 A), the situation was not changed at all in CT26 (colon) (data not shown).

In contrast, the knockdown of E-cadherin had an enormous impact on the density of activated microglia/macrophage at the MMPI and adjacent brain tissue in epithelial infiltrative models. I found significantly increased microglia/macrophage levels in the knockdown groups of both 410.4 (breast) ($P = 0.0294$) (data not shown) and CMT93Var (colon) ($P < 0.0001$) compared to the respective controls in the adjacent brain tissue and at the MMPI of CMT93Var ($P = 0.0001$) (Figure 43 B).

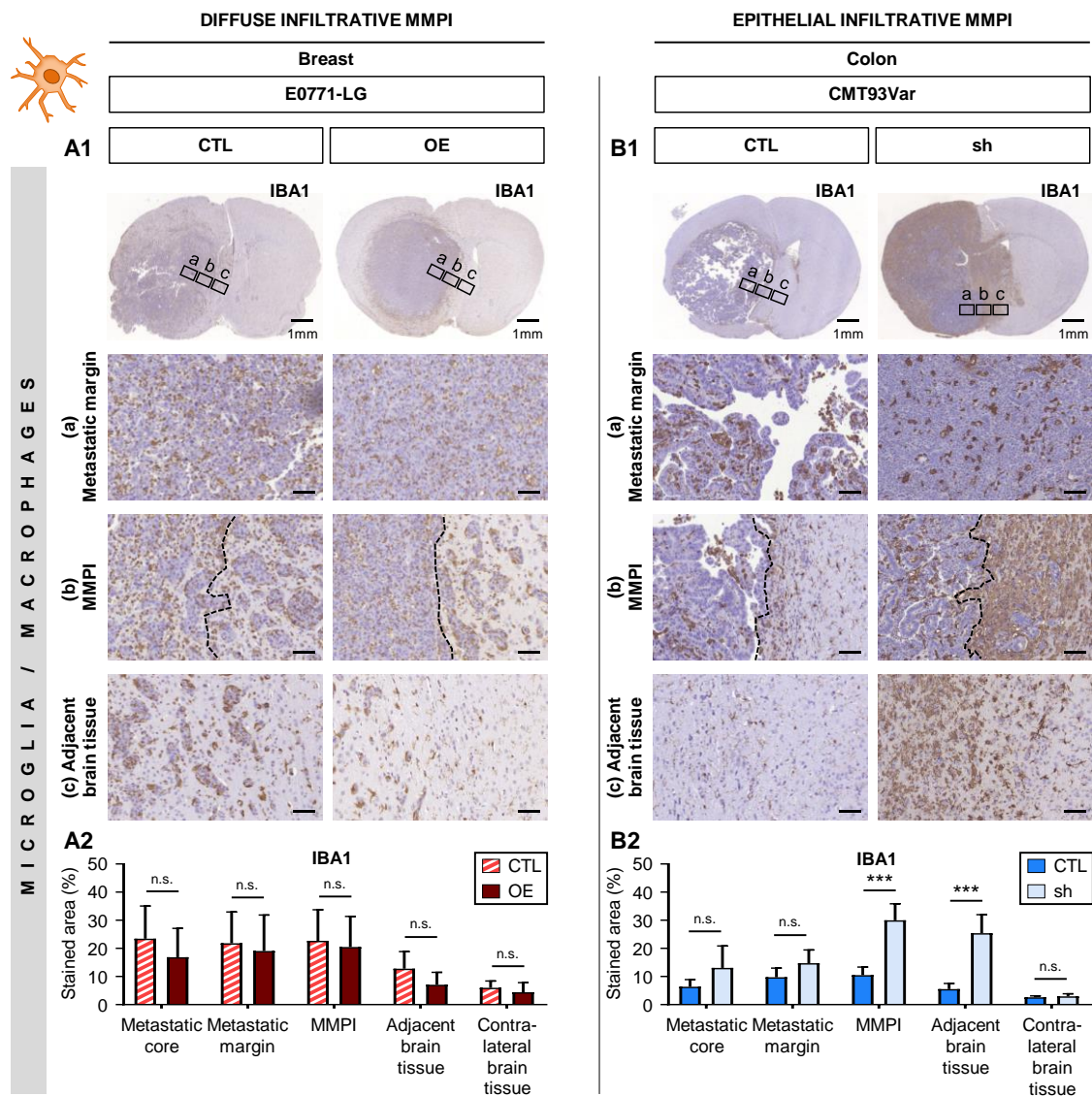


Figure 43: Characterization of microglia/macrophages in the metastatic brain tissue after E-cadherin modifications. IHC staining of activated microglia/macrophages (IBA1) in tissue sections of mice with **(A)** breast cancer brain metastasis of E0771-LG control (CTL) and E-cadherin-overexpression (OE) cells and **(B)** colon cancer brain metastasis of CMT93Var control (CTL) and E-cadherin-knockdown (sh) cells. **(A1+B1)** Representative images of coronal brain sections and images of metastatic margin, MMPI and adjacent brain tissue at higher magnification are shown. The black dotted line indicates the MMPI. Unlabeled scale bars represent 75 μ m. **(A2+B2)** Quantification of IBA1 staining is indicated as the percentage of stained area in respective brain region (mean + SD, $n = 3$; two-way ANOVA followed by Sidak's multiple comparisons; *** $P < 0.001$, n.s. = not significant).

3.4.4.2. Characterization of astrocytes in the metastatic brain tissue after E-cadherin modifications

Astrocytes are the most abundant glial cells of the CNS. In their activated state, they can be quantified in IHC stainings for GFAP. At first, I had a look at the general distribution of astrocytes within the brain. Overall, I found high levels of activated astrocytes in the adjacent brain tissue and at the MMPI similar to the microglia situation. In contrast, no activated astrocytes appeared inside the metastatic lesions in all brain colonization models apart from a few exceptions. Activated astrocytes were also absent in the contralateral hemisphere representing the situation in the healthy brain parenchyma, where these glial cells only maintain the BBB in an inactivated state. Again, none of the E-cadherin modifications had an influence on the levels in this region. When I compared the amount of activated astrocytes in the control cohorts of the diffuse and epithelial infiltrative models, I found an overall effect of MMPI pattern ($P < 0.05$ for metastatic core, MMPI and adjacent brain tissue, $P = 0.058$ for metastatic margin) with epithelial models showing higher levels of astrocyte density compared to their respective diffuse counterparts (data not shown).

In the diffuse infiltrative models, the overexpression of E-cadherin significantly decreased the amount of activated astrocytes in the adjacent brain tissue in E0771-LG (breast) ($P < 0.0001$) (Figure 44 A). Interestingly, astrocytes formed an even thicker surrounding capsule at the MMPI in CT26 (colon) (data not shown).

The knockdown of E-cadherin also had an enormous impact on the astrocytic reaction at the MMPI and adjacent brain tissue in epithelial infiltrative models. Although effects were not as pronounced in 410.4 (breast) (data not shown), I found significantly increased levels of activated astrocytes in the knockdown group of CMT93Var (colon) compared to the respective control ($P = 0.0221$ at MMPI, $P < 0.0001$ in adjacent brain tissue) (Figure 44 B). Here, the phenotype switched from an encapsulated state to an expanded activation far reaching into the surrounding brain tissue.

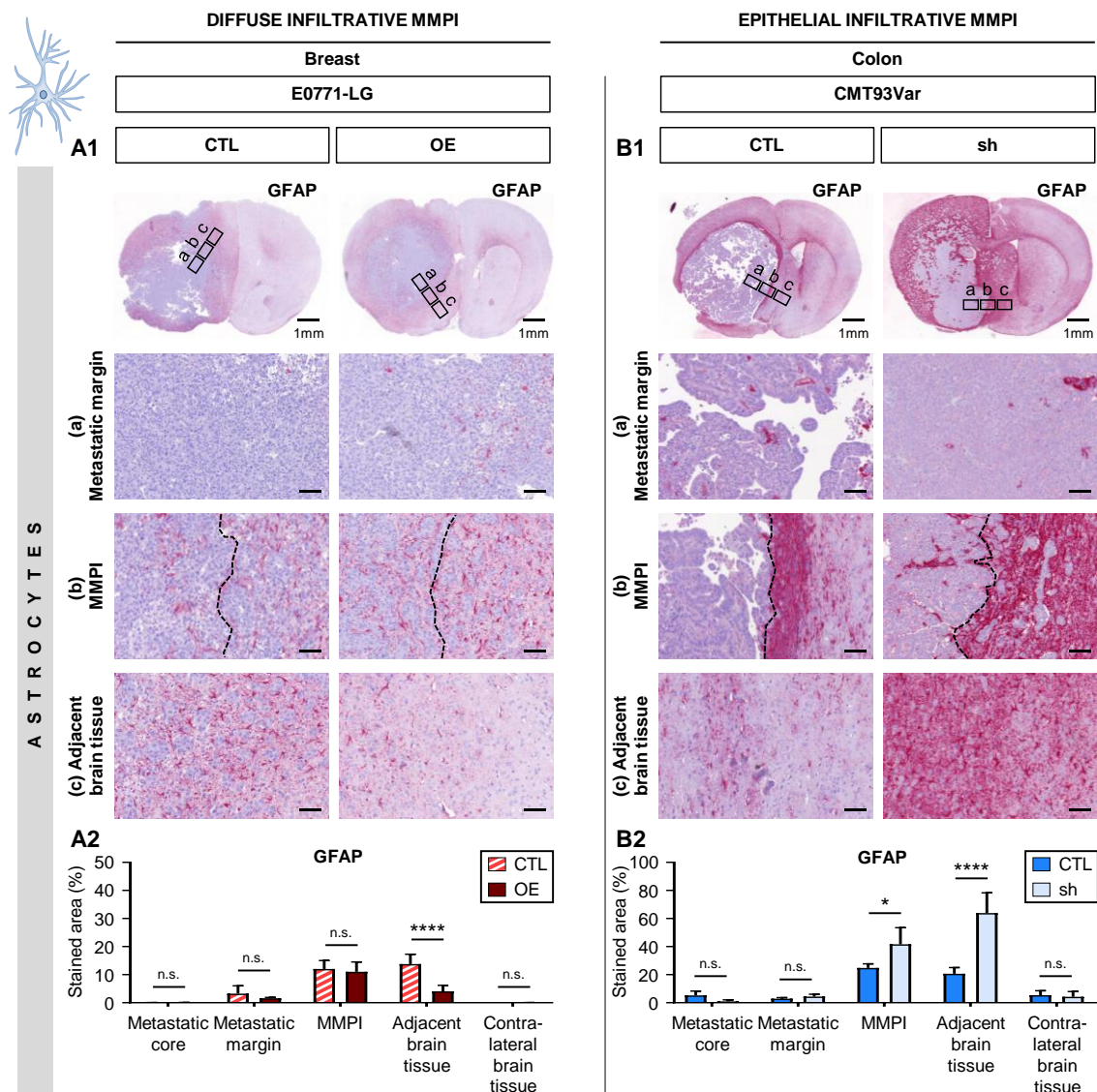


Figure 44: Characterization of astrocytes in the metastatic brain tissue after E-cadherin modifications. IHC staining of activated astrocytes (GFAP) in tissue sections of mice with **(A)** breast cancer brain metastasis of E0771-LG control (CTL) and E-cadherin-overexpression (OE) cells and **(B)** colon cancer brain metastasis of CMT93Var control (CTL) and E-cadherin-knockdown (sh) cells. **(A1+B1)** Representative images of coronal brain sections and images of metastatic margin, MMPI and adjacent brain tissue at higher magnification are shown. The black dotted line indicates the MMPI. Unlabeled scale bars represent 75 μ m. **(A2+B2)** Quantification of GFAP staining is indicated as the percentage of stained area in respective brain region (mean + SD, $n = 3$; two-way ANOVA followed by Sidak's multiple comparisons; * $P < 0.05$, **** $P < 0.0001$, n.s. = not significant).

3.4.4.3. Characterization of T cells in the metastatic brain tissue after E-cadherin modifications

T cells are the main adaptive immune system effector cells and were quantified in IHC stainings for CD3. At first, I had a look at the general distribution of T cells within the brain. Overall, I found infiltrating T cells mainly in the metastatic tissue in all brain colonization models. They were rare in the adjacent brain tissue and completely absent in the contralateral hemisphere representing the situation in the healthy CNS. The latter case was not changed by any of the E-cadherin modifications.

In the diffuse infiltrative models, the number of T cells did not significantly change after overexpression of E-cadherin in any of the metastatic regions. Nevertheless, I noticed a slight decreasing trend in both E0771-LG (breast) (Figure 45 A) and CT26 (colon) (data not shown).

The knockdown of E-cadherin in epithelial infiltrative models also had a negative effect on T cell number in both metastatic regions (metastatic core and margin). I found significantly decreased levels in the knockdown group of 410.4 (breast) ($P = 0.0043$ for metastatic core, $P = 0.0339$ for metastatic margin) (Figure 45 B) and slightly reduced ones in CMT93Var (colon) (data not shown) compared to the respective controls. However, at the MMPI and adjacent brain tissue I found contradictory results for T cell density in breast and colon models. A decrease in 410.4 ($P = 0.048$ at MMPI) compares with an increasing trend in CMT93Var.

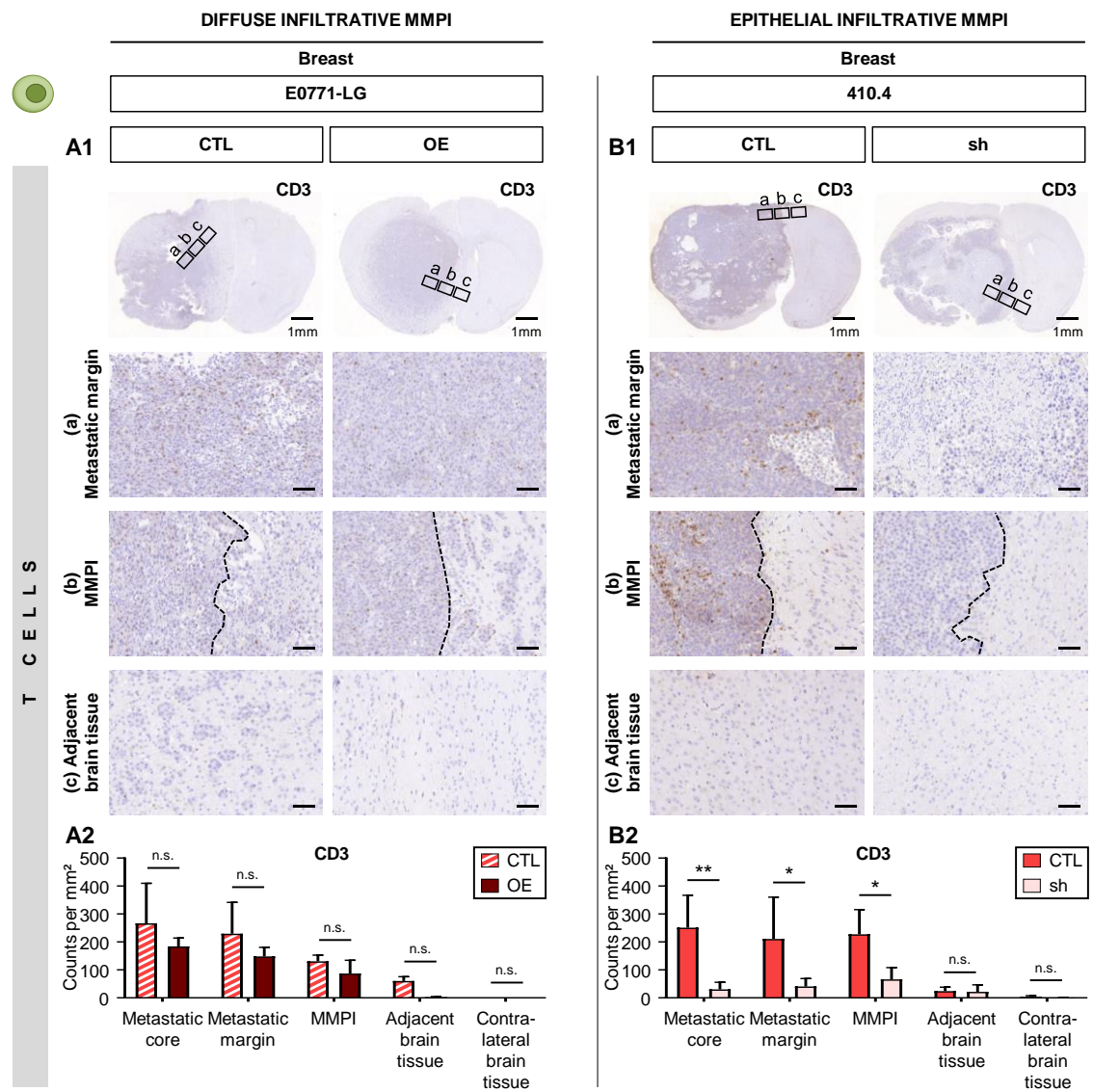

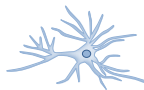



Figure 45: Characterization of T cells in the metastatic brain tissue after E-cadherin modifications. IHC staining of T cells (CD3) in tissue sections of mice with breast cancer brain metastasis of **(A)** E0771-LG control (CTL) and E-cadherin-overexpression (OE) cells and **(B)** 410.4 control (CTL) and E-cadherin-knockdown (sh) cells. **(A1+B1)** Representative images of coronal brain sections and images of metastatic margin, MMPI and adjacent brain tissue at higher magnification are shown. The black dotted line indicates the MMPI. Unlabeled scale bars represent 75 μ m. **(A2+B2)** Quantification of CD3 staining is indicated as counts per mm² in respective brain region (mean + SD, $n = 3$; two-way ANOVA followed by Sidak's multiple comparisons; * $P < 0.05$, ** $P < 0.01$, n.s. = not significant).

3.4.4.4. Overview of changes in the metastatic microenvironment

Across models and entities, the differences in the immune response observed after E-cadherin modifications were most striking in the areas MMPI and adjacent brain tissue. These regions include direct contact between metastatic cells and brain tissue and the MME is thus very reactive there. I summarized both regions in a comparative overview showing the overall changes in the metastatic microenvironment (Figure 46). The reduced infiltration due to E-cadherin overexpression in diffuse infiltrative models led to a decrease of immune reaction, while the increased infiltration after E-cadherin knockdown in epithelial infiltrative models resulted in a stronger immune response.

		Microglia/MΦ		Astrocytes		T cells		
E-cadherin overexpression								
Region	Cell line	IBA1 CTL vs. OE	P	GFAP CTL vs. OE	P	CD3 CTL vs. OE	P	Overall effect ↓
MMPI	Breast [E0771-LG]	–	n.s.	–	n.s.	–	n.s.	
	Colon [CT26]	–	n.s.	+++	*	–	n.s.	
Adjacent brain tissue	Breast [E0771-LG]	--	n.s.	--	****	--	n.s.	
	Colon [CT26]	–	n.s.	+	n.s.	–	n.s.	
E-cadherin knockdown								
Region	Cell line	IBA1 CTL vs. sh	P	GFAP CTL vs. sh	P	CD3 CTL vs. sh	P	Overall effect ↑
MMPI	Breast [410.4]	+	n.s.	+	n.s.	---	*	
	Colon [CMT93Var]	+++	***	+++	*	+	n.s.	
Adjacent brain tissue	Breast [410.4]	++	*	++	n.s.	–	n.s.	
	Colon [CMT93Var]	+++	****	+++	****	++	n.s.	

Figure 46: Overview of changes in the metastatic microenvironment after E-cadherin modifications. Summary of IHC staining quantifications of different immune response components in the metastatic brain tissue of mice after E-cadherin modifications. Results for activated microglia/macrophages (MΦ) (IBA1), activated astrocytes (GFAP) and T cells (CD3) are included. Respective control (CTL) is compared to E-cadherin-overexpression (OE) or E-cadherin-knockdown (sh) group and the difference (increase (+) or decrease (–)) is displayed for selected regions (MMPI and adjacent brain tissue; grey arrow: increase/gain, black arrow: decrease/loss; $n = 3$; two-way ANOVA followed by Sidak's multiple comparisons; * $P < 0.05$, *** $P < 0.001$, **** $P < 0.0001$, n.s. = not significant).

3.4.5. Impact of entity on angiogenesis and metastatic microenvironment

The quantifications of microvessel density and different metastatic microenvironment components across all models revealed additional interesting findings concerning the impact of the entity of the metastatic cells.

The comparison of the control cohorts of the diffuse and epithelial infiltrative models showed an overall effect of entity for the total amount of endothelial cells in the brain slices ($P = 0.0019$) with both breast models showing higher number of vessels compared to their respective colon counterparts (Figure 47 A).

In addition, I found an overall effect of entity concerning the general microglia/macrophage response ($P = 0.0125$) and T cell response ($P = 0.0233$) in the brain slices (Figure 47 B+D). Both breast models showed higher levels of activated microglia/macrophages and higher numbers of T cells compared to their respective colon counterparts. Although the entity had no direct effect on the intensity of the astrocytic reaction (Figure 47 C), it seemed to influence the distribution of activated astrocytes in the metastatic microenvironment. In both colon models, they accumulated around the MMPI in a more encapsulated state compared to their respective breast counterparts (data not shown).

This difference in the immune response between breast and colon cancer models might be interesting for clinical applications.

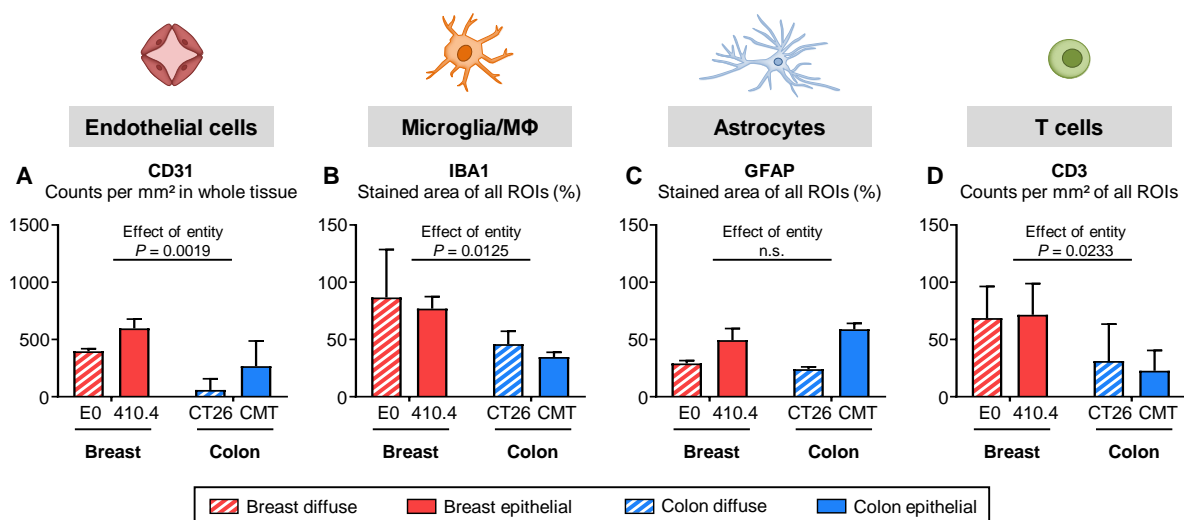


Figure 47: Impact of entity on angiogenesis and metastatic microenvironment. IHC staining quantifications for endothelial cells (CD31), activated microglia/macrophages (MΦ) (IBA1), activated astrocytes (GFAP) and T cells (CD3) in the metastatic brain tissue of mice with breast cancer brain metastasis of diffuse infiltrative E0771-LG (E0) and epithelial infiltrative 410.4 and colon cancer brain metastasis of diffuse infiltrative CT26 and epithelial infiltrative CMT93Var (CMT). CD31 staining is indicated as counts per mm² in whole tissue. Quantification of IBA1 and GFAP staining is indicated as the percentage of stained area and quantification of CD3 staining is indicated as counts per mm² summarized over all analyzed ROIs (mean + SD, $n = 3$; two-way ANOVA, n.s. = not significant).

3.4.6. Summary of *in vivo* characterization results

In summary, the modifications of the cell adhesion receptor E-cadherin did not impair the colonization capacity of the cells but had an enormous impact on MMPI pattern and infiltration grade in murine brain metastases *in vivo*, which in turn resulted in pronounced changes in overall survival rates and immune response (Figure 48). Both approaches resulted in profound morphological changes at the MMPI, with a switch from diffuse infiltrative to more epithelial-like infiltrative pattern in case of E-cadherin upregulation and the other way around in case of downregulation. Consistently, the infiltration grade was decreased after overexpression and increased after knockdown. The altered infiltration was reflected in the survival data with partly prolonged survival of mice after the overexpression of E-cadherin and significantly shortened survival after its knockdown in breast and colon models. In addition, higher levels of E-cadherin and the resulting growth in a more compact way correlated with more angiogenesis in the metastatic tissue. Remarkably, the infiltration grade also directly affected the immune response of the metastatic microenvironment. Higher infiltration rates correlated with an increased immune reaction at the MMPI. Interestingly, the entity of the metastatic cells itself also had an impact on angiogenesis and immune response as higher levels were observed in breast cancer models in both cases. These data demonstrated the different dependencies of diffuse and epithelial infiltrative models on the cell adhesion receptor E-cadherin *in vivo* and further emphasized the concept of different molecular mechanisms supporting both types of breast and colon cancer infiltration.

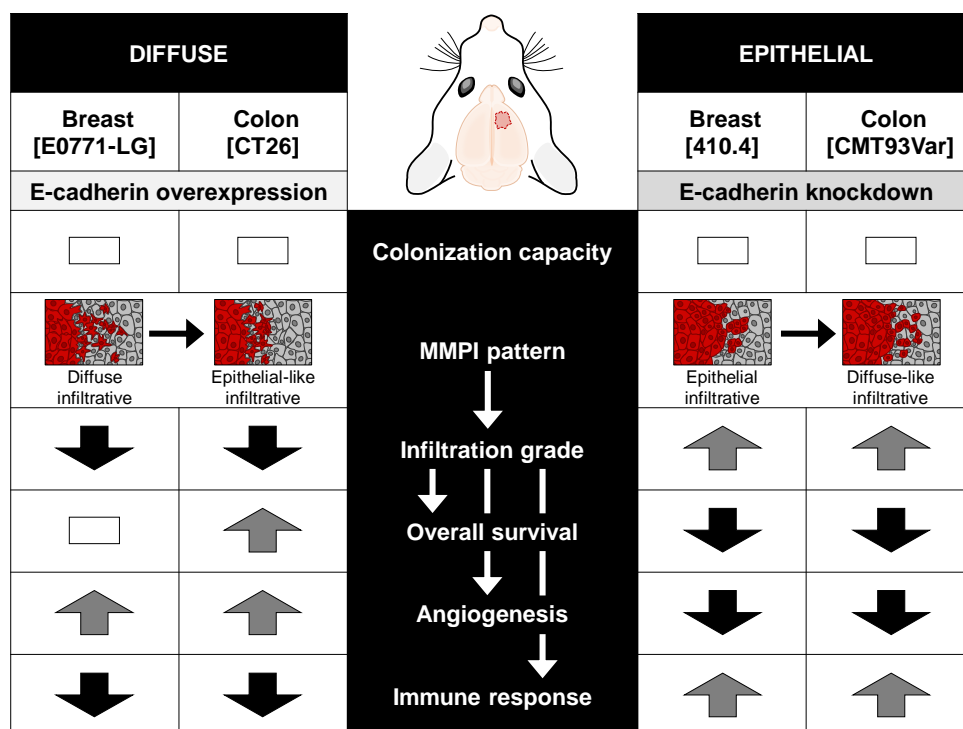


Figure 48: Summary of E-cadherin modification effects in brain metastasis mouse models
(white bar: no change, grey arrow: increase/gain, black arrow: decrease/loss).

3.5. Verification of the prognostic value of the gene expression signature

As demonstrated before, the identified gene expression signature (see 3.2.4) still differentiated diffuse and epithelial-like infiltrative cells with mesenchymal character from epithelial and diffuse-like infiltrative cells with epithelial character independent of E-cadherin modification (see 3.3.2.1). Thus, the last part of this work addressed the question of its prognostic impact *in vivo* across species. The signature was first validated in all different brain metastasis mouse models and afterwards tested in a data set of human metastases.

3.5.1. Validation of gene expression signature in mouse models

First, I validated selected targets of the gene expression signature in all brain metastasis mouse models by quantitative RT-PCR analysis of genes from the previously identified gene clusters in control brains of mice injected only with ECM and brain metastases of mice after E-cadherin modifications of diffuse and epithelial infiltrative breast and colon cancer cell lines. I could confirm that the gene expression profiles reliably separated mice with brain metastases from control mice that were injected only with ECM representing the healthy situation. Furthermore, the signature distinguished metastases formed by diffuse and epithelial-like infiltrative cells with mesenchymal character (E0771-LG and CT26 metastases) from metastases caused by epithelial and diffuse-like infiltrative cells with epithelial character (410.4 and CMT93Var metastases) independent of E-cadherin modifications (Figure 49 A). Two representative genes are shown in detail and demonstrate the exclusive significant upregulation in brain metastasis mouse models of diffuse and epithelial-like infiltrative cells with mesenchymal character or epithelial and diffuse-like infiltrative cells with epithelial character compared to brains of control mice (Figure 49 B). In addition, they once again illustrate that the E-cadherin modifications did not change the expression of other signature components. The prognostic impact of the signature was emphasized by the comparison of survival curves of all mice with brain metastases showing the significantly shorter survival of cohorts with diffuse and epithelial-like infiltrative MMPI pattern and mesenchymal character of metastatic cells (Figure 49 C). Furthermore, there was still a large gap between the most aggressive knockdown cohort (410.4 sh) and the least aggressive overexpression cohort (CT26 OE). Although the overexpression of E-cadherin had prolonged survival and the knockdown had shortened it due to a switch of the infiltration patterns, this effect alone was not sufficient to completely change the aggressiveness of the cells and adapt the overall survival to the opposite state *in vivo*.

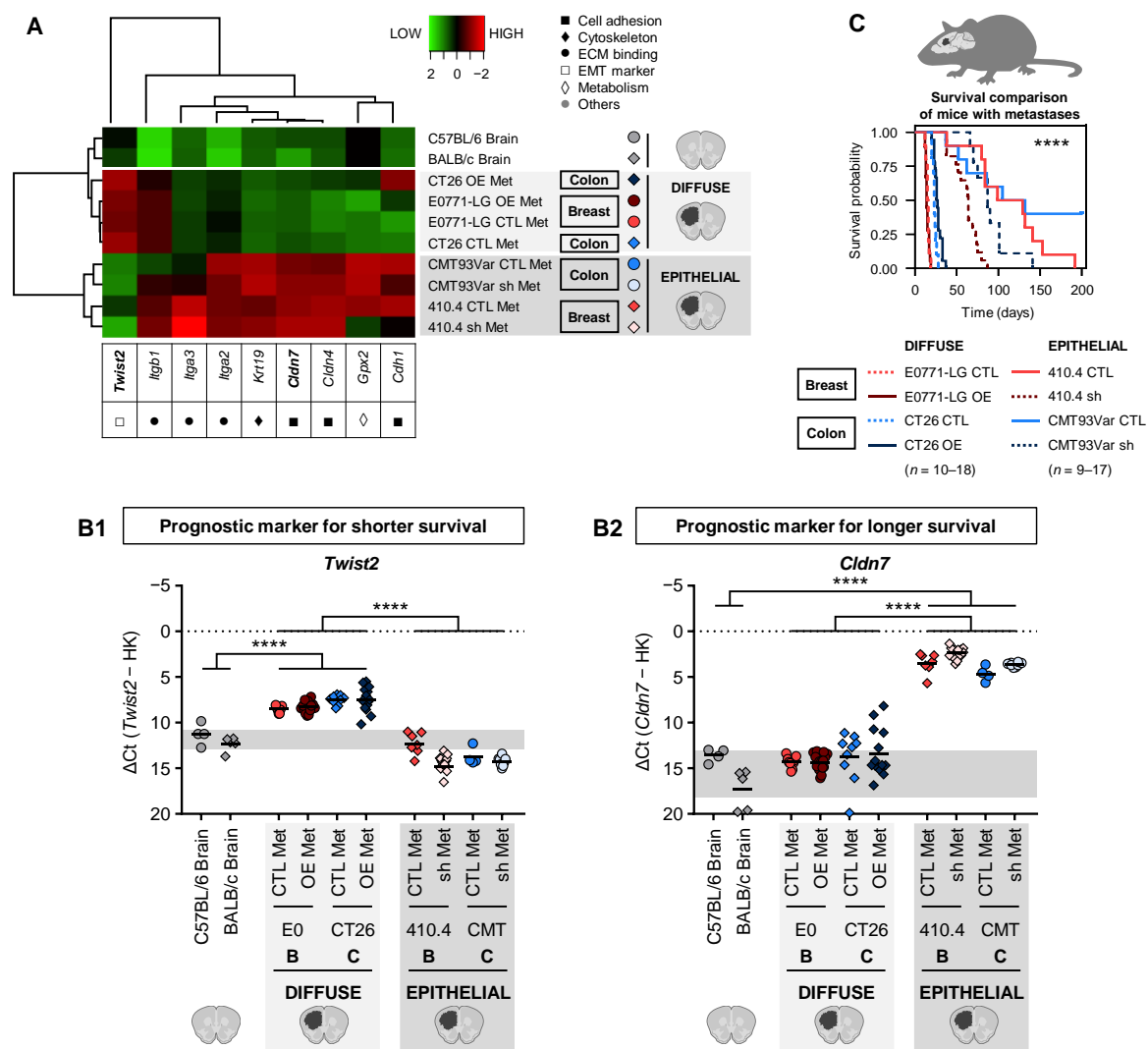


Figure 49: Validation of gene expression signature in brain metastasis mouse models. **(A+B)** Quantitative RT-PCR analysis of selected genes from previously identified gene clusters in brain metastases of mice after E-cadherin modifications of diffuse and epithelial infiltrative breast (B) and colon (C) cancer cell lines (CTL: control, OE: E-cadherin-overexpression, sh: E-cadherin-knockdown) as well as only ECM injected brains of control mice (Brain; C57BL/6 for E0771-LG and CMT93Var, BALB/c for CT26 and 410.4). *Gapdh* and *Pgk1* were used as housekeeping genes (HK). **(A)** Heatmap displaying log₂ transformed z-scores. Unsupervised hierarchical clustering clearly separates diffuse infiltrative brain metastases with mesenchymal character, epithelial infiltrative brain metastases with epithelial character as well as control brains from each other. **(B)** Representative prognostic candidate genes for **(B1)** shorter survival and **(B2)** longer survival (circles: C57BL/6, rhombs: BALB/c; mean and individual values; n ≥ 4; one-way ANOVA followed by Sidak’s multiple comparisons; ****P < 0.0001). **(C)** Kaplan-Meier survival curves of mice injected with diffuse and epithelial infiltrative control and E-cadherin-modified cell lines (n = 9–18; log-rank test; ****P < 0.0001).

3.5.2. Application of gene expression signature on human metastases

In a final step, we had the opportunity to examine the prognostic value of the final gene expression signature (Figure 50 A) in a data set of human metastases in collaboration with the department of medical bioinformatics at the University Medicine Göttingen. This data set contained gene expression values of brain and liver metastases from patients with breast, colorectal or lung cancer. Metastases were assigned to two groups based on their signature score values (HIGH: > median; LOW: ≤ median) and a survival curve was created for the resulting patient cohorts (Figure 50 B). Indeed, the signature also had a prognostic impact in human metastases. Patients with high signature score values (median OS = 26.33 months) demonstrated significantly prolonged survival rates compared to the patient cohort with low values (median OS = 8.58 months, $P = 0.0002$). This gene expression signature could therefore represent an important prognostic tool for clinical practice.

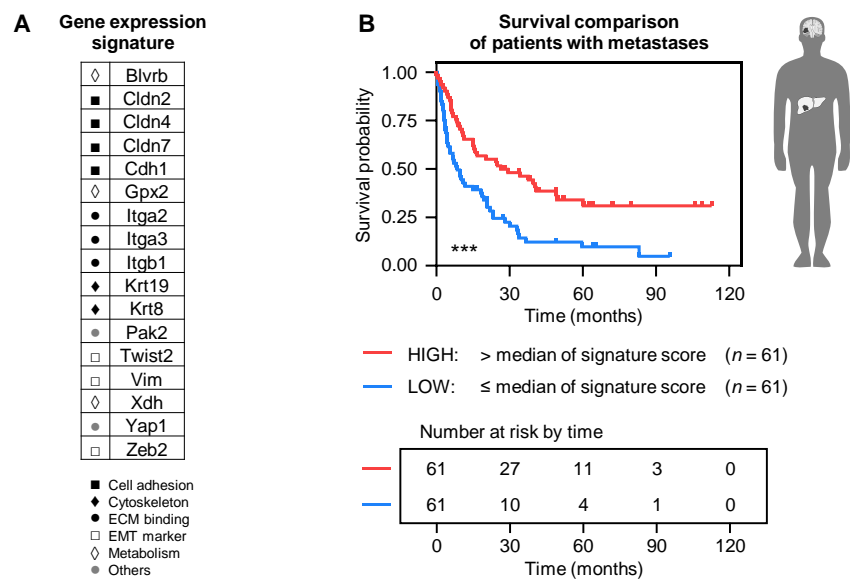


Figure 50: Application of gene expression signature on human metastases. (A) Final gene expression signature including cell adhesion and cytoskeletal components, ECM binding integrins, EMT markers, metabolic genes and others. **(B)** Kaplan-Meier survival curves of patients with brain or liver metastases assigned to cohorts based on their signature score values (high: > median; low: ≤ median; $n = 61$; log-rank test; *** $P < 0.001$).

4. Discussion

Although metastasis of primary tumors is a major clinical problem for cancer patients, research for the underlying mechanisms is still underrepresented in oncological studies. In the frame of this thesis, I aimed to shed more light on the mechanisms underlying metastatic infiltration of tumor cells in the brain parenchyma, especially in context of innate and modified E-cadherin levels, and thus contribute to our understanding of colonization mechanisms in the brain.

4.1. Selection of mouse models for the study of the MMPI in brain metastases

The existence of different MMPI patterns is widely accepted and has been confirmed across entities (Shiono et al., 2005; Siam et al., 2015; van Dam et al., 2017). The fact that the MMPI has a prognostic impact for the patient emphasizes the existence of different underlying mechanisms and a changed pathophysiology. It is necessary to understand these differences on a molecular level to be able to identify potential treatment targets as a prerequisite for the effective development of targeted therapies. As infiltrative MMPIs correlate with worst survival rates, they were the focus of this study. For the detailed study of the MMPI in brain metastases, adequate mouse models are needed that represent the different infiltrative MMPI patterns observed in human brain metastases.

4.1.1. Comparison of murine and human brain metastases

In our lab, we have established a wide variety of murine cancer cell lines in a late brain colonization model, which ensures the reliable and reproducible outgrowth of metastases within short periods. The resulting brain metastasis mouse models cover a wide range of aggressiveness and infiltration level and realistically reflect the diversity observed in oncological diagnostics.

In both human breast cancer brain metastases as well as the resembling murine models, infiltrative growth patterns displayed visible macroscopic metastases and tumor cells that were physically separated from the metastatic border. A closer examination of the MMPI revealed that diffuse infiltrative patterns were characterized by several single tumor cells with mesenchymal morphological features that deeply infiltrated the adjacent tissue, while epithelial infiltration manifested in clusters of tumor cells that collectively infiltrated into the adjacent brain parenchyma as cohorts or clusters with an inner lumen (Blazquez et al., 2020b).

The highly aggressive diffuse infiltrative models E0771-LG and CT26 and the moderate to low aggressive epithelial infiltrative models 410.4 and CMT93Var of breast and colon origin, respectively, were perfectly suited for this study. Nevertheless, one has to keep in mind that the terms high and low aggressive are relative concepts, as all those infiltrative models led to the occurrence of metastases

and the death of the animals within a few months. The usage of different entities should ensure that any identified effects were robust between entities and not a random phenomenon. Findings of this study therefore have a bigger chance to be generally valid for all brain metastases. The selection of breast and colon cancer was motivated by the fact that they are commonly involved in brain metastases and comprise some of the highest risk of brain metastasis formation (Neagu et al., 2015). In future experiments, one could include more risky entities including melanoma or lung cancer cell lines, which we partially already have established in our *in vivo* model.

In previous studies, our group came across interesting observations concerning the expression of E-cadherin, which contradicted the common knowledge of this cell adhesion receptor to be solely regulated by EMT mechanisms. In detail, we noticed an upregulation of E-cadherin at the border of metastatic tissue and adjacent brain parenchyma and even found E-cadherin positive cell clusters within blood vessels in human and murine samples (Blazquez et al., 2020a), although one would not have expected any expression in this location according to the EMT theory. However, EMT is no longer seen as the key reason, but more as a side effect, and the role of E-cadherin is currently undergoing a structural change (Petrova et al., 2016; Romeo et al., 2019). Indeed, E-cadherin has been shown to play an essential role in the metastatic process in recent studies (Bajrami et al., 2018; Gall et al., 2013; Li et al., 2017; Padmanaban et al., 2019; Wong et al., 2018).

Histological stainings of the selected mouse models could confirm the innate level of E-cadherin as one of the key differences between diffuse and epithelial infiltrative MMPI models, as it was the case in human brain metastasis samples. In both cases, human breast cancer brain metastases as well as the resembling murine models, E-cadherin was almost absent in the metastatic tissue of diffuse infiltrative models and highly expressed in epithelial infiltrative counterparts. These observations highlighted the importance of E-cadherin as an interesting candidate for more detailed studies of the underlying mechanisms in context of different infiltrative MMPI patterns.

4.1.2. Characterization of respective murine cancer cell lines

After the selection of suitable mouse models, the next logical step was the detailed *in vitro* characterization of the respective murine cancer cell lines to assess the initial situation and create a basis for subsequent genetic modifications of E-cadherin. Diffuse and epithelial infiltrative cell lines were also compared to identify MMPI pattern- or entity-specific effects.

All cell lines were adherent and easy to cultivate in cell culture. They showed a MMPI pattern-specific morphology that resembled their outgrowth pattern *in vivo*. Diffuse infiltrative E0771-LG breast and CT26 colon cell lines displayed a mesenchymal phenotype with fibroblast-like morphology and mainly remained as single cells even at high confluence levels, while epithelial infiltrative 410.4 breast and

CMT93Var colon cell lines presented a cobblestone-like morphology and pronounced cell-cell contacts. However, since no MMPI pattern-specific differences concerning cell proliferation and survival rates were present, the striking contrast in infiltration grade in brain metastases could not be simply explained based on differences in their proliferative behavior.

Furthermore, all cell lines behaved according to expectations in the broad spectrum of functional assays that have been established and refined in our lab over the years. They showed their characteristic migration behavior and invasive capacity in 2D *in vitro* assays and MMPI pattern-specific differences were clearly visible. Compared to the slower and less aggressive epithelial lines, both diffuse lines migrated faster, were accompanied by a larger number of single spreading cells and had a higher invasive capacity. This represented the situation in the brain metastasis mouse models very well, with the diffuse infiltrative cell lines being more aggressive and displaying a high number of single tumor cells invading into the brain parenchyma. The situation was similar in 3D *in vitro* assays that mimic the formation of micro-metastases and metastatic outgrowth in the brain. Diffuse cell lines formed spheroids with larger outgrowth area and a higher number of colonies compared to epithelial counterparts. The CMT93Var cell line even displayed the lowest colony formation rate and did not form quantifiable spheroids at all. This fact resembled their outgrowth ability and speed in the *in vivo* brain colonization model, where they show the slowest occurrence of brain metastases among all selected models.

Due to the fact that low levels of E-cadherin correlated with higher migration and invasiveness across entities, the specific opposing genetic modification of E-cadherin in the metastatic outgrowth models appeared to be a promising target to switch the pattern of the MMPIs.

4.2. Role of E-cadherin in metastatic brain colonization

Several methods are available for the genetic modification of specific targets. Among other factors, the strategies differ in terms of complexity, practicability, cost, and reproducibility. For this study, the method of lentiviral transduction was used to create stable cell lines either overexpressing or suppressing E-cadherin levels of diffuse and epithelial infiltrative cell lines, respectively. This method is relatively easy to handle and comes with several advantages. For example, there is no need for repeated introduction of genetic material into the cells, as the produced lentiviral vectors integrate into the nucleus of the target cells and can regulate gene expression at the translational level. The resulting overexpression and knockdown cell lines are stable and perfectly suited for long-term studies in culture and in the animal model. Furthermore, this method has a high efficiency and results are reproducible. In order to avoid effects of selection antibiotics on the tumor or other stromal or

immune cells in following *in vivo* experiments, selected constructs did not require inducing treatments and mice received no systemic therapy at any time.

For epithelial cell lines with high innate E-cadherin levels, a knockdown was chosen instead of a complete knockout. The shRNA only reduced the gene expression at the mRNA level instead of completely silencing the gene at the DNA level, as it would have been the case using CRISPR techniques. The knockdown approach better reflects the real biological situation, since mice with a complete knockout of E-cadherin are embryonic lethal (Larue et al., 1994) and those with a conditional knockout fail to survive upon activation (Bondow et al., 2012).

In order to exclude random effects in the following studies, two different modified cell lines with the most pronounced changes in E-cadherin levels and one control were chosen for each parental cell line. Interestingly, the artificially added E-cadherin did not show the typical cellular distribution as expected from the epithelial wild-type situation. It rather accumulated within the cytoplasm and did not appear at regions of cell-cell contacts. The established stable overexpression and knockdown cell lines now enabled the comparative study of the role of E-cadherin levels in metastatic brain colonization.

4.2.1. Impact of E-cadherin modifications in murine cancer cell lines

The first part focused on the direct impact of E-cadherin modifications on the cells *in vitro* since these data can give a first hint on the outcome in the animal model.

As expected, both modifications provoked profound changes in cell morphology. Across entities, the overexpression of E-cadherin clearly switched the diffuse and mesenchymal phenotype with fibroblast-like morphology towards a more epithelial-like phenotype with some cobblestone-like features and increased cell-cell contacts, while the knockdown had the opposite effect. These findings are in accordance with previous observations and the EMT theory. However, besides the morphological changes these modifications did not substantially affect the original cell character. Contrary to the current concept of EMT, the protein levels of other epithelial and mesenchymal markers, including cytokeratin-8 and vimentin, remained stable and did not change in relation to the altered level of E-cadherin. Although diffuse cells acquired a more epithelial-like morphology, they retained their mesenchymal equipment. Moreover, epithelial cells that had switched to a more diffuse-like phenotype still kept their epithelial character and structure. Gene expression studies of a variety of cell adhesion and cytoskeletal components, ECM binding integrins, EMT markers, metabolic genes and other factors reinforced that the modification of E-cadherin only resulted in a morphological EMT phenotype by changing the cell-cell adhesion, but did not change the cellular equipment or metabolism. Interestingly, the level of β -catenin showed a positive correlation to the altered levels of E-cadherin. Instead of its previously postulated predominant role as an intracellular signaling molecule,

its main function in the investigated cells seemed to be the cell adhesion as a binding partner in the α -catenin/ β -catenin/E-cadherin complex.

Since none of the modifications had major effects on cell proliferation or survival rates of the cell lines, proliferation-induced effects of E-cadherin modification on migration and invasion efficacy could be excluded. Across entities, the gain of E-cadherin significantly decreased migration speed and invasive capacity in diffuse cell lines, while the artificial loss of E-cadherin made epithelial lines faster and even more invasive. In other words, there was a negative correlation between the level of E-cadherin and the invasive capacity. As already demonstrated on a morphological basis, lowered levels of E-cadherin resulted in less cell-cell contacts by adherens junctions. Cells were predominantly in a single-mode and could infiltrate farther into the surrounding area. Conversely, increased levels of E-cadherin enabled more cell-cell contacts through adherens junctions. Cells stuck together, preferably grew as a wall connected to each other and infiltrated less far and often as clusters. These results were in accordance with previous experimental *in vitro* studies that could partially suppress the tumorigenicity of cancer cells without detectable E-cadherin expression by the re-expression of this cell adhesion molecule (Navarro et al., 1991).

Furthermore, anchorage-independent growth in soft agar was not significantly affected in any of the diffuse lines with increased E-cadherin levels while they showed significantly reduced outgrowth speed compared to controls in the 3D culture spheroid model. As these assays mimic the formation of micro-metastases and metastatic outgrowth *in vivo*, it pointed to a slowed outgrowth of brain metastases after injection of E-cadherin-overexpressing cells but no impairment of the general colonization ability.

Contrary to expectations from diffuse lines with low E-cadherin expression showing increased spheroid outgrowth, the suppression of E-cadherin in epithelial breast cancer 410.4 disabled their ability to form spheroids in 3D culture models. This observation suggested that they might depend on E-cadherin for efficient micro-metastasis formation and outgrowth and would maybe not be able to settle down in the *in vivo* setting. None of the CMT93Var colon cancer lines was able to recover the ability to form quantifiable spheroids after E-cadherin knockdown, but this was not a surprise, as already the wild-type cell line had shown no spheroid formation ability compared to the other diffuse and epithelial infiltrative cell lines. However, since all knockdown lines were able to form colonies in soft agar assays, we still expected the formation of brain metastases after injection of E-cadherin-knockdown cells.

Taken together, the *in vitro* results emphasized that the impact of E-cadherin on colonization is context-dependent and affirmed the need for further investigations of the *in vivo* situation.

4.2.2. Impact of E-cadherin modifications in brain metastasis mouse models

Indeed, previous *in vitro* data could be directly transferred from cell culture to the situation in the living animal. Intracortical injections of control and modified cell lines into syngeneic mice resulted in brain metastases in all models and revealed interesting findings concerning the impact of E-cadherin level on MMPI pattern and infiltration grade of brain metastases and its correlation with overall survival and the interplay with immune system components of the metastatic microenvironment at the MMPI.

4.2.2.1. Impact of E-cadherin level on infiltration grade at the MMPI

Based on the similar behavior of both modified cell lines in initial experiments, the modified cohorts had been pooled to one group in the following *in vivo* survival analyses. As expected from 3D *in vitro* assays, none of the modifications of E-cadherin had an effect on the general colonization capacity of the cell lines since all models resulted in quantifiable brain metastases after intracortical injections.

However, all genetic modifications resulted in profound morphological changes at the MMPI across entities. The level of E-cadherin directly correlated with the morphology of infiltrating cells that were physically separated from the metastatic border. Along with an increasing level of E-cadherin, the MMPI of diffuse infiltrative E0771-LG and CT26 overexpression lines was dominated by clusters of tumor cells that collectively infiltrated into the adjacent brain parenchyma as cohorts. Nevertheless, they still protruded far into the surrounding brain parenchyma and maintained their generally high infiltrative character. In epithelial infiltrative 410.4 and CMT93Var mouse models, infiltration was more pronounced after knockdown. Decreased levels of E-cadherin resulted in an increased number of single metastatic cells predominantly isolated from each other that invaded much farther into the surrounding tissue compared to the control situation. However, the infiltration depth of most knockdown metastases did not reach the level of the highly infiltrative diffuse models. The modification of E-cadherin thus resulted in a clear switch from diffuse to more epithelial-like infiltrative pattern in case of E-cadherin upregulation and the other way around in case of downregulation.

These morphological changes in the infiltration grade were even quantifiable in a systematic approach by analyzing the extent of infiltrative growth into the brain parenchyma along the MMPI in all brain metastases. Consequently, changes in infiltration grade were directly correlated with altered overall survival rates of mice.

4.2.2.2. Prolonged survival due to reduced infiltration at the MMPI after E-cadherin overexpression

In both diffuse infiltrative models, metastases appeared within short periods from only 2 weeks in E0771-LG to 4 weeks in CT26. This demonstrated their high aggressiveness, especially in comparison with the epithelial infiltrative models, where symptom-free survival ranged from 2 to 4 months.

While the overexpression of E-cadherin significantly prolonged survival of mice in the diffuse infiltrative CT26 colon cancer model, this effect was not observable in the corresponding variant of E0771-LG of breast origin. Taking into account that all metastases developed within 3 weeks in this model, also the modified cell lines were probably still so aggressive that possible differences had no time to become apparent. Another reason could have been the relatively low level of E-cadherin in the overexpression group, which was only detectable by quantitative RT-PCR analysis of the metastatic brain tissue but not visible in IHC stainings. In contrast, E-cadherin overexpression clearly reached higher levels in the CT26 colon model, as confirmed by immunohistological stainings of brain slices. Furthermore, there was more time for differences to become apparent and E-cadherin could thus significantly prolong survival in this model.

Taken together, the reduced infiltration at the MMPI after E-cadherin overexpression resulted in prolonged survival. These results are in accordance with clinical studies reporting lower incidence of metastases in cancer patients with increased E-cadherin expression (Li et al., 2017). With increasing expression of E-cadherin, less cells detach from the primary tumor, enter the circulation and have the potential to form critical metastases.

4.2.2.3. Shortened survival due to increased infiltration at the MMPI after E-cadherin knockdown

Contrary to considerations from 3D *in vitro* assay observations, where 410.4 knockdown cells were not able to form quantifiable spheroids, they were not impaired at all in the real *in vivo* setting in the brain. They even became much more aggressive and showed the most prominent effects of all survival analyses. The knockdown of E-cadherin reduced the symptom-free survival of experimental animals to about one-half of the original timespan in the 410.4 breast cancer model.

For reasons of comparability, the number of injected cells had been equalized to 1000 in all mouse models. As the control line of the CMT93Var colon cancer model did not successfully colonize in all animals, probably an initially higher number of injected cells would have been necessary to result in brain metastases in all animals. As already mentioned earlier, CMT93Var cells have the lowest metastatic potential of all selected model cell lines. At first glance, no significant differences were present between cohorts except for a negative trend in the knockdown group.

Originally, the modified cohorts had been pooled to one group for the analyses due to similar effects in initial experiments. However, in later analyses it became apparent that this procedure was not capable of depicting the actual situation in CMT93Var. The re-analysis of all survival curves in separate groups justified the previous pooling for all models except CMT93Var. Here, substantial differences in overall survival were revealed between the two knockdown cell lines. One of the CMT93Var knockdown lines (sh#1) showed shortened survival and remarkably higher success rates resulting in metastases in all injected animals. In contrast, the second knockdown line (sh#2) even prolonged the survival and was only successful in half of the cases. The increased colonization capacity of sh#1 and the decreased value for sh#2 were also reflected by the previously explained colonization index. Interestingly, the growth pattern of the sh#2 cohort in histological stainings was similar to the control situation and did not resemble the sh#1 knockdown cohort at all. Since the level of E-cadherin was reduced in both knockdown groups to a similar extend, this difference in aggressiveness had to be explained by another factor. We assumed a random variation or deregulation had taken place in the divergent second knockdown line and could indeed identify the mesenchymal marker vimentin to be differentially expressed in the two CMT93Var knockdown cell lines. Prolonged survival rates of mice correlated with decreasing ratios of vimentin and E-cadherin across models and entities and this effect was specific for vimentin across all investigated targets. Since the CMT93Var sh#2 cell line showed reduced levels of vimentin and consequently a decreased vimentin/E-cadherin ratio, this offered an explanation for their prolonged survival rates. The positive correlation between vimentin level and aggressiveness emphasizes that this mesenchymal factor seems to play a crucial role in long-term survival and should be further examined in following studies.

As in all probability an unintended mutation or deregulation had occurred in the second CMT93Var knockdown line, which resulted in reduced levels of the mesenchymal marker vimentin, it was thus not indicative for the assessment of the sole impact of E-cadherin knockdown in the mouse models. Although these animals were thus excluded from further *in vivo* analyses in this thesis, the two different CMT93Var knockdown cell lines represent an interesting model system to further study the interplay of E-cadherin and vimentin.

Taken together, the increased infiltration at the MMPI after E-cadherin knockdown resulted in shortened survival. These findings are in accordance with data from clinical studies that associate functional loss of E-cadherin with poor prognosis and survival (Wong et al., 2018).

4.2.2.4. Correlation of growth pattern and angiogenesis in metastatic tissue

Cancer cells ensure themselves the optimal supply with oxygen and nutrients for further metastatic outgrowth by angiogenesis, the growth of new blood vessels (Hanahan et al., 2000). Tumors rely on this vascularization and can not enlarge beyond 1 to 2 mm in diameter without it probably due to hypoxia-induced apoptosis (Erdogan et al., 2010). Angiotropic growth occurs in both diffuse and epithelial infiltrative MMPI patterns and is characterized by metastatic cells that grow as sheaths around new vessels to protrude even farther into the surrounding parenchyma (Blazquez et al., 2020b). Angiogenesis within the metastatic tissue can be quantified in immunohistochemical stainings using antibodies that are specific for vascular endothelial cells (for example, CD31) and is usually expressed as microvessel density (Sener et al., 2016).

In primary tumors, MVD has been associated with poor outcome and advanced pathologic stage in several types of cancer including breast, lung, and colon as well as malignant melanoma (Sener et al., 2016). As all those types involve major risks for brain metastasis formation, MVD is also likely to be a prognostic factor in brain metastases.

In primary brain tumors, MVD has been proved as a prognostic factor for the grade of astrocytomas, a type of glioma that originates in astrocytes. Astrocytomas can be classified based on their infiltration grade into non-invasive (WHO grade I) with clear outlines on diagnostic images and invasive (WHO grade II–IV) with diffuse zones of infiltration. In several studies, the highest MVD rates were found in the most infiltrative forms (Leon et al., 1996; Mahzouni et al., 2010). However, to our knowledge no one has focused on a direct comparison of angiogenesis rates in different infiltrative MMPI patterns in brain metastases.

Within the brain tissue itself, only few small vessels were present throughout conditions and entities and any observed effects were most evident in the metastatic tissue. Interestingly, the growth pattern had a direct effect on microvessel density since both originally epithelial infiltrative models exhibited higher vessel density in comparison to corresponding diffuse infiltrative models. Metastases of the epithelial type grew in a very compact manner without much space between single metastatic cells and thus required a higher vascularization to avoid hypoxia-induced apoptosis compared to diffuse metastases that grew less dense in a looser manner with larger areas between cells. In accordance, diffuse infiltrative metastases showed a more pronounced angiotropic growth with many vessels in the adjacent brain parenchyma being surrounded by invading metastatic cells.

Consistent with that, the overexpression of E-cadherin, which changed the morphology from diffuse infiltrative to epithelial-like infiltrative, resulted in a higher number of vessels with additionally larger diameter in breast cancer E0771-LG. Furthermore, the knockdown of E-cadherin had the opposite

effect, causing a phenotypic switch from epithelial infiltrative to diffuse-like infiltrative features and accordingly led to a lower number of vessels with even decreased size in breast cancer 410.4. Differences between colon lines showed the same tendencies, but were not as demarcated and did not reach significance. This could be partially explained by the fact that colon models showed lower vessel numbers in general compared to their respective breast counterparts.

Taken together, the altered growth pattern of brain metastases due to the modification of E-cadherin levels had a clear impact on angiogenesis and resulted in a switch from low to high angiogenic-active state in more compact diffuse infiltrative metastases after overexpression and the other way around after knockdown. These results indicate the prognostic value of microvessel density for the metastatic growth pattern and infiltration grade and thus overall survival in infiltrative brain metastases.

4.2.2.5. Impact of infiltration grade on the metastatic microenvironment

The metastatic microenvironment plays an essential role in the metastatic process. Apart from their actual task of defending the organ from potentially harmful intruders, immune cells can also be hijacked by invading cancer cells causing a shift in their behavior (Chuang et al., 2013; Pukrop et al., 2010). As a result, the MME can facilitate initial survival of disseminated cancer cells and promote their further proliferation resulting in even more efficient colonization of the target organ (Fidler, 2011; Quail et al., 2013). It is therefore of particular importance to understand the underlying mechanisms that cause this change of the brain immune system from a defensive into an advertising attitude towards metastatic cells. Previous observations of our group suggested that the MMPI pattern could influence immune infiltration and thus may affect the response to specific therapies. In this case, future therapeutic decisions for cancer patients with brain metastases could depend on prior assessment of the present MMPI pattern. To address this question, a detailed morphological analysis of the present immune response situation in the established mouse models with different infiltrative MMPI patterns before and after modification of E-cadherin levels was carried out.

As described in the introduction, the immune reaction in the brain mainly consists of macrophage response, astrocytic reaction and T cell response. The first region of interest would naturally be the MMPI, as it usually entails the largest contact area for an interaction of metastatic cells and common immune players of the surrounding microenvironment. However, as diffuse infiltrative MMPI patterns are characterized by metastatic cells that infiltrate way farer into the adjacent tissue compared to the epithelial infiltrative type, they thus offer more possible interaction sites. In fact, the distribution of immune response components was altered even within the metastatic and brain tissue across models and therefore analyzed in a region-dependent manner.

Activated microglia, the resident macrophage cells in the brain (Berghoff et al., 2015) were quantified in stainings for IBA1. However, it has been taken into account that IBA1 detects activated microglia (Ito et al., 2001) as well as activated macrophages that immigrated from the blood stream (Ohsawa et al., 2004). It is thus not possible to differentiate between tissue-resident microglia and infiltrating monocyte-derived macrophage populations in the brain tissue with this antibody. Nevertheless, the staining gives a good impression of microglia/macrophage reaction and is well established in our lab. Activated astrocytes, the most abundant glial cells of the CNS, were quantified in stainings for GFAP (Xing et al., 2013) and CD3 was used as a marker for the response of T cells, the main adaptive immune system effector cells (Berghoff et al., 2015).

The general distribution of immune cells within the brain was mainly restricted to the metastatic tissue regions and adjacent brain parenchyma independent of the infiltration pattern at the MMPI. Activated microglia and astrocytes and T cells were almost absent in the contralateral hemispheres which perfectly represented the situation in the healthy brain parenchyma. All three key players were found at the MMPI, but otherwise showed area-specific distributions. T cells mainly operated inside the metastasis, astrocytes predominantly stayed outside in the adjacent brain tissue, and microglia/macrophages were equally active on both sides.

The origin of metastatic cells also seems to play a decisive role. In general, entity-specific differences were present with breast cancer-derived models showing higher levels of microglia/macrophage response and T cell number compared to the milder reactions in colon cancer-derived models. The lower microglia and T cell infiltration in metastatic tissues of colon origin could partially explain the fact that to date checkpoint blockade has only been reported to be effective in patients with breast cancer but not in cohorts with colon cancer. Recent clinical studies showed that therapies with checkpoint inhibitors, which trigger a defense reaction of the immune system against the tumor tissue, were effective in early and advanced triple-negative breast cancer and significantly increased the percentage of patients with a pathological complete response when administered in combination with neoadjuvant chemotherapy (Schmid et al., 2018; Schmid et al., 2020). Future experiments should investigate these differences in MME composition between entities in more detail to reveal the underlying molecular mechanisms and potentially identify promising therapeutic targets.

Furthermore, the pattern of activated astrocytes in breast cancer-derived models was distributed over a wider area compared to the characteristic dense accumulation around the MMPI in colon entities. A detailed look at the growth pattern might explain this observation. Colon-derived cancer cells generally infiltrate in a more encapsulated state and thus may allow immune cells to form something like a shield by accumulating predominantly at the MMPI.

According to our theory, a difference in immune infiltration, or in other words the presence of immune cells in the metastasis, between control and modified diffuse and epithelial infiltrative MMPI models was to be expected. Indeed, this could be especially observed for activated microglia/macrophages and T cells. When metastatic cells grew less compact, as it was the case in diffuse infiltrative models or formerly epithelial infiltrative models after knockdown of E-cadherin, more immune cells could enter the metastatic region by passing the MMPI barrier and fight against the foreign intruders inside the metastatic lesion. Due to the loss of E-cadherin, those formerly epithelial infiltrative metastatic cells also adapted their tissue-destructive mechanism to the situation present in diffuse infiltrative metastases and expanded the infiltration zone over a larger area. Subsequently, the immune reaction of the MME was increased and showed an altered distribution pattern. In epithelial infiltrative models or formerly diffuse infiltrative models after overexpression of E-cadherin, a barrier was formed and provided a defined area for immune cells to attack. Consequently, they could not easily cross the barrier and were thus found only in smaller quantities inside the metastasis, while the majority accumulated outside in the surrounding parenchyma and predominantly at the MMPI. The switch from a diffuse infiltrative to a more compact epithelial-like infiltrative MMPI pattern due to the E-cadherin overexpression thus seemed to force an immune exclusion phenotype of the metastatic cells because of the newly forming epithelial barrier.

Furthermore, astrocytes and microglia, which represent the first line of defense in the MME in the brain, seemed to effectively shield compact epithelial infiltrative metastases from healthy brain parenchyma. In widely spread diffuse infiltrative metastases and less compact growing diffuse-like epithelial infiltrative ones due to the loss of E-cadherin, this demarcated shielding was not possible as immune cells had to spread over a larger area in the brain tissue to fight all infiltrating single metastatic cells. Such a shielding mechanism, characterized by activated microglia and astrocytes that form a cellular barrier at the MMPI to encapsulate the metastatic cells and thus potentially prevent inflammation and induce a local immune suppression, was also previously observed in our lab. It was present in different model systems, ranging from *ex vivo* organotypic brain slice cocultures to *in vivo* mouse models for late brain colonization and also found in samples of human brain metastases (Blazquez et al., 2018; Chuang et al., 2013; Pukrop et al., 2010).

Taken together, these findings reinforce the importance of the MMPI pattern for the composition of the metastatic microenvironment and the immune infiltrate. A switch of the infiltration pattern, as it was caused by modifications of the cell adhesion receptor E-cadherin, results in an altered reaction of the surrounding tissue and has an enormous impact on the metastatic microenvironment and organ defense. Further studies should focus on the underlying molecular mechanisms of these shielding immune cells to investigate their therapeutic potential for a targeted prevention or inhibition of metastatic colonization in the brain.

4.2.3. Contact inhibition as potential therapeutic target mechanism

The metastatic growth pattern not only correlates with the overall prognosis for the patient, but also seems to influence the efficacy of therapeutic concepts (Kienast et al., 2010). As a consequence, a therapy should be chosen according to the present MMPI pattern. Massague and colleagues have already demonstrated that YAP-TAZ signaling is essential for colonization (Er et al., 2018). For many of their experiments they used brain metastatic cancer cell lines of the diffuse infiltrative type. It thus has to be clarified if this only accounts for diffuse infiltrative models or also for epithelial infiltrative ones.

The general assessment of the situation in wild-type cell lines could identify contact inhibition as a further mechanism that clearly differed between diffuse and epithelial MMPI model cell lines. These observations reinforced the theory of different molecular mechanisms supporting both types of breast and colon cancer infiltration. On the one hand, the epithelial infiltrating 410.4 and CMT93Var cells retained the expression of E-cadherin and showed intact contact inhibition. On the other hand, the diffuse infiltrating E0771-LG and CT26 lost the expression of this adhesion molecule and seemed to have no functional contact inhibition.

Since the E-cadherin receptor in the cell membrane is a key player in contact inhibition of proliferation, we were interested whether any of the E-cadherin modifications had an influence on the basic situation. Contrary to expectations, the overexpression of E-cadherin could not restore contact inhibition in diffuse cell lines that continued to show a tonic YAP signaling. Taking into account that the artificial expression of E-cadherin did not lead to the accumulation and localization of this adhesion protein at the cell membranes, this non-existing effect might be partially explained. If the increased E-cadherin level is not present at the membranes, it can not contribute to contact inhibition of proliferation via adherens junctions as described in the introduction. In contrast, the knockdown of E-cadherin clearly led to a loss of contact inhibition. The cells had lost most of their E-cadherin expression and the remaining protein was mainly localized in the cytoplasm and not at the membranes any more. This emphasized that epithelial infiltrative cells strongly depend on E-cadherin levels for maintenance of functional contact inhibition.

Hence, this mechanism might be a feasible target for treatment of brain metastases. The blockade of contact inhibition can be achieved by the inhibition of the Hippo pathway and YAP inhibitors are one promising therapeutic target currently under investigation. Preliminary *in vitro* experiments in our lab showed that diffuse infiltrative cell lines without functional contact inhibition but tonic YAP signaling seem to be more sensitive to treatment with YAP inhibitors compared to epithelial infiltrative cell lines. This now has to be studied in detail in future experiments. First in various *in vitro* and *ex vivo* assays, and later *in vivo* in our brain metastasis mouse models. According to our theory, the epithelial infiltrative cell lines, which have intact contact inhibition and upregulate YAP during colonization, are

not accessible for a YAP therapy as soon as they have reached the status of micro-metastases, because the concentrations needed for a visible effect would be excessively high. In contrast, the diffuse infiltrative cell lines, which show a constant YAP signaling independent of cell-cell contacts, could offer an excellent target for an anti-YAP therapy. A further option would be that both MMPI types are vulnerable through YAP inhibition during early colonization. In this case, YAP inhibition would represent a general therapy option for infiltrative metastases.

4.3. Prognostic value of established gene expression signature

With all of these profound differences between diffuse and epithelial infiltrative MMPI models in mind, one should expect that the metastatic growth pattern influences the expression of certain genes. Since the MMPI pattern has been shown to correlate with survival rates in humans and mice, it was an additional aim of this thesis to find gene targets that could represent a prognostic tool to classify the outcome of patients with metastases based on the analysis of their tumor gene expression signature.

Based on previous proteomics analyses and microarray data of different mouse cancer cell lines in our lab, we selected a set of interesting candidate genes with the most pronounced differences. Initially, their expression levels were assessed in RNA samples collected from all parental murine brain metastasis model cell lines in a qRT-PCR screening and indeed several differentially expressed genes could be identified. Hierarchical clustering of these data in a heatmap resulted in one cluster of genes that were exclusively highly expressed in diffuse cells and a second cluster with high expression only in epithelial cells. This gene signature included a variety of cell adhesion and cytoskeletal components, ECM binding integrins, EMT markers, metabolic genes, and other factors. Therefore, it was a surprise that the E-cadherin modifications did not alter this gene expression signature to any substantial extent. Contrary to the current concept of EMT, the loss of E-cadherin did not switch the epithelial character of the cells into a mesenchymal state and had no influence on their metabolism. Consistently, mesenchymal cells maintained their cellular equipment and did not acquire epithelial characteristics even after the artificial overexpression of this cell adhesion receptor. Although the altered level of E-cadherin was clearly visible in the heatmap, it was not reflected in the rest of the signature and the previously identified clusters were still present.

Hence, this gene expression signature seemed to be not only determined by the infiltrative growth pattern but also by the original character of the cells, which did not change after the modification of E-cadherin in contrast to the phenotype. It rather differentiated diffuse and epithelial-like infiltrative cells with mesenchymal character from epithelial and diffuse-like infiltrative cells with epithelial character. Since cells of the first group were generally more aggressive compared to the second group in our animal experiments, we assumed that the signature could also have a prognostic impact *in vivo*.

Selected targets from the previously identified gene clusters were tested in brains with metastases arising from the different diffuse and epithelial infiltrative models as well as control brains. Indeed, the gene expression profile reliably separated mice with pathological conditions from healthy animals. Furthermore, it distinguished metastases associated with short survival rates from metastases with significantly increased survival of the animals and thus clearly had a prognostic impact on overall survival in our brain metastasis mouse models.

Finally, the signature was tested in a data set of human brain and liver metastases from patients with breast, colorectal or lung cancer in collaboration with the department of medical bioinformatics at the University Medicine Göttingen. Again, it could demonstrate its prognostic impact since it reliably splitted the patient cohort into two groups with significantly different survival rates. It might thus really represent a potential diagnostic tool for clinical practice in the future and strongly requires follow-up studies in larger patient cohorts.

4.4. Future research perspectives

In addition to possible future experiments resulting directly from previous findings described above, the following approaches could be of particular interest in the future.

As explained earlier, the profound survival differences between the two E-cadherin knockdown models of CMT93Var seemed to be caused by an unintended mutation or deregulation of the innate vimentin expression. The positive correlation between vimentin level and aggressiveness suggests that this mesenchymal factor might also play a crucial role in long-term survival. Although the affected animals bearing the vimentin variation were excluded from further *in vivo* analyses in this thesis, the two different CMT93Var knockdown cell lines represent an interesting model system to further study the interplay of E-cadherin and vimentin. A detailed comparison of both knockdown cell lines on RNA level by RNA-sequencing methods could potentially identify further candidates responsible for their different survival rates. Subsequent experiments could involve the targeted genetic modification of innate vimentin levels and investigate if an intentional downregulation of this mesenchymal marker also results in prolonged survival.

The promising results concerning a prognostic impact of the MMPI pattern in the experiments described in this study emphasize the further investigation of this concept. Future animal experiments could test if it is possible to recognize known MMPI patterns in mice after tumor cell injection using small animal magnetic resonance imaging (MRI), a non-invasive imaging technique commonly used in radiology. In the future, an early recognition of MMPI pattern via MRI could help to visualize and predict patient survival and choose adequate therapy concepts without the need for an invasive surgical procedure.

5. Summary and Conclusions

The prognostic impact of the metastatic infiltration pattern in brain metastases makes the MMPI an interesting and promising area of oncologic research. This study was designed to contribute to our understanding of colonization processes of tumor cells in the brain and shed more light on the mechanisms underlying metastatic infiltration in different MMPI patterns to potentially support the development of targeted therapies in the future.

The variety of brain metastasis mouse models in our lab enabled the detailed morphological and molecular characterization of different infiltrative MMPI patterns. Since they cover a wide range of aggressiveness and infiltration level, they realistically reflected the diversity observed in oncological diagnostics. In both species, human and mouse, one of the key differences between diffuse and epithelial infiltrative MMPI models was their innate level of E-cadherin. Since low levels of E-cadherin were associated with higher migration and invasiveness across entities, this cell adhesion receptor seemed to be not only a marker for the infiltration type, but was also a promising factor to play an important functional role in the metastatic process. The specific genetic modification of E-cadherin in the metastatic outgrowth models thus appeared to be a suitable target to switch the MMPI pattern of breast and colon cancer cells in the brain and study the outcome on the metastatic microenvironment.

Indeed, the amount of E-cadherin directly affected the morphology of the cells. Artificially increased levels caused a phenotypic switch from a diffuse and mesenchymal-like to epithelial-like morphology with more cell contacts, while the loss of this cell adhesion receptor caused cells to adapt mesenchymal-like features. However, only the morphology was affected while the cells maintained their original mesenchymal or epithelial character. Nevertheless, the altered cell adhesion alone was sufficient to change the migratory and invasive capacity of the cell lines *in vitro*.

In the animal model, both genetic approaches resulted in profound phenotypic changes at the MMPI. Diffuse infiltrative models switched to more epithelial-like infiltrative characteristics after the gain of E-cadherin and displayed less infiltration into the adjacent brain parenchyma. In accordance, its loss in epithelial infiltrative models resulted in increased infiltration rates and the cells even gained diffuse-like infiltrative features at the MMPI. In both cases, the switch of the original infiltration pattern had a direct impact on the overall survival of animals. However, this effect alone was not sufficient to completely change the aggressiveness of the cells into the opposite state. Animals with a mesenchymal character of metastatic cells displayed a generally shorter survival and a large gap was still present in relation to the most aggressive knockdown cohort. Although those metastatic cells with epithelial cellular equipment acquired an additional destructive character due to the altered infiltration pattern, they did not gain the special defense mechanisms and metabolic plasticity that are characteristic for the highly aggressive diffuse infiltrative models with mesenchymal character.

The altered infiltration pattern in turn had an enormous impact on the immune cell composition and reaction of the metastatic microenvironment. In compact growing epithelial infiltrative metastases, activated astrocytes and microglia formed a barrier to shield the metastatic cells from the surrounding healthy brain parenchyma and prevent further damage. In addition, the general immune response was lower compared to diffuse infiltrative models. The loss of E-cadherin resulted in a looser metastatic outgrowth that broadened the infiltration zone and impaired such a demarcated shielding mechanism. Consequently, immune cells had to spread over a larger area to fight the infiltrating metastatic cells and the immune reaction was notably increased. Due to the work with metastatic cells from breast and colon origin, entity-specific differences in the immune cell composition and reaction at the MME became apparent, which might explain the (non-) response to checkpoint blockade in clinical studies. In addition, there was a positive correlation between compact metastatic outgrowth and angiogenesis. The number of blood vessels in metastatic tissues might thus represent a further potential prognostic factor for the anticipated metastatic outgrowth and associated prognosis.

Furthermore, we established a characteristic gene expression signature that seemed to be determined by the infiltrative growth pattern and the original character of the metastatic cells. It clearly separated highly aggressive metastases with mesenchymal character from cohorts with epithelial characteristics and prolonged survival in our animal models and even demonstrated its prognostic impact in a data set of human metastases. Such prognostic gene targets could represent an important diagnostic tool in clinical practice to classify the outcome of patients with metastases based on the analysis of their tumor gene expression signature. In summary, the findings of this study might contribute to MMPI pattern-based therapeutic decisions for cancer patients with brain metastases in the future.

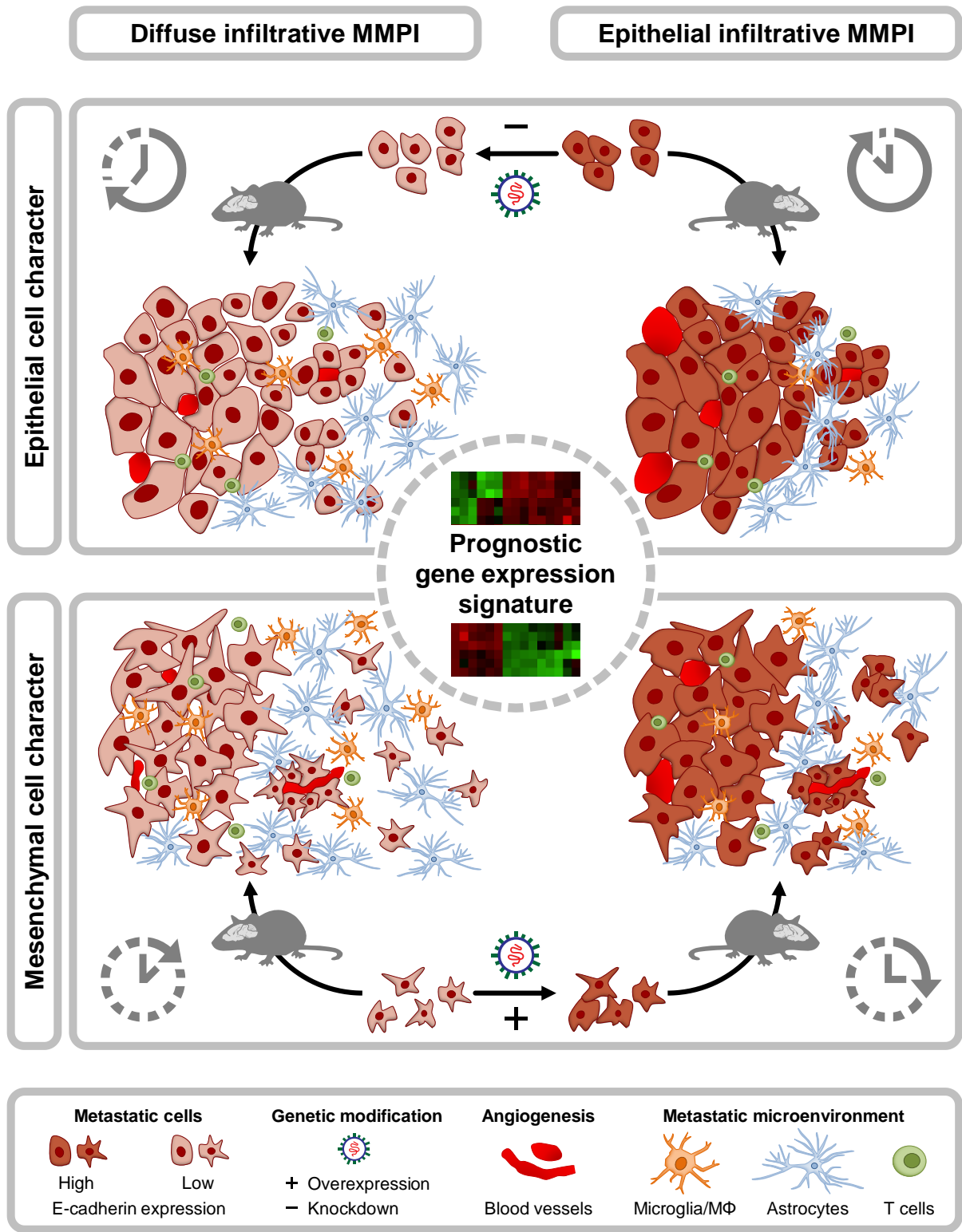


Figure 51: Schematic model of the role of E-cadherin in metastatic brain colonization.

6. Bibliography

- Bajrami, I., Marlow, R., van de Ven, M., Brough, R., Pemberton, H. N., Frankum, J., . . . Lord, C. J. (2018). E-Cadherin/ROS1 Inhibitor Synthetic Lethality in Breast Cancer. *Cancer Discov*, 8(4), 498-515. doi:10.1158/2159-8290.CD-17-0603
- Berghoff, A. S., & Preusser, M. (2015). The inflammatory microenvironment in brain metastases: potential treatment target? *Chin Clin Oncol*, 4(2), 21. doi:10.3978/j.issn.2304-3865.2015.06.03
- Blazquez, R., Rietkotter, E., Wenske, B., Wlochowicz, D., Sparrer, D., Vollmer, E., . . . Pukrop, T. (2020a). LEF1 supports metastatic brain colonization by regulating glutathione metabolism and increasing ROS resistance in breast cancer. *Int J Cancer*, 146(11), 3170-3183. doi:10.1002/ijc.32742
- Blazquez, R., Sparrer, D., Wendl, C., Evert, M., Riemenschneider, M. J., Krahn, M. P., . . . Pukrop, T. (2020b). The macro-metastasis/organ parenchyma interface (MMPI) - A hitherto unnoticed area. *Semin Cancer Biol*, 60, 324-333. doi:10.1016/j.semcancer.2019.10.012
- Blazquez, R., Wlochowicz, D., Wolff, A., Seitz, S., Wachter, A., Perera-Bel, J., . . . Pukrop, T. (2018). PI3K: A master regulator of brain metastasis-promoting macrophages/microglia. *Glia*, 66(11), 2438-2455. doi:10.1002/glia.23485
- Bondow, B. J., Faber, M. L., Wojta, K. J., Walker, E. M., & Battle, M. A. (2012). E-cadherin is required for intestinal morphogenesis in the mouse. *Dev Biol*, 371(1), 1-12. doi:10.1016/j.ydbio.2012.06.005
- Brattain, M. G., Strobel-Stevens, J., Fine, D., Webb, M., & Sarraf, A. M. (1980). Establishment of Mouse Colonie Carcinoma Cell Lines with Different Metastatic Properties. *Cancer Research*, 40, 2142-2146.
- Cardiff, R. D., Miller, C. H., & Munn, R. J. (2014). Manual hematoxylin and eosin staining of mouse tissue sections. *Cold Spring Harb Protoc*, 2014(6), 655-658. doi:10.1101/pdb.prot073411
- Chamberlain, M. C., Baik, C. S., Gadi, V. K., Bhatia, S., & Chow, L. Q. (2017). Systemic therapy of brain metastases: non-small cell lung cancer, breast cancer, and melanoma. *Neuro Oncol*, 19(1), i1-i24. doi:10.1093/neuonc/now197
- Chuang, H. N., van Rossum, D., Sieger, D., Siam, L., Klemm, F., Bleckmann, A., . . . Pukrop, T. (2013). Carcinoma cells misuse the host tissue damage response to invade the brain. *Glia*, 61(8), 1331-1346. doi:10.1002/glia.22518
- Dong, J., Feldmann, G., Huang, J., Wu, S., Zhang, N., Comerford, S. A., . . . Pan, D. (2007). Elucidation of a universal size-control mechanism in Drosophila and mammals. *Cell*, 130(6), 1120-1133. doi:10.1016/j.cell.2007.07.019
- Doron, H., Pukrop, T., & Erez, N. (2019). A Blazing Landscape: Neuroinflammation Shapes Brain Metastasis. *Cancer Res*, 79(3), 423-436. doi:10.1158/0008-5472.CAN-18-1805
- Er, E. E., Valiente, M., Ganesh, K., Zou, Y., Agrawal, S., Hu, J., . . . Massague, J. (2018). Pericyte-like spreading by disseminated cancer cells activates YAP and MRTF for metastatic colonization. *Nat Cell Biol*, 20(8), 966-978. doi:10.1038/s41556-018-0138-8

- Erdogan, N., Dengizmen, A., Igdem, A. A., Sahan, E., & Tetikkurt, U. S. (2010). Angiogenesis in breast cancers without lymph node metastasis. *Turkish Journal of Pathology*, 26(2). doi:10.5146/tjpath.2010.01010
- Esheba, G. E., Hassan, A. A., El Bostany, M. Z., & Aly, M. H. (2017). Prognostic value of cancer stem cell markers and E-cadherin expression in non-small-cell lung cancer. *Egyptian Journal of Pathology*, 37(2), 281-288.
- Fidler, I. J. (1970). Metastasis: Quantitative Analysis of Distribution and Fate of Tumor Emboli Labeled With ¹²⁵I-5-Iodo-2'-deoxyuridine. *JNCI: Journal of the National Cancer Institute*, 45(4), 773-782. doi:10.1093/jnci/45.4.773
- Fidler, I. J. (2011). The role of the organ microenvironment in brain metastasis. *Semin Cancer Biol*, 21(2), 107-112. doi:10.1016/j.semcancer.2010.12.009
- Fonseca, G. M., de Mello, E. S., Faraj, S. F., Kruger, J. A. P., Coelho, F. F., Jeismann, V. B., . . . Herman, P. (2018). Prognostic significance of poorly differentiated clusters and tumor budding in colorectal liver metastases. *J Surg Oncol*, 117(7), 1364-1375. doi:10.1002/jso.25017
- Forestell, S. P., Dando, J. S., Bohnlein, E., & Rigg, R. J. (1996). Improved detection of replication-competent retrovirus. *J Virol Methods*, 60(2), 171-178. doi:10.1016/0166-0934(96)02052-6
- Franks, L. M., & Hemmings, V. J. (1978). A cell line from an induced carcinoma of mouse rectum. *J Pathol*, 124(1), 35-38. doi:10.1002/path.1711240108
- Gall, T. M., & Frampton, A. E. (2013). Gene of the month: E-cadherin (CDH1). *J Clin Pathol*, 66(11), 928-932. doi:10.1136/jclinpath-2013-201768
- Graham, F. L., Smiley, J., Russell, W. C., & Nairn, R. (1977). Characteristics of a human cell line transformed by DNA from human adenovirus type 5. *J Gen Virol*, 36(1), 59-74. doi:10.1099/0022-1317-36-1-59
- Gumbiner, B. M., & Kim, N. G. (2014). The Hippo-YAP signaling pathway and contact inhibition of growth. *J Cell Sci*, 127(Pt 4), 709-717. doi:10.1242/jcs.140103
- Hanahan, D., & Weinberg, R. A. (2000). The hallmarks of cancer. *Cell*, 100(1), 57-70. doi:10.1016/s0092-8674(00)81683-9
- Hanahan, D., & Weinberg, R. A. (2011). Hallmarks of cancer: the next generation. *Cell*, 144(5), 646-674. doi:10.1016/j.cell.2011.02.013
- Hosseini, H., Obradovic, M. M. S., Hoffmann, M., Harper, K. L., Sosa, M. S., Werner-Klein, M., . . . Klein, C. A. (2016). Early dissemination seeds metastasis in breast cancer. *Nature*, 540(7634), 552-558. doi:10.1038/nature20785
- Ito, D., Tanaka, K., Suzuki, S., Dembo, T., & Fukuuchi, Y. (2001). Enhanced expression of Iba1, ionized calcium-binding adapter molecule 1, after transient focal cerebral ischemia in rat brain. *Stroke*, 32(5), 1208-1215. doi:10.1161/01.str.32.5.1208
- Kienast, Y., von Baumgarten, L., Fuhrmann, M., Klinkert, W. E., Goldbrunner, R., Herms, J., & Winkler, F. (2010). Real-time imaging reveals the single steps of brain metastasis formation. *Nat Med*, 16(1), 116-122. doi:10.1038/nm.2072

- Kim, N. G., Koh, E., Chen, X., & Gumbiner, B. M. (2011). E-cadherin mediates contact inhibition of proliferation through Hippo signaling-pathway components. *Proc Natl Acad Sci U S A*, 108(29), 11930-11935. doi:10.1073/pnas.1103345108
- Kitamura, T., Kato, Y., Brownlie, D., Soong, D. Y. H., Sugano, G., Kippen, N., . . . Pollard, J. W. (2019). Mammary Tumor Cells with High Metastatic Potential Are Hypersensitive to Macrophage-Derived HGF. *Cancer Immunol Res*, 7(12), 2052-2064. doi:10.1158/2326-6066.CIR-19-0234
- Klemm, F., Bleckmann, A., Siam, L., Chuang, H. N., Rietkotter, E., Behme, D., . . . Pukrop, T. (2011). beta-catenin-independent WNT signaling in basal-like breast cancer and brain metastasis. *Carcinogenesis*, 32(3), 434-442. doi:10.1093/carcin/bgq269
- Laemmli, U. K. (1970). Cleavage of structural proteins during the assembly of the head of bacteriophage T4. *Nature*, 227(5259), 680-685. doi:10.1038/227680a0
- Larue, L., Ohsugi, M., Hirchenhain, J., & Kemler, R. (1994). E-cadherin null mutant embryos fail to form a trophectoderm epithelium. *Proc Natl Acad Sci U S A*, 91(17), 8263-8267. doi:10.1073/pnas.91.17.8263
- Latacz, E., Caspani, E., Barnhill, R., Lugassy, C., Verhoef, C., Grunhagen, D., . . . Vermeulen, P. B. (2020). Pathological features of vessel co-option versus sprouting angiogenesis. *Angiogenesis*, 23(1), 43-54. doi:10.1007/s10456-019-09690-0
- Leon, S. P., Folkerth, R. D., & Black, P. M. (1996). Microvessel density is a prognostic indicator for patients with astroglial brain tumors. *Cancer*, 77(2), 362-372. doi:10.1002/(Sici)1097-0142(19960115)77:2<362::Aid-Cncr20>3.0.Co;2-Z
- Li, Z., Yin, S., Zhang, L., Liu, W., & Chen, B. (2017). Prognostic value of reduced E-cadherin expression in breast cancer: a meta-analysis. *Oncotarget*, 8(10), 16445-16455. doi:10.18632/oncotarget.14860
- Lowry, O. H., Rosebrough, N. J., Farr, A. L., & Randall, R. J. (1951). Protein measurement with the Folin phenol reagent. *J Biol Chem*, 193(1), 265-275.
- Mahzouni, P., Mohammadizadeh, F., Mougouei, K., Moghaddam, N. A., Chehrei, A., & Mesbah, A. (2010). Determining the relationship between "microvessel density" and different grades of astrocytoma based on immunohistochemistry for "factor VIII-related antigen" (von Willebrand factor) expression in tumor microvessels. *Indian J Pathol Microbiol*, 53(4), 605-610. doi:10.4103/0377-4929.71996
- Marshall, O. J. (2004). PerlPrimer: cross-platform, graphical primer design for standard, bisulphite and real-time PCR. *Bioinformatics*, 20(15), 2471-2472. doi:10.1093/bioinformatics/bth254
- Mendonsa, A. M., Na, T. Y., & Gumbiner, B. M. (2018). E-cadherin in contact inhibition and cancer. *Oncogene*, 37(35), 4769-4780. doi:10.1038/s41388-018-0304-2
- Miller, F. R., Miller, B. E., & Heppner, G. H. (1983). Characterization of Metastatic Heterogeneity among Subpopulations of a Single Mouse Mammary Tumor: Heterogeneity in Phenotypic Stability. *Invasion Metastasis*, 3, 22-31.
- Morad, G., Carman, C. V., Hagedorn, E. J., Perlin, J. R., Zon, L. I., Mustafaoglu, N., . . . Moses, M. A. (2019). Tumor-Derived Extracellular Vesicles Breach the Intact Blood-Brain Barrier via Transcytosis. *ACS Nano*, 13(12), 13853-13865. doi:10.1021/acsnano.9b04397

- Murray, N. P. (2017). Treatment of Minimal Residual Disease in Breast Cancer: A Longitudinal Case Study. *Cureus*, 9(7), e1521. doi:10.7759/cureus.1521
- Navarro, P., Gomez, M., Pizarro, A., Gamallo, C., Quintanilla, M., & Cano, A. (1991). A role for the E-cadherin cell-cell adhesion molecule during tumor progression of mouse epidermal carcinogenesis. *J Cell Biol*, 115(2), 517-533. doi:10.1083/jcb.115.2.517
- Neagu, M. R., Gill, C. M., Batchelor, T. T., & Brastianos, P. K. (2015). Genomic profiling of brain metastases: current knowledge and new frontiers. *Chin Clin Oncol*, 4(2), 22. doi:10.3978/j.issn.2304-3865.2015.06.04
- Nussbaum, E. S., Djalilian, H. R., Cho, K. H., & Hall, W. A. (1996). Brain metastases. Histology, multiplicity, surgery, and survival. *Cancer*, 78(8), 1781-1788. doi:10.1002/(sici)1097-0142(19961015)78:8<1781::Aid-cnrcr19>3.0.Co;2-u
- Ohsawa, K., Imai, Y., Sasaki, Y., & Kohsaka, S. (2004). Microglia/macrophage-specific protein Iba1 binds to fimbrin and enhances its actin-bundling activity. *J Neurochem*, 88(4), 844-856. doi:10.1046/j.1471-4159.2003.02213.x
- Padmanaban, V., Krol, I., Suhail, Y., Szczerba, B. M., Aceto, N., Bader, J. S., & Ewald, A. J. (2019). E-cadherin is required for metastasis in multiple models of breast cancer. *Nature*, 573(7774), 439-444. doi:10.1038/s41586-019-1526-3
- Perrais, M., Chen, X., Perez-Moreno, M., & Gumbiner, B. M. (2007). E-cadherin homophilic ligation inhibits cell growth and epidermal growth factor receptor signaling independently of other cell interactions. *Mol Biol Cell*, 18(6), 2013-2025. doi:10.1091/mbc.e06-04-0348
- Petrova, Y. I., Schecterson, L., & Gumbiner, B. M. (2016). Roles for E-cadherin cell surface regulation in cancer. *Mol Biol Cell*, 27(21), 3233-3244. doi:10.1091/mbc.E16-01-0058
- Pukrop, T., Dehghani, F., Chuang, H. N., Lohaus, R., Bayanga, K., Heermann, S., . . . Binder, C. (2010). Microglia promote colonization of brain tissue by breast cancer cells in a Wnt-dependent way. *Glia*, 58(12), 1477-1489. doi:10.1002/glia.21022
- Pukrop, T., Klemm, F., Hagemann, T., Gradl, D., Schulz, M., Siemes, S., . . . Binder, C. (2006). Wnt 5a signaling is critical for macrophage-induced invasion of breast cancer cell lines. *Proc Natl Acad Sci U S A*, 103(14), 5454-5459. doi:10.1073/pnas.0509703103
- Quail, D. F., & Joyce, J. A. (2013). Microenvironmental regulation of tumor progression and metastasis. *Nat Med*, 19(11), 1423-1437. doi:10.1038/nm.3394
- Rietkotter, E., Bleckmann, A., Bayerlova, M., Menck, K., Chuang, H. N., Wenske, B., . . . Pukrop, T. (2015). Anti-CSF-1 treatment is effective to prevent carcinoma invasion induced by monocyte-derived cells but scarcely by microglia. *Oncotarget*, 6(17), 15482-15493. doi:10.18632/oncotarget.3855
- Romeo, E., Caserta, C. A., Rumio, C., & Marcucci, F. (2019). The Vicious Cross-Talk between Tumor Cells with an EMT Phenotype and Cells of the Immune System. *Cells*, 8(5). doi:10.3390/cells8050460
- Rosso, M., Majem, B., Devis, L., Lapyckyj, L., Besso, M. J., Llauro, M., . . . Vazquez-Levin, M. H. (2017). E-cadherin: A determinant molecule associated with ovarian cancer progression, dissemination and aggressiveness. *PLoS One*, 12(9), e0184439. doi:10.1371/journal.pone.0184439

- Schmid, P., Adams, S., Rugo, H. S., Schneeweiss, A., Barrios, C. H., Iwata, H., . . . Investigators, I. M. T. (2018). Atezolizumab and Nab-Paclitaxel in Advanced Triple-Negative Breast Cancer. *N Engl J Med*, 379(22), 2108-2121. doi:10.1056/NEJMoa1809615
- Schmid, P., Cortes, J., Pusztai, L., McArthur, H., Kummel, S., Bergh, J., . . . Investigators, K.-. (2020). Pembrolizumab for Early Triple-Negative Breast Cancer. *N Engl J Med*, 382(9), 810-821. doi:10.1056/NEJMoa1910549
- Sener, E., Sipal, S., & Gundogdu, C. (2016). Comparison of Microvessel Density with Prognostic Factors in Invasive Ductal Carcinomas of the Breast. *Turk Patoloji Derg*, 32(3), 164-170. doi:10.5146/tjpath.2016.01366
- Sherry, M. M., Greco, F. A., Johnson, D. H., & Hainsworth, J. D. (1986). Metastatic breast cancer confined to the skeletal system. An indolent disease. *Am J Med*, 81(3), 381-386. doi:10.1016/0002-9343(86)90286-x
- Shiono, S., Ishii, G., Nagai, K., Yoshida, J., Nishimura, M., Murata, Y., . . . Ochiai, A. (2005). Histopathologic prognostic factors in resected colorectal lung metastases. *Ann Thorac Surg*, 79(1), 278-282; discussion 283. doi:10.1016/j.athoracsur.2004.06.096
- Siam, L., Bleckmann, A., Chuang, H. N., Mohr, A., Klemm, F., Barrantes-Freer, A., . . . Pukrop, T. (2015). The metastatic infiltration at the metastasis/brain parenchyma-interface is very heterogeneous and has a significant impact on survival in a prospective study. *Oncotarget*, 6(30), 29254-29267. doi:10.18632/oncotarget.4201
- Spill, F., Reynolds, D. S., Kamm, R. D., & Zaman, M. H. (2016). Impact of the physical microenvironment on tumor progression and metastasis. *Curr Opin Biotechnol*, 40, 41-48. doi:10.1016/j.copbio.2016.02.007
- Tampellini, M., Berruti, A., Gerbino, A., Buniva, T., Torta, M., Gorzegno, G., . . . Dogliotti, L. (1997). Relationship between CA 15-3 serum levels and disease extent in predicting overall survival of breast cancer patients with newly diagnosed metastatic disease. *Br J Cancer*, 75(5), 698-702. doi:10.1038/bjc.1997.124
- van Dam, P. J., van der Stok, E. P., Teuwen, L. A., Van den Eynden, G. G., Illemann, M., Frentzas, S., . . . Vermeulen, P. B. (2017). International consensus guidelines for scoring the histopathological growth patterns of liver metastasis. *Br J Cancer*, 117(10), 1427-1441. doi:10.1038/bjc.2017.334
- Vanharanta, S., & Massague, J. (2013). Origins of metastatic traits. *Cancer Cell*, 24(4), 410-421. doi:10.1016/j.ccr.2013.09.007
- Wong, S. H. M., Fang, C. M., Chuah, L. H., Leong, C. O., & Ngai, S. C. (2018). E-cadherin: Its dysregulation in carcinogenesis and clinical implications. *Crit Rev Oncol Hematol*, 121, 11-22. doi:10.1016/j.critrevonc.2017.11.010
- Wu, C., Orozco, C., Boyer, J., Leglise, M., Goodale, J., Batalov, S., . . . Su, A. I. (2009). BioGPS: an extensible and customizable portal for querying and organizing gene annotation resources. *Genome Biol*, 10(11), R130. doi:10.1186/gb-2009-10-11-r130
- Wu, S. G., Li, H., Tang, L. Y., Sun, J. Y., Zhang, W. W., Li, F. Y., . . . He, Z. Y. (2017). The effect of distant metastases sites on survival in de novo stage-IV breast cancer: A SEER database analysis. *Tumour Biol*, 39(6), 1010428317705082. doi:10.1177/1010428317705082

- Xing, F., Kobayashi, A., Okuda, H., Watabe, M., Pai, S. K., Pandey, P. R., . . . Watabe, K. (2013). Reactive astrocytes promote the metastatic growth of breast cancer stem-like cells by activating Notch signalling in brain. *EMBO Mol Med*, 5(3), 384-396. doi:10.1002/emmm.201201623
- Zhao, B., Li, L., Lei, Q., & Guan, K. L. (2010). The Hippo-YAP pathway in organ size control and tumorigenesis: an updated version. *Genes Dev*, 24(9), 862-874. doi:10.1101/gad.1909210

Acknowledgements

My thesis was like a journey. It started at the University in the lab of Michael Krahn and ended at the University Hospital in the lab of Tobias Pukrop. I was lucky to have two mentors who supported me during this stressfull but overall fascinating and valuable time I would not want to have missed.

First, I would like to thank my doctoral mentor Prof. Dr. Dr. Michael P. Krahn for offering me the opportunity to start my doctoral thesis in his laboratory and for the supervision from afar in the following years.

Equally, I want to thank my mentor Prof. Dr. Tobias Pukrop for offering me the opportunity to continue my thesis in his laboratory in Regensburg. Thank you for adopting me into your scientific lab family and for your intensive supervision during the whole time. It was a great pleasure to work with you, learn from you and laugh with you.

Danke an all meine lieben Kollegen in den beiden Laboren, vor allem Barbara, Elena, Ellinor, Gunnar, Laura und Raquel. Es hat immer Spaß gemacht mit euch zu arbeiten und zu diskutieren und ich werde diese Zeit nie vergessen. Ein besonderer Dank gilt dir, Elena, für deine großartige technische Unterstützung. Du hattest immer ein offenes Ohr und deine helfenden Hände waren unbezahlbar.

Ein herzliches Dankeschön geht an meine Eltern Claudia und Michael. Ihr habt mich von Anfang an bei meiner wissenschaftlichen Karriere unterstützt und es mir ermöglicht, meinen eigenen Weg zu gehen. Ich danke euch für alles!

Zuletzt möchte ich mich bei meinem Lebensgefährten Eric bedanken. Seit über zehn Jahren stehst du an meiner Seite und unterstützt mich auf meinem Weg. 2020 werden wir wohl nie vergessen, aber zusammen schaffen wir alles und jetzt heißt es auf zu neuen Ufern!

List of publications

Blazquez, R., **Sparrer, D.**, Wendl, C., Evert, M., Riemenschneider, M. J., Krahn, M. P., ... & Pukrop, T. (2020). The macro-metastasis/organ parenchyma interface (MMPI) - A hitherto unnoticed area. *Seminars in Cancer Biology* 60, 324-333.

Blazquez, R., Rietkötter, E., Wenske, B., Wlochowicz, D., **Sparrer, D.**, Vollmer, E., ... & Pukrop, T. (2020). LEF1 supports metastatic brain colonization by regulating glutathione metabolism and increasing ROS resistance in breast cancer. *International Journal of Cancer* 146(11), 3170-3183.

Zimmermann, V., Wittmann, J., **Sparrer, D.**, Mühlberger, A., & Shiban, Y. (2017). The generalization of conditioned startle responses from known to unknown lies. *Learning and Motivation*, 59, 64-69.